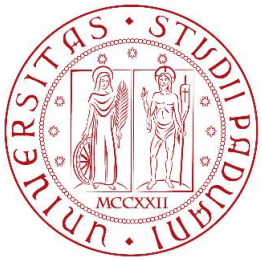

Università degli studi di Padova

Dipartimento di Fisica e Astronomia "Galileo Galilei"
Corso di Laurea Magistrale in Fisica

Tesi di Laurea

Study of the formation of circumbinary planets and comparison with SPHERE data

Candidato:
Tiziano Scatolin

Relatore:
Prof. Francesco Marzari
Correlatori:
Dott. Silvano Desidera
Dott.ssa Valentina D'Orazi

Anno Accademico 2017/2018

Ringraziamenti

Vorrei dedicare la riuscita di questo lavoro a tutte le persone che hanno contribuito alla sua realizzazione, chi in un modo e chi nell'altro. A tutti loro sono rivolti i miei sentiti ringraziamenti.

Premetto che le difficoltà incontrate in questo percorso non sono state poche, e che le forze o le motivazioni per continuare non sempre erano presenti. Ad ogni modo è con grande soddisfazione che mi ritrovo alla fine del mio percorso accademico, una meta da tanto tempo agognata. Ora che ci sono arrivato, è inevitabile sentire un pizzico di malinconia e nostalgia per il tempo passato tra i banchi che non si ripeterà più, e al contempo provo una buona dose di spavento mista a fiducia per il futuro.

Inizio col ringraziare i miei relatori, che mi hanno sempre seguito, consigliato ed aiutato durante il mio percorso di tesi, in particolare il Prof. Francesco Marzari, il Dott. Silvano Desidera e la Dott.ssa Valentina D'Orazi. Un ringraziamento particolare va anche al controrelatore, il Dott. Raffaele Gratton, i cui consigli e correzioni si sono rivelati davvero utili per rifinire il lavoro.

Sicuramente devo tutto ai miei genitori, Laura e Maurizio, i quali mi hanno sostenuto con continuità, sia economicamente che psicologicamente, nel prosieguo dei miei studi anche quando i periodi non erano dei più rosei. Si dà spesso per scontato che queste opportunità siano dovute, invece non sono sempre possibili e richiedono molto sacrificio, per questo assumono ancora maggior valore.

Un grazie va anche a nonna Luigia, figura molto importante, sempre disponibile ad aiutarmi, spronarmi e farmi credere in me stesso. Ho inoltre apprezzato il supporto e la vicinanza delle zie Nicoletta e Sara, e ai cugini Cinzia e Alessandro.

Gli amici dell'università sono stati fondamentali, grazie a loro ho affrontato con più serenità questi cinque (e più) anni nella città patavina: Lorenzo e Isacco, con i quali il viaggio in treno e le pause tra una lezione e l'altra non erano più pesanti, tra una partita a carte e mille dubbi fisici; Chiara e Sara, per le esperienze di laboratorio, i vari momenti di pausa e le preparazioni agli esami fatte assieme; Gioele, per sdrammatizzare ogni cosa ed essere sempre disponibile, ed infine Giammarco, per le feste e le infinite perle di saggezza che mi ha dispensato.

Ultimi - ma non meno importanti - gli amici, sia quelli delle superiori che quelli che ho ritrovato o conosciuto più recentemente (che non cito per non dilungarmi troppo), con i quali ho vissuto intense emozioni in questi anni tra serate, viaggi, sport e feste. La loro compagnia, grazie alla quale ho potuto distrarmi e ricaricarmi, è stata indispensabile. Vorrei poi ringraziare anche la mia ragazza, Maria Chiara, per esserci stata in questi ultimi mesi, supportandomi.

Infine a tutti coloro - amici, parenti o conoscenti - che, seppur non citati, sono stati presenti, esprimo la mia sincera riconoscenza.

> Remember to look up at the stars and not down at your feet. Try to make sense of what you see and wonder about what makes the universe exist. Be curious. And however difficult life may seem, there is always something you can do and succeed at. It matters that you don't just give up.
>
> *Stephen William Hawking*

Contents

Sommario

Questa tesi riguarda l'ambito dell'astrofisica della formazione planetaria. In particolare, è focalizzata sullo studio di V4046 Sgr, un sistema binario di ~ 20 milioni di anni, e del disco circumbinario che lo circonda, discutendo l'evidenza delle tracce di eventuali pianeti in orbita attorno a queste stelle. Infatti, gli obiettivi di questo lavoro risiedono sia nell'analisi di alcune caratteristiche del disco che nello studio della possibilità della formazione di pianeti circumbinari in questo sistema attraverso il confronto diretto con i dati osservativi dello strumento SPHERE, installato nel VLT in Cile.

Questo lavoro è strutturato come riportato di seguito, dove vengono delineate le sue principali caratteristiche, obiettivi e risultati.

Il Capitolo 1 fornisce una panoramica sui dischi protoplanetari, in particolare per quanto riguarda la loro struttura ed evoluzione, presentando i vari meccanismi che hanno portato alla struttura finale dei dischi che si osservano ed includendo argomentazioni sia teoriche che osservative.

Il Capitolo 2, invece, considera il caso specifico dei dischi circumbinari, partendo dalla descrizione dell'interazione tra il disco e la binaria e riportando alcuni esempi concreti di dischi circumbinari studiati. Inoltre, una Sezione è dedicata ai pianeti circumbinari, per quanto riguarda le loro caratteristiche e la loro individuazione, soprattutto attraverso la tecnica del direct imaging.

Successivamente all'introduzione generale sopracitata sulla fisica alla base di questo lavoro, la descrizione dello strumento di nuova generazione SPHERE è riportata nel Capitolo 3. In particolare, oltre a presentare le sue principali caratteristiche, moduli e capacità, una Sezione è riservata alle varie tecniche di direct imaging sfruttate da SPHERE, mentre la parte finale fornisce i più recenti dati SPHERE riguardanti le scoperte di pianeti e dischi protoplanetari, ed il collegamento tra tali scenari.

Data questa panoramica - fondamentale per la comprensione dell'argomento di questo lavoro, è possibile concentrarsi sul tema di questa tesi, ovvero il sistema binario V4046 Sgr: la sua descrizione generale, comprese le principali caratteristiche della binaria e del disco che la circonda, è presentata nel Capitolo 4.

Una delle peculiarità del disco attorno a V4046 Sgr è l'ombra estesa in direzione radiale che si nota nelle immagini di SPHERE. Il Capitolo 5 è pertanto dedicato allo studio di quest'ombra: invocando certe ipotesi sulla binaria e sul profilo del disco per poterne spiegare la presenza, è stato possibile creare un modello del disco e confrontare il range del raggio dell'ombra fornito dal modello con il valore osservato.

L'ultima parte di questo lavoro è descritta nel Capitolo 6 e comporta simulazioni numeriche dell'evoluzione del disco di polvere che circonda V4046 Sgr. In particolare, un programma ad N corpi è stato utilizzato per simulare l'evoluzione delle particelle di polvere in presenza di pianeti, con lo scopo di determinare quanti pianeti potrebbero riprodurre i dati osservativi, che mostrano l'esistenza di due anelli nel disco, e quali sarebbero le loro caratteristiche, tenendo conto dei limiti di rivelabilità dello strumento.

Inoltre, una piccola Sezione presenta il confronto tra la distribuzione della polvere, in base alle sue dimensioni, osservata nel disco con i risultati corrispondenti delle simulazioni.

Il Capitolo 7 trae le conclusioni della tesi, elencando i principali risultati raggiunti e le limitazioni incontrate, che potrebbero essere superate da studi futuri, sfruttando nuovi strumenti in grado di rivelare i pianeti di dimensioni Saturniane, poiché le nostre simulazioni prevedono la presenza di due pianeti delle dimensioni di Saturno/Nettuno orbitanti tra i due anelli osservati, e di fornire dati migliori riguardo l'emissione della polvere, per poter fornire stime più accurate sull'ombra osservata, sulla distribuzione della polvere in base alle dimensioni e sulle altre caratteristiche del disco.

Infine, l'Appendice A fornisce gli elementi fisici principali richiesti in questo lavoro.

Abstract

This thesis regards the research field concerning astrophysics of planet formation. In particular, it is focused on the study of the young ($\sim$ 20 Myr old) binary system V4046 Sgr and of the circumbinary disk surrounding it, discussing the evidence of the traces of eventual planets orbiting these stars. In fact, the aims of this work reside in both the analysis of certain disk's features and the study of the possibility for the formation of circumbinary planets in this system through the direct comparison with observational data from the SPHERE instrument, installed in the VLT in Chile.

This work is structured as reported below, where its main features, objectives and results are outlined.

Chapter 1 provides an overview of protoplanetary disks, in particular as concerns their structure and evolution, presenting the various mechanisms which led to the final structure of the disks we observe, and including both theoretical and observational argumentations.

Instead, Chapter 2 considers the specific case of circumbinary disks, starting from the description of the interaction between the disk and the binary host and then reporting some concrete examples of studied circumbinary disks. Moreover, a Section is dedicated to circumbinary planets, as regards their features as well as their detection, especially through the direct imaging technique.

After this abovementioned general introduction about the physics underlying this work, the description of the new-generation SPHERE instrument is reported in Chapter 3. In particular, besides introducing its main features, modules and capabilities, a Section is reserved for the various direct imaging techniques exploited by SPHERE, whereas the final part provides the latest SPHERE data concerning the discoveries of planets as well as protoplanetary disks, and the link between these scenarios.

At this point, given this overview - needed for the comprehension of the topic of this work, it is possible to concentrate on the subject of this thesis, namely the binary system V4046 Sgr: its general description, including the main features of the binary as well as the disk surrounding it, is presented in Chapter 4.

One of the peculiarities of the disk around V4046 Sgr is the radially-extended shadow it exhibits in the SPHERE images. Chapter 5 is then dedicated to the study of this shadow: invoking certain assumptions on the binary and on the profile of the disk in order to account for its presence, it has been possible to model the disk and compare the range of the radius of the shadow provided by the model with the observed value.

The last part of this work is described in Chapter 6 and involves numerical simulations of the evolution of the dusty disk surrounding V4046 Sgr. In particular, an N-body program has been used in order to simulate the evolution of the dust particles in presence of planets, with the purpose to determine how many planets could reproduce the observational data, which show the evidence of two rings in the disk, and what their features are - taking into account the detectable limits of the instrument. Furthermore,

a small Section presents the comparison between the observed dust-size distribution over the disk with the corresponding results from the simulations.

Chapter 7 draws the conclusions of the thesis, listing the main achieved results as well as the limitations encountered, which could be overcome by future studies exploiting new instruments which are able to detect Saturnian-sized planets, since our simulations predict the presence of two Saturn/Neptune-sized planets orbiting between the two observed rings, and to provide more detailed dust emission data, in order to better constraint the observed shadow, the dust-size distribution and the other disk's features.

Finally, Appendix A provides the main physical elements required in this work.

Chapter 1

Protoplanetary disks

Protoplanetary disks of gas and dust that are observed around young stars, during the first few million years of their evolution, give rise to planets formation. The formation of disks takes place because stars are born from rarefied gas (with particle number density $n \sim 10^5$ cm^{-3}) that has too much angular momentum to collapse directly to stellar densities ($n \sim 10^{24}$ cm^{-3}).

When the gas has settled into a disk around a young star, its specific angular momentum grows with radius: this allows disks survive as well-defined quasi-equilibrium structures. Angular momentum loss from (or redistributed within) the disk gas is essential to accrete, and this process requires time scales that are much longer than the orbital or dynamical time scale.

For a first study of the temperature, density, and composition profiles of protoplanetary disks, we assume - following what has been described in [1] - that the disk is a static structure.

We will finally describe the evolution of protoplanetary disks.

1.1 Protoplanetary disk structure

The inheritage of initial mass, size and chemical composition of protoplanetary disks comes from their relative star formation environment, whereas their subsequent evolution may be conditioned by environmental effects such as stellar radiation or ongoing gas accretion.

After disks formation, the dominant environmental effects are usually caused by close binary companions and external radiation produced by other stars within the cluster.

Molecular clouds do not resemble homogeneous structures: actually, they show turbulence effects, as their density and velocity fields exhibit structure across a large range of spatial scales. Then, any collapsing region will possess some angular momentum ($\neq 0$), consequently leading to the formation of disks or even binary companions around newly formed stars. Inside molecular clouds, stars originate from dense agglomerations of gas known as molecular cloud cores. These cores extend over typical scales of $\sim 0,1$ pc and densities of $n \sim 10^5$ cm^{-3}.

At these scales the dynamical importance of rotation is secondary, in fact the typical ratio of rotational to gravitational energy, which plays the most important role, in dense cores results

$$\beta \equiv \frac{E_{rot}}{|E_{grav}|} \approx 0,02.$$

Anyway, this small value corresponds to very elevated reservoirs of angular momentum. For instance, assuming a uniform density spherical core in solid body rotation of a Solar mass and radius of $R = 0,05$ pc, this core results to possess an angular momentum of about three to four orders of magnitude in excess of the total angular momentum in the Solar System[1]:

$$J_{core} \approx 10^{54} \text{ g cm}^2 \text{ s}^{-1}.$$

1.1.1 Classification of Young Stellar Objects

Young Stellar Objects (YSOs) are usually classified by evaluating the slope of the SED[2] in the infrared (IR) region of the spectrum, through the definition of a parameter

$$\alpha_{IR} \equiv \frac{\Delta \log(\lambda F_\lambda)}{\Delta \lambda}.$$

After measuring the SED, YSOs are distinguished into four classes based on the magnitude of α_{IR}, as described in [1].

The classification is structured as follows:

- **Class 0**: the SED peaks in the far-IR;
- **Class I**: the SED between near- and mid-IR wavelengths is approximately flat or rising;
- **Class II**: the SED falls noticeably between near- and mid-IR wavelengths;
- **Class III**: the IR SED is essentially that of a stellar photosphere.

It is useful to underline the presence of an older classification scheme for optically visible pre-main-sequence stars, based on the equivalent width of the Hα line, which involves the last two classes: classical T Tauri stars[3] (normally these are Class II sources) have an equivalent width of Hα that is in excess of 10 Å, whereas weak-lined T Tauri stars (Class III sources) have an Hα equivalent width that is less than 10 Å.

Figure 1.1 shows the main features of each stellar class type. The classification scheme for YSOs is actually empirical, however it finds a theoretical interpretation as an evolutionary sequence, strarting from the least evolved objects: the Class 0 YSOs, which are observed during the earliest stages of cloud collapse. Consequently, if there is a protostar at the center of the cloud, it results deeply embedded within optically thick gas and dust, being not visible.

As regards the Class I sources, they are the first objects in which disks are detected, even though these YSOs are still surrounded by an envelope of infalling material; they often produce outflows or jets.

---

[1] With an assumed angular velocity $\omega = \frac{J_{core}}{0,4 \cdot M_\odot R^2} \sim 5,3 \cdot 10^{-14}$ rad·s^{-1}; the corresponding rotational period is $T = 2\pi/\omega \sim 10^{14}$ s.

[2] The Spectral Energy Distribution (SED) measures the distribution of flux as a function of frequency or wavelength (F_λ).

[3] T Tauri stars are better presented in Section 4.1.

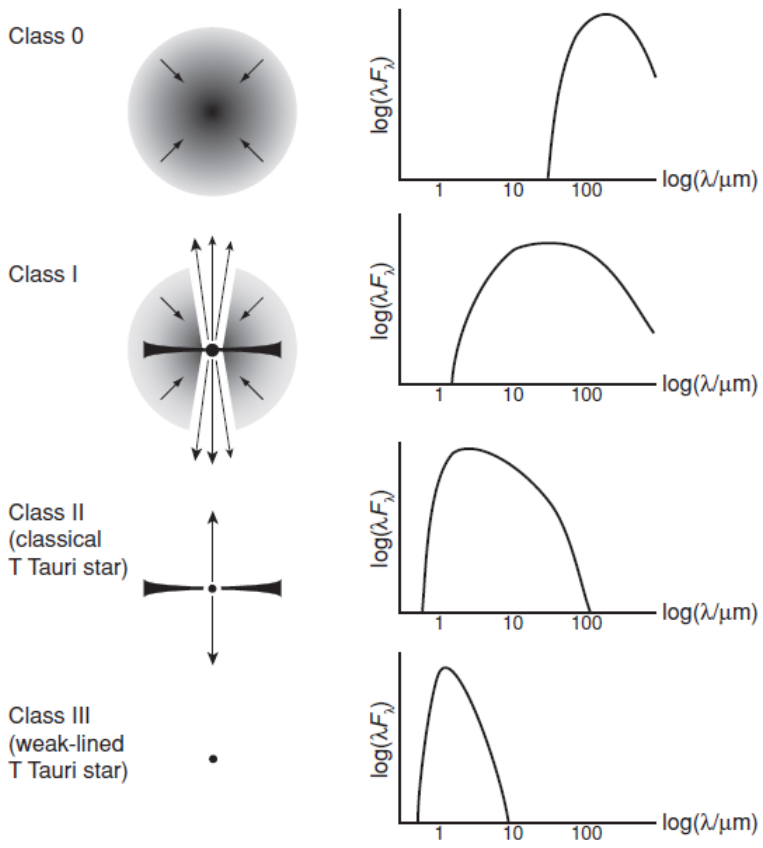

Figure 1.1: *Classification scheme for Young Stellar Objects, reported in [1].*

Focusing on Class II sources, they represent a later evolutionary phase in which the accretion of the envelope has mostly occurred. The SED of Class II sources results as the sum of that from the now optically visible star with the emission of its circumstellar disk. In Class II sources it has been observed UV excess, too, and this is caused by accretion hotspots on the stellar surface as the effect of the gas flow in the disk on to the star. This UV (and IR) excess, indicating the presence of a disk, is peculiar of the youngest stellar accumulations, but occurs in a substantially decreased amount after a few million years, namely the typical lifetime of protoplanetary disks around low mass stars.

Finally, after disks dissipation, we find what is called a Class III YSO, a pre-main-sequence star with scarce or absent presence of primordial circumstellar material. Among its features we underline its location above the main sequence in a Hertzprung–Russell diagram and a strong X-ray activity, or in some cases evidence for surrounding debris disks.

1.1.2 Vertical structure

Generally, the equilibrium structure of gas orbiting a star is determined thanks to the solutions (for a steady-state solution) of the hydrodynamic equations and the Poisson equation for the gravitational potential.

Regarding protoplanetary disks, anyway, it is possible to simplify the problem considering these assumptions:

- the total disk mass is assumed to be $M_{disk} \ll M_\star$, and then we can neglect the

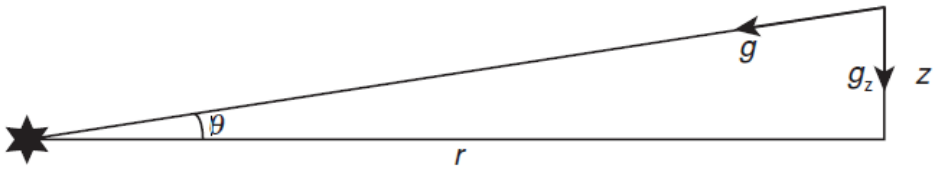

Figure 1.2: *The scheme of vertical equilibrium between the vertical component of the star's gravity g_z and a pressure gradient, in geometrically thin disks (taken from [1]).*

gravitational potential of the disk and consider only stellar gravity;

- h, which is the vertical thickness of the disk, is invariably small if compared to the orbital radius ($h/r \ll 1$).

The derivation of the structure of a geometrically thin protoplanetary disk starts from considering the vertical force equilibrium at height z above the mid-plane in a disk orbiting at cylindrical radius r around a star of mass $M_\star$: the vertical component of the gravitational acceleration (Figure 1.2)

$$g_z = g \sin\theta = \frac{GM_\star}{(r^2+z^2)} \frac{z}{(r^2+z^2)^{1/2}} \tag{1.1.1}$$

must exactly contrast the acceleration generated by the vertical pressure gradient[4] in the gas $(1/\rho)(\mathrm{d}P/\mathrm{d}z)$.

Considering the disk as vertically isothermal[5] and being the pressure $P = \rho c_s^2$, where c_s is the sound speed, we obtain

$$c_s^2 \frac{\mathrm{d}\rho}{\mathrm{d}z} = -\frac{GM_\star z}{(r^2+z^2)^{3/2}}\rho,$$

whose solution is

$$\rho = C \exp\left[\frac{GM_\star}{c_s^2(r^2+z^2)^{1/2}}\right]$$

where the constant of integration C depends on the mid-plane density.

However, having a thin disk implies that $z \ll r$ and $g_z \approx \Omega^2 z$, being $\Omega = \sqrt{GM_\star/r^3}$ the Keplerian angular velocity. In this condition the vertical density profile has the following equation:

$$\rho = \rho_0 \mathrm{e}^{-z^2/2h^2},$$

where the mid-plane density ρ_0 can be presented in function of the full-plane surface density Σ as

$$\rho_0 = \frac{1}{\sqrt{2\pi}} \frac{\Sigma}{h}$$

[4]The hydrostatic equilibrium equation is

$$\frac{1}{\rho}\frac{\mathrm{d}P}{\mathrm{d}r} = -\frac{GM_\star}{r^2}.$$

[5]A reasonable assumption if stellar irradiation determines the temperature of the gas.

and h, the vertical disk scale height, is given by

$$h \equiv \frac{c_s}{\Omega}. \tag{1.1.2}$$

It is finally important to underline that this means that the geometric thickness of the disk $h/r = \mathscr{M}^{-1}$, where the Mach number of the flow is $\mathscr{M} = v_K/c_s$ ($v_K = \Omega r$ is the Keplerian velocity).

1.1.3 Radial force balance

In order to find the orbital velocity of disk gas $v_{\phi,gas}$, we start from considering the momentum equation for an unmagnetized and inviscid fluid:

$$\frac{\partial \mathbf{v}}{\partial t} + (\mathbf{v} \cdot \nabla)\mathbf{v} = -\frac{1}{\rho}\nabla P - \nabla\Phi, \tag{1.1.3}$$

where $\mathbf{v}$ is the velocity, ρ the density, P the pressure and Φ the gravitational potential. Imposing now a stationary axisymmetric flow[6], in which the potential of the star is prominent and dominates, the radial component of the momentum Equation 1.2.1 implies that the orbital velocity of the gas is given by

$$\frac{v_{\phi,gas}^2}{r} = \frac{GM_\star}{r^2} + \frac{1}{\rho}\frac{\mathrm{d}P}{\mathrm{d}r}, \tag{1.1.4}$$

where the left member is an inertial term, related to the fact that the gas rotates with a velocity $v_{\phi,gas}$. Usually, the pressure near the disk mid-plane decreases outward, then the radial pressure gradient is negative and, consequently, the azimuthal velocity of the gas is slightly inferior than the Keplerian velocity[7] of a point mass particle orbiting at the same radius. This difference can be quantified by writing the variation of the mid-plane pressure as a power-law near a reference radius r_0,

$$P = P_0\left(\frac{r}{r_0}\right)^{-n}$$

where $P_0 = \rho_0 c_s^2$. Replacing it in Equation 1.1.4, it turns out that

$$v_{\phi,gas} = v_K\left(1 - n\frac{c_s^2}{v_K^2}\right)^{1/2}.$$

Clearly, considering a geometrically thin disk[8], the deviation from Keplerian velocity is very small - of the order of $(h/r)^2$.

As regards the motion of the gas alone, this difference is absolutely negligible and it is possible to assume the gas moves at the Keplerian velocity. Anyway, in the evolution of solid bodies within the disk, the importance of the slightly lower gas velocity is crucial because it results in aerodynamic drag and consequent orbital decay.

---

[6] This means that $\frac{\partial}{\partial t} = 0$ and there is independence of ϕ in spherical coordinates.

[7] $v_K = \sqrt{\frac{GM_\star}{r}}$.

[8] Being the scale height h (Equation 1.1.2) small if compared to the radius r.

1.1.4 Radial temperature profile of passive disks

Reaching thermal equilibrium in a disk generally requires much less time than what is necessary for evolution of both the disk and the star. Then, the equilibrium between cooling and heating determines the temperature profile of the disk, for which there are two main sources:

- *Intercepted stellar radiation*, which is usually absorbed by dust and then reradiated at longer wavelengths[9].
- *Dissipation of gravitational potential energy*, when matter in the disk spirals directed to the star.

Both of these sources generates a heating per unit area which decreases rapidly with increasing distance from the star. However, heating due to the ambient radiation field provided by nearby stars can become relevant whether the disk extends out to large enough radii, and avoids the disk temperature drops below some floor level[10].

The ratio of accretional heating over stellar irradiation depends on the accretion rate and the quantity of intercepted stellar radiation. Globally, the radiation emitted by inspiralling matter will be an amount of energy per unit mass which is approximately identified by the gravitational potential at the stellar surface, $GM_\star/R_\star$; on the other hand, the disk will intercept a fraction $f < 1$ of the stellar radiation $L_\star$.

Using a reference value $f = 1/4$, the accretion rate $\dot{M}$ above which accretional heating dominates can be roughly given by

$$\frac{GM_\star \dot{M}}{R_\star} = \frac{1}{4} L_\star.$$

At early epochs, namely when accretion is strong, the thermal structure of disks is mostly due to internal heating generated by the accretion, whereas at later times reprocessing of stellar radiation becomes dominant.

Razor-thin disks

The shape of a passive protoplanetary disk determines the temperature profile and spectral energy distribution of the disk.

Here, we consider a flat razor-thin disk in the equatorial plane absorbing all incident stellar radiation and re-emitting it locally like a single temperature blackbody (neglecting the relatively small back-warming of the star by the disk).

We start from taking a surface in the plane of the disk, distant r from a star of radius $R_\star$ which is assumed to be a sphere of constant brightness of intensity $I_\star$. Using spherical polar coordinates and imposing that the axis of the reference system is directed towards the center of the star, as shown in Figure 1.3, the stellar flux passing through this surface is

$$F = \int I_\star \sin\theta \cos\phi \mathrm{d}\Omega$$

where $\mathrm{d}\Omega = \sin\theta \mathrm{d}\theta \mathrm{d}\phi$ represents the element of solid angle, and the factor $\sin\theta$ in the integral means that the radiation must be perpendicular to the surface to give

[9] In *passive disks* this is the prominent heating contribution.

[10] For normal star forming environments this floor temperature should be $10 \div 30$ K.

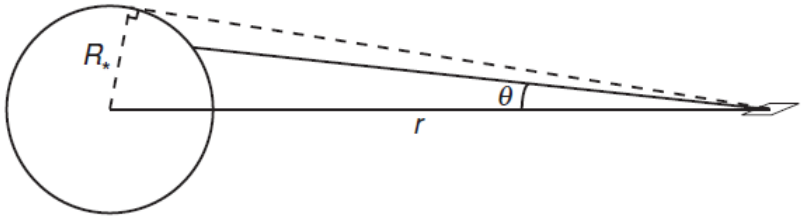

Figure 1.3: *Geometry for calculating the radial temperature profile of a razor-thin protoplanetary disk, taken from [1]. Integrating over the visible stellar surface allows to obtain the flux through the surface of the disk at distance r from the star.*

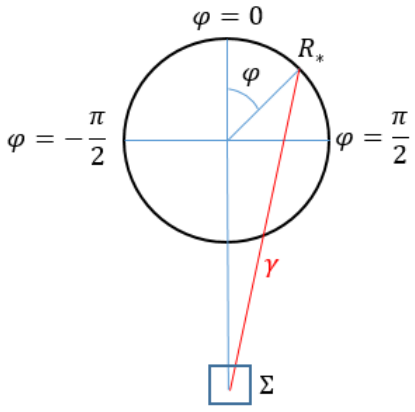

Figure 1.4: *Illustration of the angle ϕ used to compute the flux, viewed along the radial direction and over the disk plane, in perspective. The red line is a radiation ray which incides on the surface Σ.*

contribution to the flux, and the other factor $\cos\phi$ considers the decreasing contribution to the radiation coming from the non-central zones of the star when deviating from $\phi = 0$, as shown in Figure 1.4. Note that only the flux coming from the top half of the star will be counted[11], so the constraints on the integral are the following:

$$-\frac{\pi}{2} < \phi \leq \frac{\pi}{2}, \qquad 0 < \theta < \arcsin\left(\frac{R_\star}{r}\right).$$

Consequently, the flux integral becomes

$$F = I_\star \int_{-\frac{\pi}{2}}^{\frac{\pi}{2}} \cos\phi \mathrm{d}\phi \int_0^{\arcsin\frac{R_\star}{r}} \sin^2\theta \mathrm{d}\theta,$$

which results

$$F = I_\star \left[\arcsin\left(\frac{R_\star}{r}\right) - \left(\frac{R_\star}{r}\right)\sqrt{1-\left(\frac{R_\star}{r}\right)^2}\right].$$

Since the brightness of a star with effective temperature $T_\star$ is $I_\star = \frac{\sigma T_\star^4}{\pi}$ ([1]), where σ is the Stefan–Boltzmann constant, we now equate F to the one-sided disk emission σT_{disk}^4, obtaining the radial temperature profile of a razor-thin disk

$$\left(\frac{T_{disk}}{T_\star}\right)^4 = \frac{1}{\pi}\left[\arcsin\left(\frac{R_\star}{r}\right) - \left(\frac{R_\star}{r}\right)\sqrt{1-\left(\frac{R_\star}{r}\right)^2}\right]. \tag{1.1.5}$$

The total disk luminosity is finally given by the integration over radii:

$$L_{disk} = 2\int_{R_\star}^{\infty} 2\pi r \sigma T_{disk}^4 \mathrm{d}r = \frac{1}{4}L_\star.$$

As a result, we can state that a flat passive disk extending all the way to the stellar equator is intercepted by a quarter of the stellar flux: it is clear, then, that a flat passive disk is predicted to be less luminous than the star.

If we consider the limit that $R_\star/r \ll 1$ (namely far from the stellar surface) and we then expand the right member of Equation 1.1.5 in a Taylor series[12], we obtain

$$T_{disk} \propto r^{-3/4} \tag{1.1.6}$$

as the limiting temperature profile of a thin, flat, passive disk.

Flared disks

In this Section we will consider a flared disk. Assuming that at radial distance r from the star the disk absorbs stellar radiation at a height h_p above the mid-plane, the disk is considered flared if the ratio h_p/r is a function increasing with radius. Peculiarities of flared disks are the following:

- all points on the surface of the disk have a clear line of sight to the star;

[11] To be consistent, we will equate that to radiation coming from only the top surface of the disk.

[12] Being $\arcsin x = x + \frac{x^3}{6} + \mathscr{O}(x^3)$ and $(1+x)^\alpha = 1 + \alpha x + \mathscr{O}(x)$, for $x \to 0$.

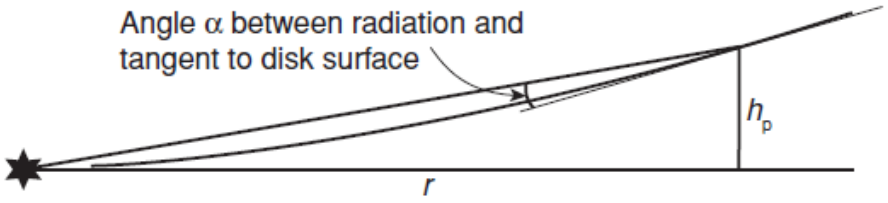

Figure 1.5: *Geometry for calculating the radial temperature profile of a flared protoplanetary disk, taken from [1]. Radiation from the star, at distance $r \gg R_\star$, is absorbed by the disk at height h_p above the mid-plane; α represents the angle between the tangent to the disk surface and the radiation.*

- the solid angle subtended by the disk, if seen from the star, is greater than a razor-thin disk.

Consequently, flared disks absorb more stellar radiation than flat disks, producing more elevated IR excesses. Moreover, the temperature profile is modified, changing the shape of the resulting SED.

The procedure to determine the temperature profile of a flared disk is the same as for a razor-thin disk, namely evaluating the flux by integrating over the part of the stellar surface visible from the disk surface at radius r: the exact calculation can be found in [1].

However, here we use an approximate method valid for $r \gg R_\star$, considering thus the star to be a point source of radiation. Stellar radiation, at distance r, is absorbed by the disk at height h_p above the mid-plane, but h_p is different from the disk scale height h: in fact, besides depending on the density, the absorption of stellar radiation also takes into account the opacity of the disk material to stellar photons[13]. Considering the geometry illustrated in Figure 1.5, the incident radiation and the local disk surface form an angle which is

$$\alpha = \frac{\mathrm{d}h_\mathrm{p}}{\mathrm{d}r} - \frac{h_\mathrm{p}}{r}.$$

The rate of heating per unit disk area at distance r is

$$Q_+ = 2\alpha\left(\frac{L_\star}{4\pi r^2}\right),$$

where the factor $2\times$ has been added because the disk has two sides and we have assumed that each point on the surface of the disk can view all of the stellar surface, and the factor $\alpha \sim \sin\alpha, \alpha \to 0$, considers the effective radiation flux perpendicular to the disk's surface. By equating Q_+ to the cooling by blackbody radiation rate

$$Q_- = 2\sigma T_{disk}^4,$$

the temperature profile becomes

$$T_{disk} = \left(\frac{L_\star}{4\pi\sigma}\right)^{1/4} \alpha^{1/4} r^{-1/2}.$$

[13]A third height is the height of the disk's photosphere, namely the surface at which the optical depth (described in the following Subsection) to the disk's own thermal radiation is $\tau = 2/3$.

Substituting $L_\star = 4\pi R_\star^2 \sigma T_\star^4$ (Stefan-Boltzmann's law) in the latter equation it is possible to obtain an equivalent expression:

$$\frac{T_{disk}}{T_\star} = \left(\frac{R_\star}{r}\right)^{1/2} \alpha^{1/4}.$$

Finally, it is reasonable to assume that the interior of an irradiated protoplanetary disk is isothermal.

Radiative equilibrium disks

As previously intoduced, we have always assumed that the stellar radiation intercepted by the disk is reradiated as a single temperature blackbody. However, for real disks the situation is more complex, because the dominant opacity is provided by dust, which absorbs relatively short wavelength starlight (at around 1 μm) more efficiently than it emits longer wavelength thermal radiation. The absorption and reradiation of stellar radiation for an optically thick disk in which dust is mixed evenly with the gas in the vertical direction is illustrated in Figure 1.6. Dust within a relatively thin surface layer, for which the optical depth[14] to grazing starlight $\tau \leq 1$, absorbs short wavelength stellar radiation; this layer is optically thin ($\tau \ll 1$) to the longer wavelength thermal radiation which the hot dust emits.

A consistent fraction of the incoming stellar flux - about 50% - is then reradiated directly to space, while the other (downward directed) half is absorbed by the interior of the disk, heating it. As a consequence, the local emission from the disk is the sum of a cool blackbody component from the disk interior with a warmer dilute blackbody originated in the surface layer.

Knowing the radiative properties of the dust, it is possible to calculate its temperature in the surface layer. Defining the emissivity ϵ as the ratio of the efficiency with which the dust emits or absorbs radiation relative to a blackbody surface[15], it results that dust is generally a good absorber of radiation at smaller wavelengths with respect to the particle size, because the emissivity drops at longer wavelengths. Considering spherical dust particles of radius s their emissivity is, approximately,

$$\begin{aligned} \epsilon &= 1, & \lambda \leq 2\pi s \\ \epsilon &= \left(\tfrac{\lambda}{2\pi s}\right)^{-1}, & \lambda > 2\pi s. \end{aligned}$$

This is the same as assuming that the wavelength dependence of the monochromatic opacity is $\kappa_\nu \propto \lambda^{-1}$. Exposing a dust particle at radius r to a stellar flux $F_\star = L_\star/(4\pi r^2)$, we determine its equilibrium temperature T_{dust} by balancing heating at a rate $\pi s^2 \epsilon_\star F_\star$ with cooling at a rate $4\pi s^2 \sigma T_{dust}^4 \epsilon_{dust}$[16]. Hence

$$\frac{T_{dust}}{T_\star} = \left(\frac{\epsilon_\star}{\epsilon_{dust}}\right)^{1/4} \left(\frac{R_\star}{2r}\right)^{1/2}. \tag{1.1.7}$$

In the case particles are small enough such that $\epsilon < 1$ for both absorption of stellar

[14] The optical depth is defined by $\tau \equiv \int_0^l \alpha(z)\mathrm{d}z$, where l is the thickness of the material through which the light travels and α is the attenuation coefficient of that material at a certain height z, namely the characterization of how easily it can be penetrated by a beam of light.

[15] Clearly, it is by definition a perfect absorber and emitter with $\epsilon = 1$.

[16] $\epsilon_\star$ is the weighted emissivity for absorption of the stellar radiation spectrum and ϵ_{dust} is the weighted emissivity for the dust particle's thermal emission.

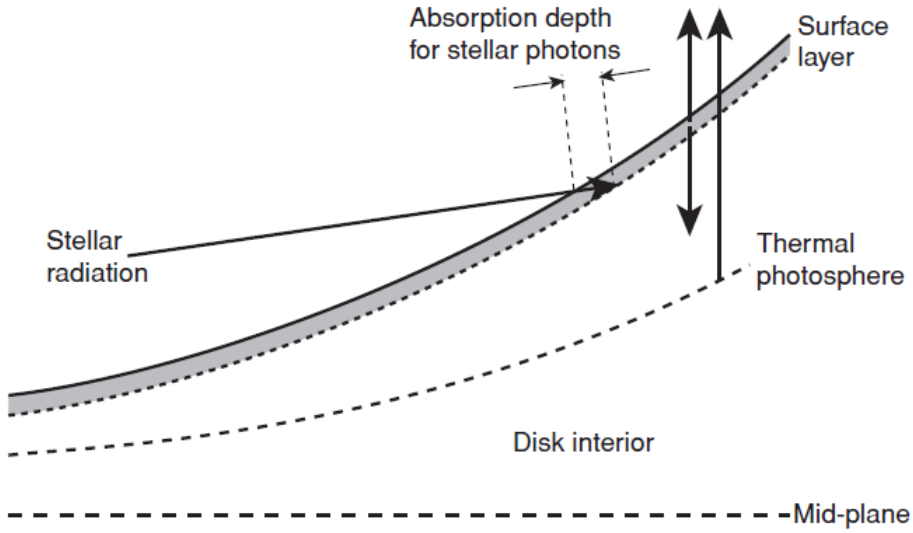

Figure 1.6: *Depiction of the physics underlying radiative equilibrium models for protoplanetary disks. Dust, which absorbes stellar radiation in a thin surface layer, reradiates in the infrared either upward into space and downward, where it is absorbed again heating the disk interior. The local emission from the disk is represented by the superposition of radiation from the hot surface layer and the cooler interior. This image is taken from [1].*

radiation and emission of thermal radiation, it is possible to obtain the ratio $\epsilon_\star/\epsilon_{dust}$ by estimating the emissivity in correspondance of the wavelength where thermal radiation reaches its peak. We then have that $\epsilon \propto \lambda^{-1} \propto T$, so that $\epsilon_\star/\epsilon_{dust} = T_\star/T_{dust}$. If we replace it in Equation 1.1.7, we find

$$\frac{T_{dust}}{T_\star} = \left(\frac{R_\star}{2r}\right)^{2/5}.$$

Inserting some reference values for the stellar radius $R_\star = 2R_\odot$ and stellar effective temperature $T_\star = 4000$ K we find that,

$$T_{dust} = 470\left(\frac{R}{1\text{ AU}}\right)^{-2/5}\text{ K}.$$

It is important to stress that this analysis assumes that the dust particles can be considered as isolated, whereas in reality they are embedded within gas whose temperature will not in general be the same of the dust temperature (given by Equation 1.1.7). However, the purpose of this work is to study a disk in which gas and dust are decoupled, as will be demonstrated in Section 6.1, and then we will not discuss the case of the nonradiative cooling of the dust (deriving from the condition $T_{gas} < T_{dust}$), which results from collisions between molecules and the dust particles.

1.2 Protoplanetary disk evolution

Thanks to observations, it is evident that protoplanetary disks are (slowly) evolving structures: the observational detection of disks[17] are almost always caused by stars in or near star forming regions.

Considering a geometrically thin disk, the angular velocity is essentially that of a Keplerian orbit; then, the specific angular momentum[18] is

$$l = r v_{\phi,gas} = \sqrt{G M_\star r} \tag{1.2.1}$$

which increases with radius: therefore, gas in the disk needs to lose angular momentum in order to flow inward, and knowledge of the mechanisms that can result in angular momentum loss is crucial in the theory of accretion disks.

However, the resulting effect of interest is subtle, making it diffucult to reveal. The observed lifetime of protoplanetary disks is of several Myr, which corresponds, at the outer edge of the disk, to $\sim 10^4$ dynamical times, and this fact makes them almost stable.

In this Section we present the evolution of disks, the origin of angular momentum transport, and the methods for gas dispersion at the end of the disk lifetime. In particular, the interest is on the evolution of the dominant disk component by mass: the gas.

1.2.1 Observations of disk evolution

Detection and observation of protoplanetary disks exploits various complementary techniques, among which there are:

- detection of near- or mid-IR excesses over the stellar photospheric flux, indicating the presence of warm dust close (usually $\leq$ AU) to the star;
- detection of an accretion signature characteristic of gas being accreted on to the star, by revealing an UV excess or Hα emission with a large equivalent width;
- observation of mm or sub-mm flux generated by cool dust in the outer disk;
- disk imaging, in scattered visible light from the central star or in profile against a bright background nebula;
- detection of line emission from molecular species such as CO or NH_3.

Nowadays, measurements of the fraction of young stars exhibiting IR excesses impose the strongest constraints on disk evolution.

The fraction of young stars in different clusters that show evidence for protoplanetary disks through IR excesses is displayed in Figure 1.7, where it is plotted against the estimated age of the clusters[19].

Valid measurement of disk evolution is provided by the IR excess measurements of disk frequency: it is close to 100% for clusters whose average stellar age is < 1 Myr,

[17] Events such as an infrared excess or detectable mm flux.

[18] It is the angular momentum per unit mass l/m.

[19] It is derived by comparing the locations of stars in the Hertzsprung–Russell diagram against theoretical stellar evolution tracks for pre-main-sequence stars.

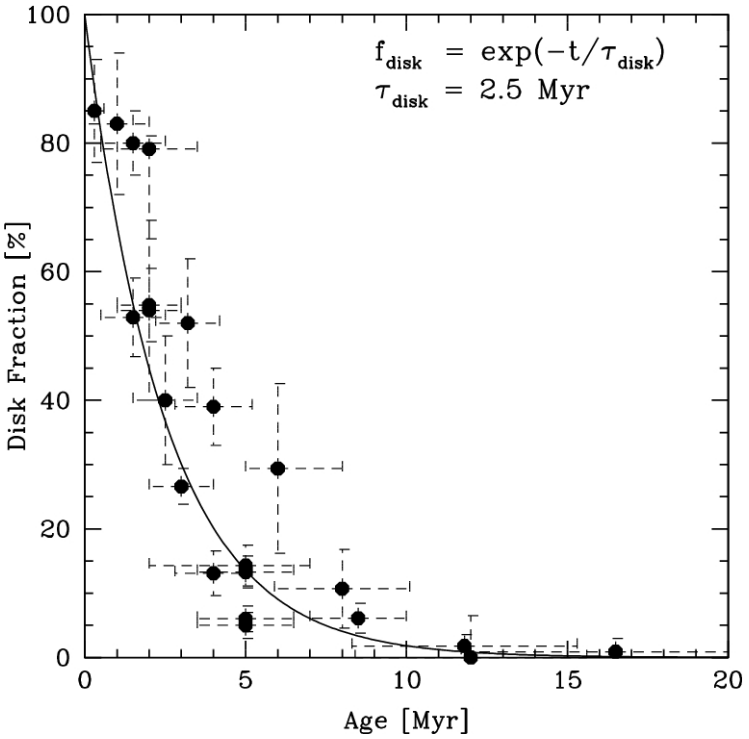

Figure 1.7: *Fraction of stars with primordial disks as a function of stellar age. The best fit exponential decay curve is plotted with timescale* $\tau_{disk} = 2,5$ *Myr. Substantial uncertainties affect the absolute ages, in particular as regards the younger clusters. The Figure has been taken from [2].*

whereas, as regards older clusters, the disk frequency decreases continuously, reaching 50% at around 3 Myr and being almost null by about 6 Myr. For stars older than 10 Myr there is no evidence for primordial disks[20]. What is possible to infer from these observations is a disk lifetime of about $3 \div 5$ Myr.

However, to be precise, this constraint on the disk lifetime refers only to the survival time of small dust grains in the innermost ($\sim$1 AU) region of the disk: even though it is not foregone, there is evidence that the whole disk may evolve on the same time scale of the dust. The following facts can explain this occurrence:

- the totally independent measurement of the accretion rate of gas on to the star, via spectroscopic observations of the hot continuum radiation generated when infalling gas intercepts the stellar surface, decreases with time on a similar time scale;

- usually, the presence of one disk signature means that the other signatures are also present, even when the different signatures arise at very different disk radii;

[20]Protoplanetary disks may be distinguished into two classes:

- *primordial disks*, in which consistent amounts of dust are blended with gas surrounding the youngest stars;

- *debris disks*, that are observed around older stars (typically above $\sim 15 \div 20$ Myr), do not present any relevant gaseous component, and it is probable that the dust in these disks has been originated from erosive collisions between larger solid bodies.

this fact implies that disks dispersal occurs across a range of radii requiring a relatively short time scale (this will be presented in Section 1.13).

1.2.2 Surface density Σ evolution of a thin disk

Henceforth we focus on the gas surface density profile $\Sigma(r,t)$ of an axisymmetric protoplanetary disk, assuming that the radial velocity $v_r(r,t)$ (using the convention that $v_r < 0$ indicates an inflow) of gas in the disk is small, and noting that the geometrical thinness of the disk ($h/r \ll 1$) implies that the predominant forces acting are rotational support and gravity.

Whether the potential is independent of time, in absence of angular momentum transport or loss, local conservation of angular momentum implies that $\Sigma(r,t)$ must be constant over time. Then, the presence of angular momentum transport known as *viscosity*, which allows local agglomerations of gas to reduce their angular momentum and spiral directed to the star[21], will make accretion and disk evolution possible.

The evolution of $\Sigma(r,t)$ can be obtained by considering the continuity equation, which denotes the conservation of mass, and the azimuthal component of the momentum equation, indicating angular momentum conservation. The rate of change of the mass within an infinitesimal ring in the disk extending between r and $r+\Delta r$ is given by

$$\frac{\partial}{\partial t}(2\pi r \Delta r \Sigma) = 2\pi r \Sigma(r) v_r(r) - 2\pi(r+\Delta r)\Sigma(r+\Delta r) v_r(r+\Delta r).$$

Being $\Sigma(r+\Delta r) = \Sigma(r) + (\partial\Sigma/\partial r)\Delta r$, we consider the limit for small Δr: the continuity equation then yields

$$r\frac{\partial \Sigma}{\partial t} + \frac{\partial}{\partial r}(r\Sigma v_r) = 0. \tag{1.2.2}$$

Progressing in the same way, conservation of angular momentum provides

$$r\frac{\partial}{\partial t}(r^2\Omega\Sigma) + \frac{\partial}{\partial r}(r^2\Omega \cdot r\Sigma v_r) = \frac{1}{2\pi}\frac{\partial G}{\partial r}, \tag{1.2.3}$$

where Ω, representing the angular velocity of the gas in the disk, remains here unspecified, not needing to be the Keplerian angular velocity of a point mass. The variation in surface density caused by radial flows (the second term on the left member) and the difference regarding the torque exerted on an infinitesimal ring by stresses at the inner and outer edges affect the rate of change of angular momentum in the disk. The torque G for a viscous fluid can be presented as follows:

$$G = 2\pi r \cdot \nu\Sigma r \frac{\mathrm{d}\Omega}{\mathrm{d}r} \cdot r,$$

in which ν is the kinematic viscosity[22]. Acting on an infinitesimal ring, the torque is the product of the circumference, the viscous force per unit length and the lever arm r, and is proportional to the gradient of the angular velocity. In the case the viscosity results from turbulence and is not a true microscopic process, the latter dependence, peculiar of a viscous fluid, is only an assumption.

[21] Global angular momentum conservation clearly implies that other agglomerations of gas in the disk must increase their angular momentum and move in the opposite verse.

[22] It is a measurement of the resistance to flowing of a fluid current under the influence of gravity: $\nu = \frac{\mu}{\rho}$, where μ is the dynamical viscosity and ρ the fluid density.

Proceeding, we eliminate v_r between Equations 1.2.2 and 1.2.3 and focus on a Keplerian potential, namely $\Omega \propto r^{-3/2}$. The evolution equation for the surface density of a geometrically thin disk influenced by internal angular momentum transport is then given by

$$\frac{\partial \Sigma}{\partial t} = \frac{3}{r}\frac{\partial}{\partial r}\left[r^{1/2}\frac{\partial}{\partial r}(\nu \Sigma r^{1/2})\right]. \tag{1.2.4}$$

This is a diffusive partial differential equation for the surface density $\Sigma(r, t)$, as will be clear in the next paragraph; moreover, if the viscosity ν is not in function of Σ, it is linear.

The viscous time scale

It is possibe to make the diffusive form of Equation 1.2.4 more evident through a change of variables: we introduce

$$X \equiv 2r^{1/2}, \qquad f \equiv \frac{3}{2}\Sigma X,$$

and impose the viscosity ν to be constant. Thus, the evolution equation assumes the standard form of a diffusion equation

$$\frac{\partial f}{\partial t} = D\frac{\partial^2 f}{\partial X^2}, \tag{1.2.5}$$

where D is the diffusion coefficient, given by

$$D = \frac{12\nu}{X^2}.$$

The utility of this version of the evolution equation is its versatile numerical use. The diffusion time scale across a scale ΔX given by Equation 1.2.5 is $(\Delta X)^2/D$; once converted into the physical variables, it represents the time scale on which viscosity will smooth out surface density gradients on a radial scale Δr:

$$\tau_\nu \sim \frac{(\Delta r)^2}{\nu}. \tag{1.2.6}$$

Given a characteristic size r of the disk, the time scale on which the surface density at all radii will evolve, usually described as the viscous time scale of the disk, is

$$\tau_\nu \approx \frac{r^2}{\nu}.$$

Its observational estimation is possible by measuring, for instance, the rapid decrement of accretion on to the star in function of stellar age; the typical value for protoplanetary disks around Solar-type stars turns out to be $\sim$ Myr.

Solutions to the disk evolution equation

If we now set $\frac{\partial}{\partial t} = 0$ in Equation 1.2.4 and integrate the resultant ordinary differential equation for the surface density, we derive a stationary solution. Starting with the angular momentum conservation Equation 1.2.3, which does not force angular velocity

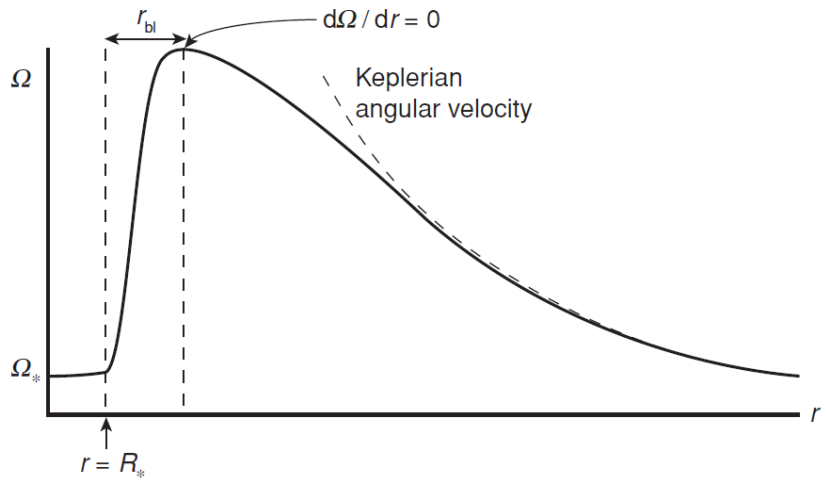

Figure 1.8: *Angular velocity profile in a disk that extending to the equator of a slowly rotating star, taken from [1]. The viscous stress disappears at the radial position* $r = R_\star + r_{bl}$*, corresponding to a maximum of* Ω*.*

to be Keplerian, is easier in order to impose the required boundary conditions. Then, setting the variation with time as null and integrating, it results

$$2\pi r\Sigma v_r \cdot r^2\Omega = 2\pi r^3 \nu\Sigma \frac{\mathrm{d}\Omega}{\mathrm{d}r} + K$$

Since the mass accretion rate is $\dot{M} = -2\pi r\Sigma v_r$ we can write this equation in this form:

$$-\dot{M} \cdot r^2\Omega = 2\pi r^3 \nu\Sigma \frac{\mathrm{d}\Omega}{\mathrm{d}r} + K. \tag{1.2.7}$$

The constant of integration K, resembling an angular momentum flux, can be determined noting that in the point of the disk at which $\mathrm{d}\Omega/\mathrm{d}r = 0$ the viscous stress vanishes, and then the constant is simply given by the flux of angular momentum conveyed inward along with the mass:

$$K = -\dot{M} \cdot r^2\Omega.$$

Considering the case in which the protoplanetary disk extends all the way down to the surface of a non-(or slowly-)rotating star, it is clear that the disk and the star are united into a single fluid system, where it is necessary for the angular velocity to make a continuous transition between $\Omega = 0$ in the star and $\Omega \propto r^{-3/2}$ within the disk[23](this behaviour is shown schematically in Figure 1.8). In correspondence of a radius $R_\star + r_{bl}$, where r_{bl} is the width of the boundary layer[24] that divides the star from the Keplerian part of the disk, the viscous stress is absent. Into the boundary layer the angular velocity increases with radius: the sub-Keplerian rotational support cannot contrast the inward gravitational force.

The purpose is now to determine the constant in Equation 1.2.7: considering a

[23]This represents the *zero-torque* boundary condition at the inner edge, which is approximately guaranteed for disks extending to the equator of a slowly rotating star. Anyway, stellar magnetic fields in classical T Tauri stars can truncate the disk before it reaches the stellar surface.

[24]In most cases the radial extent of the boundary layer is a small fraction of the stellar radius.

narrow boundary layer, $R_\star + r_{bl} \approx R_\star$ and Ω reaches its maximum close to the stellar surface. Then

$$K \approx -\dot{M} R_\star^2 \sqrt{\frac{GM_\star}{R_\star^3}}$$

and the stationary solution for the disk, within which the angular velocity is Keplerian, results to be

$$\nu\Sigma = \frac{\dot{M}}{3\pi}\left(1 - \sqrt{\frac{R_\star}{r}}\right). \tag{1.2.8}$$

This equation provides the steady-state surface density profile of a protoplanetary disk with a constant accretion rate $\dot{M}$, but needs to specify the viscosity. At large radii with respect to the inner boundary, $r \gg R_\star$, we have that $\Sigma(r) \propto \nu^{-1}$.

Most of the time-dependent analytic solutions to Equation 1.2.4, which can be obtained for several forms of the viscosity, provide the essential behavior imposed by the disk evolution equation.

In the case $\nu =$ constant, a Green's function solution to the evolution equation exists. The initial condition considers that, at $t = 0$, all of the gas is concentrated in a thin ring of mass m at radius r_0:

$$\Sigma(r, t = 0) = \frac{m}{2\pi r_0}\delta(r - r_0),$$

being $\delta(r - r_0)$ a Dirac delta function. Imposing the *zero-torque* boundary condition at $r = 0$ and allowing for free expansion toward $r = \infty$, the solution in terms of the dimensionless variables $x \equiv r/r_0$, $\tau \equiv 12\nu r_0^{-2} t$, and ${I_{1/4}}^{25}$ becomes ([3])

$$\Sigma(x, \tau) = \frac{m}{\pi r_0^2}\frac{1}{\tau}x^{-1/4}\exp\left[-\frac{(1 + x^2)}{\tau}\right] I_{1/4}\left(\frac{2x}{\tau}\right), \tag{1.2.9}$$

Figure 1.9 shows the plot of the solution of Equation 1.2.9, illustrating several generic peculiarities of disk evolution. Increasing t, the initially narrow ring expands spreading diffusively, and the mass flows toward $r = 0$ while a negligible fraction of the mass transports the angular momentum toward $r = \infty$.

Another even more practically useful solution than the Green's function one is the *self-similar* solution, derived in [3]: consider a disk in which it is possible to approximate the viscosity as a power-law in radius

$$\nu \propto r^\gamma,$$

and suppose that the disk initially has the surface density profile derived by a stationary solution with this viscosity law, out to $r = r_1$, with an exponential truncation at greater radii. In particular, the initial surface density is described by

$$\Sigma(t = 0) = \frac{C}{3\pi\nu_1 \tilde{r}^\gamma}\exp\left[-\tilde{r}^{(2-\gamma)}\right],$$

where C is a normalization constant, $\tilde{r} \equiv r/r_1$ and $\nu_1 \equiv \nu(r_1)$. Consequently, the

[25] It is a modified Bessel function of the first kind.

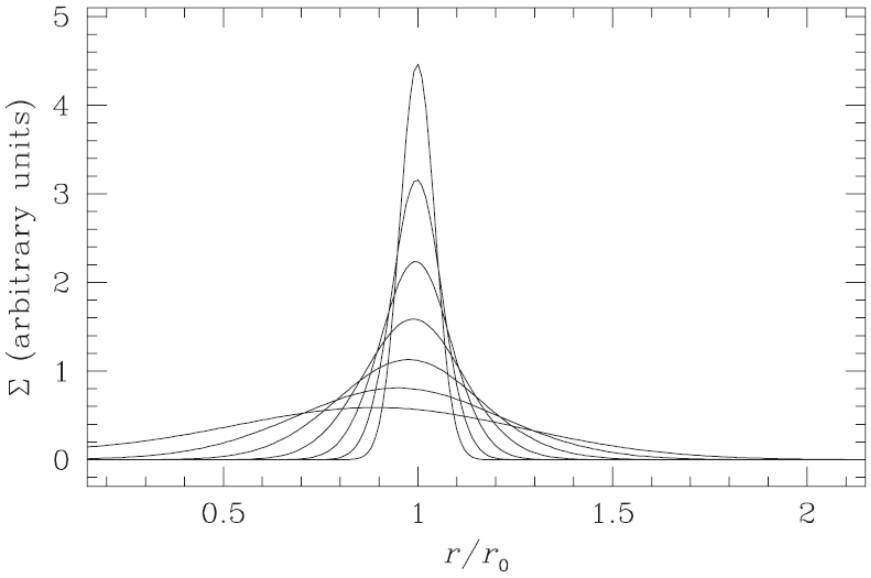

Figure 1.9: *The Green's function solution to the disk evolution equation, taken from [1], considering ν as a constant, illustrating the diffusion of a ring of mass initially orbiting at $r = r_0$.*

self-similar solution is

$$\Sigma(\tilde{r}, T) = \frac{C}{3\pi\nu_1\tilde{r}^{\gamma}} T^{-\frac{5/2-\gamma}{2-\gamma}} \exp\left[-\frac{\tilde{r}^{(2-\gamma)}}{T}\right] \tag{1.2.10}$$

in which

$$T \equiv \frac{t}{t_s} + 1, \qquad t_s \equiv \frac{1}{3(2-\gamma)^2}\frac{r_1^2}{\nu_1}.$$

From the latter surface density profile it is possible to obtain the evolution of related quantities such as the disk mass and accretion rate; its solution is plotted in Figure 1.10. Increasing time, the disk mass decreases while the characteristic scale of the disk, which was initially r_1, enhances due to angular momentum conservation. The utility of this solution can be found either in analytical studies of evolving disks and in the comparison with theory of observations of accretion rates, radii or disk masses.

Temperature profile of accreting disks

In this part we want to derive the radial dependence of the effective temperature of an actively accreting disk. This can be obtained by considering the net torque $(\partial G/\partial r)\Delta r$ on a ring of width Δr, which works at a rate

$$\Omega\frac{\partial G}{\partial r}\Delta r \equiv \left[\frac{\partial}{\partial r}(G\Omega) - G\Omega'\right]\Delta r,$$

being $\Omega' \equiv \mathrm{d}\Omega/\mathrm{d}r$. Written this form, and considering the whole disk by integrating over r, it is clear that the boundary values of $G\Omega$ are the only constraints which determine the first term on the right member of the equation. Thus, this term represents the transport of energy, related to the viscous torque, through the infinitesimal ring; however,

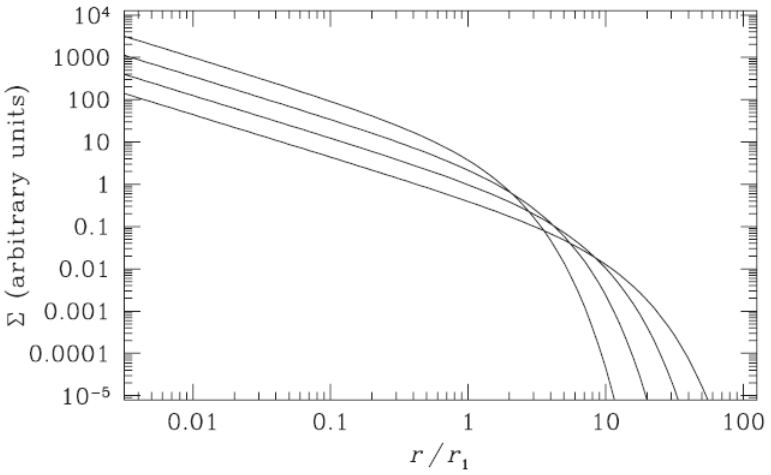

Figure 1.10: *Plot of the self-similar solution to the disk evolution equation, as reported in [1], for a form of viscosity $\nu \propto r$. The initial surface density sets the profile for a stationary disk ($\Sigma \propto r^{-1}$, Equation 1.2.8) at small radius until reaching $r = r_1$, at which the exponential cut-off occurs. The curves show the surface density at the initial value of the scaled time $T = 1$, and at following moments $T = 2$, $T = 4$, and $T = 8$.*

the second term identifies the rate of loss of energy to the gas: we assume that this is finally converted into heat and radiated, so that the dissipation rate per unit surface area of the disk[26] is

$$D(r) = \frac{G\Omega'}{4\pi r} = \frac{9}{8}\nu\Sigma\Omega^2,$$

where a Keplerian angular velocity profile has been assumed; the blackbody emission is $D(r) = \sigma T_{disk}^4$. Replacing the form of Ω and $\nu\Sigma$ (using the stationary solution given by Equation 1.2.8), it results

$$T_{disk}^4 = \frac{3GM_\star \dot{M}}{8\pi\sigma r^3}\left(1 - \sqrt{\frac{R_\star}{r}}\right).$$

It is noteworthy that away from near the inner boundary, at a radius $r \gg R_\star$, the temperature profile of an actively accreting disk is $T_{disk} \propto r^{-3/4}$: this has the same trend of a razor-thin disk reprocessing stellar radiation (Equation 1.1.6); furthermore, the temperature profile is independent of the viscosity.

Finally, we provide an estimation of the effective temperature by using a representative value for the accretion rate of $\dot{M} = 10^{-7} M_\odot \mathrm{yr}^{-1}$ and considering a Solar mass star at 1 AU, obtaining then $T_{disk} = 150$ K, which represents the *surface* temperature - substantially lower than the central temperature.

1.2.3 Vertical structure of protoplanetary disks

The dissipation of gravitational potential energy into heat, in an actively accreting disk, will be concentrated close to the disk mid-plane since the density there reaches its maximum. Along most of the disk extension there is a great optical depth between

[26] We take into account that the disk has two sides.

the surface and the mid-plane: instead of directly radiating to space, then, the heated gas will be transported vertically toward the photosphere through radiative diffusion or turbulent transport, requiring the presence of a temperature gradient between $z = 0$ and the disk photosphere.

The importance of the detemination of this gradient and its effect on the vertical structure of the disk is that the value of the viscosity - controlling the evolution - depends mostly upon the central conditions in the disk: then, viscosity and vertical structure are essential for modelling disk structure and evolution.

The approximation used here, in order to solve the equations governing the vertical structure, is to be in a plane parallel symmetry[27]. Assuming that energy transport occurs through radiative diffusion, these equations are the following:

- hydrostatic equilibrium

$$\frac{\mathrm{d}P}{\mathrm{d}z} = -\rho g_z,$$

being g_z is the vertical gravity of Equation 1.1.1;

- the vertical variation[28] of the flux F_z

$$\frac{\mathrm{d}F_z}{\mathrm{d}z} = \frac{9}{4}\rho\nu\Omega^2;$$

- the equation of radiative diffusion, which links the flux with the temperature gradient in an optically thick layer

$$\frac{\mathrm{d}T}{\mathrm{d}z} = -\frac{3\kappa_R\rho}{16\sigma T^3}F_z. \tag{1.2.11}$$

Moreover, these equations need some additional equations: the equation of state, relating the pressure P to the fundamental variables ρ and T; the expressions for the Rosseland mean opacity κ_R; appropriate boundary conditions.

The central temperature of accreting disks

The vertical temperature structure can be obtained assuming that the energy dissipation due to viscosity is mostly concentrated along the mid-plane, at $z = 0$. Defining the optical depth to the disk mid-plane as

$$\tau = \frac{1}{2}\kappa_R\Sigma,$$

and being the vertical density profile of the disk $\rho(z)$, then for $\tau \gg 1$ the vertical energy flux $F(z)$ is given by the equation of radiative diffusion (Equation 1.2.11)

$$F_z(z) = -\frac{16\sigma T^3}{3\kappa_R\rho}\frac{\mathrm{d}T}{\mathrm{d}z},$$

provided that the vertical energy transport occurs via radiative diffusion.

[27] The dependence of each function is on z.

[28] For $h \ll r$ it is self-consistent to assume that $F_z \gg F_r$.

In order to simplify the calculations, we assume that $z = 0$ is where all of the energy dissipation occurs: thus $F_z(z) = \sigma T_{disk}^4$ does not depend on height. Considering that the opacity is constant and integrating we obtain

$$-\frac{16\sigma}{3\kappa_R}\int_{T_c}^{T_{disk}} T^3 \mathrm{d}T = \sigma T_{disk}^4 \int_0^z \rho(z')\mathrm{d}z',$$

$$-\frac{16\sigma}{3\kappa_R}\left[\frac{T^4}{4}\right]_{T_c}^{T_{disk}} = T_{disk}^4 \frac{\Sigma}{2},$$

where in the latter equation we have observed that almost all of the disk gas lies below the photosphere, with $\tau \gg 1$. It results

$$\left(\frac{T_c}{T_{disk}}\right)^4 \approx \frac{3}{4}\tau. \tag{1.2.12}$$

The relevance of this result is that active disks with large optical depths are substantially hotter at the mid-plane than at the surface: for instance, $\tau = 10^2$ implies $T_c \approx 3T_{disk}$. This is noteworthy, since it is the central temperature that largely determines the composition of the dust.

Shakura–Sunyaev α prescription

As seen previously, viscosity plays an important role in protoplanetary disks evolution, since the time scale on which evolution occurs and the profile of the surface density depend directly on the viscosity and its radial variation.

As regards the physical origin of angular momentum transport, molecular collisions are to be considered firstly. They generate a viscosity in a shear flow due to the finite mean-free path λ in the gas. Molecular viscosity[29] is approximately given by

$$\begin{cases} \nu_m \sim \lambda c_s \\ \lambda = \frac{1}{n\sigma_{mol}} \end{cases}$$

where λ is the mean-free path in a gas with number density n and the cross-section for molecular collisions, σ_{mol}, approximately corresponds to the physical size of molecules. Using a value of $\sigma_{mol} \approx 2 \times 10^{-15}$ cm^2 (the case of molecular hydrogen) and assuming the sound speed at 10 AU to be $0,5$ km s^{-1} and the number density $n = 10^{12}$ cm^{-3}, it results that $\nu_m \sim 2,5 \times 10^7$ cm^{2}s^{-1}.

The corresponding viscous time scale is obtained by Equation 1.2.6:

$$\tau_\nu \approx \frac{r^2}{\nu_m} = 3 \times 10^{13} \text{ yr},$$

but this value is approximately ten million times higher than the observed time scale for disk evolution. It is evident, then, that molecular viscosity does not generate angular momentum transport within disks.

A small molecular viscosity implies a large Reynolds number[30], which can be defined as

[29] It represents the normal mechanism acting in terrestrial fluids modeled with the Navier–Stokes equations

[30] It is defined as the ratio between the inertial forces and the viscous forces acting in the fluid.

$$\mathscr{R} \equiv \frac{UL}{\nu_m},$$

where U and L are characteristic velocity and length scales in the system. Adopting $U = c_s$ and $L = h = 0,05r$, the fluid Reynolds number at 10 AU is enormous - $\mathscr{R} = 10^{10}$ - and then in presence of a physical instability the protoplanetary disk will be highly turbulent.

In the case of turbulence, the turbulent fluid motions are the result of the macroscopic mixing of fluid elements at consecutive radii, which resembles a turbulent viscosity, whose magnitude can be inferred from dimensional arguments. Reasonably, under the isotropic approximation for the turbulence, the maximum scale of the turbulent flow must be smaller than the disk scale height h; similarly, the velocity of the turbulent motions must be smaller than the sound speed c_s[31]. The turbulent viscosity is therefore

$$\nu = \alpha c_s h, \tag{1.2.13}$$

where the Shakura–Sunyaev α parameter is a dimensionless quantity which quantifies the efficiency of angular momentum transport generated by turbulence.

Exploiting Equation 1.2.13 it is possible to determine the viscosity in function of the local disk quantities c_s and h, and consequently understand the local disk structure. Clearly, it is necessary to have $\alpha \leq 1$, and α will be assumed to be constant, even though there are not constraints on its variation.

Vertically averaged solutions

Thanks to the α prescription it is possible to compute the viscosity ν in function of r, Σ and α. Subsequently, this result can be used to evaluate the stationary surface density profile $\Sigma(r, \alpha, \dot{M})$ through Equation 1.2.8, and can be exploited together with Equation 1.2.4 to obtain the evolution over time of an arbitrary initial surface density profile.

In this part the viscosity will be computed with the vertically averaged approximation, namely replacing the radiative diffusion Equation 1.2.11 with the approximate result given as Equation 1.2.12 and evaluating the vertical dependence of all other quantities in their central values.

Considering an infinitesimal ring of the disk with surface density Σ at a radius where the Keplerian angular velocity is Ω, we have that eight variables characterize the disk: the mid-plane temperature T_c, effective temperature T_{disk}, sound speed c_s, density ρ, vertical scale height h, opacity κ_R, viscosity ν and optical depth τ.

Then, all of these quantities have to be considered at $z = 0$[32]; what results is the following set of equations:

[31] Because supersonic motions result in shocks and rapid dissipation.

[32] Except for the effective temperature, which is defined at the photosphere, and the optical depth, which is evaluated between the surface and the mid-plane.

$$\begin{cases} \nu = \alpha c_s h \\ c_s^2 = \frac{k_B T_c}{\mu m_p} \\ \rho = \frac{1}{\sqrt{2\pi}} \frac{\Sigma}{h} \\ h = \frac{c_s}{\Omega} \\ T_c^4 = \frac{3}{4} \tau T_{disk}^4 \\ \tau = \frac{1}{2} \Sigma \kappa_R \\ \nu \Sigma = \frac{\dot{M}}{3\pi} \\ \sigma T_{disk}^4 = \frac{9}{8} \nu \Sigma \Omega^2 \end{cases}$$

Specifying the opacity $\kappa_R(\rho, T_c)$ allows to solve these eight equations in eight unknowns in order to determine the disk structure.

1.2.4 Angular momentum transport mechanism

The questions about the origin of the postulated tubulence, the value of α and its dependence on the physical conditions within the disk have not found an exhaustive answer, yet; however, in this part we will discuss the currently most important physical considerations.

The Rayleigh criterion

In the case of a nonmagnetized, non-self-gravitating disk - for which $M_{disk}/M_\star < h/r$ - Rayleigh suggested the appropriate stability criteria as follow: such a disk flow is linearly stable under axisymmetric perturbations if and only if the specific angular momentum is an increasing function of radius. Then, instability occurs if

$$\frac{\mathrm{d}l}{\mathrm{d}r} = \frac{\mathrm{d}}{\mathrm{d}r}(r^2\Omega) < 0.$$

For a Keplerian disk, in which the specific angular momentum is $l \propto \sqrt{r}$ (Equation 1.2.1) the flow is predicted to be hydrodynamically stable, in spite of the enormous value of the Reynolds number: it is unlikely, then, to identify hydrodynamic turbulence as the cause of the turbulent viscosity needed in the accretion mechanism.

The magnetorotational instability

When a magnetic field is coupled to the gas, the fluid increases its degrees of freedom, causing the violent destabilization of the disk. According to [1], the condition under which a weakly magnetized disk flow becomes linearly unstable[33] is the decrease of the angular velocity (rather than the specific angular momentum, considering the fluid case) with radius[34]:

$$\frac{\mathrm{d}}{\mathrm{d}r}(\Omega) < 0. \tag{1.2.14}$$

[33]The magnetorotational instability (MRI) denotes the linear instability of a disk coupled to a magnetic field.

[34]This condition is satisfied by Keplerian disks.

The disk, considering the limit of ideal magnetohydrodynamics (MHD), can be described by the equations of continuity

$$\frac{\partial \rho}{\partial t} + \nabla \cdot (\rho \mathbf{v}) = 0,$$

momentum conservation

$$\frac{\partial \mathbf{v}}{\partial t} + (\mathbf{v} \cdot \nabla)\mathbf{v} = -\frac{1}{\rho}\nabla\left(P + \frac{B^2}{8\pi}\right) - \nabla\Phi + \frac{1}{4\pi\rho}(\mathbf{B} \cdot \nabla)\mathbf{B} \tag{1.2.15}$$

and magnetic induction

$$\frac{\partial \mathbf{B}}{\partial t} = \nabla \times (\mathbf{v} \times \mathbf{B}). \tag{1.2.16}$$

The symbols used refer to the following quantities: ρ is the density, $\mathbf{v}$ is the velocity, $\mathbf{B}$ is the magnetic field, P is the pressure, $B = |\mathbf{B}|$ and Φ is the gravitational potential. The presence of magnetic tension[35] influences magnetized disks leading them to have qualitatively different stability properties from fluid disks.

Instability arises by the interaction between magnetic tension and flux freezing (Equation 1.2.16) within a differentially rotating system. In this Section an axisymmetric, incompressible disk being threaded by a vertical magnetic field will be considered.

It results, from [1], that the instability criterion is

$$(k v_A)^2 + \frac{\mathrm{d}\Omega^2}{\mathrm{d}\ln r} < 0,$$

where $v_A = \sqrt{\frac{B_z^2}{4\pi\rho}}$ is the Alfvén speed[36], ω is the frequency of the in-plane perturbation varying with height z and time, and k is its wavenumber.

Considering the limit of a field which is vanishingly weak (so that $B_z \to 0, v_A \to 0$), we obtain the previously introduced condition (Equation 1.2.14), valid in the case of the local linear instability of a differentially rotating disk subject to a weak magnetic field.

Assuming now a Keplerian rotation law, for which $\mathrm{d}\Omega^2/\mathrm{d}\ln r = -3\Omega^2$, it results that the dispersion relation follows the trend shown in Figure 1.11: once fixed the magnetic field strength (which means to fix the Alfvén speed v_A), the flow becomes unstable for wavenumbers $k < k_{crit}$, namely on considerably large spatial scales, where

$$k_{crit} v_A = \sqrt{3}\Omega.$$

When the magnetic field increases its intensity, the smallest scale $\lambda = 2\pi/k_{crit}$ which is unstable grows until reaching the disk's vertical extension, which can be interpreted as $2h$ (being h the scale height): for a stronger vertical field it will not be possible to fit unstable MRI modes within the thickness of the disk, then suppressing the instability.

A Keplerian disk turns out to have its maximum instability in correspondence of

$$(k v_A)_{max} = \frac{\sqrt{15}}{4}\Omega,$$

[35] It is described by the third term on the right member of Equation 1.2.15 and exerts a force on the fluid that attempts to straighten curved field lines.

[36] An Alfvén wave is an oscillating perturbation of the plasma, whose propagation is due to ions oscillations under a magnetic field. Its propagation velocity follows the direction of the field lines.

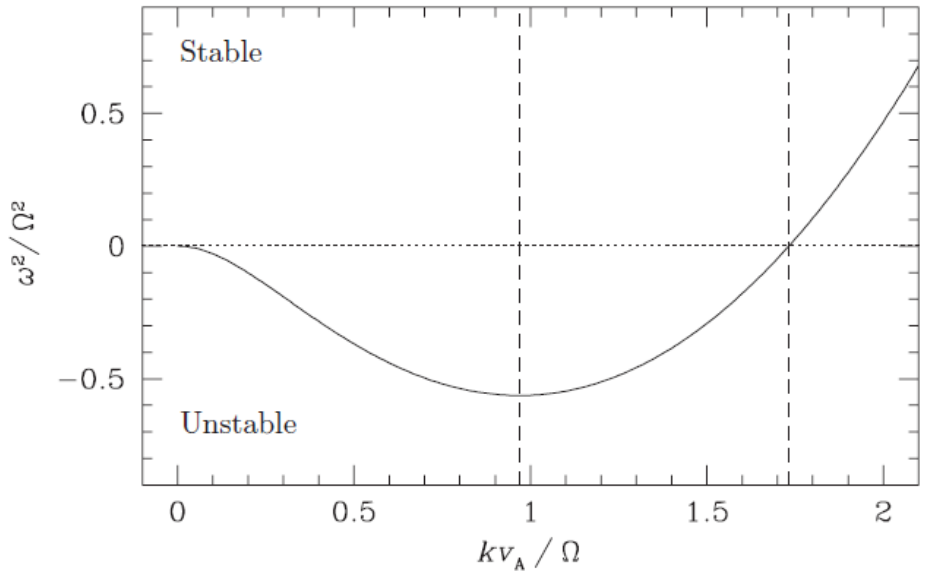

Figure 1.11: *The unstable branch of the dispersion relation for the magnetorotational instability presented in [1] is plotted for a disk in which a Keplerian angular velocity profile is used. The quantities ω and kv_A have all been scaled to the orbital frequency Ω; flow instability ($\omega^2 < 0$) occurs for all spatial scales for which $kv_A < \sqrt{3}\Omega$ - rightmost dashed vertical line. The maximum of instability, represented by the dashed centered vertical line, is $kv_A = (\sqrt{15}/4)\Omega$.*

with a related growth rate ([1])

$$|\omega_{max}| = \frac{3}{4}\Omega.$$

Regarding the latter result, it is noteworthy that the fact that the exponential growth time scale is a fraction of an orbital period implies an extremely high growth of the instability. Consequently, if a disk is unstable to the MRI, this process will dominate its evolution since it operates at a time scale which is almost always smaller than that of other physical processes.

Disk winds and magnetic braking

The assumption made so far is that the disk evolution is governed by redistribution of angular momentum within the protoplanetary disk. Instead, Figure 1.12 schematically shows a qualitatively different vision, according to which it is angular momentum loss, made possible by open magnetic field lines which thread the disk, which drives evolution.

The magnetic field at the disk surface has vertical and azimuthal components B_z^s and B_ϕ^s, respectively: they exert a torque on the disk. For a sufficiently weak magnetic field, for which the angular velocity remains Keplerian (thus neglecting magnetic pressure gradients), the loss of the angular momentum through the magnetic torque results in a radial velocity $|v_{r,m}|$. The comparison of this inflow velocity to that which results from internal redistribution of angular momentum due to viscosity, $|v_{r,visc}|$, has been derived in [1] and leads to

$$\frac{|v_{r,m}|}{|v_{r,visc}|} \sim \frac{B_z^s B_\phi^s}{B_r B_\phi} \left(\frac{h}{r}\right)^{-1},$$

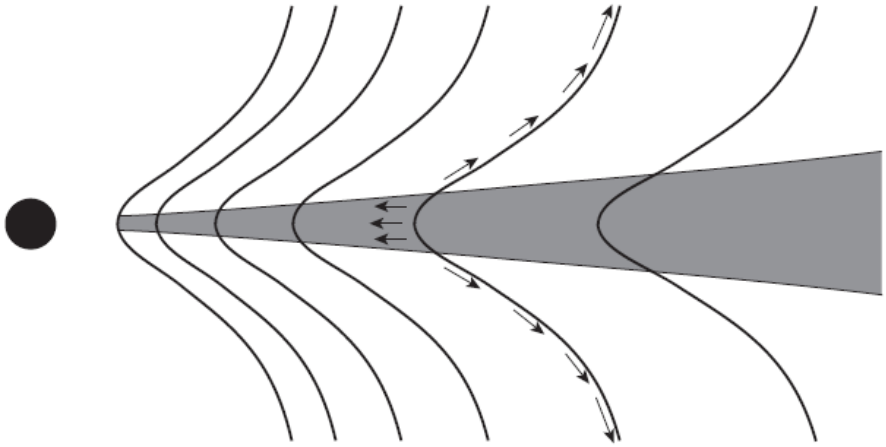

Figure 1.12: *Geometry assumed in disk wind models for protoplanetary disk evolution, as reported in [1]: the disk is connected to a nearly force-free disk corona by open magnetic field lines, which accelerate a small part of accreting matter outward along them forming a magnetically launched disk wind, whereas the magnetic field exerts a torque at the disk surface causing disk's angular momentum loss and controlling accretion.*

where the magnetic fields B_r and B_ϕ in the denominator represent the turbulent fields evaluated near the mid-plane. The almost intuitive result is that if organized large scale fields thread the disk and have the same magnitude of the turbulent fields, the wind prevails in carrying away angular momentum over the internal processes which can redistribute it; this effect is amplified if the disk is thin.

It is then possible to generalize the surface density evolution 1.2.4 by including the effect of angular momentum loss due to the presence of a disk wind. Still considering the angular velocity to be Keplerian, the effect of the wind on the disk finds its counterpart in an additional term as follows:

$$\frac{\partial \Sigma}{\partial t} = \frac{3}{r}\frac{\partial}{\partial r}\left[r^{1/2}\frac{\partial}{\partial r}(\nu \Sigma r^{1/2})\right] - \frac{1}{r}\frac{\partial}{\partial r}(r \Sigma v_{r,m}).$$

Hydrodynamic turbulence

As shown previously, when the gas in disks is well coupled to the magnetic field the MRI can occur and, independently of whether other angular momentum transport (or loss) processes act, we expect MHD turbulence to be sustained by the fluid. However, the decoupling between the magnetic field and the fluid dynamics of the gas in certain zones within protoplanetary disks makes the MRI unable to operate in such regions. As regards the existence of angular momentum transport mechanisms which can act without the presence of magnetic fields, the three following possibilities represent the most accredited candidates: disk self-gravity, nonlinear or transient instabilities in purely hydrodynamic flows, and vortices.

We have always considered that disks gravity is a small fraction of the force from the central star, then it has been neglected; these disks are axisymmetric, meaning that no torque acts on gas at one radius caused by the gravitational force from other matter in the disk. However, when the disk inceases its mass there is a corresponding enhanced tendency, due to its own self-gravity, to form overdense *clumps*: angular momentum transport can be then generated by the gravitational interactions between these clumps.

Involving planetesimal formation, an important potential mechanism is self-gravity. Within a disk, the formation (due to the self-gravity of the disk gas) of denser clumps is contrasted by both pressure forces and by shear. The estimation of the conditions under which self-gravity exceedes these stabilizing effects requires the collapse time scale to be shorter than the time scales for sound waves to cross a clump or for shear to destroy it. Imposing the equality among these three time scales, what results (from [1]) is the following condition for instability:

$$\pi G\Sigma > c_s\Omega.$$

Considering that $h = c_s/\Omega$ and being the disk mass $M_{disk} \sim \pi r^2\Sigma$, the instability threshold can be written in the more intuitive form

$$\frac{M_{disk}}{M_\star} > \frac{h}{r}.$$

A representative value for protoplanetary disks is $h/r \approx 0,05$, and then consistently massive disks are required in order to expect the effects of self-gravity to become important. It is probable that such disks have existed at early epochs, possibly before the optically visible T Tauri phase of YSO evolution (Section 1.1.1).

If self-gravity is relevant within a disk, there are two possible results:

- collapse may continue undisturbed, leading to disk destruction and consequent formation of some bound objects[37];
- the clump contraction to higher density results in adiabatic heating which may produce sufficient pressure to avoid complete collapse: this leads to the development of spiral arms (induced by the self-gravity within the disk) whose gravitational forces act much like magnetic tension in an MRI-unstable disk, and their effects is to transport angular momentum outward and mass inward.

The capability of the disk to radiate away its thermal energy determines the boundary between these aforementioned possibilities: in fact, if the disk can cool on a short time scale, then fragmentation occurs because pressure cannot build up within contracting clumps; on the other hand, slow cooling[38] results instead in stable angular momentum transport.

Returning now to consider *non-self-gravitating* protoplanetary disks, the point is to understand if there may be hydrodynamic instabilities, causing turbulence, even without the presence of dynamically relevant magnetic fields: the Rayleigh stability criterion allows two possibilities thanks to which fluid effects could be consistent within protoplanetary disks:

- disks might be unstable under nonlinear (or finite) amplitude perturbations, for which it is not possible to neglect the term $(\mathbf{v} \cdot \nabla)\mathbf{v}$ on the left member of the momentum Equation 1.2.15;
- the existence of transiently growing disturbances in perturbed Keplerian disk flows.

[37]Disk fragmentation through this process is one of the mechanism acting toward planetesimal formation.

[38]It is physically more probable to occur in most protoplanetary disks.

Finally, vortices[39] represent a special class of hydrodynamic structure, whose relevance in planet formation lies in their ability to accumulate solid particles into dense zones in correspondence of their core, almost regardless of any possible role that vortices might play in angular momentum transport. Their role within protoplanetary disks is twofold: first, in a barotropic fluid (one in which $P = P(\rho)$ only), equal pressure surfaces are always parallel to equal density surfaces, and this leads to the fact that vorticity is an approximately conserved quantity; second, vorticity can be generated within disks if $\nabla\rho \times \nabla P \neq 0$[40].

1.2.5 Disk dispersal

The gaseous protoplanetary disk is subject to depletion due to stellar accretion, and this is expected to be a gradual process. Considering the self-similar solution 1.10 we obtain that, for a time-independent viscosity scaling with radius as $\nu \propto r^{\gamma}$, the long-term trend of the surface density is given by

$$\Sigma \propto t^{-\frac{5/2-\gamma}{2-\gamma}},$$

which is a power-law as a function of time - in particular, $\Sigma \propto t^{-3/2}$ if $\nu \propto r$. If the disk evolution is based only on accretion, the disk is expected to gradually become optically thin when increasing the radius, involving a rather slow transition from a Class II to a Class III YSO source (Section 1.1.1). However, this is not what results from observations: the scarcity of such systems, among the elevate number of candidate transition disks known, suggests that the dispersal phase of protoplanetary disks occurs for a period of about 10^5 yr ([1]).

This relatively short dispersal time scale implies that, besides viscous evolution, other physical processes contribute to the loss of gas from the disk: the most accredited evolutionary agents are photoevaporation and MHD winds.

Photoevaporation

When UV radiation heats the disk surface to a sufficiently elevate temperature that allows the thermal energy of the gas to overcome its gravitational binding energy, this mechanism is known as photoevaporation. Subsequently, this unbound gas is driven away from the star by a pressure gradient, depleting the disk. The sources of the irradiating flux, namely the star surronded by the disk or other external stars in a cluster, and the energy of the photons contribute in determining the features of photoevaporation. Extreme ultraviolet (EUV) radiation - for which $E > 13,6$ eV, $\lambda < 912$ Å - ionizes hydrogen atoms, resulting in a layer of hot gas whose temperature (of about 10^4 K) is almost independent of the density of the disk given a certain radius. On the other hand, far ultraviolet (FUV) radiation - for which 6 eV $< E <$ 13.6 eV - dissociates H_2 molecules, producing a neutral atomic layer whose temperature is determined by the precise balance of heating and cooling processes (typical values are $100 - 5000$ K).

[39] Their presence is associated to the fluid *vorticity* $\omega \equiv \nabla \times \mathbf{v}$.

[40] For a thin disk we expect that both the gradient in density and the gradient in pressure will be almost vertical; however, small misalignments might arise due to the presence of stellar irradiation or in the proximity of planets (after their formation within the gas disk).

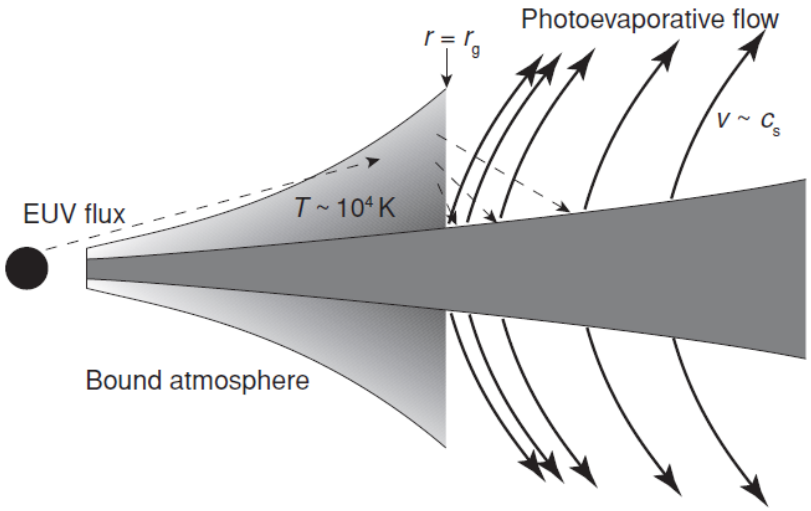

Figure 1.13: *Geometry involved in simple models of disk photoevaporation due to a central stellar EUV source, as reported in [1]. The surface layers of the disk are ionized by the incident EUV flux, which heats them to a temperature of* $\sim 10^4$ *K. The ionized layer, inside a critical radius* r_g*, forms a bound atmosphere that absorbs the stellar flux and reradiates recombination radiation. At more external radii the gas moves outward as a thermally driven disk wind.*

Figure 1.13 shows a disk subject to incident EUV flux from the central star[41]: the photoionized gas reaches a temperature $T \approx 10^4$ K, and the related sound speed results to be $c_s \approx 10$ km s^{-1}. We introduce the gravitational radius r_g in correspondence of which the sound speed in the ionized gas equals the orbital velocity:

$$r_g = \frac{GM_\star}{c_s^2} = 8,9\left(\frac{M_\star}{M_\odot}\right)\left(\frac{c_s}{10 \text{ km s}^{-1}}\right)^{-2} \text{AU}.$$

A simple analysis considers gas at $r < r_g$ to be bound, forming an extended atmosphere of scale height $h \propto r^{3/2}$ above the neutral disk surface, whereas the ionized gas beyond r_g is unbound, and flows away from the disk at a rate

$$\dot{\Sigma}_{wind} \sim 2\rho_0(r)c_s,$$

where ρ_0 (the density at the base of the ionized layer) is determined by the strength of the irradiating EUV flux.

The estimation of the total mass loss rate from a disk subject to an ionizing EUV flux Φ results to be, according to [1],

$$\dot{M}_{wind} \approx 1,6 \times 10^{-10}\left(\frac{\Phi}{10^{41} \text{ s}^{-1}}\right)^{1/2}\left(\frac{M_\star}{M_\odot}\right)^{1/2} M_\odot \text{ yr}^{-1},$$

and this allows to almost reproduce the observed evolution of T Tauri disks: at early epochs, the expected mass loss rate from the disk for an ionizing photon flux $\Phi \sim 10^{41}$ s^{-1} is practically negligible[42], but becomes overwhelming after a few viscous

[41] This is one of the four different regimes of photoevaporation, since the EUV or FUV flavors of ionizing radiation can be originated by two geometrically different sources - the central star or an ambient radiation field.

[42] At that times, the stellar accretion rate is three orders of magnitude higher than the mass loss

times of disk evolution.

Viscous evolution with photoevaporation

A direct consequence is the incorporation of photoevaporation into time-dependent models of protoplanetary disk evolution. The same specific angular momentum of the disk at the launch point is carried by the flow away from the disk, thus the effect of photoevaporation results in a surface density loss rate in the disk evolution equation:

$$\frac{\partial \Sigma}{\partial t} = \frac{3}{r}\frac{\partial}{\partial r}\left[r^{1/2}\frac{\partial}{\partial r}(\nu \Sigma r^{1/2})\right] + \dot{\Sigma}_{wind}(r,t).$$

The evolution of protoplanetary disks subject to both angular momentum redistribution and EUV photoevaporation has been reported in [1], where three evolutionary phases can be distinguished:

- first, the disk evolves as if there were no mass loss due to photoevaporation because its contribution is negligible if compared to the mass flux flowing through the disk due to viscous transport of angular momentum;
- subsequently, the mass accretion rate decreases until it becomes comparable to the wind mass loss rate and mass flowing inward from large disk radii is deviated into the wind instead of reaching the inner disk, leading to an annular gap development in the disk at r_g and to the quick conveying of the inner disk (now without supplying) toward the star[43] - the mass accretion rate and disk surface density behaviour until this phase is presented in Figures 1.14 and 1.15;
- finally, at radii $r < r_g$ the disk becomes optically thin to the stellar EUV flux, allowing direct exposition of the inner edge of the outer disk to this flux, consequently increasing the rate of mass loss due to photoevaporation and eventually dispersing the whole outer disk on a time scale of a few 10^5 yr.

MHD winds

Photoevaporation represents an important component of disk evolution both for theoretical and observational reasons. However, other processes may also contribute to disk dispersal: according to [4], a direct candidate is represented by MHD winds, which are expected to be present if mature disks still possess a dynamically relevant net magnetic field.

What distinguish MHD disk winds from photoevaporation are their following features:

- the disk's net flux, instead of the stellar radiation field, determines their strength;
- they can be accelerated from arbitrarily small radii, even from $r < r_g$;
- the local mass loss rate approximately scales with the disk surface density, instead of being nearly constant;

rate.

[43] This happens on its own viscous time scale, of the order of 10^5 yr.

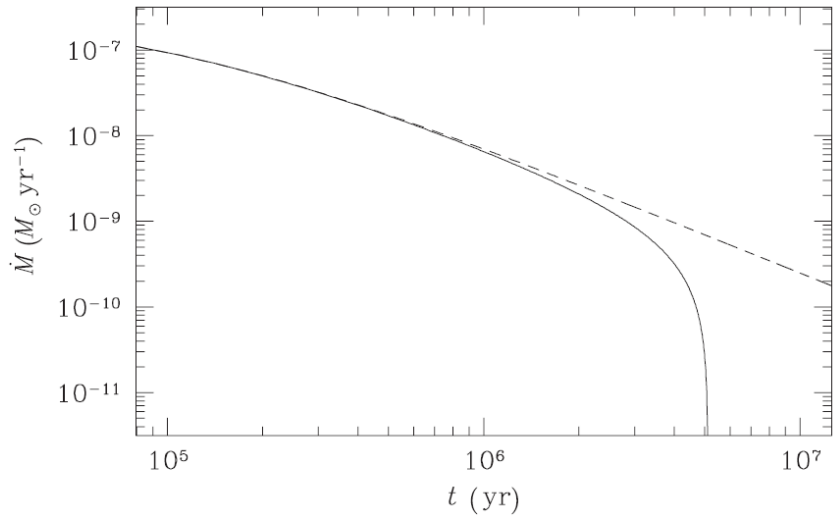

Figure 1.14: *Numerical computation of the stellar accretion rate for protoplanetary disk models with and without photoevaporative mass loss (solid and dashed lines, respectively), reported in [1]. Viscosity has been assumed $\nu \propto r$ and photoevaporative mass loss scales as $\dot{\Sigma}_{wind} \propto r^{-5/2}$ outside $r_g = 5\ AU$. A sharply defined epoch of disk dispersal is the result of the presence of a wind from the outer disk.*

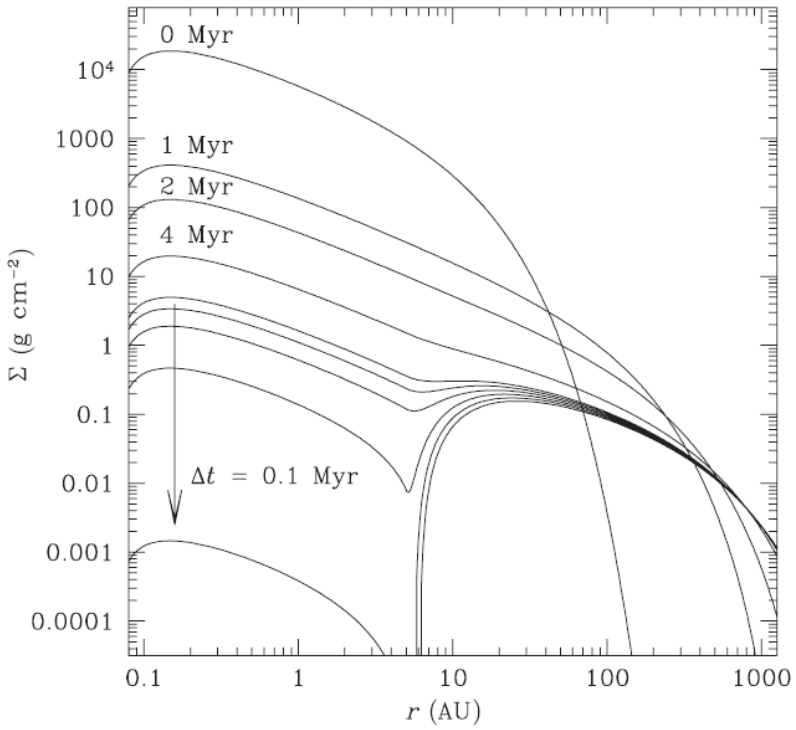

Figure 1.15: *The surface density evolution within a protoplanetary disk model including photoevaporative mass loss, reported in [1], in which the same assumptions of Figure 1.14 have been used. Disk evolution occurs slowly on Myr time scales until the stellar accretion rate drops to $\dot{M} \sim \dot{M}_{wind}$: then the inner disk becomes separate from the outer disk and is quickly ($\sim 10^5$ yr) drained towards the star.*

- predominantly neutral or molecular gas could be accelerated, even though it would subsequently be dissociated or ionized by stellar radiation.

MHD disk winds, if strong enough, can influence disk dispersal through the combination of mass and angular momentum loss, driving disk's evolution similarly to the photoevaporative case.

1.2.6 Magnetospheric accretion

With the absence of a magnetic field of the star, the stellar surface represents the inner boundary of the protoplanetary disk[44]. However, observations show that T Tauri stars are magnetized, usually possessing ∼kG magnetic fields. The strength of these fields is sufficient to disintegrate the disk near the star: this leads to a magnetospheric accretion flow geometry, where gas at small radii flows inward following the field lines until it reaches the star in specific zones, away from the stellar equator, which are accretion hot spots.

Here, a simple geometry will be considered, which assumes a dipolar stellar magnetic field, aligned with the stellar rotation axis and perpendicular to the disk plane. The vertical component of the unperturbed field at the disk surface is

$$B_z = B_\star \left(\frac{r}{R_\star} \right)^{-3},$$

which drops sharply with increasing radii.

With the presence of a disk, the vertical field will thread the disk gas and differential rotation between the Keplerian disk and the star will distort the field, twisting the field lines that couple the disk to the star and then generating an azimuthal field component at the disk surface B_ϕ. To an order of magnitude it is plausible to consider the rapid differential rotation to result in a field

$$B_\phi \sim B_z,$$

that is limited by the settlement of instabilities that influence very strongly twisted fields.

Defining then the co-rotation radius r_{co} as the radius at which the angular velocity of the field lines (rotating with stellar rotation period P) corresponds to the Keplerian angular velocity of gas in the disk, namely

$$r_{co} = \left(\frac{G M_\star P^2}{4\pi^2} \right)^{1/3},$$

we can distinguish two regimes of star-disk magnetic interaction:

- $r < r_{co}$: the disk gas, interior to co-rotation, has a higher angular velocity than the field lines, which link the disk and the star and are dragged forward by the disk, exerting a braking torque whose tendency is to decrease angular momentum of the disk gas;

[44] As described in Section 1.2.2, this is the boundary layer geometry of accretion exploited to justify the zero-torque boundary condition.

- $r > r_{co}$: the disk gas, outside co-rotation, has a smaller angular velocity than the field lines; the disk drags them backwad and what results from the coupling is a positive torque on the disk gas.

Taking $P = 7$ days (the typical period of young stars since they are rapid rotators), for instance, the co-rotation radius around a Solar mass star is located at $r_{co} \approx 15R_{\odot}$ (0.07 AU), lying in the inner disk.

The determination of the radius within which the external torque, caused by the star-disk magnetic interaction, overwhelms the internal viscous torque derives by the comparison of the time scales for the removal of the angular momentum of the disk gas. From [1], the magnetospheric radius results then

$$r_m \approx \left(\frac{3B_{\star}^2 R_{\star}^6}{2\dot{M}\sqrt{GM_{\star}}} \right)^{2/7}.$$

Variations of the magnetic field intensity and mass accretion rate are relevant in determining the variation of the magnetospheric radius. The magnetospheric radius for reference T Tauri parameters[45] results

$$r_m \approx 16R_{\odot}.$$

It is possible to infer that stellar magnetic fields of intensity of $\sim$ kG are strong enough to drive the dynamics of protoplanetary disks in the innermost regions; moreover, a stellar magnetosphere is expected to extend out to roughly the co-rotation radius.

An implication of the magnetospheric accretion, occurring instead of the boundary layer accretion, is that the inner edges of protoplanetary disks around magnetic stars lie at $r \approx r_m$ - not on the stellar surface, then. A low density magnetospheric cavity is present at smaller radii, and within it gas is directed towards the star along field lines at approximately the free-fall velocity. This configuraton determines various observational implications:

- the innermost region of the disk, which would normally produce strong near-IR emission, is absent: the IR colors of classical T Tauri stars are then altered;
- the final accretion on to the stellar surface occurs at approximately the free-fall velocity;
- the zero-torque inner boundary condition is not justified iin this case: instead, through the torque exerted by the magnetic field (which can modify the stellar rotation rate), coupling between the star's spin angular momentum and the disk angular momentum is made possible.

However, planet formation is practically unaffected by most of these effects, since they apply at radii that are too small ($r < 0,1$ AU). Even though the variation of the inner boundary condition formally alters the stationary disk surface density profile everywhere, the variation becomes small distant from the inner boundary, which is located at $r \approx r_m$. Finally, as regards models of planet migration[46], great interest is dedicated to the presence of a low-density magnetospheric cavity: migrating planets are expected to slow until they stop when entering the magnetospheric cavity.

[45] These are the following: $B_{\star} = 1$ kG, $R_{\star} = 2R_{\odot}$, $\dot{M} = 10^{-8} M_{\odot}$ yr^{-1} and $M_{\star} = M_{\odot}$.

[46] Orbital decay is driven by angular momentum loss to the gaseous protoplanetary disk.

Chapter 2

Circumbinary disks

Before considering the effects of disks around binaries, we briefly introduce the updated multiplicity rate of stars and the separation distribution for binaries, as reported in [5] and shown in Figure 2.1.

What results is that for FGK stars, which are typically studied for exoplanet surveys, $\sim 40 \div 50\%$ of stars present additional companions, and this multiplicity is more frequent for more massive stars. As for binaries, a log-normal function (with a mean of 293 years) can reasonably fit the distribution of their separations, which corresponds to semi-major axis[1] of approximatively 50 AU for a mass sum $M_{primary} + M_{secondary} = 1,5 M_{\odot}$. The distribution of the semi-major axis grows wider in function of increasing primary mass (when divided into different primary spectral types).

2.1 Dynamics of binary-disk interaction

In this Section, referring to [6], we examine the gravitational interaction of a generally eccentric binary star system in presence of circumbinary and circumstellar gaseous disks. The following assumptions on the disks are made: disks are coplanar with the binary, geometrically thin and essentially governed by gas pressure and viscosity[2].

A binary system may present three separate disks (which interact with the tidal field of the binary and are coplanar with its orbit), depending mostly on the binary separation as well as mass ratio and the quantity of gas in different spatial regions, that are two circumstellar disks surrounding each component and one circumbinary disk. It could happen that a very low-mass secondary component is incorporated within the circumprimary disk.

Young systems, in particular binary protostars and pre-main-sequence binaries, are the most important environments with a great reservoir of gas which allows disks formation and sustainment for $10^6 \div 10^7$ yr. Almost all binaries have formed before the pre-main-sequence evolutionary stage and they result to be surrounded by molecular cloud envelopes, which accrete onto them. As regards main-sequence binaries, an average period of about 180 yr corresponds to binary separations of $\sim$ 30AU: since it is smaller than the typical protostellar disk size ($>$ 100 AU), there should be a large number of pre-main-sequence binaries with circumbinary disks. What results from observations and modeling ([6]) is that the major part of the orbital evolution in

[1] This distribution of separations is calculated using primaries of all masses.

[2] Being geometrically thin, their self-gravity is overwhelmed by these factors.

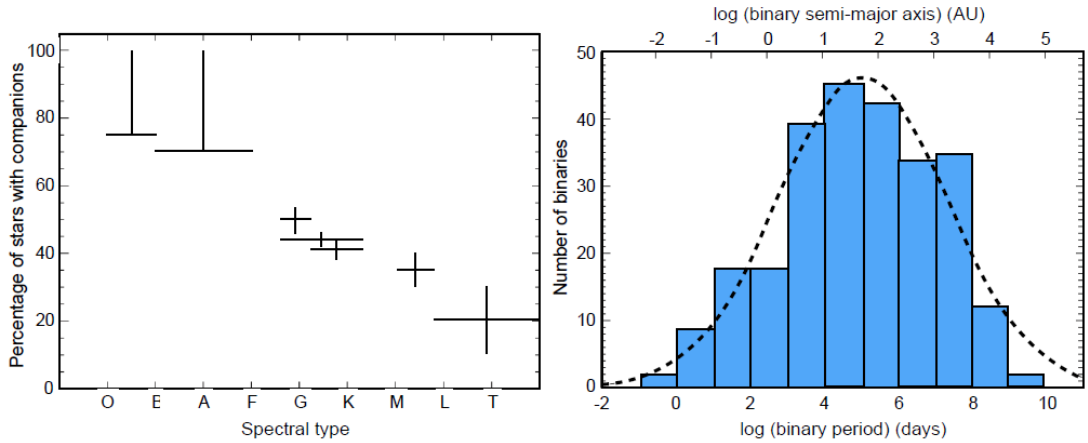

Figure 2.1: *Left: stellar companion percentage in function of spectral type. Right: period distribution of observed binaries, with a semi-major axis distribution obtained by considering a total binary mass of* $1,5M_{\odot}$ *(representing the mean observed value) and fitted by the dashed line in a log-normal distribution. This Figure has been taken from [5].*

all (except the closest) binary stars occurs very early, likely due to interactions with protostellar disks.

In order to solve the theoretical problem of binary-disk evolution, it is possible to study the influence of a near-Keplerian binary system of two point masses on the structure and dynamics of the surrounding disks; this could lead to the knowledge of the mean sizes of all the possible disks for a given binary. The utility of such results on the geometry of the disks is that they could provide a guide to the magnitude of the viscosity of the disks, which is difficult to measure directly and, as seen previously, it plays an important role as regards star formation process.

Disks in binaries are truncated mainly due to both ordinary and eccentric Lindblad resonances[3]. Initially, a smooth disk configuration is considered, which reaches quasi-equilibrium after the gravitational field of the binary truncates the disk on the dynamical timescale; in this situation, the tidal/resonant torque balances viscous torque. Subsequently, variations in the structure of the disk, such as viscous evolution, occur slowly, preserving the average size of the gap.

Resonances

The interaction usually varies between nonresonant or near-resonant to resonant.

The former (nonresonant, known as "tidal") interactions are originated by the action of the disturbing bodies, such as the secondary, which create tidal distortion in the disk parts nearest to them. A viscosity-dependent torque on the binary is generated by this moving body, since the distortion it causes lags behind it.

Instead, resonant interactions result in excitation of density waves at Lindblad (LR) and/or corotational (CR) resonances. Independently of the character of resonant

[3]A Lindblad resonance is an orbital resonance in which an object's epicyclic frequency (the rate at which one periapse follows another) is a simple multiple of some forcing frequency; this tends to increase the object's orbital eccentricity and to cause its longitude of periapse (orbital elements are described in Appendix A.1) to line up in phase with the forcing.

interactions, angular momentum is transferred (in the outward direction) by gravity between the binary and the disk.

However, the difference between the nonresonant and resonant case is physical: in fact, while the amount of tidal lag related to the nonresonant torque depends directly on the viscosity of the disk material, the resonant torque does not depend on disk parameters such as the soundspeed, viscosity or self-gravity.

As long as the disk is not thick (hot), gas soundspeed plays a minor role in determining the disk-binary interaction. The sharpness of the surface density profile at the disk edge is determined by the soundspeed, which does not affect the average gap size. Considering the resonant interaction, a growing soundspeed (which means disk thickness) is related to an increased wavelength of density waves; this implies an amplified width of the resonance responsible for truncation and then a less localized torque and smoother density profile. A shift of the half-density gap radius is induced by the variation of soundspeed, but it is only a fraction of the separation between the consecutive strong resonances ([6]).

Viscosity generates torques and determines the gap size directly, differently from pressure. The variation of viscosity displaces the disk edge freely from one resonance to another[4]. It is possible, then, to neglect the indirect effect of soundspeed on the size of the disks.

Potential

In the perturbative theories it is usually made the assumption that the nonaxisymmetric potential perturbations are small[5], thus allowing for the application of a Fourier decomposition of the time-periodic gravitational potential of the binary Φ; consequently, each harmonic component of the disturbed disk density can be treated separately. The potential is given by a double series

$$\Phi(r,\theta,t) = \sum_{ml} \phi_{ml}(r) \exp\left[i(m\theta - l\Omega_B t)\right],$$

where l is the time-harmonic number, $m \geq 0$ is the azimuthal number, $\phi_{ml}(r)$ is the radially variable potential component and $\Omega_B = (GM/a^3)^{1/2}$ is the mean motion of the binary, where M and a represent the total mass and semi-major axis of the binary, respectively. $\Omega_p = (l/m)\Omega_B$ are the uniform rotation pattern speeds of the individual potential harmonics[6]. Each ϕ_{ml} originates density perturbations that corotate with the harmonic pattern, and each (m,l) combination corresponds to a specific set of LRs, whose torque strength is determined by ϕ_{ml}.

A binary consisting of spherically symmetric stars, each with mass parameter μ_j, generates the following potential: $\Phi = -\sum_{j=1}^{j=2} \mu_j GM/|\mathbf{r} - \mathbf{r}_j|$, in which index $j = 1$ refers to the primary and $j = 2$ to the secondary star, $\mu_1 = 1 - \mu$, $\mu_2 = \mu$, $\mathbf{r}_j(t)$ is the position of the jth component and $\mathbf{r} = (r,\theta)$ is the Eulerian position vector in polar coordinates. Clearly, when considering circumstellar disks, the coordinate system is centered on the appropriate star, whereas it rests at the center of mass of the system in the case of a circumbinary disk.

According to [6], the $k = m - l = 0$ resonances correspond to the strongest torque

[4]This happens especially in high-eccentricty systems, in which many resonances are available

[5]In other words, the disk is far from the tidally disturbing components.

[6]However, the binary system's angular speed is not, in general, constant.

applied to the disk, while higher order resonances ($k = 1, 2, \dots$) are of gradually minor relevance for the gap-opening process as long as $e \ll 1$.

In Figures 2.2 and 2.4, the positions of the most relevant LRs and CRs in the circumbinary and circumstellar disks, respectively, are presented. On the vertical axis, the distance is plotted in units of a, while on the horizontal axis the combinations $m+l/10$ and $l + m/10$ are only chosen for convenience in order to distinguish various resonances in one plot. Figure 2.4 is valid to both the circumprimary and the circumsecondary disks, provided the plotting of radial distances is multiplied by $\mu_\star^{1/3}$, being $\mu_\star$ the mass fraction of a given star component of the binary system.

As stated previously, the strongest resonances are characterized by $k = m - l = 0$ and correspond to the largest symbols in the plot; then, the $|k| = 1$ resonances are presented with the second-largest symbols, because their torques are weaker by a factor of order e^2, and so on[7]. Moreover, one should consider that the resonant torque grows with the square of the mass of the perturber.

2.1.1 Circumbinary case

Considering a circumbinary disk, Figure 2.2 shows that below the 2:1 commensurability the strongest torques come from OLRs (Outer LRs) of the $(m, l) = (m, m)$ potentials whose positions converge to the semi-major axis of the binary with increasing m. Their combined effect, provided the mass ratio is not extremely small, is to clear a gap around the binary system.

Once fixed the value of m, the eccentricity-dependent resonances reach the more external region of the circumbinary disk due to an increasing value of $|k| = |m - l|$. For a given eccentricity, looking at the resonances coexisting at any of the main commensurabilities shown in Figure 2.2, it is clear the outermost position of the $l = 1$ OLRs makes them the most important in the circumbinary disks.

Let us now consider the evolution of a binary with initial null eccentricity, embedded in a circumbinary disk and subject to possible addition of low-mass circumstellar disks: the effect of the binary-disk interaction is to increase the binary eccentricity e. In [6] they observe that the disk torquing at "eccentric" resonances with $|k| > 0$ will become gradually stronger when eccentricity increases its value. The "switching on" of consecutive resonances corresponding to higher $|k|$ values can occur, contributing to the binary evolution; their strength enhances with growing eccentricity, resulting in a wider gap around the secondary component. Each resonance holds the disk rim for only the needed period of time for the next-lying one to exert sufficient torque to open a greater gap. As regards the corotational resonances, they do not play a relevant role in disk truncation due to the resonance geometry for binaries with non-extreme mass ratio.

In order to provide an estimation of the size of the gap cleared by the binary within the surrounding disk, we will then consider the resonances which are able to overcome the action of disk viscosity (which results in a gap-closing effect) for a given set of binary and disk parameters. Once set the binary mass parameter $\mu = 0, 3$, Figure 2.3 presents the eccentricities, on the horizontal axis, which are sufficient to open gaps at radii presented on the vertical axis, corresponding to $(m, 1)$ OLRs in circumbinary disk. Points corresponding to the same Reynolds numbers[8] of the disk gas (numbers

[7] Anyway, either size or area of the symbols are not directly proportional to the resonant torque, in fact they are bigger than their actual size for clarity.

[8] For a typical disk thickness of $h/r \sim 0, 1$, the Reynolds number can be converted to viscosity

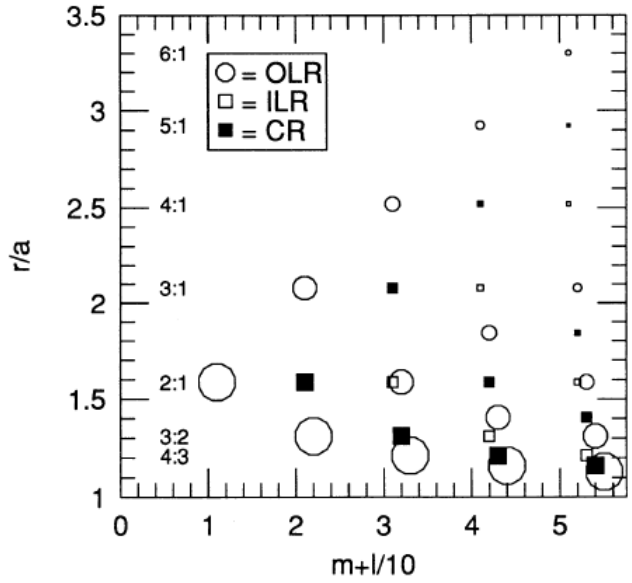

Figure 2.2: *Positions (represented in units of semi-major axis a of the binary) of Lindblad and corotational resonances in a circumbinary disk for different* (l, m) *potentials assuming* $|k| = |m - l| < 5$*, reported in [6]. The biggest symbols identify the strongest* $(k = 0)$ *resonances, whereas smaller symbols indicate the progressively weaker resonances (larger* k*). Along the vertical axis, the locations of the most relevant commensurabilities of disk and binary orbital periods are indicated.*

indicate $\log \mathscr{R}$) are connected by the dotted lines, which approximately determine the location of the circumbinary disk edge. What results is that, during the continuing orbital evolution, the elongated stellar orbits do not tend to intersect or even come close to the disk edge; furthermore, the disk seems to withdraw from the binary (in terms of a, denoting the binary semi-major axis) with increasing eccentricity.

Results

For typical viscous disk parameters, what results is that the inner edge of a circumbinary disk is located between $1,8a$ and $2,6a$ with binary eccentricities $0 < e < 0,25$; instead, the minimum distance between a component star and the circumbinary disk inner edge, for eccentricities $0 < e < 0,75$, is greater than a.

In particular, assuming $\alpha_\nu \sim 0,1$ and binary mass ratio of about 2:1, for nearly circular binaries the inner portions of circumbinary disks are truncated close to the 3:1 resonance with $r = 2,08a$; instead, for $e \sim 0,2$, disk truncation at $r = 2,52a$ occurs close to the 4:1 resonance. Eccentric Lindblad torques are responsible for the constant outward progression of the location of the inner edge with increasing binary eccentricity (see Figures 2.2 and 2.4).

Finally, as regards the possibility for planets formation in circumbinary disks, we note that (according to [7]) studies have shown that disks around close (< 100 AU) binary systems are subject to faster dissipation than those around single stars or more widely separated systems. Consequently, giant planets forming around close binary systems must accrete more rapidly than what would be required around single stars, thus

parameter (referred to the Shakura–Sunyaev α prescription, presented in Section 1.2.3) α_ν via $\alpha_\nu \sim 10^2/\mathscr{R}$ ([6]), then the lowest dotted line refers to $\alpha_\nu = 1$ and the highest one to $\alpha_\nu = 10^{-9}$.

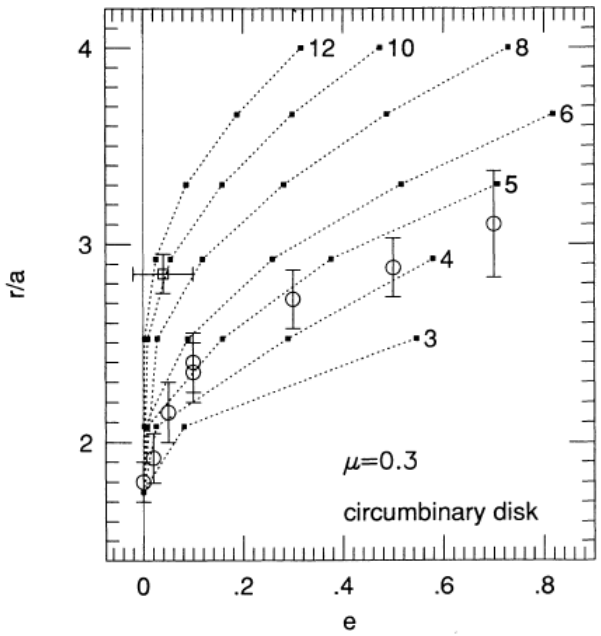

Figure 2.3: *Estimated (as reported in [6]) radius of the inner edge of the circumbinary disk for a binary with mass parameter* $\mu = 0,3$*, depending on the locations of resonances due to* $(m,l) = (m,1)$ *potentials, and eccentricities satisfying the conditions for marginal gap opening (black squares). For a disk with thickness ratio* $h/r = 0,03$*, the dotted lines (connecting data with the same Reynolds number of the disk gas) in the Figure are labelled by the values of* $\log \mathscr{R} = 12, 10, \ldots, 3$*, which correspond to the viscosity parameter* $\log \alpha_\nu = -9, -7, \ldots, 0$*. Circles with error bars are the results of the modeling adopted in [6].*

leading to higher masses as a (possibly) natural consequence of rapid planet formation via gravitational instability[9].

2.1.2 Circumstellar case

Potentially powerful ILRs (Inner LRs), outside the 1:2 period commensurability, can occur in circumstellar disks as proved by Figure 2.4; however, due to the phenomenon of orbit crossing, these resonances can only be found within a circumstellar disk for small (planetary) mass ratios. In short, for usual binaries, the importance of the resonances plotted with biggest symbols is to be found in the fact that they are too strong, removing then the gas from their surroundings. Therefore, the effective extent of disks in and around an eccentric binary is often given by the eccentricity-dependent resonances with $|k| > 0$.

Once fixed the value of m, the higher the value of $|k| = |m - l|$, the closer to the center is reached by the eccentricity-dependent resonances in circumstellar disks. As regards the resonances coexisting at any of the main commensurabilities reported in Figure 2.4, we see that, for a given eccentricity, the $m = 2$ ILRs play a special dominant role in circumstellar disks, representing the innermost resonances truncating the disks.

Similarly to what we reported for the circumbinary case, for a choice of a binary mass parameter $\mu = 0,3$ Figure 2.5 shows the eccentricities sufficient to open gaps at certain radii[10]. The resonances considered are the $(m, l) = (2, l)$ OLRs. Points referring to the same Reynolds numbers of the disk gas are connected by the dotted lines (as in Figures 2.2 and 2.4), which provide an estimation of the location of the circumstellar disk edge.

Results

What results in the circumstellar case, assuming $\alpha_\nu \sim 0,1$ and binary mass ratio of about 2:1, is described by the following points.

- The outer edge of a *circumprimary* disk is located close to the 1:3 resonance, at $r = 0,46a$, for nearly circular binaries, whereas for $e \sim 0,1$, the disk is truncated near the 1:4 resonance where, for $\mu = 0,1 \div 0,3$, $r = 0,38 \div 0,35$.

- The outer edge of a *circumsecondary* disk is located close to $r = 0,2a$ for nearly circular binaries, whereas for $e \sim 0,05$, the disk is truncated near the 1:4 resonance where, for $\mu = 0,1 \div 0,3$, $r = 0,18 \div 0,27$.

The case of HD 100453A: binary-driven spiral arms in a protoplanetary disk

As an example of the influence of an external binary companion (secondary) on the circumprimary disk, we report the case of HD 100453AB, which is a (10 ± 2) Myr old binary whose protoplanetary disk was recently revealed to host a global two-armed spiral structure[11], as shown in Figure 2.6. Since the binary has a relatively small

[9]Indeed, there is evidence that planets in binary systems with separations < 100 AU are biased towards higher masses.

[10]They are presented on the vertical axis and identified with commensurability ratios on the right.

[11]Structures in protoplanetary disks are often exploited to predict the possible properties of planets that may have originated them. The strong interaction with the protoplanetary disk may arise once the planetary core has gained sufficient mass to undergo run-away gas accretion, inducing large-scale

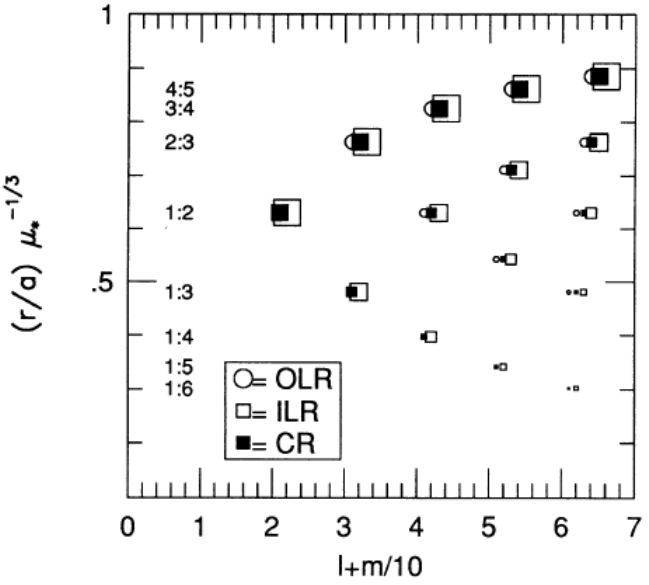

Figure 2.4: *The Figure has the same meaning of Figure 2.2, but considering a circumstellar disk around the binary component with a mass parameter which is $\mu_\star$ (taken from [6]). Moreover, on the horizontal axis it is reported a different convenient combination of indexes m and l.*

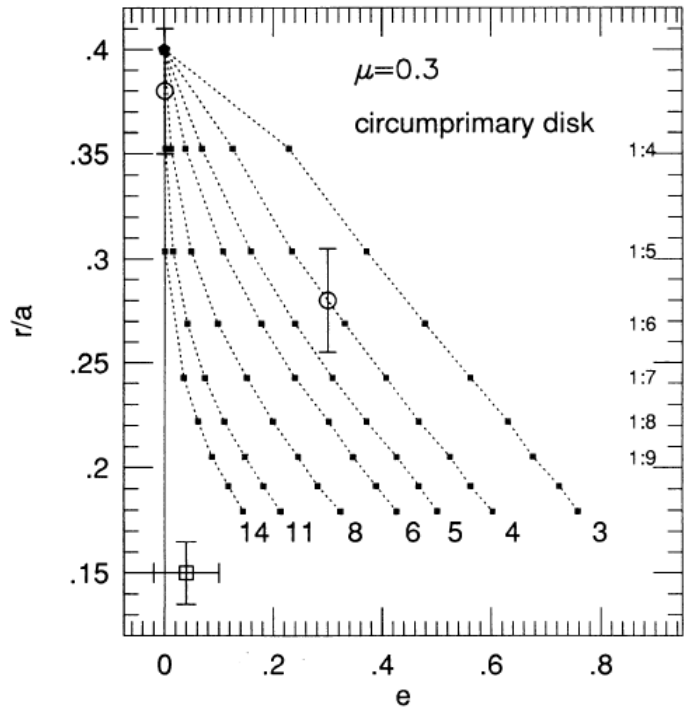

Figure 2.5: *Approximate size of a circumprimary disk (the circumsecondary disk has the approximately same qualitative trend of the circumprimary disk, but present a maximum size which is smaller than its) in binaries with mass parameter $\mu = 0,3$, reported in [6]. Symbols have the same meaning of Figures 2.2 and 2.4, and the black pentagon identifies the tidal truncation size.*

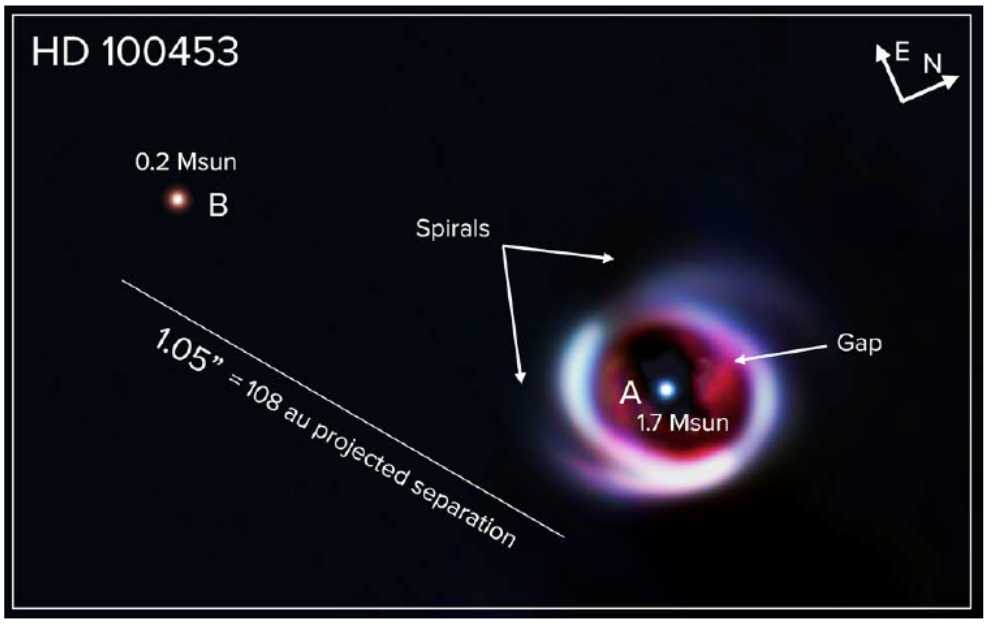

Figure 2.6: *Schematic structure of the HD 100453 system obtained by the SPHERE data, reported in [8]. The primary A-star hosts an M-dwarf companion and a spiral protoplanetary disk, which in turn presents a gap comparable to Uranus's orbit size about the Sun ($R \sim 20$ AU). The luminosity of the stars with respect to the disk and to each other are less than their actual values for clarity, and the image colors of red, green and blue are composed of Y-, J- and H-bands, respectively.*

projected separation (~ 108 AU), the driving force behind the formation of the spiral arms seemed to be due to gravitational perturbations produced by the binary. The disk is relatively co-planar with respect to the orbit of the companion.

In order to model the structural evolution of the disk, hydrodynamic and radiative transfer simulations are performed in [8]; their result is that the companion could have consistently driven the origin of the spiral structure and truncation of the circumprimary disk in HD 100453 (this mechanism is described in [6]). In fact, their outcome is that the companion generates a two-armed spiral structure in the simulated disk that is qualitatively compatible to the observed general properties of the spiral arms in HD 100453: as a consequence, it is likely that their origin is explained without necessarily invoking any additional effects, such as differential thermal and radiation pressure in the shadowed regions.

Furthermore, the primary star's rotation, its outer disk and the companion result to exhibit approximately aligned angular momenta, and thus it is possible that the system formed from the same agglomeration of material.

disk structures which could be gaps, vortices and spiral density waves. The effect of these interactions is to contribute to the disk evolution, consistently modifying the environment of planet formation.

2.2 Circumbinary disks

2.2.1 The case of GG Tau A

The GG Tau system

Circumbinary disks in wide binaries have been imaged in only a few cases[12], among which we find GG Tau: the quantity of observational data available for it, make this system particularly interesting, allowing for comparisons with theoretical models.

GG Tau is a multiple system, composed of A and B binaries: at an assumed 140 pc distance of Taurus, the components of each binary are distant ∼35 AU and ∼207 AU respectively, whereas the distance between the hierarchical pairs is ∼1400 AU.

Since the discovery of GG Tau A, which represents the much more massive (*primary*) component of the system, it has been studied exhaustively, making a sufficiently detailed picture of the system possible.

In a model discussed by [9], the circumbinary material around GG Tau A presents two components consisting of a ring (or *torus*) and a disk with a combined mass of $\sim 0,12 M_{\odot}$[13]. The torus' inner and outer edges are located at distances of 180 AU and 260 AU from the apparent system center, respectively, and they are both quite sharp[14]. Assuming that the torus is circular, its inclination of 37° is determined from the observed projected image.

Even though the disk's outer edge is not clearly resolved, it appears to extend to ∼ 800 AU, which is consistent with the location of the tidal truncation due to the B components of the combined quadruple system. The total mass of the A components is constrained by kinematic measurements of the circumbinary material, and results to be $(1,28 \pm 0,07) M_{\odot}$. Circumstellar environment presents a lower limit on the mass of such material to be $\sim 0,8 \times 10^{-4} M_{\odot}$, determined by its unresolved emission.

However, the large number of observations of GG Tau present inconsistencies, based both in the data themselves and in the search for theoretical models which can fit them.

Similarly, the orbital parameters of the stars have been established from fits to their relative motions, and are determined to define an orbit whose parameters are a semi-major axis of $\sim 32,4$ AU and an eccentricity of $0,34$. Theoretical expectations[15] of these parameters appear to be inconsistent with their inferred values.

Finally, it has been demonstrated that an alternate fit (which employs a slightly increased error bar on the system's observed inclination) to the data provides a semi-major axis of 62 AU and an eccentricity of 0,35: this orbit is consistent with the dynamical constraints implied by both the inner disk edge location and the observed projected separation of ∼ 36 AU.

Simulations

In [9], modelled configurations (providing two-dimensional hydrodynamic simulations) in which a circumbinary torus+disk surrounds a pair of stars in orbit around each other and a circumstellar disk surrounds each star, similar to that observed for the GG Tau A system, are presented.

[12] Considering the fact that the total number of observed circumbinary disks is not large, too.

[13] About the 70% of this total mass is contained in the torus.

[14] The edges are wide less than 10 AU.

[15] From models which predict a semi-major axis > 50 AU ([6]) based on the positions of various orbital resonances and the ∼ 180 AU inner diameter of the circumbinary disk.

The following assumptions have been made:

- the disks cool as blackbodies, using rates determined independently at each position in the disk by the temperature of the photosphere there, which is time-dependent;
- heating is generated by hydrodynamical processes and by radiation from the two stars, using rates approximated from a measure of the radiation which the disk intercepts at its photosphere.

Simulations involve a suite of systems configured with semi-major axes of either $a = 62$ AU or $a = 32$ AU, and assuming orbital eccentricity to be either $e = 0$ or $e = 0, 3$.

Results

Results from simulations prove that the stirring action of the binary combined with its own self gravity generate strong, sharply defined spiral structures which, in some cases, fragment into 1 or 2 massive clumps.

These spiral structures are well defined in space, present edges large less than $5 \div 10$ AU, and often extend for an angle $> 2\pi$ around the center of mass. Consequently, observations of sharply defined structures in the GG Tau A torus are to be interpreted as evidence for such spiral structures.

What results is that structures created at different times often interact with one another and subsequently fragment into one or two clumps, with initial masses of the order of brown dwarves, in the late evolution of several simulations. Since in a model, where the binary has been replaced with a single star of the same mass, 38 clumps formed in less than a single orbit of the torus, it is clear the relevance of the binary's stirring action, which contributes to the thermal energy input of the torus and represents a reliable indication of the importance of self gravity in the GG Tau A torus. Moreover, the formation of fragments occurs even when neglecting radiative heating.

The inward extension of the spiral structures reaches circumstellar environment, since large scale material streams[16] for which most material is found on trajectories that return it to the torus on a timescale of $1 \div 200$ yr. The outward extension of the spiral structures passes through the torus, generating net outwards mass flow which extends into the low density circumbinary disk surrounding the torus, and subsequently loses coherence distant from the stars[17]. About 15% of the mass of the torus (as regards torus-only configurations) moves outwards during the ~ 6000 yr duration of the simulations, representing approximately half of the observed mass of the present disk (30% of the torus mass); instead, in the torus+disk initial configuration, the rates result to be much lower. Consequently, the expectations are that on longer timescales, while the disk component gains mass, the outwards mass transport into the disk and the mass escaping from it through its outer edge (or other mechanisms) balance each other.

During most of its evolution, the torus becomes consistently eccentric in shape; in all configurations, accretion onto the stars occurs at a stationary rate of a few $\times 10^{-8} M_{\odot}$ yr^{-1}, with the outcome that the disk lifetimes would be inferior to $\sim 10^4$ yr,

[16]Only a small fraction accretes into the circumstellar environment.

[17]The presence of the disk component of the circumbinary material is interpreted as an excretion feature generated by the mass transported there via the spiral structures.

in absence of replenishment. Simulations show that the only configurations which are able to retain circumstellar disks are represented by wide orbit ones, since accretion driven from the relevant material streams[18] generated in wide configurations - those streams are very weak in close configurations[19]. In wide, eccentric orbit configurations, accretion is sporadic and affects mainly the secondary[20], presenting rates which are mostly concentrated near the binary periapse.

The conclusion, inferred by the results in [9], is that the GG Tau A torus is consistently self gravitating and that shock dissipation, related to spiral structures[21], represent the main contribution to its thermal energy input. Moreover, the sharply defined peculiarities revealed in the torus are to be considered as expressions of such spiral structures, and the low density disk surrounding it is interpreted as an excretion disk generated by the outward mass flux originated by the spiral arms while propagating outwards.

As regards the supposed $\sim 20^\circ$ mutual inclination between the stellar orbit plane of GG Tau A and its surrounding torus (through a degeneracy regarding the interpretation of inclination of the torus and its eccentricity), typical eccentricities calculated for the shape of the tori modeled in the simulations are sufficient to justify that value. The observations are then interpreted favoring a coplanar system with an eccentric torus. Due to the fact that only in wide orbit configurations accretion onto the disks is able to sustain them, it is possible to state that the gas, which is currently present in the circumstellar disks of the GG Tau A system, has been accreted by the torus during the last few thousand years. The overall environment of circumstellar disks remains unfavorable due to high temperatures and other conditions, even though such disks will exist for periods long enough to guarantee planet formation.

Finally, given the presence of circumstellar disks, relevant accretion streams and the interpretation of the GG Tau A stellar orbit plane to be coplanar with the torus surrounding it, the final conclusion is that the GG Tau A system is in an eccentric ($e \sim 0,3$), $a \sim 62$ AU orbit: this resolves questions in the literature concerning its orbit parameters.

2.2.2 The case of HD 106906

HD 106906

HD 106906, which is a Lower Centaurus Crux (LCC) member, hosts a massive ($M = (11 \pm 2) M_J$) circumbinary giant planet (GP) detected in projected separation at (732 ± 30) AU, with a long orbital period of at least 3000 years. The system is named HD 106906AB, since it is a close binary, with a total stellar mass higher than $2,5 M_\odot$; moreover, it hosts a high-luminosity ($L_d/L_\star = 1,4 \times 10^{-3}$) circumbinary disk[22].

[18] A small part of the material in such streams is directed towards the circumstellar environment, whereas the remainder returns to the torus.

[19] Differently from the wide configurations, the streams in close binary configurations involve much less material, making the accretion rate into the circumstellar environment $\sim 10^2$ times smaller.

[20] In wide binary configurations (over the duration of the simulations) mass of the order of the disks masses is accreted onto each of the components.

[21] These structures are generated by self gravitating disturbances as well as by the stirring action of the binary.

[22] Being the binary very close, in correspondence of the inner ring its effects are the same of a single, massive central star.

As described in [10], HD 106906AB is, to date, the only young binary system around which a planet has been imaged and a debris disk observed exploiting a strong IR excess. The morphology of a debris disk can be strongly affected by the structure of the underlying planetary system.

This system, given its youth ((13 ± 2) Myr), represents the perfect environment to study early dynamics of planetary systems, in particular to answer the question about where and how the planet formed, since there are various possible scenarios.

- If originated by core accretion or disk gravitational instability close to the star, it must have been ejected on its current orbit by some mechanisms, preserving the disk material supposedly located at ~ 20 AU.
- If formed bound to the star at its current position, however, cloud collapse could represent an alternative formation mechanism.
- Finally, the planet may have been captured from another star; this is a plausible scenario since the largescale (cluster) environment of HD 106906AB is, and was, surely even denser at earlier epochs.

Observational data

In order to observe HD 106906, in [10] they used the extreme AO fed, high contrast imager SPHERE (see Chapter 3 for its description) installed on the VLT, requiring the use of both the IRDIS imager and the Integral Field Spectrometer.

They derived an inclination of $(85,3 \pm 0,1)^\circ$ and a disk position angle (PA[23]) of $(104,4 \pm 0,3)^\circ$, which is oriented counterclockwise from the position angle of the companion, constraining the orbit of the companion relative to the disk. A relevant peculiarity of the disk is its E-W brightness asymmetry, as clearly shown in Figure 2.7: in fact, the SE side results to have a luminosity about 10% higher than the NW side. The most extended peak of the disk's luminous intensity profile extends up to 550 AU towards west, whereas the east edge reaches, by diffusion, the maximum of 120 AU. On the contrary, within 120 AU the disk is brighter on its east side than on its west side: the explaination of this asymmetry could be due to a disk which may be an eccentric ring and which will present a brightness asymmetry towards the pericenter side (NW) and a faint, extended tail in the direction of the apocenter side. On the other hand, according to [11], it might also indicate the presence of a spiral density wave extending over the entire disk, and viewed edge-on from the Earth.

As reported in [12], different observations noted other features of the disk morphology and system geometry, such as that the inner disk does not show evidence for vertical extension, suggesting that the inclinations of the disk particles have not been excited; moreover, a large cavity divides the disk into two debris belts located at radii of 13,7 and 46 AU.

A dynamical scenario for planet formation

Classical mechanisms of planet formation are challenged by the large separation between the planet and the central binary and by the possible mutual inclination between the planet orbit and the debris disk.

[23]It is defined strarting from N toward E.

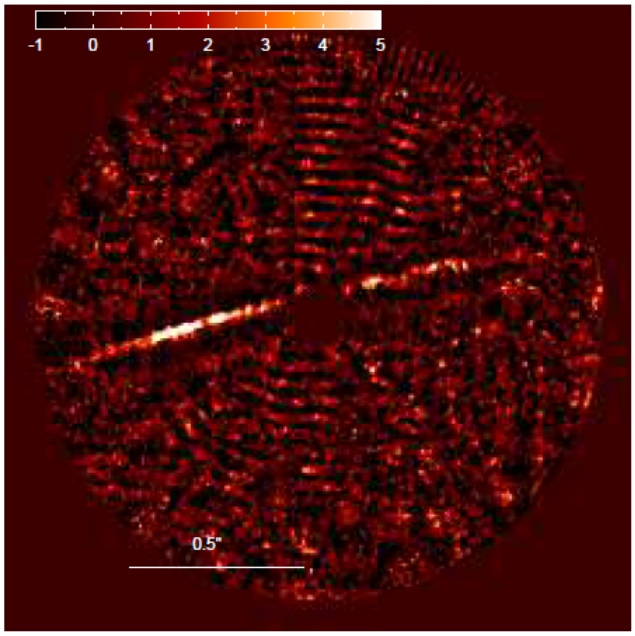

Figure 2.7: *IFS YJH SNR (Signal to Noise Ratio) map of the HD 106906AB disk, taken from [10]. N is up and E to the left.*

Referring to current theories, planet formation takes place in the primordial gaseous disk; however, the formation a giant planet through core accretion or gravitational instability at 700 AU or more from any central star results improbable: in fact, the lack of circumstellar gas at that distance, in addition to the fact that the corresponding formation timescale would exceed the lifetime of the gaseous disk ([11]), are limiting conditions. The disk asymmetries, in particular the possible spiral structure, indicate relevant ongoing dynamical interaction with the dust, suggesting that the planet may have formed inside and then be scattered[24], reaching its current location. As shown in [11], the planet (HD 106906AB b) could have formed within the primordial disk before being scattered away on a wide orbit in the first ten million years of the system life, and this situation requires the combined actions of disk-induced migration and meanmotion resonances with the binary. If the scattering is probable, however, the stabilization of the planet on its current wide orbit, being delicate, needs more than gravitational interactions with the binary: a fly-by[25] scenario has been considered, even though the stabilization only occurs for a limited part of the overall encounters trajectories. Instead, destabilization by a fly-by is much more probable, since the low density ($< 0,11$ stars/pc^3) of the LCC makes a close encounter even more unlikely.

Multiple features characterize the disk, and ther explaination could be found within the frame of our scenario as well as outside of this frame. Whether the planet, during the last ten million years, has had an eccentric orbit with periastron of ~ 200 AU, then two spiral density waves may have been created. The ejection of the planet could have originated a needle extending to 500 AU, while a smaller needle could be due to an eccentric inner orbit or to an eccentric and inclined outer orbit. Moreover, the secular effect of the latter orbit configuration for HD 106906 b could provoke asymmetries in

[24]In fact, the fact that HD 106906AB is a binary represents a source of potentially strong dynamical perturbations that could prime planet scattering.

[25]It is a close encounter with a celestial body.

brightness[26] which are in agreement with the observations.

The scenario explored in [11] is based on the observed components of the system, such as disk and binary stars, and on the hypothesis that core accretion or gravitational instability coud not have explained planet formation at several hundreds of AU. However, those assumptions must be reconsidered, since the probability of occurrence of that scenario is low. Alternative hypothesis, such as the circularization of the planet orbit due to the interaction with the disk gas or in situ formation, could account for the observed structure of the system; this requires, however, that the disk extends up to the separation of the planet and contains enough gas in that position.

External perturbations of the debris disk

Dynamical modeling of debris disk morphology indicates that eccentricities of the particles in the disk can be excited by an exterior perturber, through Laplace-Lagrange secular perturbations in the near-coplanar case or Kozai-Lidov perturbations[27] for mutually inclined companions and disks, provoking asymmetries in the disk and triggering a collisional cascade among the disk particles; smaller dust grains, whose thermal emission or scattered light can be spatially resolved with infrared or optical imaging, are produced by the collisions.

HD 106906 represents an ideal example of a system with an exterior perturber - the GP previously introduced, which can shape the system's debris disk into a flat, eccentric, dust-producing ring and reproduce its observed morphological features and asymmetries, as demonstrated in [12]. Their simulations also place constraints on the orbit of the companion using the morphology of the disk.

Furthermore, they showed that a companion with an orbit completely exterior to the disk can reproduce the observed asymmetries without causing vertical extension of the disk[28], in favor of the in situ formation scenario of the companion.

Considerations

In conclusion, the very inclined ring-like disk around HD 106906, which is distant 65 AU from the stars, shows a strong brightness asymmetry with respect to its semi-major axis; moreover, ejection of small grains by the stellar radiation pressure is compatible with its smooth outer edge. As regards the planet's projected position, in [10] they showed that it is significantly above the disk's PA (see Figure 2.8); nevertheless, given the inferred disk inclination, it is still possible that the planet could still orbit within the disk plane if at a large separation ($\sim 2000 \div 3000$ AU). Finally, the presence of additional massive inner planets is likely, since they could account for the inner void of material within the disk.

[26] In particular, ejection, outer and inner orbits can generate relevant asymmetries in the disk during the first ten million years of a system: in fact, an inner orbit enhances the dynamical perturbations created by an outer orbit by accelerating the precession, whereas the outer orbit, if eccentric, can increase the perturbations created by the inner orbit by providing eccentricity to the disk.

[27] It represents a periodic exchange between the orbital inclination and its eccentricity, thus causing a libration (an oscillation over a constant value) of the argument of periapsis.

[28] It was previously supposed that the companion formed interior to the disk and was then scattered onto a highly eccentric orbit; in addition, according to the same study, the result was that the disk can survive perturbations by a companion with an apocenter distance of 650 AU and a pericenter distance interior to the disk if the companion's inclination is $> 10°$. Anyway, this implied a significantly vertically perturbed disk by 10 Myr, independently of the companion's inclination.

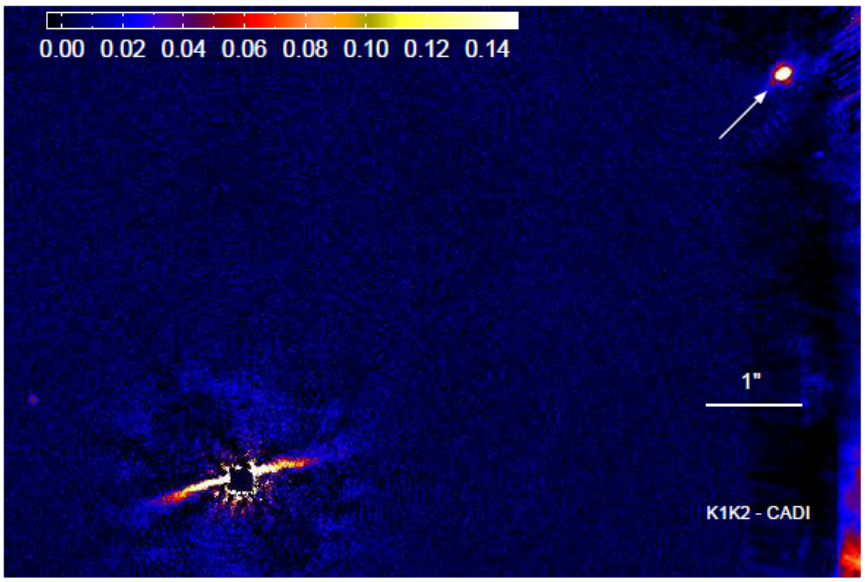

Figure 2.8: *The disk and the planet around HD 106906AB, as reported in [10]. North is up and East is to the left. HD 106906AB b is the bright source top-right.*

2.3 Circumbinary planets

As stated in [5], about half of Sun-like stars are present in multiples and about a third in binaries; it is also known that there are several extra-solar planets, with most stars hosting at least one planet. The next step is to link the two concepts and concentrate on planets in binaries: considering the distribution of both planets and binaries throughout the Galaxy, their coupled existence is naturally expected.

We will then examine the *Kepler*'s discoveries as regards circumbinary planets, and finally we will discuss the search for planets orbiting two stars, in particular considering the stability criteria and the direct imaging method.

2.3.1 Circumbinary planets with Kepler

According to [13], among the exciting discoveries of NASA's *Kepler* photometer, the detection of transiting circumbinary planets plays an important role: in fact, these plantes are continuously growing in number, and a multi-planet system with one of the planets in the habitable zone (Kepler-47) has been observed.

The first transiting circumbinary planet, Kepler-16b, was announced in September of 2011. Transits are crucial since they unambiguously establish the presence of the circumbinary body. Besides being a key to circumbinary planet detection, the pieces of information derived by the transits allow to obtain very precise stellar and planetary masses and radii, through the exact geometrical configuration required to produce the detailed shape, duration and timing of the transits.

Soon after the discovery of Kepler-16, five additional transiting circumbinary planet systems have been confirmed and several candidate systems are under investigation. Thus, Kepler-16 did not represent an isolated case: the circumbinary planets have become indeed a new class of planets.

We will now examine the multi-planet Kepler-47 system and the rapidly developing picture of the nature of circumbinary planets.

The circumbinary planet "smoking gun"

The detection of transits in a circumbinary system is more difficult than for transits in a single-star system for several reasons. First, the eclipses are generally very much stronger than the transits, and their presence tends to overwhelm or mask the transit signal; second, the transits are neither periodic nor of equal duration, and this represents the more challenging issue[29].

The well-known transit timing variations (TTVs), occurring in the case of a perturbed planet (in a multiple planetary system) around a single star, can be used for planet confirmation and mass determination. On the other hand, for a circumbinary planet, the transit period is very far from being strictly periodic[30].

The reason for the variation of the period resides in the fact that the primary star is not stationary with respect to the planet, because its orbit is around the barycenter of the binary star system: then, the transits can occur when the star is before as well as after stellar conjunction. Clearly, if $M_{planet} \ll M_2 \ll M_1$, the TTVs induced by the geometrical configuration will be approximately null, being the primary always near the system's center of mass. The largest TTVs are caused by equal mass stars configurations[31]. The efficiency of planet searches based on a periodic signal will be limited by TTVs.

Another important effect involves the substantial variations of the widths of the transits, known as transit duration variations (TDVs), which are often easily detectable by eye in the light curves and are again due to the "moving target" effect. In fact, assuming the planet orbits in the same sense and in approximately the same plane as the binary, the transit duration is determined by the size of the star (and planet) and the relative transverse velocity between the star and the planet. In proximity of binary phase zero, set by the primary eclipse, the star and planet are moving in the opposite verse, then the transits duration is short; on the contrary, near secondary eclipse, the star and planet are moving in the same verse, leading to long transits duration. Instead, next to the quadrature points of the binary orbit, the transits duration is "normal". The outcome is strong, provoking variatons of eclipse durations by factors of several; for instance, durations can vary from a few hours to a few days.

Besides making circumbinary planet hunting difficult, TTVs and TDVs do have a very important positive consequence. In particular, when a candidate transiting circumbinary planet is found, the confirmation or rejection of the fact it is a physically bound body is easy. In fact, the binary star phase-specific TTV and TDVs provide a *smoking gun*, since no other known astrophysical phenomenon can induce such variations.

In the case the planet is sufficiently massive to measurably affect the stars' orbits, stellar eclipse timing variations (ETVs) will be apparent; being generally much deeper than transits, eclipse times can usually be measured with more elevate accuracy than

[29]In fact, a single planet orbiting a single star will exhibit strictly periodic transits. Searches based on a periodic signal can be highly efficient at detecting the planet. The presence of other planets in the system, that strongly gravitationally interact with the transiting planet, makes the times of transits no longer periodic, and they can vary by a few tens of minutes to a few hours, typically.

[30]For example, in Kepler-16, the third transit across the primary star (a transit across the primary star is called *primary transit*) occurs 8,8 *days* early compared to the expected time based on the first two transits.

[31]In a configuration in which the planet and stars are on circular coplanar orbits, the variation between the primary transit times and a linear ephemeris is a minimum of $\pm \sim 0,11$ times the orbital period of the binary stars. For more general orbital orientations and eccentricities the TTVs can be even larger, and the transits of the secondary star will have even larger TTVs.

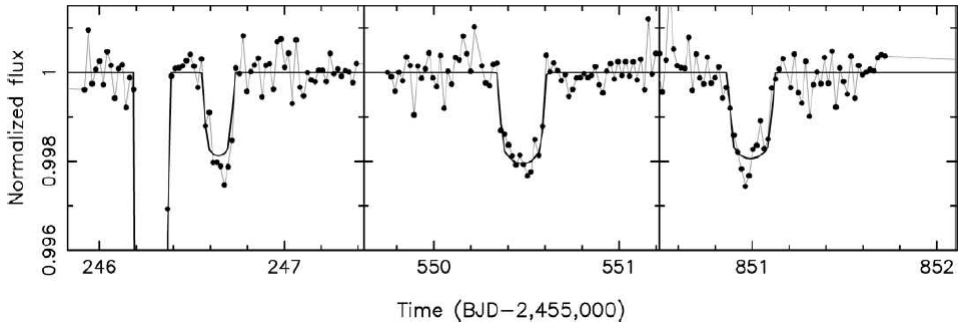

Figure 2.9: *The three observed Kepler-47 c transits with model fits, as reported in [13]. The large excursion in the first panel represents a primary eclipse.*

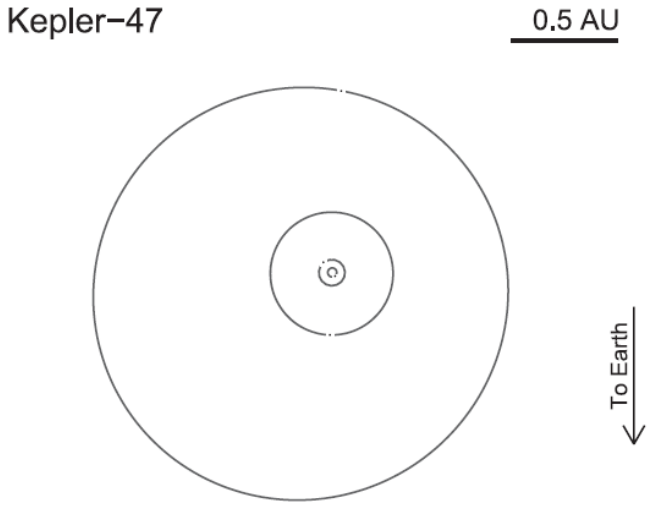

Figure 2.10: *Bird's eye view of the binary and planetary orbits for Kepler-47, as reported in [13]. The small gaps in the orbit curves provide the position of the bodies at this particular epoch.*

transit times, allowing for detection of timing variations[32] of the order of ∼seconds.

The presence of a light-travel time effect (LITE), in addition to this dynamical perturbation, may also provide constraints on the mass of the planet relative to the binary.

Kepler-47

As concerns the multi-planet Kepler-47 system (in which there are two candidate circumbinary planets revealed through transits, as shown in Figure 2.9 for planet c), planetary transits set tight constraints on the primary star's position and orbital motion. What resulted is the mass ratio of the system, and consequently the whole set of binary star system parameters: the primary star is approximately Sun-like, with a mass of $(1,04 \pm 0,06)M_{\odot}$, radius $(0,96 \pm 0,02)R_{\odot}$, and temperature of (5635 ± 100) K, whereas the secondary is a smaller star of mass $0,36M_{\odot}$ and radius $(0,351 \pm 0,006)R_{\odot}$.

[32]For instance, the most easily detectable effect of a planet on the binary stars is the precession of the stellar orbits, resulting in the difference between the orbital period determined by the primary eclipses and the orbital period determined by the secondary eclipses.

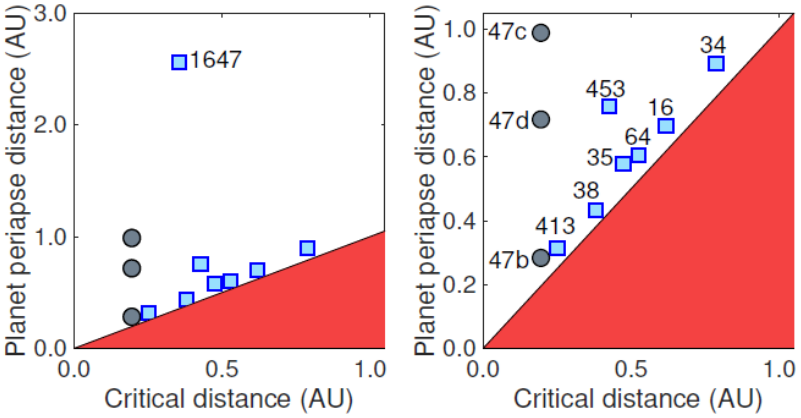

Figure 2.11: *Circumbinary periapse distance, $a_p(1-e_p)$, as a function of the critical distance for the Kepler transiting circumbinary planets, as reported in [5]. The red zone leads to the instability for planetary orbits in that region. The multi-planet Kepler-47 system is represented by grey circles, and the blue squares correspond to the other, single planet systems. The right plot is zoomed near the stability limit. Kepler numbers are labelled.*

Once determined the stellar radii, the planetary radii can then be obtained, resulting in a radius of $3,0R_\oplus$ for planet b, whereas planet c has a radius of $4,6R_\oplus$. Moreover, it is possible to set upper limits of $< 2M_J$ and $< 28M_J$ on the masses.

The orbital periods of the planets are 49,5 d and 303,1 d, respectively; the eccentricity of planet b is low ($e < 0,035$), instead, for planet c, only 3 transits are measured so the eccentricity is more difficult to constrain[33]. Planet b's period (which is 6,6 times the binary period) results to be 77% higher than the critical period below which interaction with the binary stars could imply dynamical instability. Moreover, while planet b resides well interior to the habitable zone (HZ), planet c is located completely within the HZ for $e < 0,2$, and even assuming $e = 0,4$ the mean insolation[34] is 96% of the Sun-Earth insolation.

The relevance of Kepler-47 resides also in the fact that it establishes that planetary systems, and not just single planets, can form[35] and survive in the chaotic environment close to a binary star, as shown in Figure 2.11, which demonstrates that the circumbinary planets have generally been found extremely close to the stability limit set by the dynamical influence of the binary. Planet-planet interactions tend to be enhanced by the binary stars, then planetary orbits lying close to the binary may be strongly influenced by dynamical instability. As previously discussed, Kepler-47c shows that circumbinary planets can persist in the habitable zones around their host stars, providing and opening up new habitats for life to potentially exist.

[33] A 95% upper limit of $e < 0,41$ is found, with $e \sim 0,1$ preferred.

[34] It is the mean insolation that is relevant for habitability.

[35] As suggested in [5], however, in situ formation (very close to the binary) for circumbinary planets appears to be unfavorable, due to a hostile disk environment. The most accredited theory is an inwards migration of the planets, which will subsequently park near the stability limit, where the disk is expected to have been truncated ([6]).

The developing circumbinary planet picture

From observations in [13], the presence of a wide variety of stellar configurations for which circumbinary planets can exist is evident. In fact, primary star masses range from 0,69 to 1,53$M_\odot$, mass ratios from 1,03 to 3,76 and eccentricity from 0,023 to 0,521.

Similarly, the planetary orbits present a considerable spread in eccentricities, ranging from nearly circular ($e = 0,007$) to significant values ($e = 0,182$). Besides the absence of orbital resonances with the binary, it results that no particular geometry is favored, exept for two relevant configurations, namely co-planarity and close-in orbits.

While it has been observed that the action of tidal forces forces alignment of the spin axes with the orbital axis, the planet and stellar orbital co-planarity evidenced by *Kepler* circumbinary planets favors a single-disk formation and migration scenario.

Since the discovery of Kepler-16, the tendency of circumbinary planets to orbit close to their host stars has been noted: in fact, the (inner) planets orbit extremely close to the boundary where dynamical instabilities caused by perturbations induced by the binary can be present (as previously shown in Figure 2.11). The observed circumbinary planets present semi-major axes ranging between 1,09 and 1,46 times the critical radius[36]; moreover, those planets tend not to exist around the shorter period *Kepler* eclipsing binaries. The fact that all of the circumbinary planets have a size (mass and/or radius) smaller than Jupiter is another relevant characteristic, presented in [13].

Finally, the tendency for the observed circumbinary planets to lie next to their critical stability limit has implications for habitability. According to the stability criterion, the planet needs to orbit outside approximately $\sim 2 \div 4$ times the binary semi-major axis, with periods of $\sim 3 \div 8$ times the binary period: since the known circumbinary planets have binaries with periods of about $\sim 10 \div 40$ days, the planets will have periods a bit larger than $\sim 30 \div 320$ days. Then, being the *Kepler* targets especially G and K type stars, the habitable zone surrounding the binary is rather compatible with this orbital period.

2.3.2 The search for planets orbiting two stars

More than one hundred planets have been discovered in binary systems to date, allowing for the study of formation and evolution of exoplanets. Two types of orbits, in which planets have been observed in binary star systems, are present: first, when the planet presents a wider orbit than the binary ($a_p > a_{bin}$) and orbits around the barycentre of the inner binary, this is called a circumbinary or "p-type" planet; instead, if the planet has a smaller orbit than the binary ($a_p < a_{bin}$) and only orbits around one component, this configuration is known as a circumstellar or "s-type" planet[37]. Figure

[36] The reason for this is not clear yet, leading to various possible explainations:

- migration might become inefficient in the proximity of the critical radius, stopping planets just outside this radius;
- migration may act normally, leaving planets at larger radii but making any planet within the critical radius lost;
- this represents an observational bias, since a closer planet corresponds to a more rapid transit.

[37] Alternatively, it is known as a circumprimary or circumsecondary planet as a function of which star is being orbited.

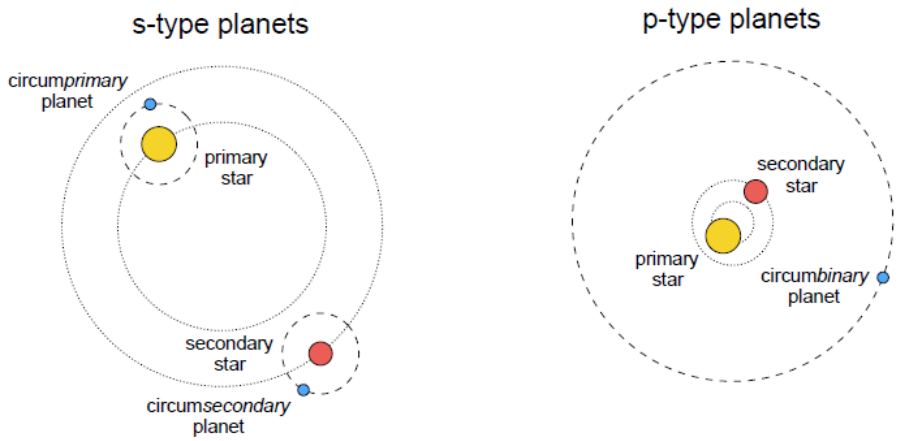

Figure 2.12: *Left: circumstellar "s-type" planets in binaries, individually around both primary and secondary stars. Right: circumbinary "p-type" orbits in binaries collectively around both stars. Taken from [5].*

2.12 illustrates these configurations.

Indirect detection methods such as Doppler spectroscopy or transit photometry methods were exploited for most of these discoveries; however, they favour s-type configurations around individual components of wide binary systems, being heavily biased towards planets with short orbital periods. Anyway, ~ 20 of these planets have been detected in circumbinary p-type orbits around tight binary systems, despite this bias: the existence of an extensive unseen number of circumbinary planets is then expected.

According to [5], the smallest circumbinary planet discovered to date is $3R_{\oplus}$, whereas the rest consists of planets larger than Neptune, with periods ranging from 49 to 1108 days[38]. Figure 2.13 depicts this situation, where the circumbinary planets occupy the top right of the parameter space. The detection of circumbinary planets with long periods is favored by both a higher transit probability, with respect to that around single stars, and by a scarce dependence on orbital period.

On the left panel of Figure 2.14, the occurrence frequency of circumbinary planets is calculated for different radius intervals: the trend results in a decreased frequency for larger planets, in agreement with what has been observed for single stars. As regards the right panel of Figure 2.14, it shows how the true frequency of circumbinary planets depends on the underlying distributions of the mutual inclination between the binary and planet orbital planes.

The Kozai-Lidov effect must be taken into account for circumstellar planets in binaries. In particular, if the planet and binary orbits present mutual inclinations between 39° and 141°, then a secular oscillation of both the planet's eccentricity, e_p, and its inclination with respect to the binary, I_p ([5]), occurs. The representation of an example of Kozai-Lidov cycles is shown in Figure 2.15. As regards an initially circular circumstellar planet, it reaches a maximum eccentricity of

$$e_{p,max} = \sqrt{1 - \frac{5}{3}\cos^2 I_{p,0}},$$

[38]These values span those in the inner Solar System and are considered long for transit surveys.

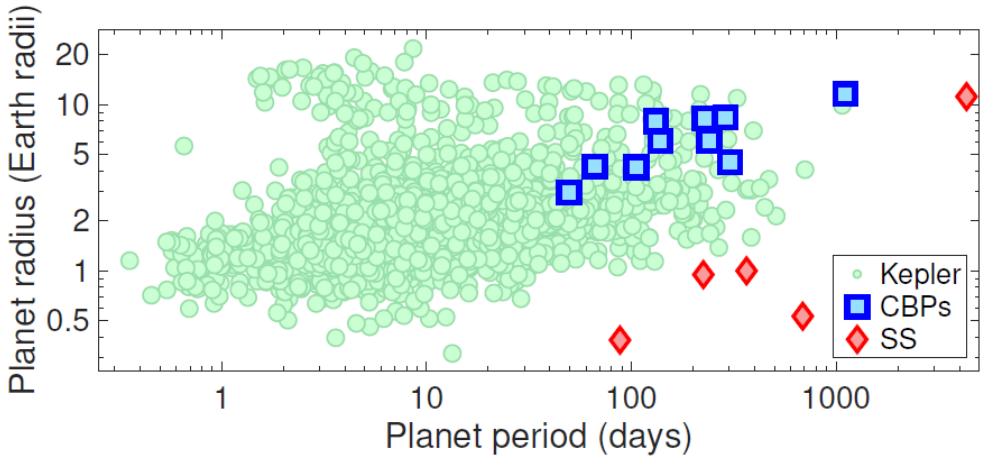

Figure 2.13: *Period (in days) in function of radius (in Earth radii units), taken from [5], for the Kepler objects of interest around all stars (green circles), transiting circumbinary planets (CBPs, blue squares) and the five innermost Solar System planets (SS, red diamonds).*

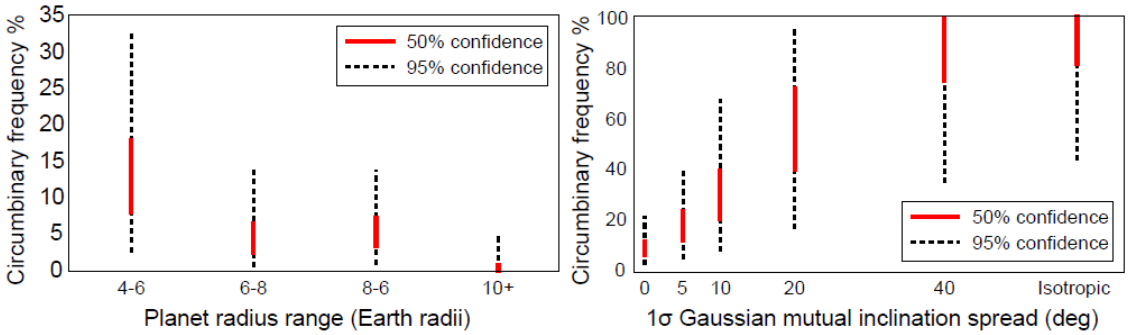

Figure 2.14: *Occurrence rate of circumbinary planets orbiting within 10,2 times the binary orbital period, taken from [5]. Left: planets drawn from a Gaussian distribution of mutual inclinations with a 5° standard deviation, versus the planet radius. Right: planets between* $(4 \div 10)R_{\oplus}$ *in function of the standard deviation of the Gaussian mutual inclination distribution.*

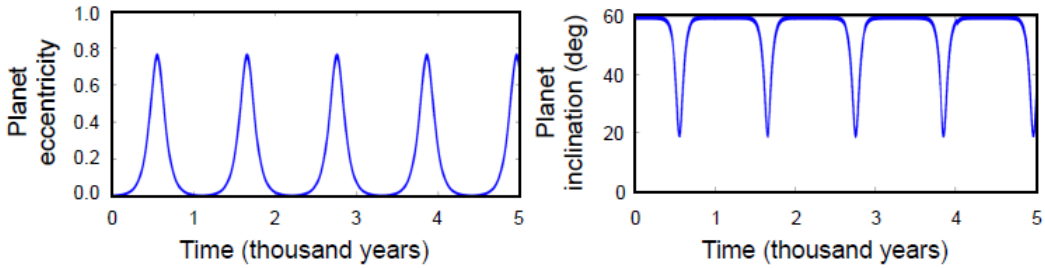

Figure 2.15: *Example of Kozai-Lidov cycles, taken from [5], for a 0,5 AU circumprimary planet in a 5 AU binary, showing the variation of* e_p *(left) and* I_p *(right). Initially, the planet has an inclination of 60° with respect to the binary's orbital plane.*

where $I_{p,0}$ stands for the planet's inclination in correspondence of $e_p = 0$, and this is derived assuming that the outer orbit (in this case the binary) possesses the most of the angular momentum. The outer eccentricity and inclination do not vary. The Kozai-Lidov effect in the case of circumbinary planets, in which the outer angular momentum is typically negligible, practically disappears.

In general, according to [14], stability on long time scales for planetary orbits in a binary system occurs if the overall system structure is definitely hierarchical. As regards circumstellar (s-type) planet orbits, this means that the planet's semi-major axis a must be inferior to a critical upper limit a_c, which represents a fraction of the binary's separation a_b in function on the binary's mass ratio and eccentricity. Considering sufficiently close binary systems[39] ($a_b < 5 \div 10$ AU), another regime of stable planet orbits becomes possible, namely the circumbinary (p-type) orbits: in this case, the stability criterion imposes a lower limit on the planet's semi-major axis, $a > a_c$, with $2 < a_c/a_b < 4$. From Figure 2.16 it is possible to have an overview of the distribution of the planets semi-major axes in function of the binary semi-major axis, in multi-star systems[40]: the previously discussed critical limits divide the plot in two different regions of stability, corresponding to the circumbinary and the circumstellar cases. Finally, it is clear that circumstellar planets tend to locate well within the stability zone, whereas circumbinary planets are usually next to the stability limit.

Direct imaging survey

Direct imaging is a powerful planet detection technique, which works particularly well for planets on wide orbits; the limited parameter space of the indirect detection methods is complemented by this procedure. In fact, several direct imaging surveys for exoplanets have been performed in the last years, providing the first directly imaged planets and setting constraints on the distribution (and abundance) of wide planetary systems.

In order to widen the possibilities of direct imaging, which typically reject binary systems from the target sample of the surveys, the Search for Planets Orbiting Two Stars (SPOTS) is conducting the first dedicated direct imaging survey for circumbinary planets: as reported in [15], it is an ongoing direct imaging study of a large sample of close binaries with VLT/SPHERE.

According to [14], the scientific motivation of the SPOTS project to search for circumbinary planets by direct imaging can be summarized in the following four points.

1 - Unexplored territory

It is intrinsically interesting to explore the largely unknown parameter space of circumbinary planets: in fact, they may constitute a significant fraction of the overall planet population since stellar binarity is wide-spread, with approximately half of all Sun-like stars presenting a stellar companion.

[39] It is noteworthy the fact that circumbinary planets around close binaries are disadvantaged for essentially two reasons: Kozai-Lidov effect and strong UV activity over a time of ∼Gyr (superior to the typical irradiation time of a circumstellar planet) due to the synchronous rotation of the planet(s) with both the stars.

[40] To date, we do not precisely know if the violet group of circumbinary planets, with long periods, around close binaries is actually real (eccept for one case, which has been confirmed): in fact, the eclipse timing variations (ETVs) method to discover planets around such binaries could be affected by other astrophysical effects.

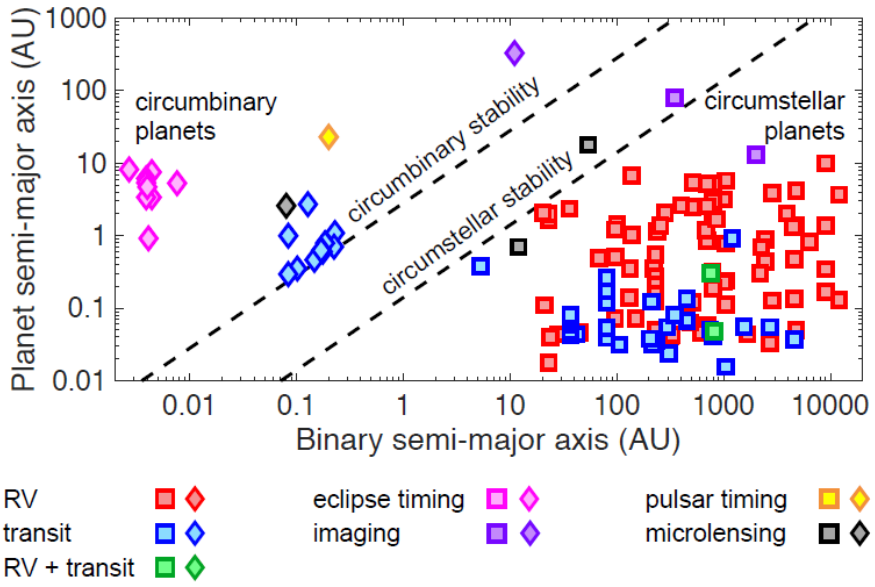

Figure 2.16: *Planets in multi-star systems, taken from [5]. Circumbinary planets are denoted by diamonds and circumstellar planets by squares. The different colours indicate the discovery technique for the planet, not the binary. The circumbinary and circumstellar stability limits are calculated assuming* $M_{primary} = 1M_{\odot}$, $M_{secondary} = 0,5M_{\odot}$. *For circumbinaries* $e_{bin} = 0,15$ *(mean for transiting discoveries) and for circumstellar planets* $e_{bin} = 0,5$.

Both observational and theoretical arguments support the existence of circumbinary planets. The existence of circumbinary disks and the growth and crystalization of dust in such disks provide the necessary ingredients for planet formation; however, several scenarios for this process may take place, favoring or destructing it. Nevertheless, *Kepler*'s discoveries of transiting circumbinary planets ([13]) determines that planet formation does successfully occur in close circumbinary configurations; moreover, planets in wider orbits, where the perturbing influence of the central binary decreases, provide a favorable enviroment for direct imaging.

2 - Great observability with direct imaging

Direct imaging, differently from Doppler spectroscopy and transit photometry, is not affected by technical difficulties arising from spectroscopic binary targets. In particular, for the purposes of adaptive optics guidance and differential imaging methods, the binary acts as a single star as long as it is not resolved; in the case of resolved binaries, their performance could be comparable if the secondary star is relevantly fainter than the primary, as observations from the SPOTS survey ([14]).

The ideal conditions for stable circumbinary planet orbits, such as close stellar separation and/or high stellar mass ratio, coincide with these observational constraints. Furthermore, circumbinary planets may offer a relevant advantage as regards contrast. Empirically, the number of massive planets formed in a system is expected to scale with the available mass of the protoplanetary disk, which in turn scales with the mass of the host star; then, around a tight binary planets may be more easily detectable than around a single star of corresponing system brightness.

3 - The occurrence of planets on wide orbits

Two mechanisms, which may enchance the number of planets on wide orbits (being the favored targets of direct imaging), are offered by close binary systems.

- *Scattering* - A close encounter with the host system's secondary star may be experienced by planets forming or migrating close to the inner boundary of the stability region, resulting in dynamical scattering of the planet. While the outcome of most of these processes is the ejection of the planet from the system, in some cases the production of highly eccentric and bound orbits, with large semi-major axes, occurs. Subsequently, the interaction between these planets and the protoplanetary disk may damp them towards less eccentric wide orbits.

  Massive giant planets, which have masses $\geq 1M_J$ and represent favorable objects for direct imaging, lean for scattering; on the contrary, lower-mass planets may persist near the inner limit of the stability region.

- *Migration* - Continuous outward migration represents a second possibility: this requires to transfer angular momentum from the binary stars system to a planet through viscous disk interaction, shrinking the binary orbit and widening the planet's orbit[41].

4 - Improved constraints on planet formation theories

To conclude, an excellent laboratory for testing theories of planet formation and evolution is offered by circumbinary systems. Both positive and negative effects of binarity on planet formation have been predicted by theoretical studies, either in the core accretion scenario and in the gravitational instability scenario: such effects should consistently affect the planet's distribution around binary systems. A better undestanding of the underlying physical processes may be provided by measurements of the differences with respect to the case concerning the planet demography around single stars.

2.3.3 Discussion of the SPOTS results

The analysis of the SPOTS survey indicates that the occurrence rate of sub-stellar companions ($2M_J < M_c < 70M_J$) in wide orbit is considerably low[42] within 1000 AU. Considering only planetary mass companions ($2M_J < M_c < 15M_J$), the best frequency value becomes 2,70%[43], for a semi-major axis inferio to 1000 AU, whereas it results to be 1,35% for separations restricted to 100 AU.

Consequently, the possible existence of small differences between the frequency of sub-stellar companions around isolated stars and close binaries is suggested by these results.

[41] A small variation in the binary's orbit causes a relevant effect on the planet's orbit, which may extend out to $(20 \div 50)$ AU, as a consequence of the low mass ratio between the planet and the stars as well as the non-linearity of the gravitational potential.

[42] In particular, it is $< 13\%$ with a best value of 6% at 95% confidence level.

[43] With a 95% CL upper limit of $\sim 9\%$.

Implications for the origin of planet candidates around post-common envelope binaries

An additional method to discover circumbinary planets is represented by the timing technique. Some post common envelope[44] binaries have observational signatures stable enough to allow the detection of planets around the binary. A significant number of detections have been reported in the literature although some of them are rather controversal.

There are two possibilities regarding the formation of circumbinay planets, if the observed timing variations are due to their presence.

- The *first generation scenario* considers the fact that they formed together with the central binary and survived the common envelope evolution of central pair: this possibility, in most cases, turns out to be compatible with the observed wide separation.
- In the *second generation scenario*, circumbinary planets formed subsequently to the common envelope evolutionary phase in the circumbinary disk, which is expected to form from the material lost in the process[45].

One relevant implication of the results, obtained in [15], is that the very consistent frequency of circumbinary planets in wide orbits around post-common envelope binaries (implied by eclipse timing) cannot be uniquely attributable to planets formed before the common-envelope phase - *first generation* planets: instead, either *second generation*[46] planet formation or some non-Keplerian physical mechanisms, presenting a timing signature which is compatible to that of planetary companions, are supported possibilities.

Finally, results provided by [15] nicely complement those coming from the *Kepler* spacecraft, being the separation range explored with direct imaging quite different: as previously mentioned, circumbinary planets discovered by *Kepler* are often close to the dynamical stability limit, differently from most the companions identified with direct imaging, which are instead much further out.

[44] A common envelope (CE) is gas containing a binary star system, which does not rotate at the same rate as the surrounding gas and is said to be in a common envelope phase. During a common envelope phase the embedded binary system is subject to drag forces from the envelope which cause the separation of the two stars to decrease. The phase ends either when the envelope is ejected, leaving the binary system with much smaller orbital separation, or when the two stars become sufficiently close, merging and forming a single star. A common envelope phase is short-lived if compared to the lifetime of the stars involved.

[45] Planet formation process in these environments could be consistently favored by the large amount of heavy elements expected in such disks.

[46] It should be noticed that second generation planets are expected to be significantly brighter than 1st generation ones, since they are much younger than the age of the system, and this strongly favors their direct detection.

Chapter 3

SPHERE

The Spectro-Polarimetric High contrast Exoplanet REsearch (SPHERE) is an ESO[1] facility that performs imaging, low/medium resolution spectroscopic and polarimetric observations of giant planets in wide orbits, exploiting direct imaging[2] (as explained in Section 3.2) of their circumstellar environment ([16]). SPHERE has been purposedly designed and optimized for this specific scientific project. In this Chapter we report from various articles (each of them is properly cited) the main features of such an instrument, and its achievements.

Direct imaging represents the currently most promising technique, with respect to the other methods to reveal exoplanets, that allows to substantially reduce the photon noise generated by the host star, by minimizing its light intensity while retaining the light from the exoplanet. The acquisition of spectral or polarimetric data of faint exoplanets, with contrast lower than $\sim 10^{-6}$, is required.

Moreover, relevant complementary information to radial velocity studies of exoplanets as well as the possibility for dynamic mass measurements of individual exoplanets are provided by direct imaging: in fact, it can present additional diagnostic data (for instance, through polarimetry) and enhances observing efficiency since it allows to confirm a detection in a couple of nights[3] ([17]).

The challenge that SPHERE has to face is the very large contrast between the host star and the planet, which is higher than 12,5 magnitudes - namely 10^5 in flux ratio, at very small angular separations (see Section 3.1) and usually within the seeing halo. Therefore, the whole design of such an instrument aims at reaching the highest contrast in a limited field of view and in proximity of the central star, around bright targets ($R < 11$, being R the magnitude in the R band) observed in the visible or near infrared, due to the limitations of AO[4]. The detection of evolved planetary systems exploits their reflected light, mostly by visible differential polarimetry, whereas in the case of young planetary systems it involves the intrinsic planet emission (using IR[5] differential imaging - see Section 3.2.1 - and integral field spectroscopy), as will be clear in the description of the instrument. The two components of the near-infrared arm of

[1] European Southern Observatory: `http://www.eso.org/public/italy/`.

[2] As previously seen, it is not the only method to reveal an exoplanet: for instance, other observational techniques are radial velocities, photometric transits or thermal IR imaging.

[3] Instead, following an orbit may take years.

[4] Adaptive Optics, which is a technology used to improve the performance of optical systems by reducing the effect of wavefront distorsions: in fact, it aims at correcting the deformations of an incoming wavefront by deforming a mirror in order to compensate for the (atmospheric) distortion.

[5] InfraRed.

SPHERE provide complementary detection capabilities for the field of view, contrast and spectral range.

The field of extrasolar planet studies, already very active, greatly benefits from SPHERE, since it provides direct detections of planets more massive than Jupiter at various evolutionary phases, ranging in semi-major axes $> 5 \div 10$ AU, in order to improve the current understanding of the mechanisms responsible for the formation and evolution of planetary systems.

Observations are concentrating towards the following classes of targets.

- Detection of low-mass planets is optimised in nearby young ($\approx 10 \div 50$ Myr) associations, since they have bright enough substellar companions and therefore the maximum number of planets per star observed.
- Stars with known planets, in particular those with long-term residuals in their radial-velocity curves, suggesting the possibility for the presence of a more distant planet.
- The only opportunities for detecting planets by directly reflected light is provided by the nearest stars, since measuring these targets allows to examine the smallest orbits.

Having SPHERE such a prime objective, many other research fields are expected to benefit from its characteristic large contrast performance: in particular, protoplanetary disks, brown dwarfs, evolved massive stars and even Solar System and extragalactic science (like AGN[6] or QSO[7]).

3.1 Scientific requirements and general structure

The most important scientific requirements, based on the science analysis and determining the design of the SPHERE instrument, are summarised below.

- High contrast, in order to detect giant planets (sensitivity down to magnitude $H \sim 24$) 14 to 16 magnitudes less bright than their host star.
- Reaching very small angular separations, $0,15$" to 3" from the host star.
- Sensitivity to extended sources down to ~ 17 magnitudes per square arcseconds at less than $0,2$" from the host star.

In order to satisfy these requirements SPHERE, which is installed at one of the UT3 Nasmyth foci of the VLT (Very Large Telescope) in Paranal (Chile), has been realized into a central instrument and its three subsystems.

The CPI is the Common Path and Infrastructure, which receives direct light from the telescope and provides highly stabilized, AO-corrected and coronagraphic beams to the three sub-instruments, introduced below and better described in Section 3.3.

[6]An active galactic nucleus (AGN) is a compact region at the center of a galaxy that has a much higher than normal luminosity over some portion of the electromagnetic spectrum, with characteristics indicating that the excess luminosity is not produced by stars. The radiation from an AGN is believed to be a result of accretion of matter by a supermassive black hole at the center of its host galaxy.

[7]A quasar, or quasi-stellar object (QSO), is an active galactic nucleus of very high luminosity, consisting of a supermassive black hole surrounded by an orbiting accretion disk of gas.

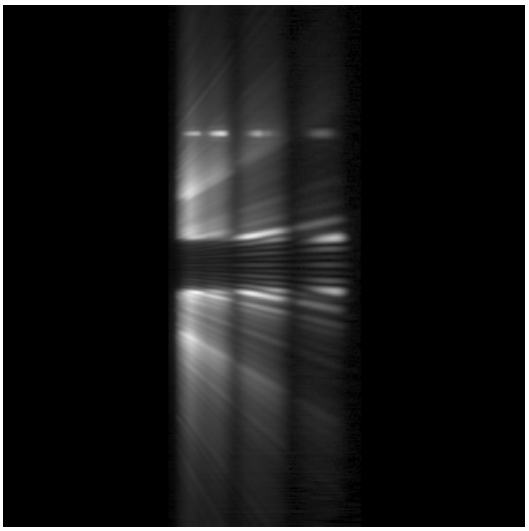

Figure 3.1: *Low resolution ($R = 35$) simulated spectrum with coronagraphy in the J, H and K bands of an $M0$ star with a relatively bright companion at an angular separation of 1,0", taken from [18]. Wavelength is along the horizontal axis, and angular separation along the vertical axis, starting from the center. The obscured central part represents the position of the 0,2" coronagraph mask. The speckles (which are defined in Section 3.2) produce oblique lines in the spectrum since their angular separation scales linearly with wavelength, whereas the planet position is fixed.*

- IFS: The Integral Field Spectrograph provides a data cube of 38 monochromatic images either at spectral resolution[8] of $R \sim 50$ between $0,95 \div 1,35$ μm ($Y - J$ bands) or at $R \sim 30$ between $0,95 \div 1,65$ μm ($Y - H$ bands).

- IRDIS: The InfraRed Dual-band Imager and Spectrograph provides classical imaging (CI), dual-band imaging (DBI, described in Section 3.2.3), dual-polarization imaging (DPI, introduced in Section 3.3.4) and long slit spectroscopy (LSS[9]) either between $0,95 \div 2,32$ μm, with resolving power of $R \sim 50$ (LRS[10] with 0",12 wide slit) or between $0,95 \div 1,65$ μm with $R \sim 350$ (MRS[11] with 0",09 wide slit).

- ZIMPOL: the Zurich IMaging POLarimeter provides near diffraction limited classical imaging and dual-polarization imaging with a resolution inferior to 30 mas in the visible.

[8]Spectral resolution is defined as $R = \frac{\lambda}{\Delta\lambda}$, where $\Delta\lambda$ is the full width half maximum (FWHM) of the spectral line.

[9]Long Slit Spectroscopy. As described in [18], the location and size of a speckle in the FOV is linearly wavelength-dependent, whereas a fixed physical object, such as a planetary companion, will not vary its position with wavelength. This property guarantees a great determination and subtraction of wavelength-dependent characteristics at a given position, and allows the detection of physical objects in the proximity of the star: in the case of LSS, several images of the slit at increasing wavelengths are dispersed and superimposed to create a spectrum as shown in Figure 3.1, where the speckles and the planet are clearly distinguishable.

[10]Low Resolution Spectroscopy.

[11]Medium Resolution Spectroscopy.

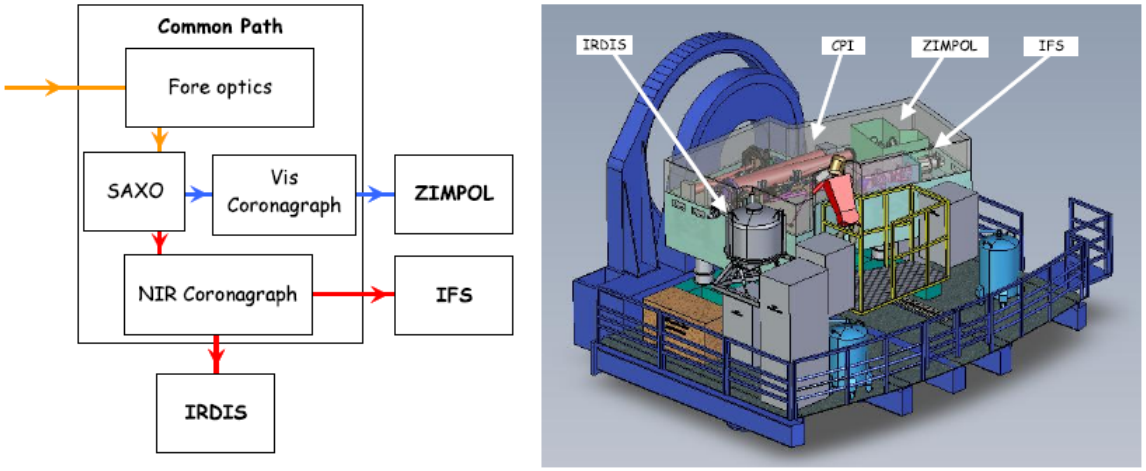

Figure 3.2: *SPHERE sub-systems (left), including the common path (CPI) with adaptive optics system SAXO (described in Section 3.3.1), coronagraphs, and sub-instruments IRDIS, IFS and ZIMPOL. Left: schematic view of the instrument on the Nasmyth platform. This picture has been taken from [19].*

Simultaneous observations with IRDIS and IFS (IRDIFS modes) are allowed by dichroic[12] splitters. Figure 3.2 is taken from SPHERE User Manual[13] ([19]), and briefly shows how the telescope is structured.

3.2 Direct Imaging in SPHERE

The planet image results to be extremely fainter with respect to the background from the bright stellar image: then, photon noise in the brilliant star point-spread function (PSF) represents a problem (however, the major problem is the speckle[14] noise). A solution is provided by *coronagraphy*, a method which attenuates the coherent diffraction pattern of the on-axis PSF. In correspondence of high Strehl ratios[15], the PSF is mostly dominated by the diffraction pattern and coronagraphs allow obtaining relevant reduction. However, considering the relatively low Strehl ratios[16] obtained with adaptive optics systems on large ground-based telescopes, efficient coronagraphy is affected by the presence of a rapidly changing halo of speckles generated by atmospheric phase distortion. As a consequence, the local PSF variance increases by orders of magnitude with respect to that due to photon noise; moreover, speckles of a much longer lifetime, and then

[12] A dichroic prism splits light into two beams of different wavelength.

[13] Available at `https://www.eso.org/sci/facilities/paranal/instruments/sphere/doc/VLT-MAN-SPH-14690-0430_v100_p2.pdf`.

[14] A speckle pattern is an intensity pattern produced by the mutual interference of a set of wavefronts; it typically occurs in diffuse reflections of monochromatic light such as laser light. The speckle effect is a result of the interference of many waves of the same frequency, having different phases and amplitudes, which add together to give a resultant wave whose amplitude, and therefore intensity, varies randomly: in the case of AO, speckles are residual aberrations due to the atmospheric turbulence which cannot be corrected by that technique.

[15] The Strehl ratio is the measure of the quality of optical image formation. It varies from 0 to 1, which corresponds to a perfectly unaberrated optical system.

[16] In the J band, this corresponds to Strehl ratios $< 60\%$.

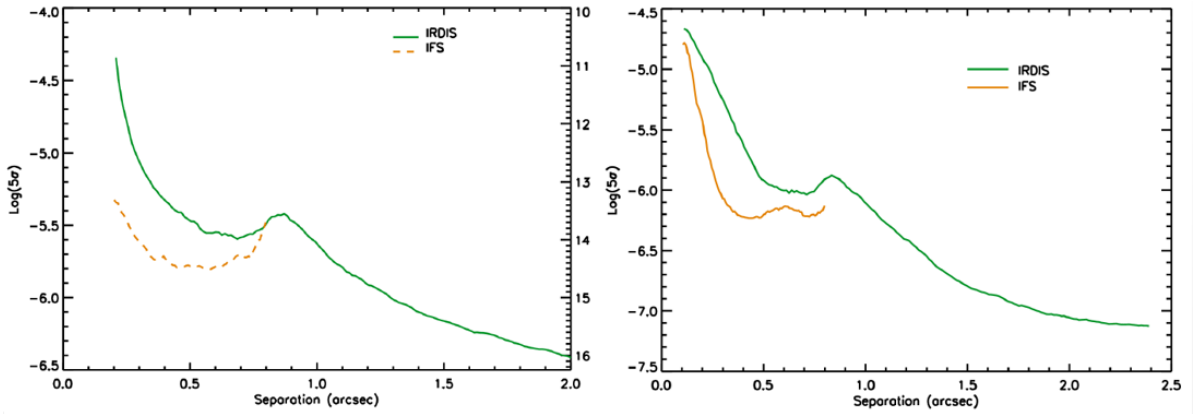

Figure 3.3: *Contrast plot for HR3549 (left) and HR2562 (right) observations, reported in [20] and [21], respectively. The IRDIS contrast is plotted with a green line while the IFS contrast is plotted with an orange line.*

extremely more luminous than atmospheric speckles in a long-exposure image[17], are produced by aberrations in the optical train[18]. It is clear, thus, that PSF calibration for high-contrast imaging is essential.

Examples of the 5σ contrast (between the companion and the host star) curves for the two different systems HR3549 and HR2562, derived from the IRDIS and IFS final images, are shown in Figure 3.3, where the green line is the contrast obtained using IRDIS whereas the orange line is the one obtained from IFS.

With the purpose to provide the expected contrast performance, the differential imaging methods (which are described below, in Section 3.2.1) are based either on spectroscopic features (IRDIS) or a certain fraction of polarised flux (ZIMPOL).

3.2.1 Differential Imaging

Differential imaging, and in particular Angular Differential Imaging (ADI), exploits the fact that the field and the pupil rotate with respect to each other. Most speckles, in pupil-stabilized mode, are generated by instrumental artifacts and are fixed in the pupil plane; on the other hand, the object of interest (a companion or a disk) corotates with the field. Thanks to this fact it is possible to distinguish the stellar halo from the object. An example of the ADI process is provided by Figure 3.4.

In order to minimize the effect of speckles, simultaneous observations of several monochromatic images can be exploited. The position of a companion around a star, for a given observation, is constant; instead, enhancing the wavelength results in the increase of the speckles-star distance followed by the decrease of the speckles intensity. As a consequence, for a sufficiently wide wavelength range, this fact allows subtraction of the speckles[19] This approach is used in IFS and in IRDIS LSS.

Different spectral features are exhibited by planets and the host star: this information can be used to reduce, or even suppress, speckle noise. To account for this, simultaneous images at two similar wavelengths in correspondence of which the luminosity of the planet changes, are necessary: this method is known as spectral differential imaging

[17]This noise can be dominant for integrations longer than a few seconds.
[18]Because these aberrations are unfiltered by the AO system.
[19]This process is known as spectral deconvolution, as will be seen in Section 3.2.3.

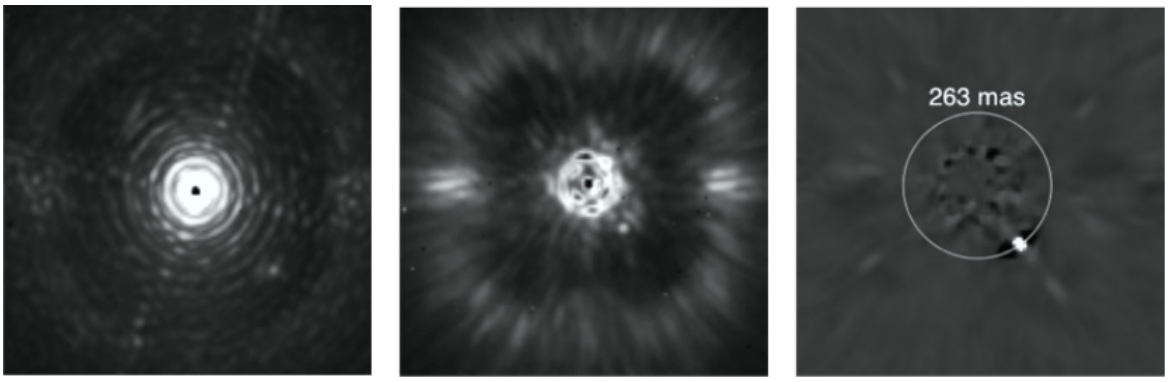

Figure 3.4: *Illustration, from SPHERE User Manual ([19]), of the three foundations of high contrast imaging. Left: raw on-sky J-band PSF of SPHERE with IRDIS, showing the diffraction pattern resulting from the almost perfect correction provided by the extreme AO system (this will be described in Section 3.3.1). Middle: raw on-sky J-band coronagraphic image of Iota Sgr, displaying the efficient removal of diffraction rings and pinned speckles by the coronagraph. Right: result of angular differential imaging (ADI) strategy (and post-processing using principal component analysis, removing the remaining speckles in the field after extreme AO and coronagraphy) allowing the detection of a faint off-axis companion.*

(SDI, described in Section 3.2.3), and is used in IRDIS DBI[20].

The peculiarity of stars of being often unpolarized, in contrast to circumstellar environments and planets, which may be highly polarized, is used to increase the image contrast and is known as dual polarization imaging, being employed in ZIMPOL polarimetric imaging and in IRDIS DPI.

As previously stated, efficient *coronagraphy*, which is a quickly evolving research field, is required for reaching the science goals of SPHERE: in fact, besides reducing the intensity of the stellar maximum by a factor of at least 100, it eliminates the diffraction features caused by the pupil edges. Figure 3.5 shows the removal of the instrumental residual aberrations.

3.2.2 Angular Differential Imaging

Quasi-static speckle artifacts primarily affect and limit the sensitivity of high-contrast ground-based AO imaging; the most relevant source of speckles is surface errors on the telescope primary mirror and internal optics, at large separations ($> 0,5$"). To suppress this noise, it is possible to use ADI, as explained in [22].

This method exploits the intrinsic field-of-view rotation of altitude/azimuth telescopes to separate exoplanets from optical artifacts. Setting the telescope pupil fixed on the science camera and allowing the field-of-view to slowly rotate with time around the star provide an ADI sequence, as shown in Figure 3.6.

[20]It can also be used with ZIMPOL imaging provided different filters are used in ZIMPOL's two arms (for instance, $H\alpha$ and continuum).

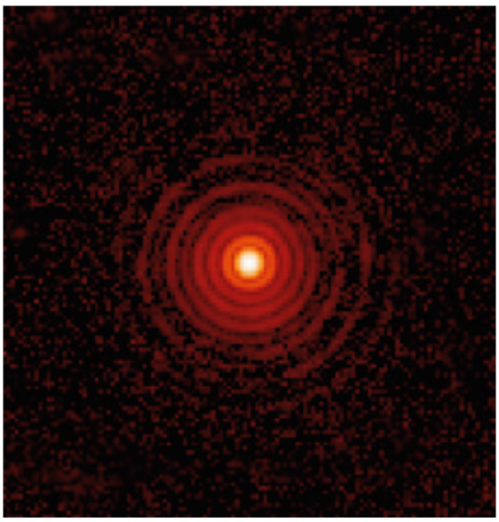

Figure 3.5: *The SPHERE H-band point spread function, corrected from residual aberrations (Strehl ratio of 99%), taken from [17].*

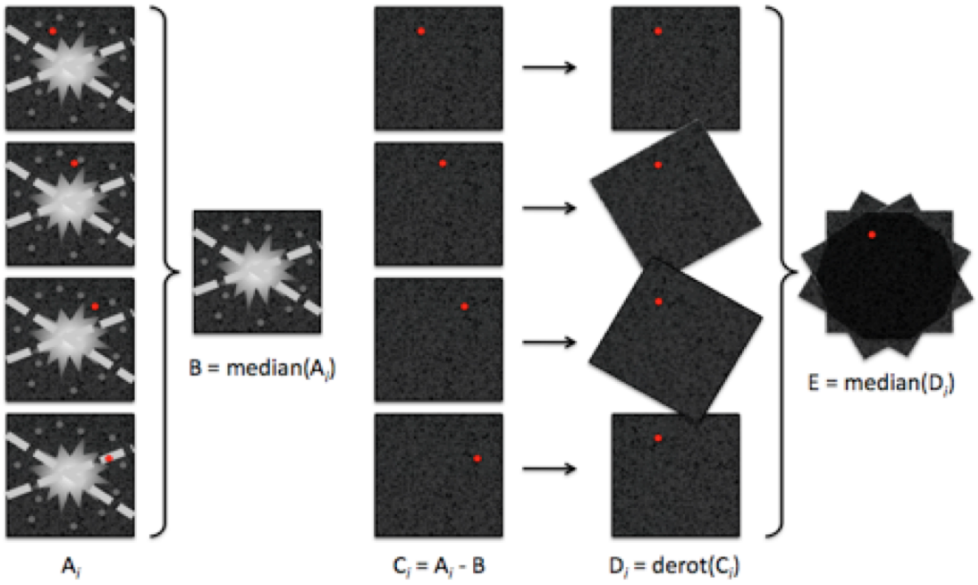

Figure 3.6: *Explicit illustration of an ADI sequence: the A_j images show the rotation with time of a planet (red dot), whereas the speckles (white dots) and the star remain fixed in place over time; subsequently, the production of the median of these images, B, clearly removes the planet, presenting only the speckles and the star. The subtraction of B from each of the A_j images leads to the $C_j \equiv A_j - B$ images, each of which only shows the planet in a time-dependent position. Finally, the de-rotation of the C_j images generates the D_j images, which are then superposed and mediated providing the ADI-corrected image E: as wanted, it only exhibits the planet without neither the speckles nor the starlight.*

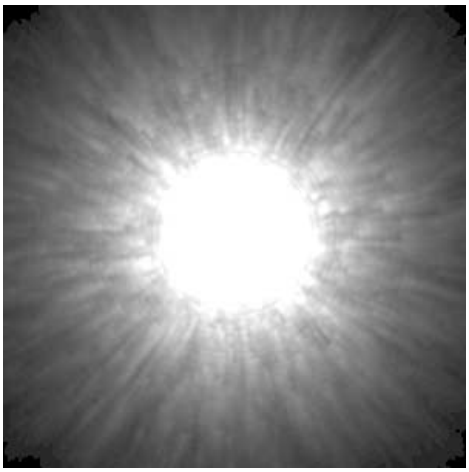

Figure 3.7: *Simulation of space-based coronagraphic observation of Solar-type star at a distance of 2 pc ranging in wavelength from 7000 Å to 1 μm, taken from [25]. The spectrally integrated PSF is shown, which is representative of a direct image taken with an I-band filter.*

3.2.3 Spectral Differential Imaging

Simultaneous *spectral differential imaging* ([23]) is a PSF calibration technique for high-contrast imaging thanks to which the reduction of noise from atmospheric speckles and optical aberrations is possible. It is based on the simultaneous images acquirement at adjacent wavelengths in a spectral range where it is possible to perceive the difference between the planetary and stellar spectra. Subsequent image subtraction allows the removal of the stellar image, preserving that of any companion. The sharp methane absorption band head at 1,6 μm present in relatively cold atmospheres[21] provides a useful spectral feature for this purpose, as explained in [24].

According to [25], the consequences of potentially strong amplitude modulation of spectra introduced by wavelength dependencies in the PSF may result in a set of rings, the Airy pattern[22], caused by the diffraction by the telescope optics with spacing at the diffraction limit of the telescope in addition to several speckles[23]. The ring pattern scales to larger size proportionally to the increase of wavelength; moreover, a similar trend is followed by the speckles.

Spectral deconvolution represents an effective method to eliminate the stellar PSF in this case: a simulation (generating PSFs at various wavelengths), performed in [25], in which a Jovian planet is orbiting around its Solar-type host star, helps understanding the relevance of SDI. Figure 3.7 illustrates the average PSF of the data cube, in presence of the extrasolar planets, which are entirely covered by the scattering wings of the stellar PSF.

[21] For instance, the atmospheres of cold T-type brown dwarfs and Jovian planets.

[22] The Airy disk and Airy pattern are descriptions of the best focused spot of light that a perfect lens with a circular aperture can make, limited by the diffraction of light. The diffraction pattern resulting from a uniformly-illuminated circular aperture has a bright region in the center, known as the Airy disk, which together with the series of concentric bright rings around is called the Airy pattern. Due to diffraction, the smallest point to which a lens or mirror can focus a beam of light is the size of the Airy disk.

[23] These speckles are generated from scattering from mid-frequency surface irregularities, and are of the same typical size of the diffraction limit of the telescope.

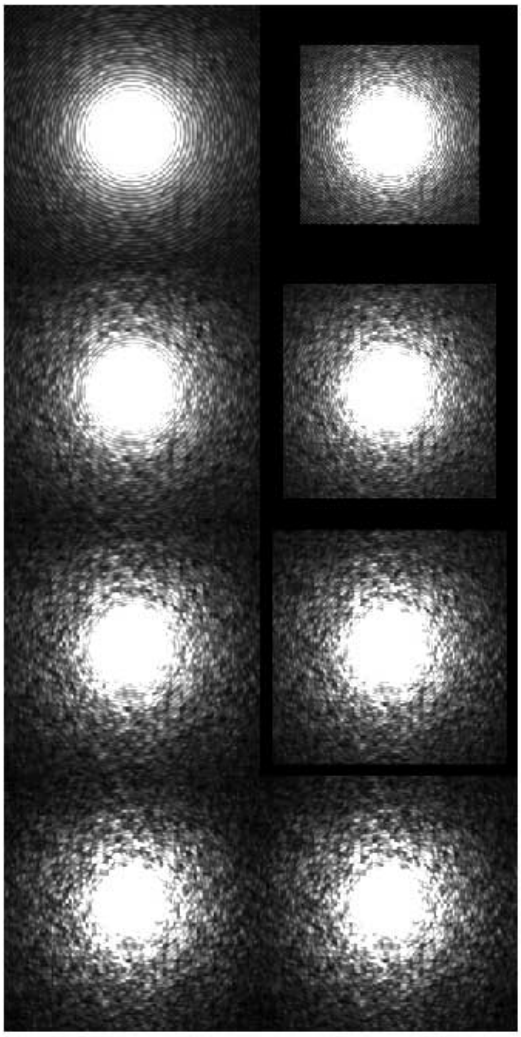

Figure 3.8: *Sequences, taken from [25], showing cuts through the data cube at wavelengths of* $0,70 - 0,76 - 0,84 - 1,0$ μm*, in order from bottom to top. The left panels show the speckles and ripples expanding with wavelength, while the right panels present the adjusting of the image scale in function of wavelength, where PSF features remain always in the same place.*

Considering the left-hand panels of Figure 3.8, they show slices through the data cube before the application of the light smoothing, at four different wavelengths from 7000 Å to 1 μm, from bottom to top, respectively. Accurate study of these Figures reveals the expansion of the PSF with wavelength, since features move out and everything scales with wavelength, as expected.

Subsequently, the spatial scale of the data cube is adjusted, while progressing through it in wavelength: the right-hand panels of Figure 3.8, differently from the previous data cube, demonstrate that there is much more similarity between the PSFs in function of wavelength, when resampled spatially.

After the subtraction of the emission from the star, it is possible to reconstitute the original subtracted data cube through the resampling of the subtracted data back onto its original spatial scale: collapsing the data cube along the spectral dimension allows the detection of the extrasolar planet.

Moreover, diffraction very strongly affects the host star spectrum at the location of

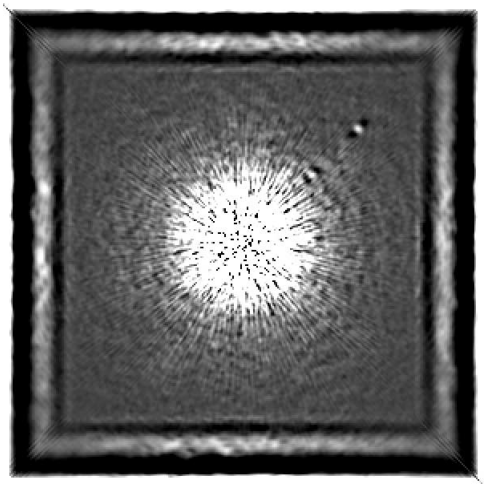

Figure 3.9: *Spectrally collapsed image of the reconstructed, subtracted data cube illustrating the detection of a Jovian planet whose peak is only 1% of the PSF wing background, using a 2 m telescope (taken from [25]).*

the extrasolar planet, whereas its action on the planet's spectrum is negligible. Since the center of the planet's Airy pattern indicates the planet's location, its spectrum is fully preserved, except for a slow variation as regards peak brightness due to the decrease of resolution towards higher wavelengths.

Figure 3.9 exactly shows such an image from the simulation described, where the Jovian planet is now easily visible in the top-right corner; the difference between this Figure and Figure 3.7, in which spectral deconvolution was still to be applied, is evident.

Dual Band Imaging

Another strategy to remove speckles can be achieved by exploiting pairs of images taken simultaneously, thus having (almost) identical speckle patterns, in two narrowband filters of very similar wavelength[24] through which the contrast between primary and companion is consistently appreciable. For instance, this is generally obtained across the methane band head at 1,59 μm in cool brown dwarfs.

A first experiment with this *dual band imaging* technique was presented in 1997, as reported in [26]: Figure 3.10 illustrates the setup and shows two images, each taken in different filters and from alternate sides of the array; moreover, the difference image, resulting from characteristic intensity and dimensional scaling which compensate for differences in effective wavelengths, is shown between the others. The speckle pattern is reduced in the intensities by a factor of ~ 50 by the subtraction; an artificial companion, 5 mag fainter than the primary, was added to one of the original images at a separation of 0,5" resulting clearly visible in the difference image of Figure 3.10.

Moreover, we report more updated and relevant SPHERE data about the DBI technique in Figure 3.11, to show the obtained improvements in this field.

[24] In fact, the speckle pattern is chromatic.

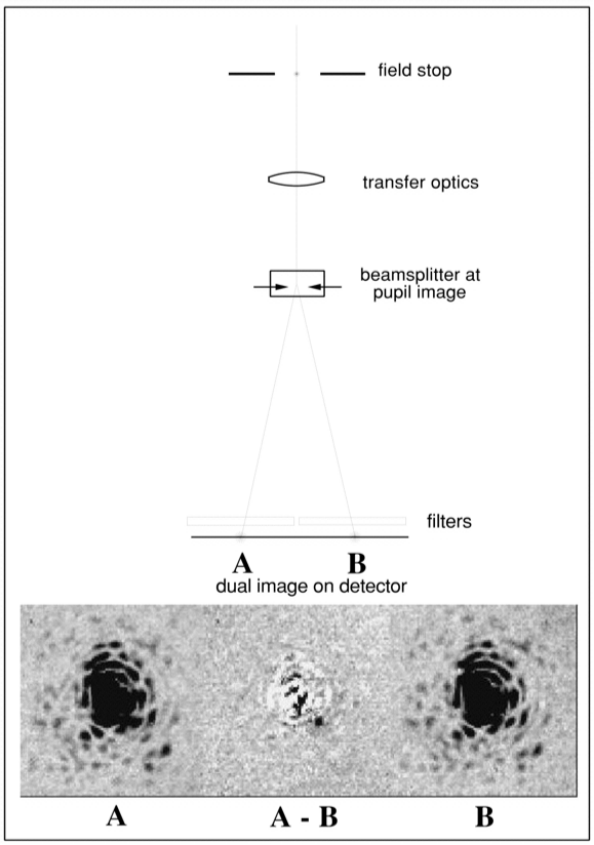

Figure 3.10: *Dual-imaging arrangement, resulting images and their difference, taken from [26]. The three displays have the same stretch. The technique results to be effective at subtracting the speckle pattern. The artificial image of a companion, 5 mag fainter that its primary and 0",5 away, has been inserted in the image on the left, and it is clearly visible in the difference image.*

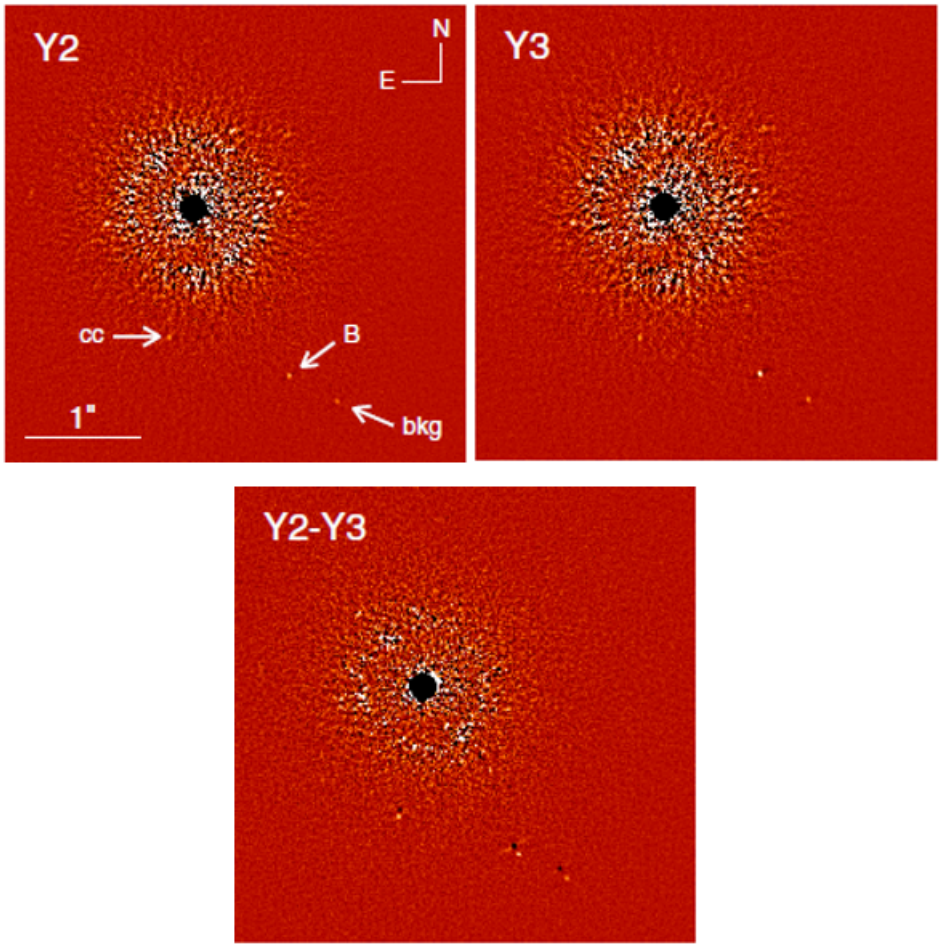

Figure 3.11: *Images of GJ 758 after ADI and SDI processing in IRDIS DBI Y2 and Y3 filters, taken from [27]. The top left and right cells present the ADI analysis of the data in the first and second filters respectively, and the bottom cell presents the result of the SDI+ADI analysis. Three objects are clearly identified in the data: GJ 758 B (B), a background star (bkg) and a new candidate companion (cc).*

3.3 SPHERE modules

It is now possible to better describe each part of the instrument, by underlining its main features and purposes.

3.3.1 CPI

The Common Path and Infrastructure consists of various interconnected parts.

- The first part of the CPI is the *Common Path Optics* (CPO), which transmits the telescope beam through the various correcting elements of the adaptive optics system and through the coronagraphic unit to the adaptive optics wavefront sensor and to the science channels.

- As regards *extreme adaptive optics*[25], the design of the SPHERE Adaptive optics for eXoplanet Observation (SAXO[26]), is determined by a global compromise involving optical design, technological aspects, cost and risk issues.

  A prime objective of SAXO is to provide a very efficient and accurate correction of low spatial frequency aberrations, which is necessary in order to obtain a high-contrast (dark hole) close to the PSF centre since exoplanets are to be found at small angular separations, generally well below 0,5 arcseconds. Figure 3.12 shows the action of AO in correcting the SPHERE SAXO H-band PSF.

  Moreover, image and pupil stability are required in high-contrast instruments: therefore, differential image movements, caused by thermo-mechanical effects and ADC[27] mechanism precision, are measured in real time, whereas the measurement of non-common path aberrations occurs offline[28].

3.3.2 IRDIS

The Infra-Red Dual-beam Imaging and Spectroscopy sub-system represents the most versatile science module of SPHERE.

IRDIS's most important features include a spectral range from 950 to 2320 nm and an image scale of 12,25 mas per pixel; both direct and dual imaging require a FOV

[25] In Extreme AO, the pupil is sampled at the Fried radius r_0, which is the parameter indicating a measure of the quality of optical transmission through the atmosphere due to random inhomogeneities in the atmosphere's refractive index and it is defined as the diameter of a circular area over which the RMS wavefront aberration due to passage through the atmosphere is equal to 1 rad.

[26] SAXO is the core of the SPHERE instrument and is essential for reaching the extremely high contrast requirements: it must satisfy the following three high-level requirements, according to [28].

- It has to guarantee the measurement and correction of the turbulent phase perturbations of the telescope and system common optics aberrations and of the noncommon path aberrations (NCPAs, namely aberrations related to the beam splitting between the wavefront sensor, WFS, and the instrument).
- It should provide an extremely elevate stability of the optical axis at the level of the coronagraphic mask.
- It should ensure the measurement and the correction of any pupil motion.

[27] Atmospheric Dispersion Corrector.

[28] Exploiting specific algorithms and then making online adjustments through references.

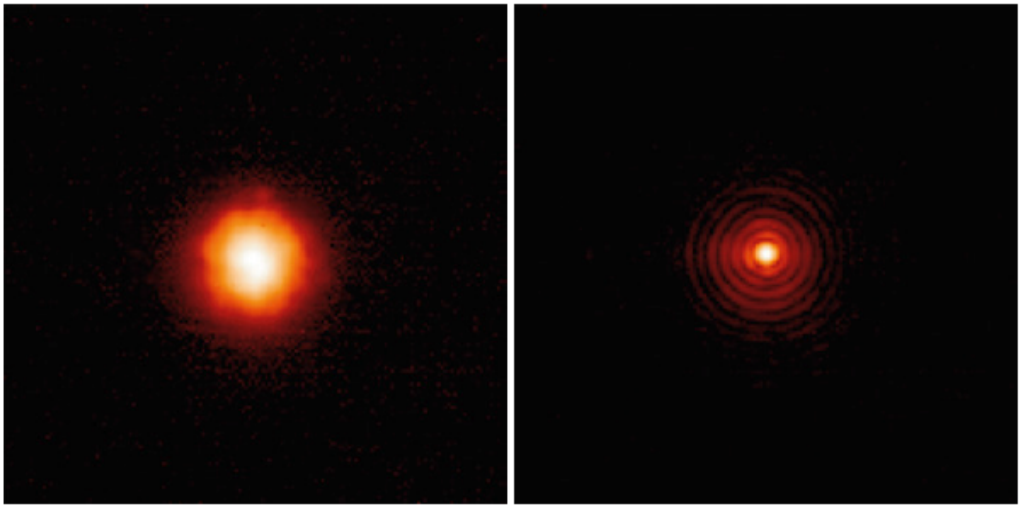

Figure 3.12: *Illustration of the SPHERE SAXO H-band point spread function, as reported in [17]. Left: uncorrected image. Right: corrected image.*

(Field Of View) greater than 11" × 11". Dual imaging is the main mode of IRDIS, providing images in two neighbouring spectral channels with minimised differential aberrations.

Ten different filter couples are defined corresponding to different spectral features in modelled exoplanet spectra, whereas in the direct imaging mode 12 broad, medium and narrow-band filters are defined. Moreover, besides direct and dual imaging, long-slit spectroscopy at resolving powers of 50 and 350, as well as a dual polarimetric imaging mode, are provided.

A beam-splitter combined with a mirror allows dual imaging separation, which produces two beams in parallel.The use of high-quality materials with high homogeneity is found to satisfy the expected differential aberrations requirement, which represents the prime challenge.

A dual-imaging simulation model is reported in [16], in which the coronagraphic action on a perturbed wavefront[29] as well as the influence of post-coronagraphic aberrations (within the IRDIS science module) are studied. It is noteworthy that the influence of differential aberrations, with respect to common aberrations, on the speckle reduction process is extremely more consistent.

3.3.3 IFS

Besides being conceptually challenging, an Integral Field Spectrograph[30] for planet imaging could concretely represent an extremely useful science module for a planet-searching instrument. In fact, two reasons support this argument: firstly, the IFS can be built with virtually zero differential aberrations; secondly, better correction of speckle chromaticity and even some data-analysis techniques[31] can be obtained by the multiple spectral channels.

[29]It is affected by time-variable residuals of the AO correction of atmospheric turbulence, as well as quasi-static instrumental aberrations.

[30]It has been entirely created in Padova, Italy, as an INAF project: this represents the major italian contribution to SPHERE.

[31]Which are not based on the presence of a priori assumed features in the planet's spectrum.

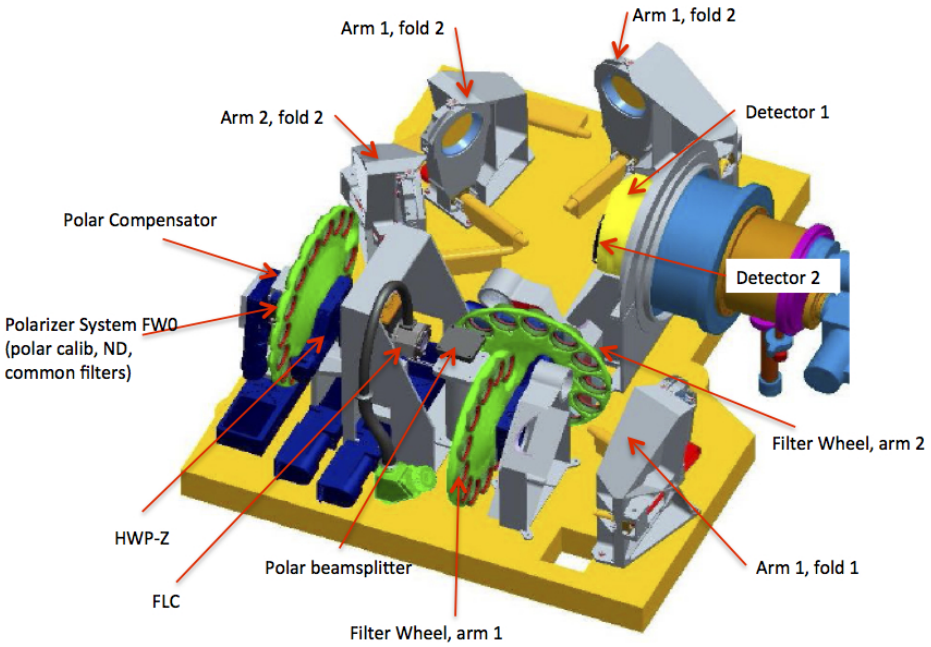

Figure 3.13: *Representation of ZIMPOL's structure.*

Regarding SPHERE, the required 5σ detectivity at $0,5$" is $\sim 2 \times 10^{-7}$ in comparison with the un-occulted PSF peak, whereas the spectral range of the IFS is limited to the $Y-J$-bands $(0,95 \div 1,35\ \mu\text{m})$[32]. Finally, a resolving power per pixel of 30 is fixed, with a minimum FOV of $1,35$" square and a relevant best value of 3" square.

3.3.4 ZIMPOL

The Zurich IMaging POLarimeter sub-system consists of a high-precision imaging polarimeter exploited in the visual band, which ranges from 600 to 900 nm. Fast modulation, using a ferroelectric retarder, and demodulation of the polarisation signal, using a modified CCD array, constitute the instrument's principle (Figure 3.13). This technique allows the simultaneous detection of two perpendicular polarizations, since the modulation is faster than seeing variations, and the recording of both images on the same pixel.

As a consequence of this approach, a polarimetric precision of 10^{-5} or even better could be reached. Besides allowing for polarimetric imaging, ZIMPOL provides the peculiar possibility for high-resolution imaging in the visual range exploiting a set of broad and narrow-band filters.

3.4 Observing modes

Aiming at obtaining the maximum benefit from the peculiar instrumental capabilities of SPHERE, three main observing modes have been exploited.

- The *NIR*[33] *survey mode* represents the prime observing mode, being used for $\sim 80\%$ of the observing time. Through the use of dichroic beam separation after

[32]This allows the use of a single detection channel and simultaneous operation of IRDIS and IFS.
[33]Near InfraRed.

the coronagraph, it combines IRDIS and IFS that can operate in IFS YJ+IRDIS H bands or IFS YH+IRDIS K bands. Thanks to this configuration[34], it is possible to exploit simultaneously the relevant capabilities of both dual imaging, covering a large field (out to ~ 5" radius), and spectral imaging in the inner region (out to at least $\sim 0,7$").

- The *NIR characterisation mode* involves the use of IRDIS alone in its various modes, allowing for observations with a greater FOV in all bands, from Y to short-K, either in dual imaging or in broad and narrow-band filters. Its utility resides in obtaining complementary information on already detected and relatively bright targets in order to better characterize them. Moreover, the long-slit mode allows spectroscopic characterisation at low/medium resolution. These observing modes will also improve the study of additional science cases, such as disks or brown dwarfs.

- The *visible search and characterisation mode*, exploits the polarimetric capabilities of ZIMPOL, providing unique efficiency in reflected light very close to the star (reaching the level required in order to directly detect old close-in planets[35] in the visible); moreover, classical imaging in the visible is allowed by ZIMPOL.

3.5 Latest SPHERE data about planets and proto-planetary disks

Planet formation around young stars occurs very frequently, since exoplanets have been discovered in large quantity. Besides being generally different to that of our Solar System, the structure of the observed planetary systems is unexpectedly varied: for instance, the frequency of planets presenting masses ranging between our terrestrial and gaseous planets is considerably high. Moreover, exoplanets well populate orbital distances inferior to that of Mercury, whereas only a few giant planets have also been detected orbiting at distances much more external than Neptune's.

A relevant diversity in the initial conditions of planet formation ranging among all evolutionary stages, from dust grain growth to planet-disk interactions and possibly planet migration, could explain this variety[36]: in particular, different scenarios have been proposed. They do not necessarily exclude each other, and occur over a range of timeframes. Therefore, a better characterisation of the physical and chemical properties of protoplanetary disks is necessary in order to widen our knowledge in planet formation.

SPHERE has invested considerable effort and observing time[37] in the characterisation of circumstellar disks[38] ([29]).

[34] In particular, it minimizes the presence of false alarms and helps confirming potential detections obtained in one channel by data from the other channel, thus advantaging the case of detections very close to the limits of the system.

[35] However, these planets constitute a relatively small number of targets.

[36] However, the mechanisms of planet formation are definitely not completely understood.

[37] It began operating on the VLT on May 2014.

[38] The telescope time results in ~ 10 complete nights dedicated to debris disks and a similar period of time dedicated to protoplanetary disks.

3.5.1 Planets with SPHERE

The occurrence of giant planets at wide orbits ($\sim 20 \div 40$ AU) is relatively low, as revealed by more than a decade of direct imaging surveys dedicated to the study of various hundred young nearby stars. Each new imaged giant planet has provided peculiar indications of the formation, evolution and physics of young Jupiters, even though the number of discoveries results to be very small if compared with other techniques, such as radial velocity and transit. As previously described, SPHERE, among the most recent and performant instruments, exploits extreme adaptive optics systems with coronagraphic and differential imaging techniques, providing unprecedented detection, astrometric and spectrophotometric capabilities allowing for discovery and characterization of fainter and closer giant planets.

In [30], the observation of the close environment of the young star HIP 65426 (described below) is presented. The deep coronagraphic NIR observations detected a young, warm and dusty massive Jovian planet[39] (HIP 65426 b), orbiting at ~ 92 AU (projected distance): this is the first planet discovered with SPHERE.

HIP 65426

HIP 65426 is an A2-type star, distant $d = (111,4 \pm 3,8)$ pc, which is a member of the Lower Centaurus-Crux (LCC) association. No clue of neither a debris disk nor a remnant planetesimal belt have been found for HIP 65426, differently from the majority of the young, intermediate-mass stars hosting an imaged planet. If the star is actually hosting a debris disk, it would be found at distances higher than 100 AU (namely, externally with respect to the planet position), as demonstrated by the analysis of the optical to mid-infrared photometry. Multiplicity could have explained a rapid dispersal of the primordial protoplanetary disk; however, so far there is no evidence for this feature in the case of HIP 65426, since observations show it is a single star.

It is noteworthy, for the system, that HIP 65426 is an extremely fast rotator, and this represents an interesting feature: in fact, rapid stellar rotation is in agreement with the picture of a rapid disk dispersal disabling disk-braking, but it is also true that planetary formation needs time to occur, in order to explain the formation of HIP 65426 b.

As regards HIP 65426 b, shown in Figure 3.14, spectro-photometric measurements obtained by IFS and IRDIS between 0,95 and 2,2 μm suggest the presence of a warm, dusty atmosphere representative of young L5$\div$L7 dwarves with low gravity on the surface. A luminosity consistent with a giant planet, characterized by $6 \div 12 M_J$, $T_{eff} = 1300 \div 1600 K$ and $R = (1,5 \pm 0,1) R_J$, is expected by evolutionary models in [30].

The $5 \div 20$ Myr-old Scorpius-Centaurus association (Sco-Cen) presents a very interesting sequence of young brown dwarfs and exoplanets, among which HIP 65426 b could be placed, since its inferred chemical and physical properties are compatible. This spectral and physical sequence is relevant because it could be exploited in order to study the main phase of transitions which occur in the atmosphere of brown dwarfs and exoplanets and affect their spectra and luminosity[40].

[39] Multi-epoch observations confirm that it shares common proper motion with HIP 65426.

[40] These transitions are, for instance, the formation of clouds and their features as a function of particle size, composition (see Figure 3.15) and position in the atmosphere, or the role played by non-equilibrium chemistry processes.

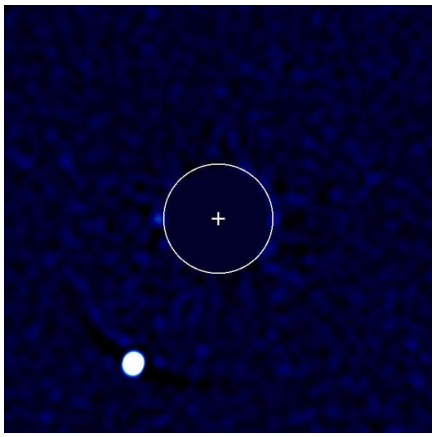

Figure 3.14: *The Figure (taken from [30]), corresponding to the near-IR band (IFS YJ-band), displays the exoplanet (in the bottom left corner) orbiting around HIP65426. Its location is provided by a cross and its light is suppressed by a coronagraph.*

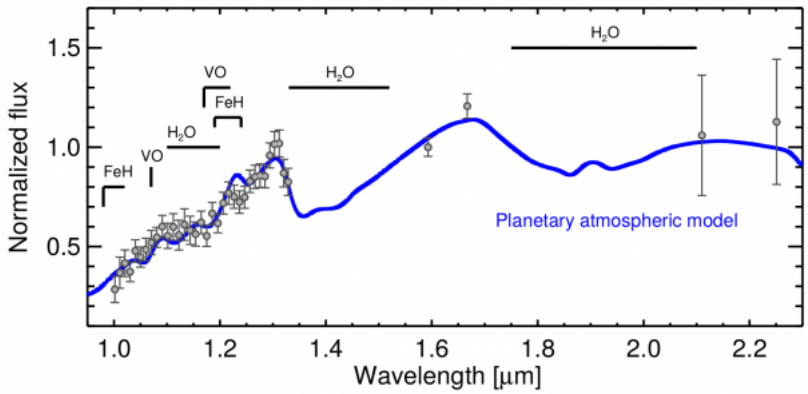

Figure 3.15: *The spectrum of the light generated by the exoplanet HIP65426b in the near-IR, taken from [30], which shows, in particular, the presence of water in its atmosphere.*

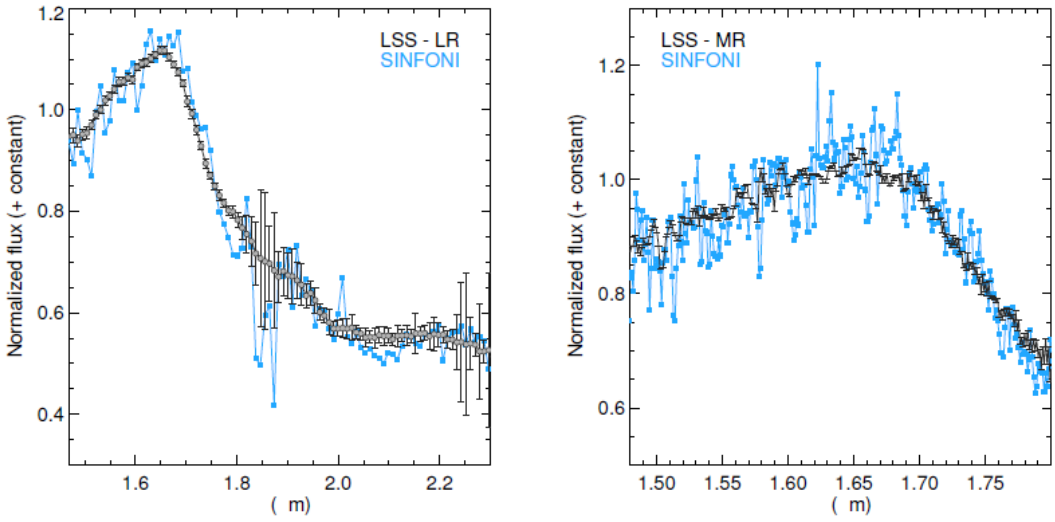

Figure 3.16: *Comparison of the SINFONI H+K band spectrum and the SPHERE long-slit spectra of PZ Tel B at comparable resolutions, taken from [31].*

As regards the formation of HIP 65426 b, the following hypothesis are the most probable.

- Unless HIP 65426 b formed significantly closer to the star before undergoing a planet-planet scattering event, the planet position would not favor a formation by core accretion. An increase of angular momentum by incorporating an inner massive scatterer[41] could account for the fast rotation of HIP 65426.
- Formation by disk instability could explain the in-situ formation scenario at its current location, being consistent with the metallicity of the host star.
- The formation of an extreme mass-ratio binary due to gravo-turbulent fragmentation should also be considered.

Characterization and orbital properties with SPHERE

SPHERE has also been exploited in other systems, such as PZ Tel, with the aim to refine their physical properties and architecture ([31]).

PZ Tel is a $G9$IV star member of the young (21 ± 4) Myr stellar association β Pictoris and located at a distance $d = (51,5 \pm 2,6)$ pc. A late-M brown dwarf companion to PZ Tel is present.

All the features of the low-resolution LSS spectra of PZ Tel B obtained with SPHERE are well reproduced by the SINFONI[42] HK-band spectrum (Figure 3.16). Moreover, the LRS spectrum of PZ Tel B was compared to the low-resolution spectra of M, L and T standard dwarfs of the SpeXPrism library ([31]), leading to the confirmation of the $M7 \pm 1$ spectral type and the low surface gravity of the companion.

Another system for which SPHERE has been used, thanks to its capabilities in detection and characterization of planets (providing spectra and photometry of them),

[41] The presence of unseen inner massive planets, of possible masses of $\leq 5 M_J$ beyond 20 AU, in that system that could have scattered out HIP 65426 b cannot be excluded.

[42] SINFONI is a near-infrared $1,1 \div 2,5$ μm integral field spectrograph fed by an AO module.

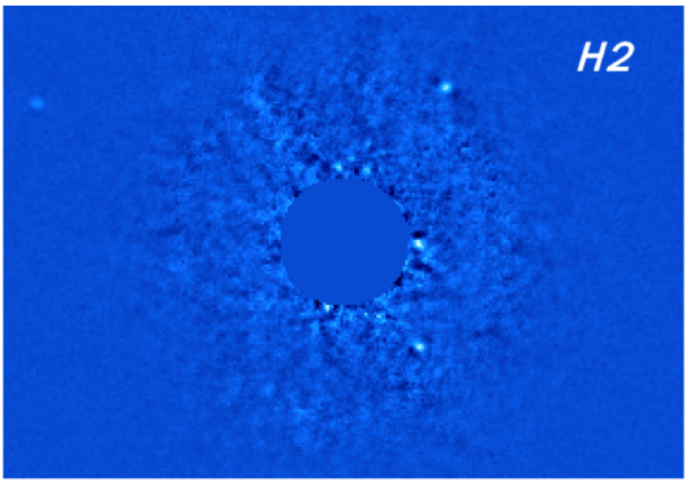

Figure 3.17: *IRDIS images for H2 filter with the four planets around HR8799, taken from [32]. The color scale is in unit of contrast with respect to the host star.*

is the planetary system discovered around the young A-type HR8799, which provides a unique laboratory to:

- test planet formation theories;
- explore the various different system architectures at these separations;
- operate comparative (exo)planetology.

In [32] they present and exploit new near-infrared images and integral-field spectra of the four gas giants surrounding HR8799 obtained with SPHERE, aiming at completing the spectral energy distribution (SED) of these bodies in the $(1,0 \div 2,5)\mu$m range. Moreover, new astrometric data are provided, in particular for planet e, to better constrain the orbits.

The final image obtained, after data reduction, for one of the IRDIS filters is shown in Figure 3.17, where the four planets orbiting HR8799 are evident.

In addition, in [33] the photometry of the four planets and low-resolution ($R \sim 30$) spectra of HR8799 d and e are employed to apply their comparison with known objects, besides understanding what the planet physical properties are and how their atmospheres work.

It is then clear that SPHERE opens new horizons in the study of young brown dwarves and giant exoplanets using direct imaging thanks to its unique features.

3.5.2 Protoplanetary disks with SPHERE

Excellent spatial resolution may be guaranteed by optical and near-infrared observations of stars distant a few hundred parsecs; however, imaging the circumstellar environments at these wavelengths is limited by the low contrast of the circumstellar emission with respect to the stellar flux.

Differential imaging represents the most efficient way to overcome this difficulty: in particular, polarimetric differential imaging (PDI) provides great imaging of extended structures, such as circumstellar disks at tens of AU from the star, by exploiting the different nature of the stellar (mainly *unpolarised*) light and scattered (strongly

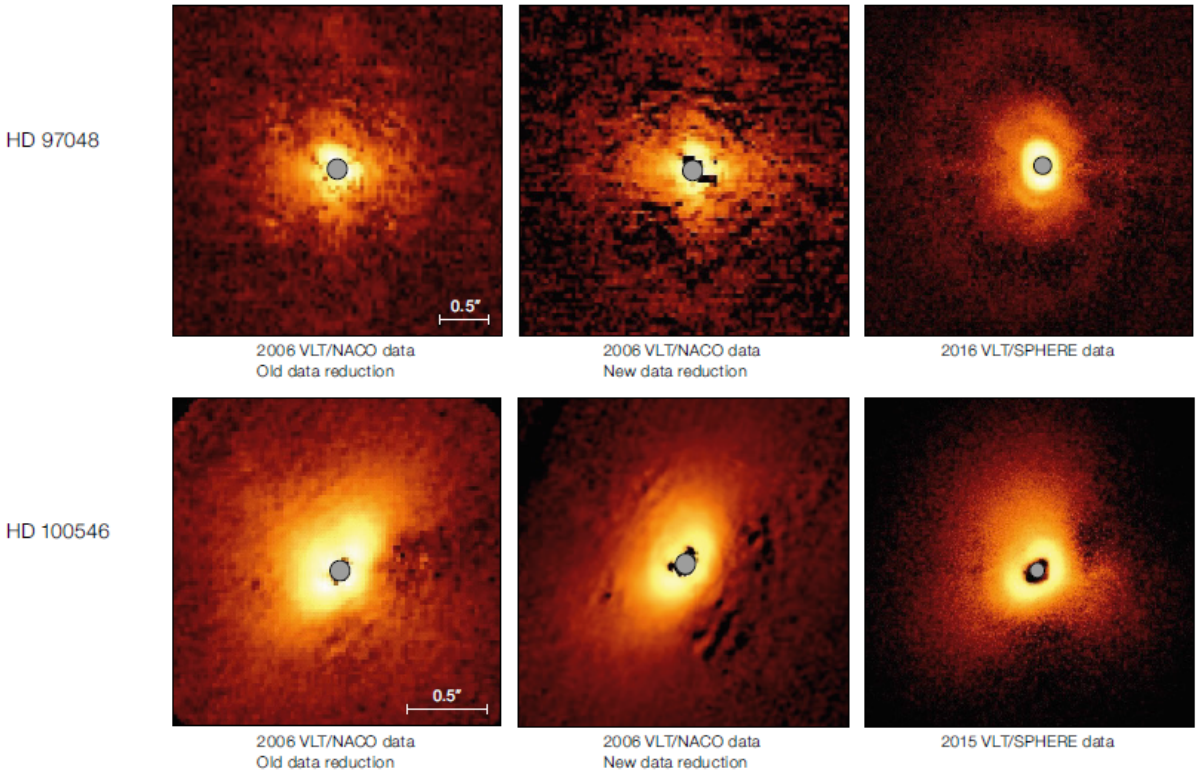

Figure 3.18: *The improving data quality over time with the new reduction procedures and the impact of SPHERE are shown for the two disk systems HD 97048 and HD 100546 ([29]).*

polarised[43]) light from the disk surface. The separation of these two light components is allowed by the (quasi-)simultaneous observation of orthogonal polarisation states.

PDI has consistently improved its capabilities throughout the last few years, as shown in Figure 3.18, thanks to SPHERE and to advancement in data reduction.

SPHERE, besides being the only instrument installed on an AO-assisted 8-metre telescope to perform PDI in the visible, represents one of the best instruments to perform PDI of circumstellar disks: in fact, exploiting its SAXO, ZIMPOL and IRDIS modules, this combination provides an unprecedented combination of optimal sensitivity and angular resolution[44].

A small fraction of the whole sample of disks imaged so far with PDI is represented by the ten sources in Figure 3.19; nevertheless, they exhibit all the morphological features now continuously found in all protoplanetary disks. In particular, in most of the sources, either concentric rings (such as HD 97048 and TW Hya) or spiral arms (MWC 758, HD 135344B) are revealed; moreover, some disks, especially those with spirals, exhibit radially extended dips which could represent shadows cast by an inclined disk at a few AU from the central star.

Considering disk geometry and illumination effects in inclined disks is required for the interpretation of features from these sources. However, in order to understand planet formation, this analysis is necessary since it determines the composition of dust

[43]For instance, the reflected light of a planet is polarised and in the visible band.

[44]In particular, sensitivity is more than 10^4 in contrast, while angular resolution is ~ 3 AU in the visible and ~ 7 AU in the NIR for sources at 150 pc.

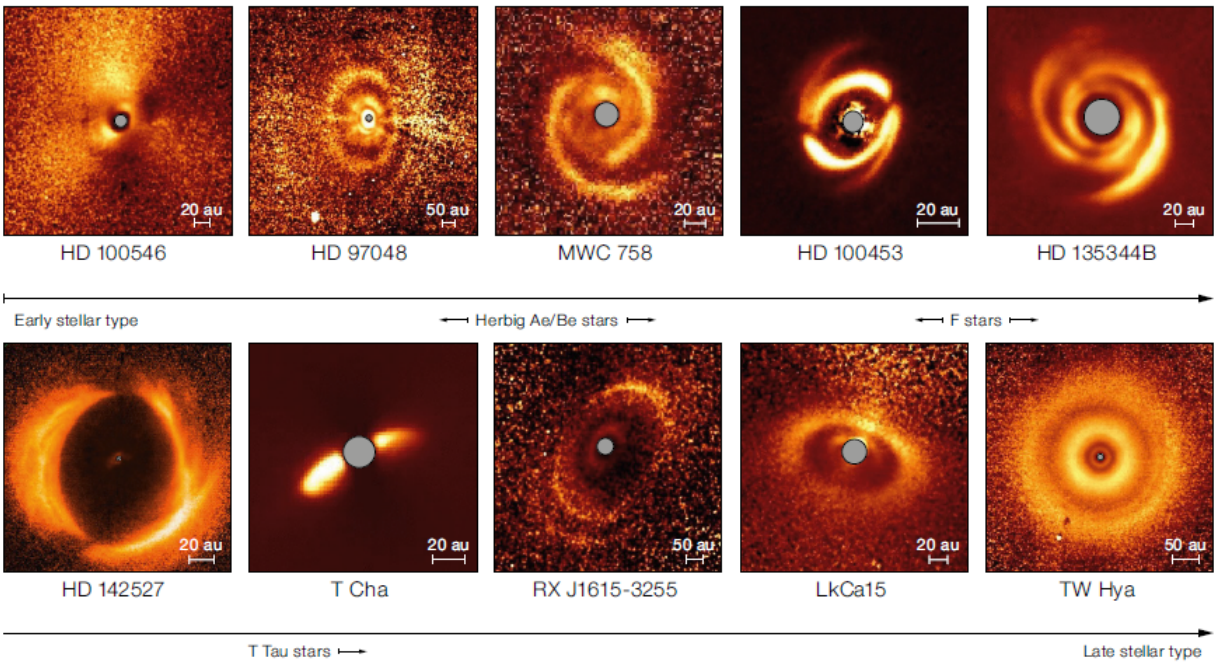

Figure 3.19: *Collection of images of protoplanetary disks observed in PDI with SPHERE, reported in [29].*

grains and the geometry of the disk surface.

3.5.3 The presence or the absence of a disk cavity

Both near-infrared and millimetre images revealed the elevate frequency of large (> 10 AU) central cavities, which is a fundamental aspect. In many cases, these cavities result to be smaller in PDI with respect to the millimetre images; alternatively, they are not revealed in PDI down to the instrument coronagraph[45]. An accurate analysis of these differences is crucial as regarding planet-disk interactions, since the most probable context for the formation of these cavities involves the dynamical action of orbiting companions.

Figure 3.20 illustrates the high occurrence of cavities in disks surrounding Herbig stars[46]: it can be seen that the presence or absence of a large disk cavity could explain the long-standing observational difference between sources with large far-infrared excess (Group I) and small far-infrared excess (Group II). Discs with large cavities represent more than half of the total, as evidenced by the sample of Herbig stars with available PDI images, which covers the vast majority of sources within 200 pc. Moreover, excluding low-mass disks which are undergoing disk truncation from outer stellar companions at hundreds of AU (bottom-left of the map), this fraction reaches the value of $\sim 75\%$.

Figure 3.20 also determines that disks which do not exhibit a large cavity (Group II) are fainter as regards scattered light. In fact, the photometric ratio of the x-axis is a valid indicator for the amount of signal detected in PDI, whereas the millimetre flux

[45]Even though this is up to four times smaller in size than the millimetre cavity.

[46]V4046 Sgr, which is the subject of this work and is not an Herbig star, would occupy the position indicated by the yellow star in the Figure, namely the point of coordinates $(\sim 4, \sim 90)$, according to the data inferred by [7] and [34]. Its location places it among the disks which exhibit a large cavity: as described in Chapter 4, this is in agreement with the observations.

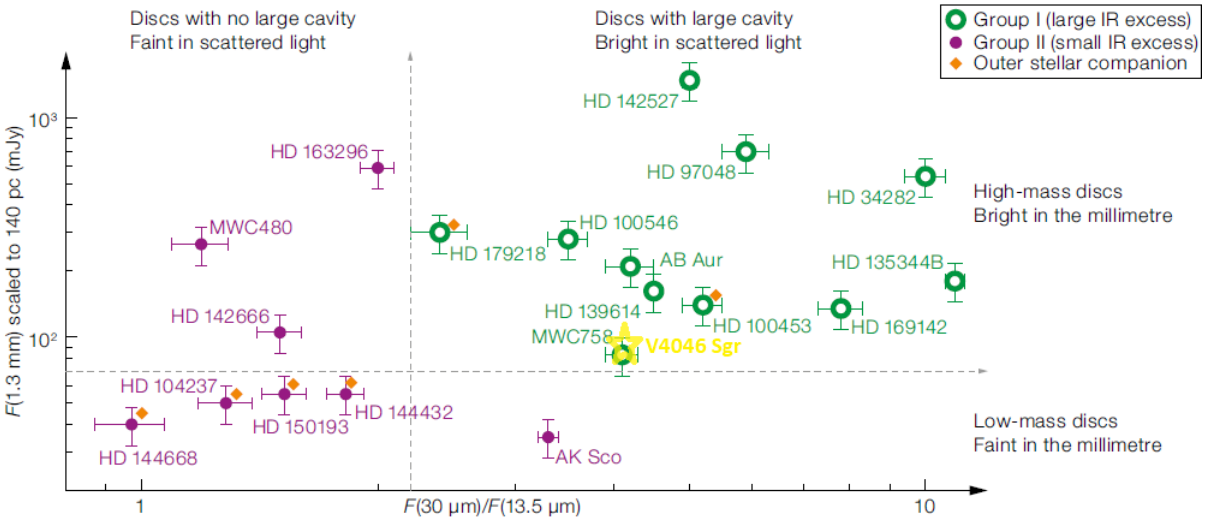

Figure 3.20: *Millimetre to mid-infrared chart reported in [29]. The photometric ratio between 30 μm and 13,5 μm on the x-axis represents the amount of scattered light traced by SPHERE. The y-axis presents the millimetre luminosity scaled to the same distance. Sources with outer stellar companions are indicated by the brown diamonds. Among these systems, AK Sco and HD 142527 are circumbinary disks as well as V4046 Sgr, which is indicated by the yellow star.*

along reported on the y-axis provides an approximate estimation of the dust mass. Two sub-categories of Group II sources can be distinguished in function of their millimetre flux, likely accounting for their modest scattered light: both disks as massive as Group I (which are possibly shadowed by their own inner ring) and those with low mass and an outer companion (which are probably smaller than the size of the coronagraph and are thus faint) are revealed by millimetre flux observations.

The morphology of the resulting planetary systems may be in correspondence with either the presence and the size of the disk cavity, as well as the extension of the disk[47].

3.5.4 Link between protoplanetary disks and planetary systems

Unfortunately, the absence of detectable emission arising from m- to km-sized bodies does not allow to study observationally the intermediate phases of the planet formation process. As a consequence, the most immediate approach in order to set a correspondence between protoplanetary disks and planetary systems is to directly compare their physical scale, as shown in Figure 3.21.

Considering systems such as HR 8799 or our own Solar System, the planetary orbits are located at scales comparable to the position of some disk features like rings, cavities and spirals. Most of the currently known exoplanets have been detected by the *Kepler* space mission exploiting the transit method (discussed in Section 2.3.1), which is mainly referred to planets within a few AU from the host star. This fact, in addition to the scarce presence of gas giant planets imaged beyond 30 AU, means that the there is not a correspondence between the continuously discovered disk features and the exoplanet distribution. A possible explaination of this can be provided by one or more of the

[47]However, more accurate studies and classifications of the resolved features of the disks as well as the structure of planetary systems have still to be performed.

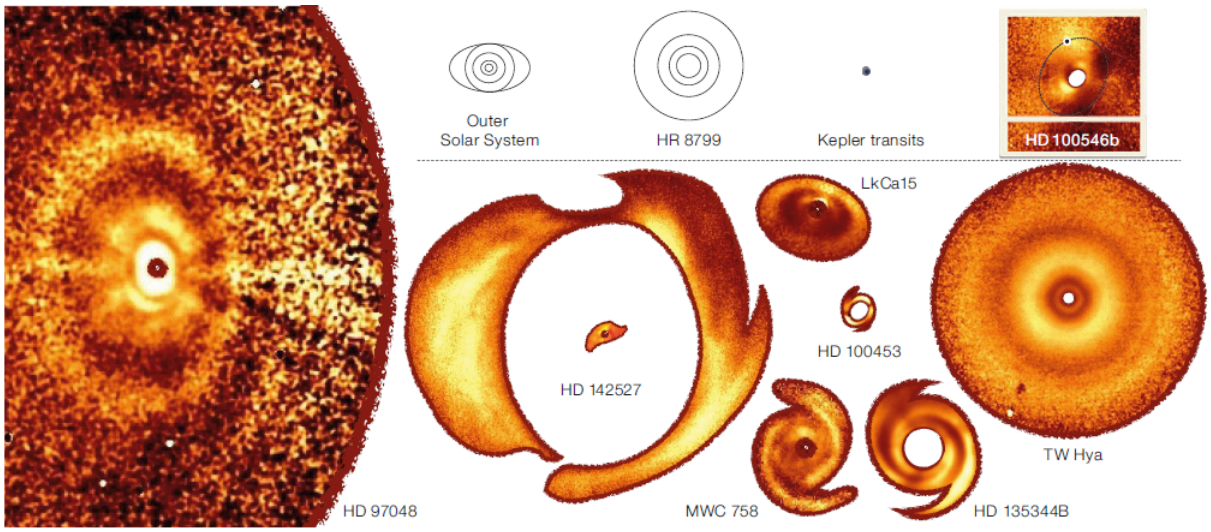

Figure 3.21: *Illustrative protoplanetary disks and planetary systems all presented at the same physical scale, as reported in [29].*

following considerations.

- Planet migration caused by disk forces is a very efficient and rapid process.
- A consistent population of low-mass planets is present at large orbits but is yet undetected.
- The disks that we observe are peculiar cases.
- The interaction with planets does not determine the commonly observed disk features.

However, the mechanisms of planet formation could provide the solution to this apparent incongruity: in fact, disc fragmentation led by instability is considered to be a possible process in the primordial evolution of disks (< 1 Myr), whereas the stars we observe surrounded by disks are much older. At this stage, accretion of gas onto planetary cores of some Earth masses results to be more probable; in this scenario, disk gaps and cavities may be determined by giant planets, thus favoring the creation of kilometre-sized planetesimals from the relevant growth of millimetre-sized particles by a dust trap.

The observation and characterisation of forming planets still incorporated in the disk (and possibly of their circumplanetary disk) is considered the most efficient observational approach to these issues; however, very few such examples have been found so far. One of the best studied among these is HD 100546b, even though its influence on the disk morphology is not clear. Another one, which is the subject of this work and will be treated in detail in Chapter 4, is V4046 Sgr.

In conclusion, as regards the evolution of disks, there have not been determinant results on the evolution of disk features with time, due to the small number of objects and the uncertainty in pre-MS models.

Chapter 4

V4046 Sgr

4.1 Description of V4046 Sgr binary system

T Tauri stars represent fully convective, contracting pre-MS[1] objects of about the solar mass; part of this class of stars, the *classical* T Tauri stars (CTTSs), are characterized by consistent and broad emission lines in the optical spectral region. Rather thick and dusty disks surround these stars, thus it has been supposed that an interaction between the disk and the star is related to the strong line emission. In fact, models which involve accretion of matter from the disk to the star along stellar dipole magnetic fields turned out ot be capable of reproducing many of the peculiarities observed in CTTSs ([35]).

Several T Tauri stars are double or multiple, and the closer pairs may generate a central gap in the disk, leading to a circumbinary disk. Most of the discovered close binaries are the so called *weak-lined* T Tauri stars, showing scarce (or absent) evidence of interaction between star and disk. As regards CTT binaries with separations smaller than 1 AU, only a few are known, namely GW Ori, RX J0530.7-0434, UZ Tau E, DQ Tau and V4046 Sgr. Accretion, in the case of binary components inside a circumbinary disk, is characterized by the same evolution of single CTTSs since all of the aforementioned CTT binaries present emission line signatures characteristic of single CTTSs.

Focusing on the latter of these CTTS binaries with small separation, namely V4046 Sgr, observations reported in [35] suggest that gas co-rotates with the stars, but at a distance of $0,75(a_1 + a_2)^2$ from the center of mass, which is well within the inner edge of the circumbinary disk[3] (see Figure 4.1). Substantial gas flows is then expected in the gap cleared by a binary in circular motion.

Henceforth we analyze the pre-MS close binary system V4046 Sagittarii, distant $d = 73$ pc and composed of two K-type stars. It is a member of the β Pic Moving Group, with an age of about $12 \div 24$ Myr. The following parameters ([7], [36] and [37]) characterize this system:

[1]Main Sequence (MS) of the Hertzsprung-Russel diagram.
[2]The semi-major axes of the stars a_1 and a_2 are reported in the following table.
[3]Located at $1,8(a_1 + a_2)$.

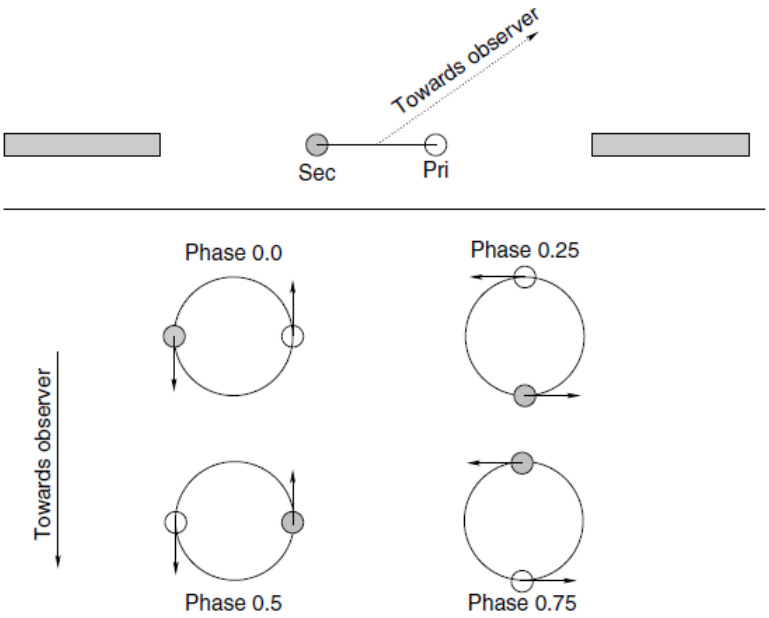

Figure 4.1: *Schematic presentation of V4046 Sgr system, taken from [35]. The upper Figure illustrates an edge-on impression of the system; distances and stellar radii are proportional. The inner boundary of the circumbinary disk is located at* $1,8(a_1 + a_2)$ *from the center of mass (CM). The bottom Figures show the relative disposition of the stars at selected phases. Clearly, "Sec" and "Pri" stand for "secondary" and "primary" star, namely star 2 and 1, respectively.*

Disk parameters	
i_d (°)	$33,5^{+0,7}_{-1,4}$
e	$< 0,01$
r_{DISK} (AU)	~ 370
m_{DUST} ($M_\oplus$)	40
m_{GAS} ($M_\oplus$)	110

Binary parameters	
T (d)	$2,4213459$
m_1 ($M_\odot$)	$0,90 \pm 0,05$
m_2 ($M_\odot$)	$0,85 \pm 0,04$
a_1 ($R_\odot$)	$4,52$
a_2 ($R_\odot$)	$4,72$
r_1 ($R_\odot$)	$1,20$
r_2 ($R_\odot$)	$1,12$
$T_{eff,1}$ (K)	4350
$T_{eff,2}$ (K)	4060
s ($R_\odot$)	9

where i_d is the disk's inclination, e is the eccentricity, a is the stellar semi-major

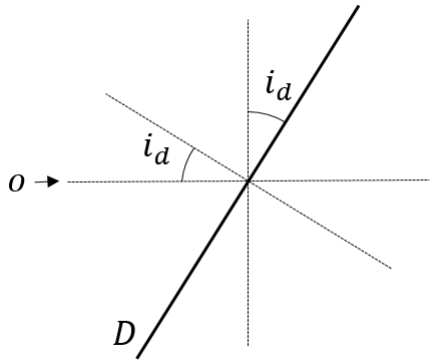

Figure 4.2: *Geometry of the system studied.*

axis with respect to the center of mass CM, r and m[4] refer to the radius and to the mass respectively, T is the orbital period of the stars, $T_{eff,i}$ is the temperature of the stars $i = 1, 2$ and s is their separation.

Images from SPHERE data show that the dust disk has a prominent shadow, which will be analyzed in Chapter 5; moreover, it presents two rings at radii of about 14 and 29 AU, which probably indicate the presence of a planet (the two rings are shown clearly in Figure 5.3: the inner one is related to the binary, the outer one is probably generated by a planet[5]).

As mentioned previously, V4046 Sgr is a close T Tauri binary which is coplanar[6] with the disk and both stars are in synchronous rotation and co-rotating with the disk, as shown in Figure 4.1. Figure 4.2 reports the geometry of the circular thin disk, where O stands for the observer line and D is the plane of the disk seen from within.

Anyway, it is important to stress that, even though V4046 Sgr is known as a binary, it is actually a more complex system: in fact, a recent discovery with SPHERE has confirmed the presence of a debris disk around a star which had been previously identified as the third wide companion of V4046 Sgr, about 12000 AU distant from the binary (as will be described in Section 4.5).

4.2 Dynamical mass estimate for V4046 Sgr

Unique information about the star formation process are provided by the masses of young stars, which are thought to play an important role on the evolution of their circumstellar material, and consequently the performance of the planet formation process, as asserted in [36].

Nevertheless, the uncertain information given by the location of pre-MS star in the H-R diagram makes the measurements of their masses difficult and therefore rare.

Orbital dynamics is the only basis for the direct methods available for measuring stellar masses. In sufficiently close pre-MS binary star systems, $M_\star$ can be inferred from the stellar orbits exploiting multi-epoch radial velocity (RV) measurements as well as long-term astrometric monitoring. For a double-lined spectroscopic binary

[4]Their estimation is discussed in Section 4.2.

[5]The possibility of finding a planet in V4046 Sgr is argumented in Section 4.4, whereas simulations are provided in Chapter 6.

[6]As reported in [36], the difference between the inclination of the disk i_d and that of the binary $i_\star$ is $|i_d - i_\star| \approx (0, 1 \pm 1)^\circ$.

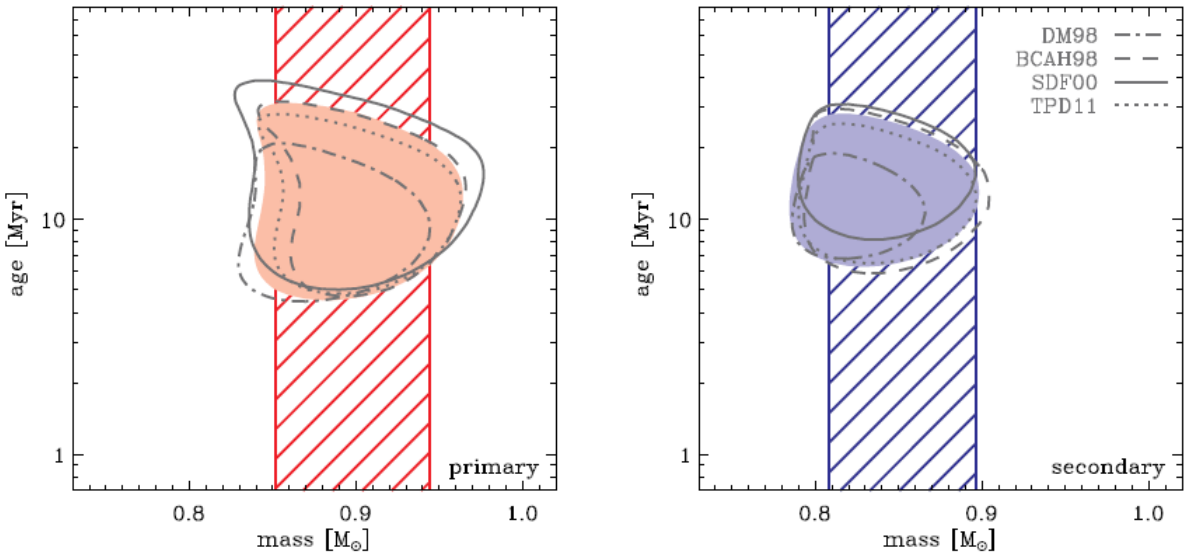

Figure 4.3: *The 68% confidence intervals for the posterior likelihood distribution in the* $(M_\star, t_\star)$*-plane derived from the H-R diagram for each model type (the key is in right panel) superposed together on the individual V4046 Sgr components (left primary; right secondary). The filled shaded region represents the averaged likelihoods from the four different pre-MS models. The dynamical masses and their uncertainties are marked as a hatched, shaded vertical column. The Figure was taken from [36].*

(SB2), a consistent estimate of $M_\star \sin^3 i_\star$ for each component is provided by the RV method; furthermore, the astrometric monitoring technique determines a constraint on the quantity $M_{TOT} d^3$, being M_{TOT} the total mass of the stars and d the distance to the binary: in order to estimate $M_\star$ with a small uncertainty it is then necessary to precisely estimate $i_\star$ and d.

V4046 Sgr, which has been kinematically associated with the $\sim 12 \div 24$ Myr-old β Pic moving group, is completely isolated from any known molecular clouds and it satisfies the requirements for the traditional RV technique for a SB2 system. Setting a dynamical constraint on the mass of the central binary has been possible by employing basic radiation transfer calculations for a disk structure model which involves a Keplerian velocity field:

$$M_{TOT} = 1,75^{+0,09}_{-0,06} M_\odot.$$

Several pre-MS evolution model predictions are in good agreement with the inferred obtained masses of the V4046 Sgr binary.

The outcomes of the comparison of four pre-MS evolution models considered in [36], in which the component masses are combined with the dynamical constraints, is shown in Figure 4.3; there, it is possible to infer a small range of acceptable dynamical ages from each set of the models. The averaged results of the different pre-MS model predictions indicate ages of 12^{+17}_{-3} and 13^{+11}_{-3} Myr for V4046 Sgr star 1 and 2, respectively, whereas the corresponding coeval age is 13^{+8}_{-3} Myr. Thus, V4046 Sgr represents a system which hosts one of the oldest and nearest gas-rich primordial accretion disks currently known.

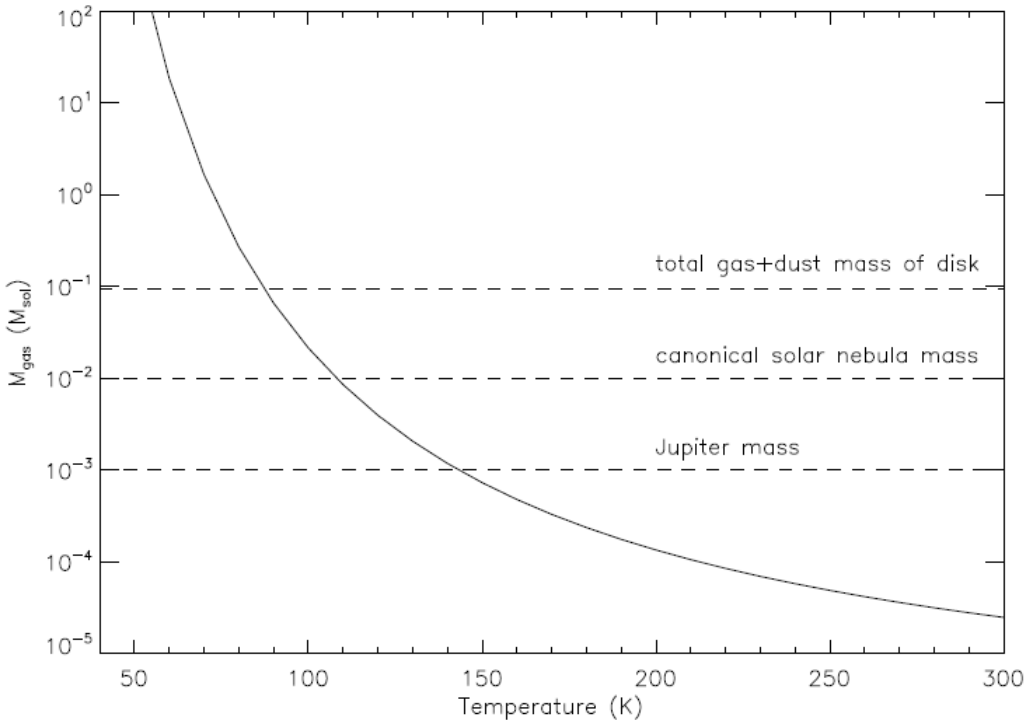

Figure 4.4: *H_2 gas mass inferred from the strength of the 17 μm S(1) emission line in function of temperature (solid curve), taken from [34]. The horizontal dashed lines correspond to the masses of Jupiter, canonical solar nebula and the total gas+dust mass of the disk around V4046 Sgr.*

4.3 Gas and dust constituents within the disk

The majority of the dust mass of the disk, according to [38], is distributed in a limited ring (centered at 37 AU with a FWHM of 16 AU) which is 5 times more compact than the gas disk; as a consequence, this implies that the mass ratio of dust over gas has a strong spatial variation: in fact, it ranges from a value much larger than typical of the interstellar medium (ISM) at the ring to much smaller than that of the ISM at more external disk radii[7].

In [34], results from a spectroscopic mid-to-far infrared study of the circumbinary disk orbiting V4046 Sgr are presented: the estimation of the gas mass in the relatively warm surface layers of the inner disk exploits the H_2 S(1) line luminosity, as shown in Figure 4.4. The other elements and compounds whose emission lines have been detected, such as Ne, CO_2, HCN and H_2O are presented in Figure 4.5.

As regards the composition of the dust disk, modeling of silicate dust grain emission features in the mid-infrared suggests that the inner disk is composed mainly of large ($r \sim 5\ \mu$m) amorphous pyroxene and olivine grains, representing $\sim 86\%$ by mass, besides presenting a relatively large proportion of crystalline silicates. Their radial temperature distribution is reported in Figure 4.6. This dust distribution together with other traces

[7]As will be explained in this Section, these basic structural features could represent observational evidence for the accumulation of solids at a local gas pressure maximum. Furthermore, a consistent population of μm-sized grains inside the central disk cavity indicates that, even though photoevaporation cannot be excluded, this structure is likely the outcome of dynamical interactions with a low-mass companion.

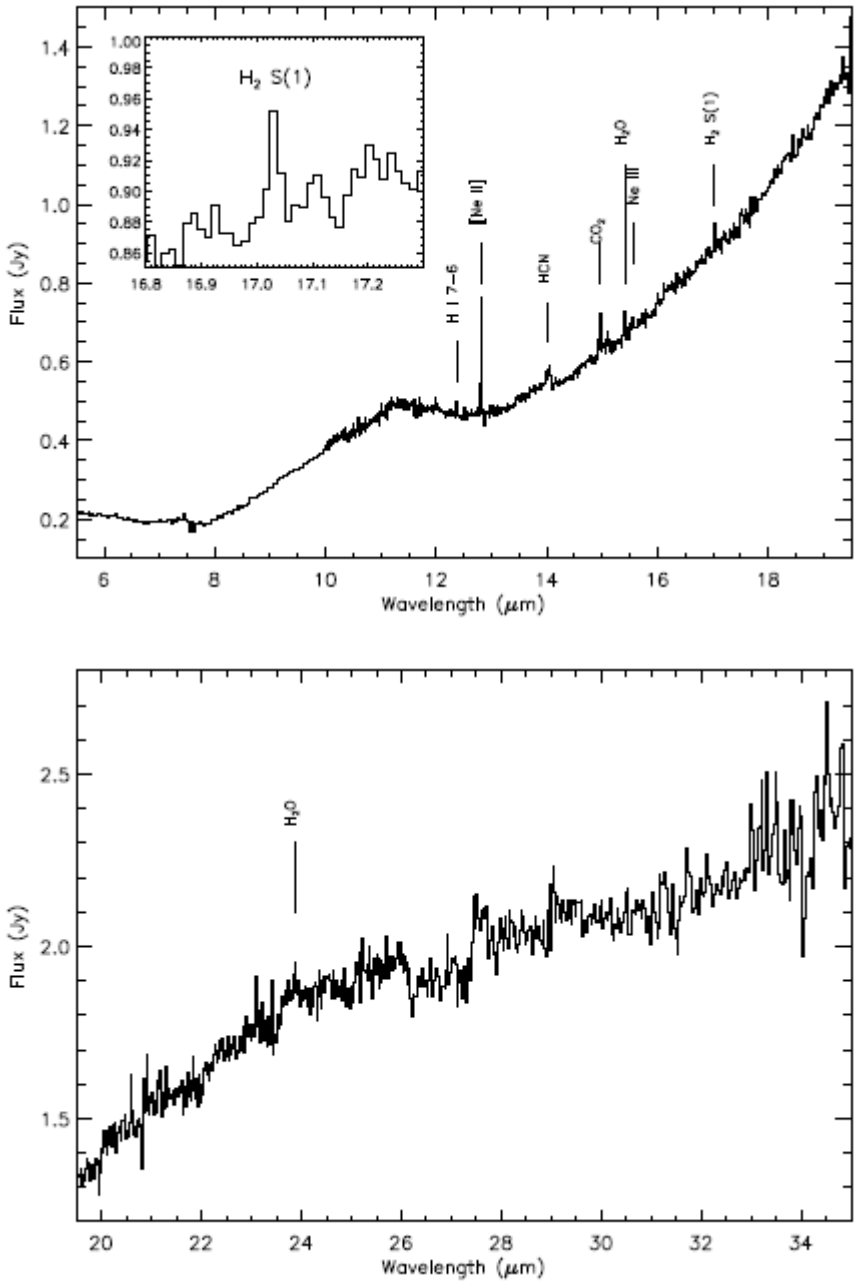

Figure 4.5: *IRS spectrum of V4046 Sgr with emission features labeled, taken from [34]. Top:* $5,5 \div 19,5$ μm *spectrum with an inset showing the pure rotational* H_2 *S(1) line at 17,035* μm*. Bottom:* $19,5 \div 35$ μm *spectrum with emission features labeled.*

([34]) suggest that planet building is acting in regions of the disk within ~ 30 AU of the central close binary. In fact, nearby[8] T Tauri stars represent excellent candidates[9] for studying planet formation processes, since due to their proximity it is possible to examine the contents and structure of circumstellar disks where young protoplanets are probably forming.

The contents of these protoplanetary disks are explored thanks to near to far-infrared spectroscopy, since the strongest emission from such disks derives from infrared and (sub)-mm wavelengths.

- *Mid-IR* ($5 \div 40$ μm) spectroscopy allows to investigate the inner ($R < 10$ AU) planet forming regions of the disk, outlining both its gas and dust constituents. Emission features caused by the increasing disk temperature from the disk midplanes to their exteriors are detected at medium to high resolution: these spectral features, in most cases, only explore the disk atmosphere, becoming the disk optically thick towards the midplane; however, they may also be originated by optically thin regions of the disk as a consequence of dust sublimation or grain growth and planetesimal formation. Moreover, in the case in which giant planet formation and/or disk photoevaporation carves out an inner gap in transition disks, these disks may present cavity walls showing emission features caused by direct exposition to stellar UV radiation.

- *Far-IR* ($50 \div 700$ μm) spectroscopy detects emission from colder gas and dust in the outer ($R > 10$ AU) disk: in correspondence of these longer wavelengths, emission features deriving from gas mass tracers[10] are to be expected.

Despite their age, at which the disk would be expected to have dissipated, the central stars of V4046 Sgr are actively undergoing material accretion from the disk, which has an inner gap[11] of radius ~ 30 AU (in particular, in [37] two rings[12] have been detected, with the most internal at ~ 14 AU). High energy radiation from the central stars causes the disk's evident photoevaporation, which, in conjunction with planet formation, may play a relevant role in the inner disk clearing.

As concerns the inner gap, since V4046 Sgr is a multiple star system presenting a large mass fraction of cool large grains rather than warm large grains, the scenario in which a planetary companion in the inner disk is clearing away smaller particles and enhancing the large grain population at larger (cooler) radii cannot be rejected ([34]).

As demonstrated in [37], dust segregation by size into rings[13] may be determined by multiple young giant planets orbiting at particular semi-major axes, around the V4046 Sgr binary system, which are similar to those of the giant planets in the Solar System. As regards the dust size distribution within the disk, it results to be composed of relatively small (μm-sized or smaller) grains within its central, ~ 29 AU large-grain

[8] Nearby stars are considered those within ~ 100 pc of Earth.

[9] Even though their presence is relatively scarce.

[10] They may be *CO* and atomic species tracing photodissociation regions at disk surfaces.

[11] It is possibly generated by ongoing Jovian planet formation.

[12] From Figure 6.18 it is possible to infer that the two rings - resolved in scattered light observations - are not resolved in SMA (SubMillimeter Array) observations. New sub-millimeter observations (ALMA - Atacama Large Millimeter Array) are required.

[13] It is due to pressure gradients, which trap larger (millimeter- to centimeter-sized) particles outside the planet-forming regions of the disk, whereas smaller (μm-sized) grains freely pass through the pressure traps, generating strong dust particle size gradients.

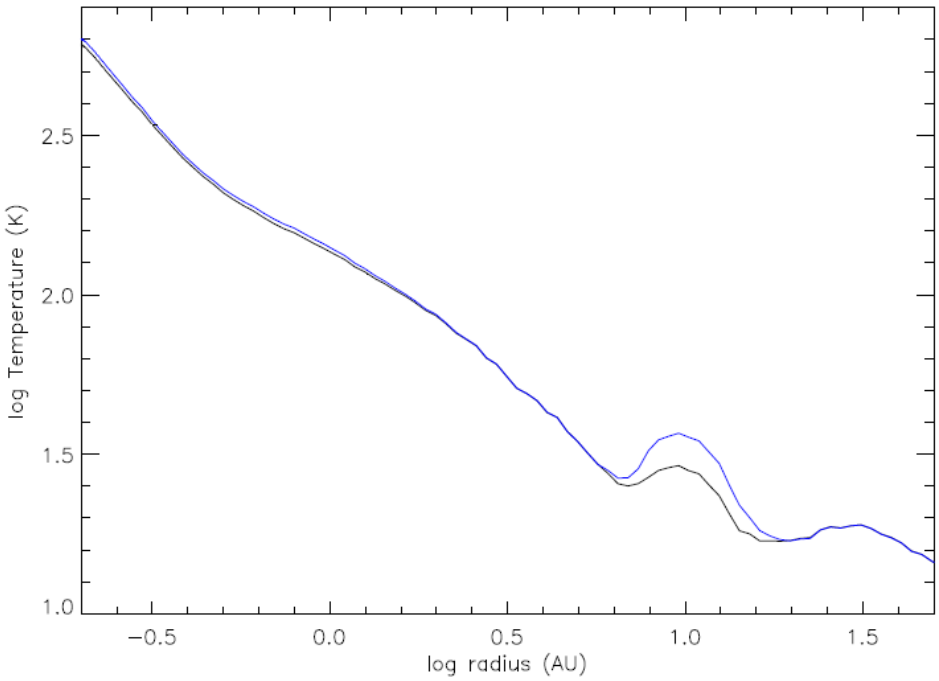

Figure 4.6: *Temperature at a given disk radius in the [34] model for large grains ($R > 5$ μm; black line) and small grains ($R \sim 5$ μm; blue line).*

cavity; moreover, there is evidence about the absence of even small grains interiorly to the < 14 AU radius region. The possibility of the presence of gas giant planets, which are actively carving gaps at $R < 14$ AU and at $R \sim 20$ AU in the V4046 Sgr disk, has been suggested by the comparison with models of protoplanet-disk interactions.

Finally, in order to account for the crystallinity of V4046 Sgr disk, one should explain how crystalline silicates form in protoplanetary disks: one of the most accredited mechanism considers amorphous silicates to be thermally transformed resulting into crystalline silicates. This thermal annealing is the consequence of star-disk interactions, in the case the disk is sufficiently massive, or of local gravitational instabilities related to planet formation: in fact, these phenomena produce shock fronts within the disk, which subsequently result in heating. The combination of moderate crystallinity and large dust grains could be explained by the planet formation activity in V4046 Sgr: grain growth and planet formation may have occurred recently in the disk, thus generating a crystallinity fraction which is larger than typical for a disk with an inner gap and advanced age. Either the central binary star or protoplanet(s) likely represent the targets onto which crystalline silicates, in correspondence of (or within) these planet formation zones, would likely accrete.

4.4 Possibility for giant planet formation

Referring to the core accretion model of gas giant planet formation ([37]), the formation of such planets occurs in circumstellar disks through the agglomeration of dust particles which generates a planetary core; subsequently, the accretion of disk dust and gas takes place. Angular momentum loss onto the disk transports outward disk material co-orbiting with a planet massive enough, thus clearing a large gap.

According to [7], giant planet formation in disks can occur in one of the following

two ways: core accretion or disk instability, with timescales of a few Myr and a few $\times 10^3$ yr, respectively. Old disks, such as that around V4046 Sgr, are expected to favor the formation of giant planets if compared to shorter-lived disks, independently of their formation mechanism, until reservoirs of gas become empty[14].

Therefore, V4046 Sgr represents a particularly interesting and relevant case: in fact, the outer regions of its circumbinary disk, in which giant planets formation could likely occur, will remain nearly unaffected during the system's lifetime, since it presents a tight separation. Instead, within ~ 1 AU dynamical effects due to the proximity with the central binary are expected to consistently influence the disk. Extrasolar planets have been detected in binary systems in a proportion of about 20%, and every detection of an extrasolar planet for a binary with separation < 20 AU has never been ambiguous: therefore, V4046 Sgr disk is expected to host a planet.

Moreover, systems similar to V4046 Sgr which have dust ring structures, resulting from planet-disk dynamical interactions, with sharp radial gradients in both surface density and particle size, do not contain centimeter- and millimeter-sized dust grains within the central regions of their disks: the formation of giant planets with orbital semi-major axes inferior to 30 AU could account for the presence of such central disk *holes* ([37]).

4.5 The wide companion of the binary in V4046 Sgr

As confirmed by [39] (submitted), V4046 Sgr is a wide, hierarchical triple system, where the projected separation between the binary and the third companion is of 12300 AU, very wide but still acceptable for a bound system (especially because of its young age).

The young M-dwarf GSC 7396-0759 ($P = 12,05$ d) is the wide companion of V4046 Sgr, with a temperature of (3632 ± 19) K, a luminosity of $(0,14 \pm 0,02) L_\odot$ and a stellar radius of $(0,95 \pm 0,08) R_\odot$; moreover, it does not show evidences of accreting gas.

It is surrounded by a quite extended (likely) debris disk[15], whose detection is typically related to the infrared excess over the photospheric level of its host star. The disk, shown in Figure 4.7, is clearly detected up to 1.5"($\sim$ 110 AU) from the star with inclination $i \sim 83°$ and in the north-west side reveals a fainter asymmetric structure at wider separation. The stellar orbit results to be nearly coplanar with the disk, being close to edge-on. Since stellar IR excess is not present, the disk is cold and this also suggests the presence of a central cavity; as a debris disk, it should consist of sub-μ-sized grains coupled with large stellar mass loss rates. Upper limits for the presence of giant planets were set to be $< 2M_J$.

This disk, which is asymmetric and shows swept-back wings, in scattered light has the same extension ($r_0 = 73$ AU) of the AU Mic disk, the most extended debris disk known around M dwarves; the similarities between the two disks also lie in the detection of ripples in the disk spine and in the compatible detection of Hα and Hβ profiles, which indicate the probable absence of gas accretion.

Comparing these results (of the GSC 7396-0759 disk) with previous detection of the disk around AU Mic, thanks to SPHERE it has been possible to image these two disks

[14] V4046 Sgr disk is the only gas-rich disk in the β-Pic moving group ([38]).

[15] A debris disk is a circumstellar disk of dust and debris in orbit around a star. Debris disks have been found around both mature and young stars. Younger debris disks can constitute a phase in the formation of a planetary system following the protoplanetary disk phase, but they can also be produced and maintained as the remnants of collisions between planetesimals, namely asteroids and comets.

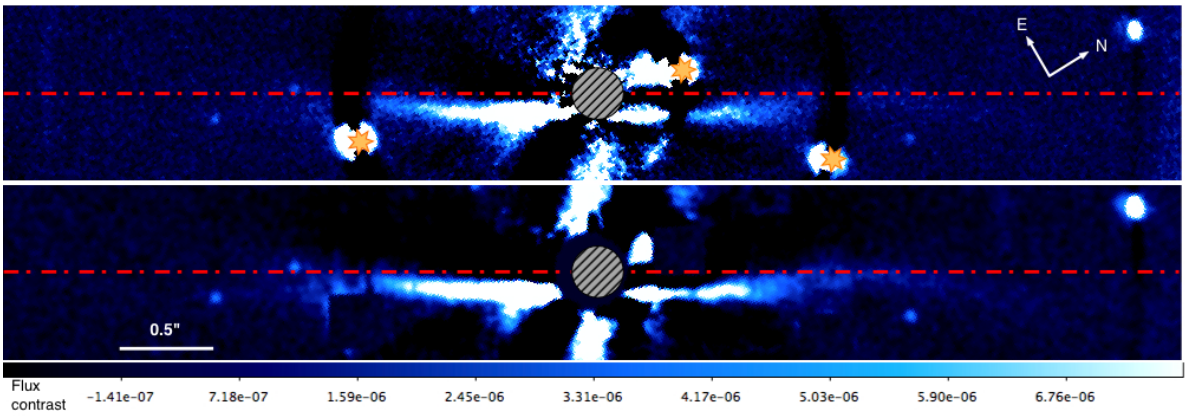

Figure 4.7: *The disk detected around GSC 7396-0759 taken from [39] (submitted), shown before (top) and after (bottom) the subtraction of the most contaminant stars, identified with star-like points in the upper Figure. The grey shadded region in the center corresponds to SPHERE coronagraph, while the dash-dotted line is parallel to the disk semi-major axis and crosses GSC 7396-0759. Behind the star-shaped region, a bright background object has been masked.*

around M stars by using its standard planet search imaging mode. This deals with expectation of easier detectability as regards nearly edge-on debris disk.

It is also likely that the fraction of M dwarves hosting debris disk should be large, with respect to their detectability expectation. In fact, the statistics of debris disk detected around low mass M-type stars (very cool objects) is very scarce, probably bacause of a lower frequency of disks or to the shift toward longer wavelengths of the disks emission, due to the fact that dust particles are less heated. In fact, the most suitable stars for debris disk detections have spectral types between A and K.

The importance of debris disks around young M stars is that they allow to explore the possible link between their occurrence and the presence of terrestrial planets (whose frequency around low-mass stars is elevated) in the system.

Chapter 5

The shadow in V4046 Sgr disk

It is clear, as shown in Figures 5.1 and 5.2, that there is a shadow[1] in the disk due to the position of the stars and to their projected light on the disk. SPHERE data (Figure 5.3) show that this shadow is truncated at a certain radius, and this implies that the disk is flared. The disk flaring occurs at least until the observed extension of the shadow, since for higher radii we do not detect scattered light: this means that our observed radius of the shadow (onward: r_S^{obs}) is a lower limit for its extension. In particular, the observed value of the radius results to be[2] $r_S^{obs} = r_S \cos i_d \approx 35$ AU, and then $r_S \approx 42$ AU.

Referring to Figure 5.1, we now introduce H, which is the height scale, namely the height at which a certain quantity is decreased by a factor e: in this case, the dust density. Using the parametric scale height profile defined in [38]

$$H(r) = H_0 \left(\frac{r}{r_0} \right)^{\Psi}, \tag{5.0.1}$$

where $r_0 = 10$ AU and $H_0 = 0,4$ AU[3], we obtain

$$\Psi = \frac{\ln \frac{H_S}{H_0}}{\ln \frac{r_S}{r_0}}, \tag{5.0.2}$$

considering $H(r_S) \equiv H_S$. We now need to know the value of H_S to obtain an estimate of the flaring index Ψ, which will be compared to the one used in [38], namely $\Psi^{literature} = 1,25$, altough this parameter is not well determined in transition disks ([40]).

However, the estimation of Ψ given by Equation 5.0.2 represents an upper limit to the disk flaring, because we do not observe dust emission outside r_S^{obs}, and then the disk flaring is described by a coefficient Ψ which must be higher than 1 but smaller than (or equal to) that of Equation 5.0.2.

[1] Actually, two shadows are present, but we refer only to the more evident one, since the other is much fainter and then less defined.

[2] This refers to Figure 4.2.

[3] The value of $H_0 = H(r_0)$ is the scale height that has been used to fit the excess spectrum in the mid infrared ([38]).

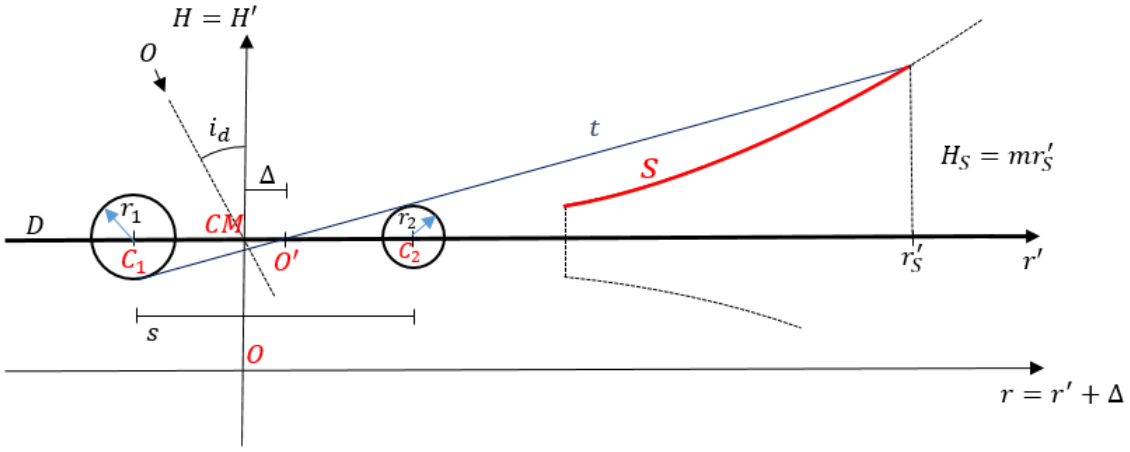

Figure 5.1: *View of the flared disk (not in scale) and the binary along the orbital plane, and reference systems used. S stands for the shadow of star 1 caused by star 2 and projected on the disk, whereas Δ is the axial difference between the two different reference systems r and r′, whose origins are the center of mass and the intersection of the straight line t with the horizontal axis, respectively.*

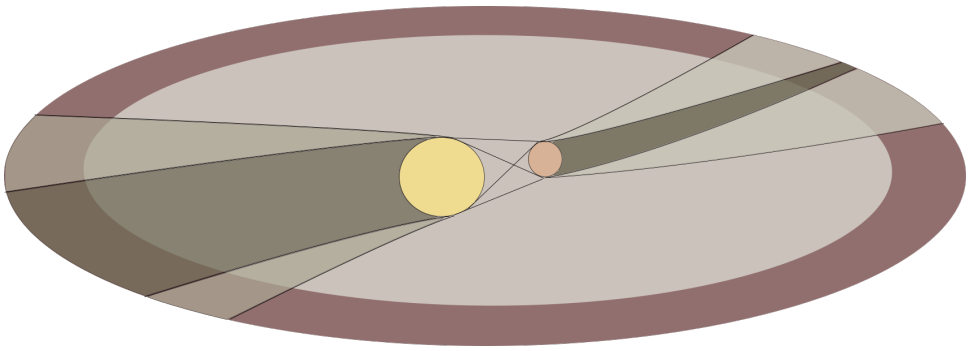

Figure 5.2: *Representation of the shadows originated by the eclipsing of each of the stars by the other, adapted from D'Orazi et al. (submitted), not in scale. Shadows are curved due to light-travel effects, since the disk is rotating with respect to the binary.*

5.1 Determination of the flaring index Ψ

The reference system we are using onward is $(x, y) \equiv (r', H)$, as illustrated in Figure 5.1, in which there is also shown the straight line t tangent to each of the stars (for star 1 the tangency point has coordinate $H < 0$, whereas for star 2 it has $H > 0$) and which intersects the disk in the point (r'_S, H_S). Above that straight line, one point on the surface of the disk has no shadow, whereas under it the shadow grows while reaching $H = 0$. A more representative image of the eclipsing of the stars composing the binary is depicted in Figure 5.2, where there are, clearly, two shadows, one of which is fainter than the other as a function of what configuration is the most eclipsed: since from the SPHERE images only one shadow is evident, we will consider that in our calculations.

The stars are viewed as two circumferences of radii r_1 and r_2 centered in $C_1 < 0$ and $C_2 > 0$, where 0 (O' point) refers to the center of mass of the binary (CM point) plus the quantity Δ and corresponds to the intersection of the straight line with the horizontal axis. We can thus write their equations:

$$\begin{cases} \mathscr{C}_1 : y^2 + (x - C_1)^2 = r_1^2 \\ \mathscr{C}_2 : y^2 + (x - C_2)^2 = r_2^2 \end{cases}$$

which must be tangent to the straight line described by the equation $t : y = mx$, being m the angular coefficient, namely imposing that the discriminant ($\Delta_{1,2}$) of the equation of each star (after replacing $y \to mx$) must be zero. Then we obtain, for star 1 (the case for star 2 is totally symmetrical)

$$(1 + m^2)x^2 - 2C_1x + (C_1^2 - r_1^2) = 0,$$
$$\Delta_1 = 0 \implies 4C_1^2 - 4(1 + m^2)(C_1^2 - r_1^2) = 0,$$

resulting

$$m = \frac{r_1}{\sqrt{C_1^2 - r_1^2}} = \frac{r_2}{\sqrt{C_2^2 - r_2^2}}.$$

Now, considered that $s = C_2 - C_1$ we replace $C_2 = C_1 + s$ in the latter equation to obtain

$$\frac{r_1}{\sqrt{C_1^2 - r_1^2}} = \frac{r_2}{\sqrt{(C_1 + s)^2 - r_2^2}}$$

and, being C_1 the variable, one finds

$$\left[1 - \left(\frac{r_2}{r_1}\right)^2\right] C_1^2 + 2sC_1 + s^2 = 0,$$

$$C_1 = \begin{cases} -s\frac{r_1}{r_1 - r_2} < -s \text{ because } r_1 > r_2 \implies \text{NOT acceptable.} \\ -s\frac{r_1}{r_1 + r_2} \end{cases}$$

It is now straightforward that $C_2 = s\frac{r_2}{r_1 + r_2}$. Replacing these quantities in the expression of the angular coefficient leads to

$$m = \frac{r_1 + r_2}{\sqrt{s^2 - (r_1 + r_2)^2}}.$$

Then we obtain the following equation of the scale height of the shadow:

$$H_S = \frac{r_1 + r_2}{\sqrt{s^2 - (r_1 + r_2)^2}}(r_S - \Delta) \approx 0,269 \cdot (r_S - \Delta). \tag{5.1.1}$$

Let us now consider the influence of Δ by giving an estimation of it:

$$\Delta = \left| C_1^{CM} - C_1 \right|,$$

where C_1^{CM} is the center of star 1 in the center of mass reference system (namely (r, H) of Figure 5.1), so it is given by

$$\begin{cases} C_2^{CM} - C_1^{CM} = s \\ C_1^{CM} m_1 + C_2^{CM} m_2 = 0 \end{cases} \implies C_1^{CM} = -s\frac{m_2}{m_1 + m_2}.$$

It follows that

$$\Delta = \left| s\frac{m_2}{m_1 + m_2} - s\frac{r_1}{r_1 + r_2} \right| \approx 0,286 \cdot R_\odot.$$

If replaced in Equation 5.1.1 it is clear that Δ is negligible with respect to r_S because $R_\odot = 6,96 \cdot 10^8$ m $\ll 1$ AU $= 1,496 \cdot 10^{11}$ m. Thus we have obtained the final expression

$$H_S \approx 0,269 \cdot r_S = 11,3 \text{ AU}.$$

It is finally possible to use this value to obtain the maximum flaring index (Equation 5.0.2) having

$$\Psi = 2,66 \tag{5.1.2}$$

which - as previously stated - is an upper limit[4]. In addition, in Section 1.13 we noticed that, within the gravitational radius, the atmospheric scale height is $h \propto r^{3/2}$ and then the upper limit to the flaring index suggested by that analysis led to the value of $1,5$.

5.2 Analysis of the shadow

It is now interesting to focus on the peculiarity of the binary system V4046 Sgr: it is a close binary with a very small separation between the two stars which is, as previously introduced, $s \sim 9R_\odot$ (Section 4.1); the main question about this system is then about how the two stars could have become so close during their evolution, considering their relatively young age (~ 20 Myr). Moreover, it is clear that being so close, at a separation of the same order of magnitude of the stellar radii, implies a certain (not negligible) eclipsing of one star by the other one along the radial direction: this generates a relevant shadow on the disk, visible on the SPHERE images in Figure 5.3.

5.2.1 Interpretation of the disk darkening

At this point we are going to find the percentage of the eclipsing of the binary on the disk at a certain angle. The geometry we are using is described by Figure 5.5,

[4]In fact, the value reported in literature is smaller than this.

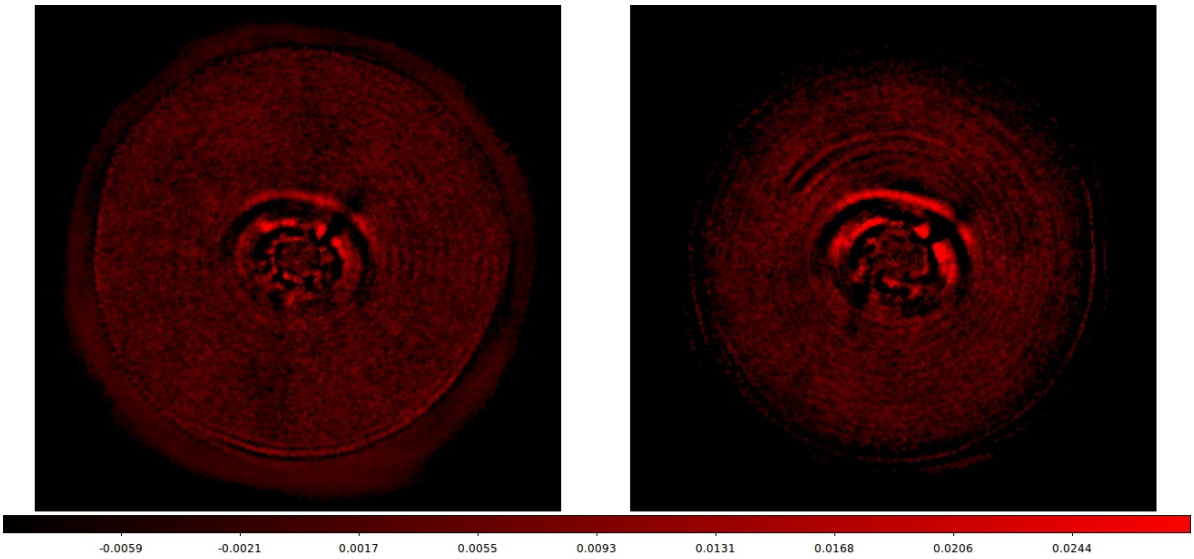

Figure 5.3: *These SPHERE images, taken from D'Orazi et al. (submitted), show the circumbinary (1 μm) dust disk of the binary system V4046 Sgr in two different observational periods: 2015 (on the left, with YJ set up) and 2017 (on the right, with YJH set up). It is also evident the rotation of the shadow.*

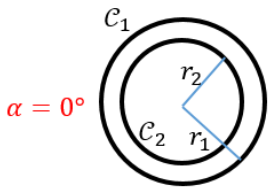

Figure 5.4: *Illustration of the eclipsing of star 1 by star 2 for* $\alpha = 0°$.

where $\alpha_{MAX} = \arctan \frac{H_S}{r_S} = 15,1°$ is the maximum angle at which there is the shadow (corresponding to the straight line t of Figure 5.1) and α is the angle that the straight line $\hat{k}$, tangent to star 2 and intersecting the disk in the point P, forms with the plane of the disk. Furthermore, $A(\alpha)$ is the surface of star 1 covered by star 2 from the point of view of an observer in P along $\hat{k}$.

Since the distance of the disk from the binary is much higher than the dimension of the stars, we assume that the light rays emitted by the stars are parallel. So, if $\alpha = 0$ there is the eclipsing of a portion of star 1 that is equal to star 2 (Figure **??**), namely the percentage of the eclipsed surface of star 1, of total surface A_1, is

$$\frac{A(0°)}{A_1} = \frac{\pi r_2^2}{\pi r_1^2} = 87\%.$$

As regards the luminosity of the stars $L(\alpha)$ at a certain angle along the direction of $\hat{k}$, we must consider the difference in temperature of the two stars, because $L_i \propto r_i^2 T_i^4$ (Stefan-Boltzmann's law), where T_i refers to the effective temperatures of the stars $T_{eff,i}$. As a consequence

$$\frac{L(0°)}{L_{TOT}} = \frac{(1-0,87) r_1^2 T_1^4 + r_2^2 T_2^4}{r_1^2 T_1^4 + r_2^2 T_2^4} = 47\%$$

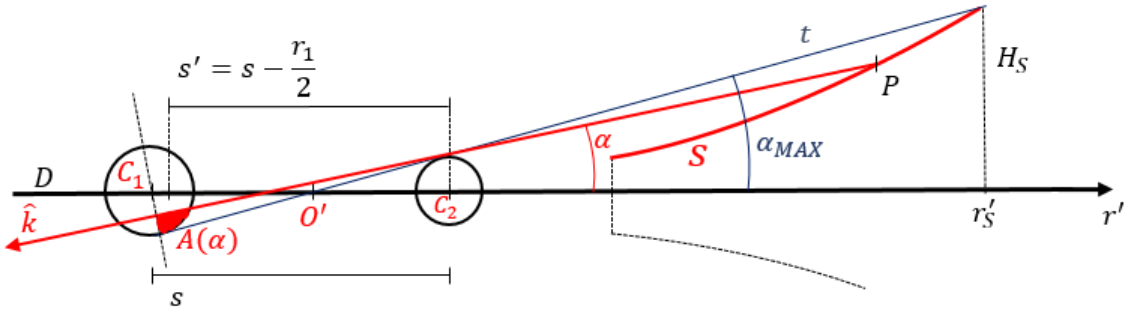

Figure 5.5: *Geometry of the system studied for the analysis of the shadow. An observer on the disk's surface in P, watching along the straight line $\hat{k}$ that is tangent to star 2 and forms an angle α with the disk's plane, sees an eclipsed area $A(\alpha)$ of star 1 due to the presence of star 2.*

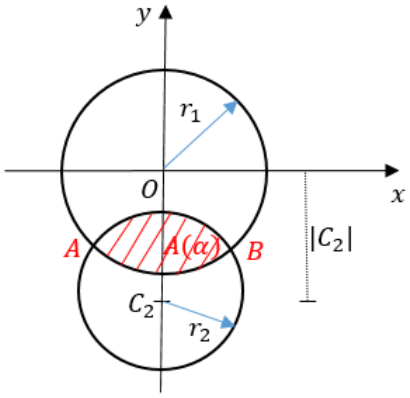

Figure 5.6: *The new coordinates used (x,y), which refer to a plane perpendicular to $\hat{k}$ along which the point P on the disk watches. C_2 is the center, along y, of star 2, whereas the origin is the center of star 1.*

and it means that one point along the plane of the disk in the direction of r' sees the luminosity of the stars that is about a half of their total luminosity. Clearly, for $\alpha > \alpha_{MAX}$, $L(\alpha) \equiv L_{TOT}$.

Instead, for an angle $0 < \alpha < \alpha_{MAX}$, we want to study what the point P on the disk sees along $\hat{k}$, building then a new (x, y) reference system that will be used onward, shown in Figure 5.6.

The first assumption is to consider[5] $\alpha \equiv \arctan \frac{|C_2|}{s'}$, which works for $\alpha = 0$ because in that case $|C_2| = 0$[6], and is expected to be a good approximation also for other values of the angle, because $|C_2|$ increases - while increasing α - until reaching the zero-eclipsing condition for $|C_2| = r_1 + r_2$, in correspondence of $\alpha = 15,4° \approx \alpha_{MAX} = 15,1°$[7], as can be inferred from Figure 5.6.

[5] s' will be soon introduced.

[6] $|C_2|$, of Figure 5.6, is now the separation, along y, of the center of star 2 with respect to the origin, which is the center of star 1.

[7] The agreement between these two independent estimations of the zero-eclipsing condition supports the validity of our approximation.

Another assumption regards $s' \equiv s - r_1/2$ (represented in Figure 5.5), which is the new approximated separation of the stars used to calculate the horizontal distance between the intersection of the $\hat{k}$ straight line with $\mathscr{C}_2$ and the midpoint (along the r' direction) of $A(\alpha)$: this area is now considered to be a plane surface (so we neglect both its curvature and radial extension) perpendicular to $\hat{k}$ and located at $r_1/2$ from the center of star 1 in the (r', H) reference system towards increasing r' (Figure 5.5). It follows that

$$C_2(\alpha) = -\left(s - \frac{r_1}{2}\right)\tan\alpha. \tag{5.2.1}$$

The equations of the visible boundaries of the two stars are the following, in the (x, y) reference system:

$$\begin{cases} \mathscr{C}_1 : y^2 + x^2 = r_1^2 \implies y_1^{\pm}(x) = \pm\sqrt{r_1^2 - x^2} \\ \mathscr{C}_2 : (y - C_2)^2 + x^2 = r_2^2 \implies y_2^{\pm}(x) = \pm\sqrt{r_2^2 - x^2} + C_2 \end{cases}$$

which have their intersection (namely when $\mathscr{C}_1 = \mathscr{C}_2$) in the two points $A \equiv (x_A, y_A)$ and $B \equiv (x_B, y_B)$, where

$$y_A(C_2) = y_B(C_2) = \frac{r_1^2 - r_2^2 + C_2^2}{2C_2},$$

$$x_A(C_2) = -x_B(C_2) = -\sqrt{r_2^2 - \left(\frac{r_1^2 - r_2^2 - C_2^2}{2C_2}\right)^2}.$$

Then the area $A(\alpha)$ enclosed between the two circumferences is

$$A(\alpha) = \left|\int_{x_A}^{x_B} (y_1^-(x) - y_2^+(x))dx\right| = \left|\int_{x_A}^{x_B} \left(C_2 + \sqrt{r_2^2 - x^2} - \sqrt{r_1^2 - x^2}\right)dx\right|$$

and, since $\int \sqrt{k - x^2}dx = \frac{1}{2}\left(x\sqrt{k - x^2} + k\arctan\frac{x}{\sqrt{k-x^2}}\right) + \text{const}$ and $\arctan x$ is an odd function of x, we obtain

$$\begin{aligned} A(\alpha) = \Bigg| & C_2(x_B - x_A) + \frac{1}{2}\left[x\sqrt{r_2^2 - x^2} + r_2^2\arctan\frac{x}{(r_2^2 - x^2)^{1/2}}\right]_{x_A}^{x_B} - \\ & - \frac{1}{2}\left[x\sqrt{r_1^2 - x^2} + r_1^2\arctan\frac{x}{(r_1^2 - x^2)^{1/2}}\right]_{x_A}^{x_B}\Bigg| = \\ & = \Bigg|2C_2x_B + x_B\left(\sqrt{r_2^2 - x_B^2} - \sqrt{r_1^2 - x_B^2}\right) + \\ & \quad + r_2^2\arctan\frac{x_B}{(r_2^2 - x_B^2)^{1/2}} - r_1^2\arctan\frac{x_B}{(r_1^2 - x_B^2)^{1/2}}\Bigg|. \end{aligned} \tag{5.2.2}$$

The dependence of α in Equation 5.2.2 is obviously included in $C_2(\alpha)$ and in $x_B(C_2) \equiv x_B(\alpha)$.

5.2.2 Determination of the shadow angle α_S

SPHERE cannot distinguish between the 100% of the total luminosity of the binary and a low darkening of the total luminosity on the disk surface. In order to account for such a limitation, we provide here a calculation which leads to the value of the angle α_S - under which the shadow is seen to extend radially with a radius $r_S(\alpha_S)$ - corresponding to a darkening of 10% of the total luminosity, on the disk surface. In other words, we assume that the minimum darkening on the disk (namely, the maximum luminosity on the disk), with respect to the total luminosity, that can be revealed occurs when

$$\frac{L(\alpha_S)}{L_{TOT}} \simeq 90\%.$$

We must precise that the latter value is a lower limit to the SNR that SPHERE can achieve, since it is certainly higher than 90%: thus, our case represents an example.

Once found the angle of the shadow α_S, it should be inserted in the equation of the radius of the shadow given by[8]

$$H_S = r_S \tan\alpha_S = H_0 \left(\frac{r_S}{r_0}\right)^{\Psi} \implies r_S(\alpha_S) = \left(\frac{r_0^{\Psi} \tan\alpha_S}{H_0}\right)^{\frac{1}{\Psi-1}}, \tag{5.2.3}$$

which could then be compared to the observed value of the radius r_S. To be precise, as regards this comparison one could notice that the estimation of $r_S(\alpha_S)$, which is calculated under the condition of being at 90% of the total luminosity, takes into account the value of Ψ obtained by assuming a luminosity on the disk of 100% and then it seems to be uncompatible with the case of darkening: however, this is not totally uncorrect, because the presence of the gap in the disk implies that the dust density decreases very quickly, and so it is possible to approximate the 90% of the total luminosity with the total one.

Consequently, if we consider a certain angle, for instance $\alpha = 14,8°$, we have to calculate the percentage of the corresponding darkened surface in order to determine the luminosity on the disk at that considered angle. It results that

$$C_2(14,8°) \simeq -2,22R_\odot, \quad x_B(14,8°) \simeq 0,338R_\odot \implies A(14,8°) \simeq 1,55R_\odot^2.$$

The last calculation is simple if we consider that the maximum visible surface of star 1 is the half of its total surface, so

$$\frac{A(14,8°)}{2\pi r_1^2} \simeq 17\% \implies \frac{L(14,8°)}{L_{TOT}} \simeq \frac{(1-0,17)r_1^2T_1^4 + r_2^2T_2^4}{r_1^2T_1^4 + r_2^2T_2^4} \simeq 90\% \tag{5.2.4}$$

and it means that

$$\alpha_S \simeq 14,8°.$$

[8]We assume, in Equation 5.2.3, that $H(r) = r\tan\alpha$ because the separation of the stars is very small if compared to the values of $r \sim$ AU.

5.2.3 Determination of the shadow radius $r_S(\alpha_S)$

It follows that, according to Equation 5.2.3 and using the value of Ψ obtained in Section 5.1,

$$r_S(\alpha_S) \simeq 31 \text{ AU},$$

which is the same order of magnitude of $r_S \simeq 42$ AU. The probable causes of the difference between these two values are imputable to the fact that r_S is not well determined, and in second place also the approximation we made to compute $A(\alpha)$ plays a minor role. Nevertheless, the agreement between r_S and $r_S(\alpha_S)$ is satisfactory, because one should remember that $r_S(\alpha_S) = 31$ AU is a lower limit since the value of Ψ adopted for its estimation represents the upper limit to the flaring index.

Another case to be considered is the one in which the two stars have the same temperature: in fact, we know that they are similar as regards dimensions and temperature, and it is then interesting to see what happens if we consider that each star has the average temperature of the binary system

$$T = \frac{T_1 + T_2}{2} = 4205 \text{ K}.$$

What results is, as one could expect, not so different from what obtained previously, namely the new luminosities become the following:

$$\frac{L(0^\circ)}{L_{TOT}} \simeq 53\%, \qquad \frac{L(14,8^\circ)}{L_{TOT}} \simeq 91\%$$

instead of 47% and 90% respectively, and then we can state that the separation, with respect to the case of different temperatures, is negligible being the difference of the order of percent.

To conclude, we would like to point out that if we exchanged the position of the two stars, meaning $1, 2 \mapsto 2, 1$ respectively, we would have a darkening of $\sim 10\%$ on the disk for a value of α that is certainly smaller than α_S previously calculated: in fact, since star 1 (which is bigger and hotter than star 2) is closer to the disk in this case, one has to reduce the angle α to obtain the same darkening, because it is necessary to reduce the contribution of star 2. Consequently, a lower α_S means a lower value of $r_S(\alpha)$ which would be more distant from r_S. This suggests that the original order of the stars should be the correct one: in fact, it has been recently confirmed.

5.3 Limb darkening

As regards the temperature distribution in the stellar photosphere, one should consider the effect of the limb darkening: it exists because the continuum source function[9] decreases outward, so when looking toward the limb, we see systematically higher photospheric layers that are less bright ([41]).

Linear limb darkening provides a simple law for the intensity at a certain angle of observation θ, as shown in Figures 5.7 and 5.8.

[9]The source function is a characteristic of a stellar atmosphere and, in the case of no scattering of photons, it describes the ratio of the emission coefficient to the absorption coefficient. It is a measure of how photons in a light beam are removed and replaced by new photons by the material through which it passes.

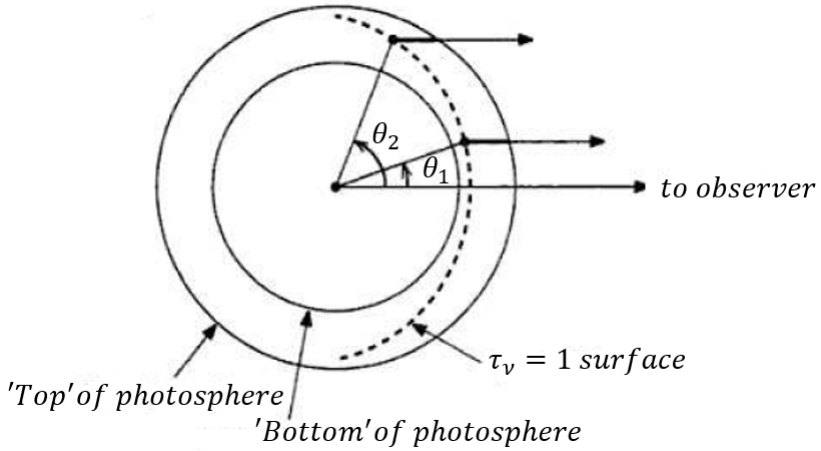

Figure 5.7: *Geometry of limb darkening ([41]).*

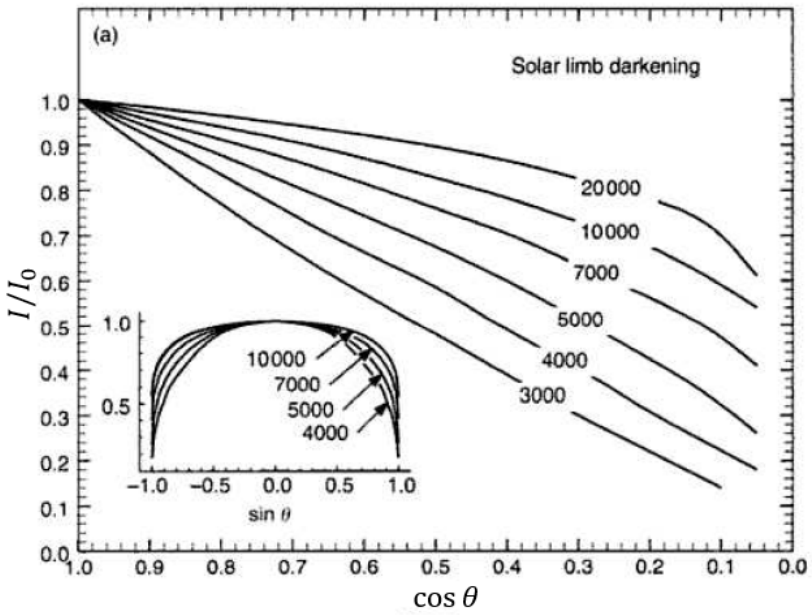

Figure 5.8: *Effect of limb darkening on the intensity, in the case of the Sun (taken from [41]).*

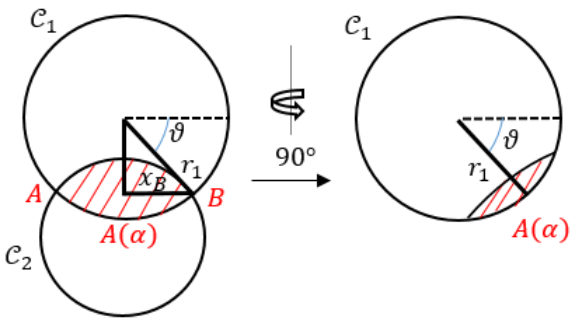

Figure 5.9: *The approximation used to calculate* $I_c(\theta)$.

$$I_c = I_c^0(1 - \epsilon + \epsilon \cos\theta), \tag{5.3.1}$$

where I_c^0 is the continuum intensity at the center of the disk and ϵ is the limb darkening coefficient, which varies with the color index of the star and with the wavelength.

In this case, a qualitative consideration suggests that limb darkening should not be relevant for the shadow in V4046 Sgr. In fact, as seen in the previous Section 5.2, the darkening of star 1 at the angle α_S is about 17% of its total visible area, so it is a small region; furthermore, the darkened part of the star is near its external region: if limb darkening would be relevant, the angle at which the luminosity on the disk is the 90% of the total would be certainly smaller that $\alpha_S = 14,8°$, because the covered area of the star should be bigger in order to darken the contribution of brighter parts of the star[10]. Consequently, the value of $r_S(\alpha_S)$ would become smaller than 31 AU and then more distant from the observed one.

Anyway, one could give an estimation of the limb darkening effect, knowing the behaviour of the limb darkening coefficients in function of $B-V$[11] at a given wavelength λ.

In V4046 Sgr's case, we can adopt the Solar value of $\epsilon \approx 0,40$. The last parameter to determine, in order to calculate the intensity, is the angle θ: the approximation we act here is to consider a unique angle corresponding to the average height of the darkened area of star 1 (being this a small region) and it is displayed in Figure 5.9; as shown before, $x_B(14,8°) \simeq 0,338 R_\odot$, where x_B refers to Figure 5.6; it is then clear that we could take θ as the angle at which

$$\sin\left(\frac{\pi}{2} - \theta\right) = \frac{x_B}{r_1} \implies \theta = \arccos\left(\frac{x_B}{r_1}\right) = 74°.$$

Thus, the intensity results to be (Equation 5.3.1)

$$I_c = I_c^0(1 - 0,40 + 0,40\cos 74°) \approx 0,71 \cdot I_c^0.$$

This means that the darkened area makes an average contribution to the intensity

[10]In fact, once fixed the 90% detectable luminosity, in the case of relevant limb darkening the most external parts of the star contribute less to the star's luminosity and it is then necessary to darken a more central region of the star in order to obtain the same darkening as in the absence of limb darkening.

[11]It is the difference between the stellar magnitude in the B and V bands.

of the 71% of the continuum intensity at the center of the disk[12]: we now have to find the value of the new angle of the shadow α'_S at which we still have

$$\frac{L(\alpha'_S)}{L_{TOT}} = 90\%.$$

The first consideration regards the intensity on the disk, because we have to determine the new darkened area of star 1 at which there is the same darkening of the no-limb darkening case (which is 17%), namely making the following proportion:

$$0,17 \cdot I_c^0 = \frac{x(\%)}{100} \cdot 0,71 \cdot I_c^0 \implies x = 24\%.$$

We have assumed that the percentage $x(\%)$ of the area of star 1 emits an intensity of $0,71 \cdot I_c^0$, whereas the rest of the star has an intensity of $y = 1,09 \cdot I_c^0$, in order to preserve the total intensity emitted in the absence of limb darkening, I_c^0:

$$\frac{x(\%)}{100} \cdot 0,71 \cdot I_c^0 + y \cdot \left(1 - \frac{x(\%)}{100}\right) \cdot I_c^0 = I_c^0.$$

Given $x(\%)$, it is immediate to obtain the angle α'_S and the corresponding new radius of the shadow $r'_S(\alpha'_S)$ by using Equations 5.2.2 and 5.2.3. It results

$$\alpha'_S = 14,0^\circ \implies r'_S = 30,0 \text{ AU}.$$

As a final check, using the expression of Equation 5.2.4 for this case, one has:

$$\frac{L(\alpha'_S)}{L_{TOT}} \simeq \frac{(1-0,24) \cdot 1,09 \cdot r_1^2 T_1^4 + r_2^2 T_2^4}{r_1^2 T_1^4 + r_2^2 T_2^4} \simeq 90\%.$$

This guarantees a luminosity at the angle α'_S which is equal to the wanted value (90% of the total), too.

We can then confirm that the effect of limb darkening is not relevant within the uncertainty, as we guessed by a qualitative study, because it gives a value of the radius of the shadow which is nearly the same (but smaller) of the one obtained without considering it, namely $r'_S = 30$ AU (compared to $r_S = 31$ AU).

To conclude, one should consider that the estimation of the observed radius of the shadow $r_S \approx 42$ AU is uncertain, because the point at which the shadow disappears is not clearly visible due to the fact that it vanishes very slowly. Then, the difference between this value and the calculated one (namely $r_S(\alpha_S) = 31$ AU) is expected to be comparable with the uncertainties intrinsic in these two values. However, being $r_S(\alpha_S)$ a lower limit to the radial extension of the shadow, we confirm its compatibility with the observed minimum value of the shadow, r_S.

[12]Considered our approximation, this represents an upper limit to the suppressed luminosity ($\sim 29\%$ of I_c^0) due to limb darkening.

Chapter 6

Numerical simulations

6.1 Stokes Number

In this Section we want to calculate the influence of the dust on the gas of the disk surrounding V4046 Sgr: this is possible by considering the Stokes number

$$S_t \equiv t_S \Omega, \qquad t_S \equiv \frac{\delta}{\rho} \frac{s}{v_{therm}}$$

where these quantities are identified as below:

- t_S is the stopping time;
- Ω is the angular velocity;
- s is the dust size ($\sim 1 \div 5$ μm diameter);
- δ is the particle density;
- ρ is the gas volumetric density;
- $v_{therm} = \sqrt{\frac{8 k_B T}{\pi \mu m}}$ is the thermal velocity, being $\mu = 2,37$ ([38]) the mean molecular weight, k_B the Boltzmann's constant and m the mass of the gas particles.

Considering to be at $z = 0$, namely along the plane of the disk, then the following laws are used, according to [38] and [36]:

$$\begin{cases} T_{gas}(r) = T_{dust}(r) = T_{a,0} \left(\frac{r}{r_0} \right)^{-q} \\ T_{a,0} = (115 \pm 5) \text{ K}, \quad r_0 = 10 \text{ AU}, \quad q = 0,63 \pm 0,01 \end{cases}$$

in fact at the midplane the gas and dust are assumed to be thermally coupled. Moreover

$$\begin{cases} \rho(r) = \frac{\Sigma}{\sqrt{2\pi} H_p} \\ H_p = \frac{c_S}{\Omega}, \qquad c_S = \frac{k_B T}{\mu m_H} \end{cases}$$

where Σ is the radial surface density profile, H_p the pressure scale height, c_S the sound speed and m_H the mass of the hydrogen atom. Finally, assuming that $\Sigma_{gas}(r) = \Sigma_{dust}(r)/\zeta(r)$

$$\begin{cases} \delta(r) = \delta_{atm}(r) + \delta_{mid}(r) = (1+\chi)\frac{\Sigma\zeta(r)}{\sqrt{2\pi}H(r)} \\ H(r) = H_0\left(\frac{r}{r_0}\right)^{\Psi}, \quad r_0 = 10 \text{ AU}, \quad H_0 = 0,4 \text{ AU}, \quad \chi = 1/2 \end{cases}$$

in which $\zeta(r)$ is the vertically integrated dust-to-gas mass ratio and it is assumed to be constant outside of the cavity ($\zeta = 0,01$), $H(r)$ is the scale height previously introduced and χ is a scaling factor which appears in the parametric scale height profiles referring to two different dust populations: a *midplane* population that dominates the disk mass and is composed of larger grains that are vertically settled, and a less-abundant *atmosphere* population with smaller grains distributed to larger heights from the midplane, so it is possible to write

$$\begin{cases} H(r) = H_{atm}(r) + H_{mid}(r) \\ H_{atm}(r) = H_0\left(\frac{r}{r_0}\right)^{\Psi}, \quad H_{mid}(r) = \chi H_{atm}(r) \end{cases}$$

We are now able to calculate the Stokes number: after replacing each parameter with its expession we obtain

$$S_t = \underbrace{\frac{(1+\chi)s}{H_0}\sqrt{\frac{T_{a,0}\pi k_B m}{8\mu m_H^2}}}_{\equiv K}\zeta(r)\left(\frac{r}{r_0}\right)^{-\left(\Psi+\frac{q}{2}\right)} \tag{6.1.1}$$

If we consider $m = m_H$, then $K \approx 10^{-14}$; furthermore $\Psi + \frac{q}{2} < 3$ and $\frac{r}{r_0} \sim 10 \div 10^2$, consequently the Stokes number results to be $S_t \sim 10^{-20} \ll 1$ even though we consider the cavity, in which we do not exactly know ζ but it should be enormous to make $S_t \sim 1$: we can then assess that dust and gas are decoupled in this disk.

6.2 The N-body program

The purpose is to model V4046 Sgr disk using an N-body code which provides the features of the disk constituents after an evolutionary time compatible to the binary age ($\sim 10 \div 15$ Myr). The program considers the evolution of the orbits of either dust particles or planetesimals, depending on what evolutionary phase we are interested to. Dust particles and planetesimals possess a volume but are massless (they do not perturb the planet(s)). We used a number of particles ($N = 4000$) that allowed us to obtain the results within our timetables, but that is high enough to provide a representative scenario of the dust/planetesimals evolution.

6.2.1 Approximations used

Since in Section 6.1 we proved that dust and gas are decoupled in V4046 Sgr disk, it is possible to use a code involving only dust without the presence of gas: in this way, besides providing simpler calculations, this guarantees much more rapid simulations.

Another approximation used in this code is the assumption of the binary as a single star of total mass $m_1 + m_2$: this is appropriate, because the distance from the CM[1] at which we study the interactions among the dust, the planet(s) and the binary ($\sim$ AU)

[1] Center of Mass.

are much bigger than the separation of the binary itself ($\sim 9R_\odot$), thus it is possible to consider the dynamical effect of the two stars as that of a single star of mass equal to the sum of the two components masses. This allows large gain in computing time, as there is no need to follow the very rapid orbital motion of the binary.

6.2.2 Description of the N-body program

As anticipated, the program considers a unique star which replaces the very close binary; as a consequence it has the same mass of the two stars forming V4046 Sgr[2]; then, it considers the presence of one planet (or more) with planetesimals and, subsequently, the dust particles.

One then has to insert the number of the bodies wanted[3] N, the minimum and the maximum semi-major axis of the disk a, as reported in the following table, in which IR and OR stand for the *inner region* and *outer region* of the disk, respectively.

Input parameters	
$M_\star$ $(M_\odot)$	$1,75$
N	4000
a_{min}^{IR} (AU)	3
a_{max}^{IR} (AU)	13
a_{min}^{OR} (AU)	30
a_{max}^{OR} (AU)	50

In order to justify our approach, in which we considered two separated simulations for each region and considered each region to evolve independently of the other, we briefly discuss about the zone in the disk cleared by a planet around itself. In fact, as reported in [42], a planet sweeps an entire zone around its orbit which is proportional to its semi-major axis a_p and to a certain power law of the ratio μ between its mass and the mass of the star: the half width of the chaotic zone surrounding the planet results to be

$$\Delta a = 1,3\mu^{2/7} a_p.$$

Differently from the chaotic zone, the clearing zone is a more restricted area around the planet's orbit in which dust particles result unstable and from which are quickly expelled. The clearing zones interior and exterior to the planet's orbit are finally

$$(\Delta a)_{in} = 1,2\mu^{0,28} a_p, \qquad (\Delta a)_{ext} = 1,7\mu^{0,31} a_p. \tag{6.2.1}$$

SPHERE data suggest that there is a gap between ~ 13 AU and ~ 30 AU, then its extension is fixed and what we have to impose, in order to account for this clearing zone, are the mass and the semi-major axis of the planet.

At this point, a first program generates an input file containing the star mass and the orbital elements of the planet(s) and of the planetesimals (being the first evolutionary phase), in a random way with low values of eccentricities ($< 0,01$) and inclinations ($< 0,5$): these are the initial conditions.

[2]The third companion introduced in Section 4.5 will not be considered, being well outside the circumbinary disk we want to model (separation > 10000 AU). Its dynamical influence is then negligible.

[3]It contains the central star, the planet(s) and the dust particles.

Then, the N-body program uses the latter input file to create an output file in which there are the coordinates (x, y, z) and the orbital elements of the planetesimals/dust particles[4] at a certain evolutionary moment.

The code numerically integrates the input N bodies in heliocentric coordinates using the *Everhart subroutine RA15* [43], taking into account the following interactions:

- Keplerian force, which allows the planet(s) and the planetesimals/dust particles to orbit the binary because of the gravitational interaction;
- radiation pressure[5] originated by the binary on the planetesimals/dust particles;
- Poynting-Robertson drag force[6], which slows the dust particles;
- mutual direct and indirect[7] perturbations, due to the gravitational interactions as a consequence of the presence of the planet(s), the stars and the planetesimals/dust particles.

6.3 Simulations

Our simulations involve the primordial evolution of planetesimals, providing the initial conditions for the subsequent evolution of dust. They have been performed in the cases in which we consider the presence of *one* massive planet and *two* low-mass planets.

6.3.1 One massive planet simulations

Planetesimals evolution

We simulate the planetesimals evolution[8] (~ 4000 planetesimals) in presence of a massive ($10 M_J$) planet, inclined $5°$ with respect to the reference plane and located at 20 AU from the binary.

The expectations are to obtain a flared profile, with resonances in inclination at semi-major axes a of about ~ 13 AU and ~ 30 AU (corresponding to the observed inner and outer rings), showing maximum inclinations of $(6, 2 \pm 0, 6)°$ and $\sim 13, 9°$, respectively[9]. Figure 6.1 represents the initial spatial (3D) distribution of planetesimals.

What results, after an evolutionary phase of ~ 10 Myr (at this age, planetesimals are certainly in a stable condition), is the following situation, which is divided into the two reference regions in the disk (containing the inner and outer rings[10]):

[4]The output file regards planetesimals firstly, whereas their evolution will represent the initial condition for the evolution of dust, which will provide an output file regarding dust particles, clearly. Their different evolutionary phases will be better described in Section 6.3.

[5]Its description is reported in Appendix A.2.1.

[6]Its description is reported in Appendix A.2.2.

[7]Due to the adopted reference system, if it is not inertial.

[8]In this case we clearly do not consider the Poynting-Robertson drag force.

[9]The first of these values is provided by observations, whereas the second has been obtained by evaluating the scale height via Equation 5.0.1, using the value of Ψ obtained in Equation 5.1.2 as an upper limit. For the inner ring we do not consider as a reference value the scale height, obtained by Equation 5.0.1, since it would represent an extrapolation in a region which is too distant from the point around which the scale is valid (the radius of the shadow) to be considered reliable; moreover, the provided value is highly accurate, deriving from the geometric measurement of the shadow's depth.

[10]They are compatible with the boundaries of the clearing zone calculated from Equations 6.2.1, which provide $(\Delta a)_{in} \approx 6$ AU and $(\Delta a)_{ext} \approx 7$ AU.

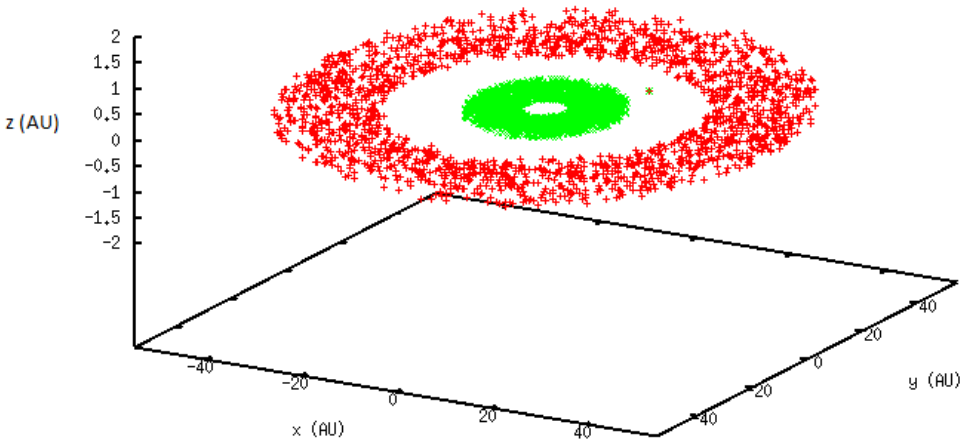

Figure 6.1: *3D plot for the planetesimals distribution in the inner (green dots) and outer (red dots) regions, in presence of one massive planet, at time $t = 0$ yr. The isolated point between the two rings is the planet.*

- *outer region*: in the region from ~ 30 AU and for more external radii we observe, in Figure 6.2, that the profile of the disk remains flat in inclination, only enhancing its inclination from an initial angle of $\sim 0,5°$ to a final value of $\sim 10°$ (no clear resonances can be distinguished);

- *inner region*: in the region before 15 AU we still observe a flat profile of the planetesimals inclination (as shown in Figure 6.3), namely the inclination is constant at $\sim 10°$, with some planetesimals presenting higher values in correspondence of certain semi-major axes - however, their scarce presence cannot make their distributions considered as resonances.

In Figure 6.4 we report the 3D plot of the outer region of the disk after the evolutionary phase; the inner region shows the same qualitative spatial distribution, but at smaller semi-major axis (we do not show it in the same 3D plot of the inner region because it would be impossibe to distinguish the spatial positions of its points). Moreover, in Figure 6.5 we report the 2D distribution of both the inner and the outer region after the evolutionary phase, in the (x, y) plane. As regards the disk's height profile we could consider the fact that, from Figures 6.2 and 6.3, it is clear that planetesimals exhibit the same maximum inclinations in the two different regions, and this means that the disk's profile in height grows proportionally with the semi-major axis (it could be interpreted as a flared disk with flaring index $\Psi = 1$).

The picture emerging from the planetesimals evolution is not in agreement with the expectation of a flared disk, neither in the inner nor in the outer region; moreover, no clear resonance has been identified. However, it is the preliminary stage for the disk's evolution, meaning that the subsequent evolutionary phase, consisted of dust, could lead to different results, in particular because dust, generally, is more excited than planetesimals and tends to move inward.

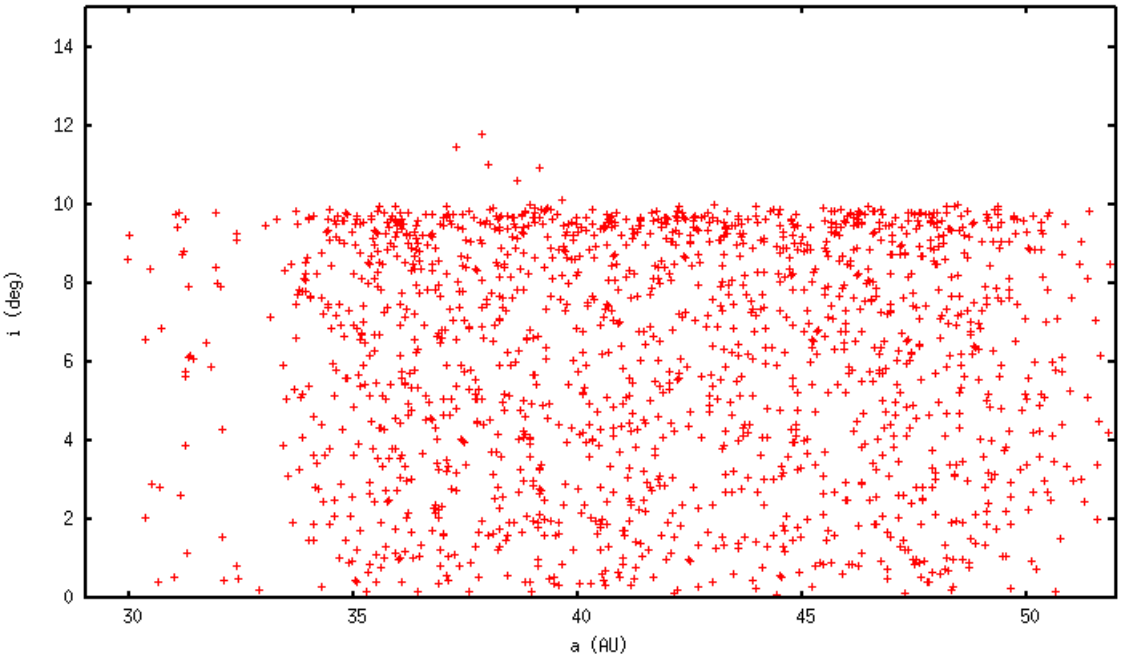

Figure 6.2: *The Figure represents the planetesimals evolution, in the outer region, in presence of one massive planet, plotting the planetesimals inclination as a function of their semi-major axes. It is clear that a flat profile in inclination is present, with the planetesimals which are distributed with inclination concentrated especially around* $\sim 10°$*, whereas the others are below this value.*

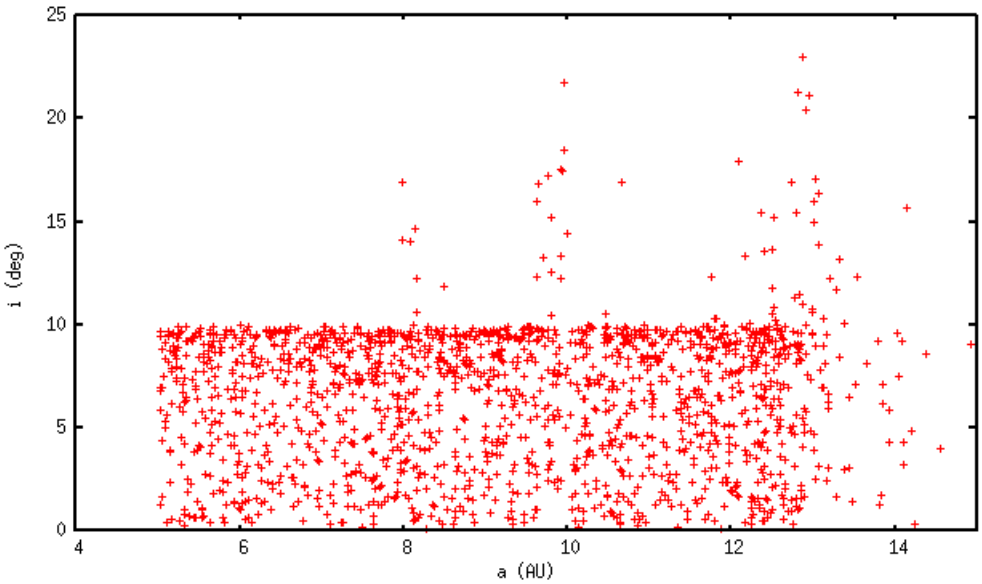

Figure 6.3: *The Figure represents the planetesimals evolution, in the inner region, in presence of one massive planet, plotting the planetesimals inclination as a function of their semi-major axes. A flat profile in inclination is evident, with the planetesimals which are inclined especially around* $\sim 10°$ *or less; however, some of them show higher inclinations at certain locations as a consequence of scattering, but they are not enough in number to allow those distributions to be interpreted as resonances.*

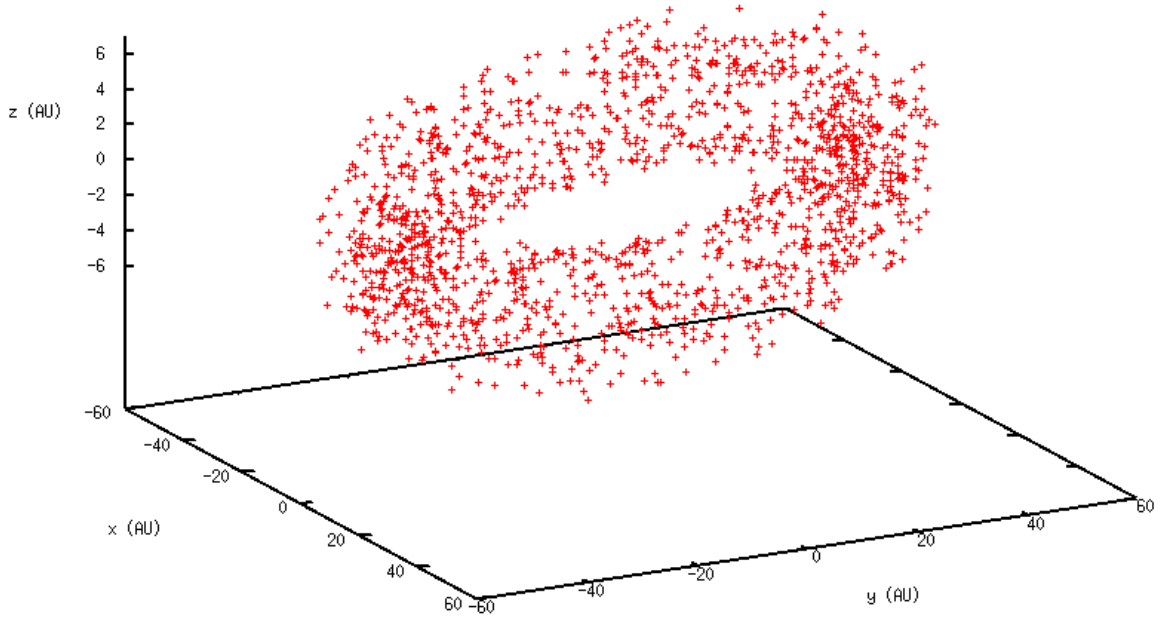

Figure 6.4: *3D plot of the outer region of the evolved disk of planetesimals, in presence of one massive planet. There are no evident resonances, being the disk's outer region similar to a torus.*

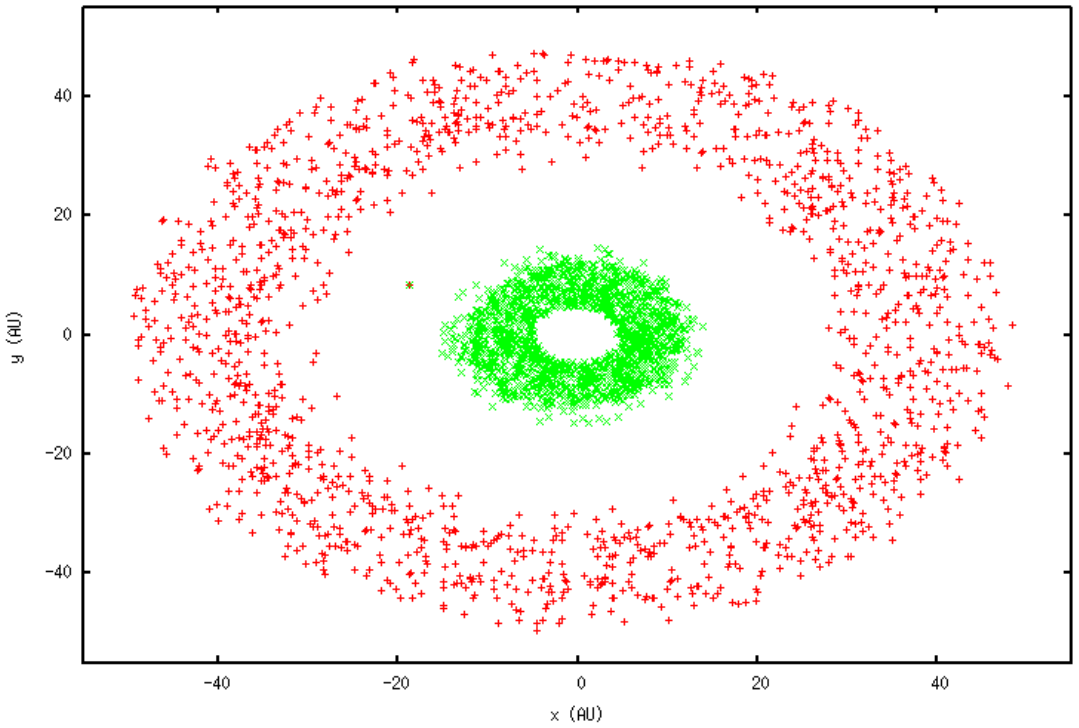

Figure 6.5: *2D plot of the inner (green dots) and outer (red dots) regions of the evolved disk of planetesimals, in presence of one massive planet, in the (x,y) plane - the reference plane.*

Dust evolution

Once planetesimals have evolved, after about 10 Myr, we consider this scenario to be the initial condition for dust (composed of grains of $r \sim 5$ μm) evolution, which occurs in a minor time (< 1 Myr) and is continuously produced by planetesimals collisions.

Results from simulations can be studied separately for the two previously examined disk's regions.

- *Outer region* - Figure 6.6 and 6.7 show the superposition of dust particles inclination and eccentricity distribution, respectively, at different ages of evolution[11]: we considered ages of $1, \ldots, 4$ Myr, with 1 Myr steps. The resonances in inclination (and the related resonances in eccentricity), occurring at various semi-major axes, are progressively higher and are then compatible with a flared-disk profile. The first resonance of this region is in good agreement with observed SPHERE data, being located at ~ 33 AU[12] and presenting an inclination of $\sim 13°$ - it is certainly between $(10 \div 15)°$ - as we expected. However, the other (higher and more consistent) resonances[13] could only account for the global flaring of the disk, but are not expected, since observational data do not show evidence for their presence.

  It is also evident that, increasing time, dust particles tend to concentrate inward, around the locations in correspondence of those resonances. Moreover, the similar behaviour found for eccentricity and inclination in this region is not an isolated case, since we notice it for every age and region, for dust as well as planetesimals[14]: then, there is a strong bond between e and i, symptom of mean motion resonances.

- *Inner region* - However, in Figure 6.8 it is possible to ascertain that the flat profile in inclination for the planetesimals case still remains in the dust-evolved case, presenting the same maximum constant inclination of $\sim 10°$ and the absence of resonances.

To summarize, while in the outer region the obtained behaviour of the dust partially resembles that of the SPHERE data, the inner region does not evidence any similarity with them. What is possible to hypothize is that the flat profile in inclination obtained in the inner region is due to the fact that we assumed only one massive (and outside the inner region) inclined planet: in fact, planetesimals in turn (and dust, a fortiori) must be inclined, in order to preserve angular momentum. This is the reason for which we exclude the presence of one massive planet. Moreover, it is noteworthy that a planet of mass higher than a certain limit would probably have been detected by SPHERE: in particular, the contrast limit of the image is about $\sim 13,4$ mag at 0,55 arcsec (12,9 mag at 0,3 arcsec, where we would expect the presence of one, or more, possible planet), then objects with magnitude in the J-band $J < 17,1$ ($J < 16,6$ in the planet's position)

[11] We do not distinguish each evolutionary phase since dust is continuously produced in the disk.

[12] It is slightly outer than the observed location of the outer ring, but dust tends to be attracted by the stars during evolution, so the actual value could be consistent with this one.

[13] Their presence could be explained by considering the periastron of the dust particles $a(1-e)$: once fixed the value of a, there is a maximum eccentricity e_{crit} above which the dust particle enters the unstable region (the gap), from which it could be sent inward or outward in the same (or another) resonance; it is clear that, enhancing a, in turn the maximum e_{crit} grows. Then, the increasing value of the resonances in eccentricity when growing the semi-major axis (Figure 6.7) could be generated by this "instability" mechanism.

[14] Clearly, dust undergoes higher excitations in both eccentricity and inclination than planetesimals.

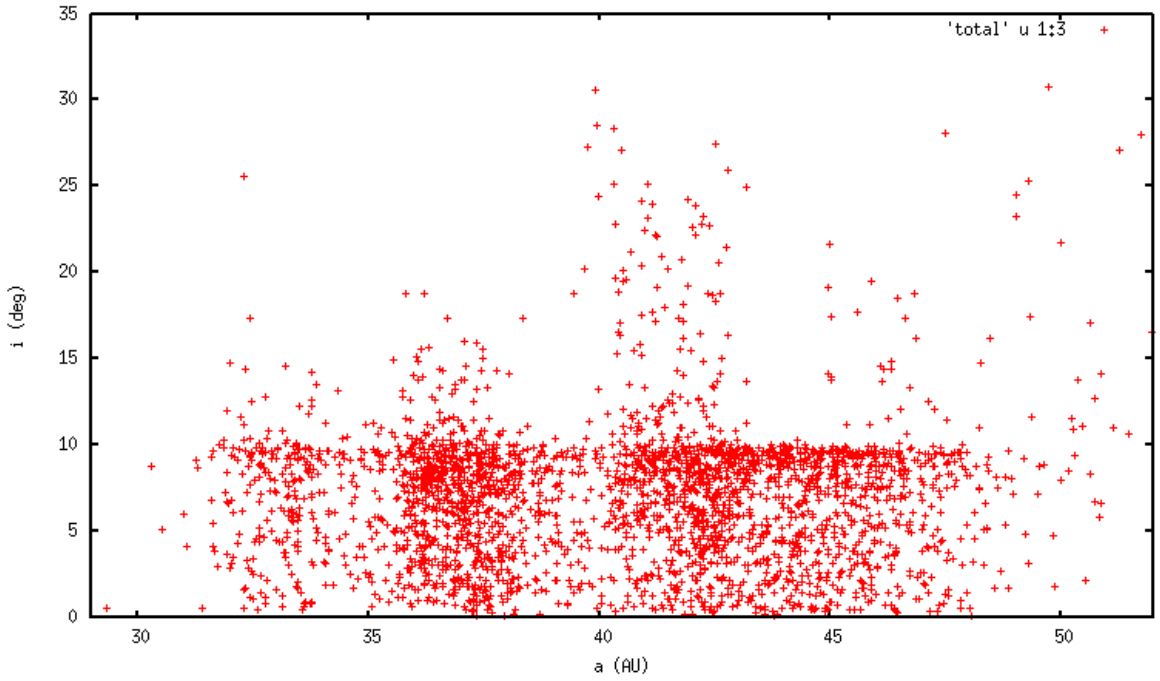

Figure 6.6: *Superposition of 1 Myr, 2 Myr, 3 Myr and 4 Myr dust simulations for the outer region, in presence of one massive planet, in which the inclination of the dust particles is plotted in function of their semi-major axis. It is clear that the various distance-growing resonances, at* ~ 33 *AU,* ~ 37 *AU and* ~ 42 *AU, indicate that the disk is flared, even though the most of the particles present* $\sim 10°$ *or less of inclination.*

would have been revealed; these values correspond to $2M_J$ for COND models and $\sim 8M_J$ for DUSTY models. Instead, it is likely the presence of one or more planets of lower masses.

In conclusion, the case in which one massive planet is considered does not represent the whole scenario observed by SPHERE. We then concentrate on the case of two low-mass planets.

6.3.2 Two low-mass planets simulations

Since one massive planet do not represent the whole observed scenario of V4046 Sgr disk, but only its outer region, we examined the case in which we include two low-mass planets, each of mass $< 1M_J$ and orbiting within the gap. We noted that even for low masses $\sim 0,5M_J$ and inclinations $i \sim 2° \div 3°$ of the planets, the resulting inclinations of the dust particles turned out to be too high with respect to the expected values. The suggested trend was then to reduce the planets masses and inclinations again.

However, we found an interesting fact in order to explain the reasons for which, even for very low planets masses and inclinations, we still observed excessive excitations of planetesimals and dust particles: the external planet excites the internal one, whether the former is more massive than the latter. In fact, we had first implicitly assumed the most massive planet to be external; instead, when we exchanged the planets positions (namely considering the most massive one to be internal) we observed a consistent decrease in the inclinations.

Now we will briefly report the main features of the first case, in which the *most massive planet* is in the *external* orbit, showing and discussing the reasons that con-

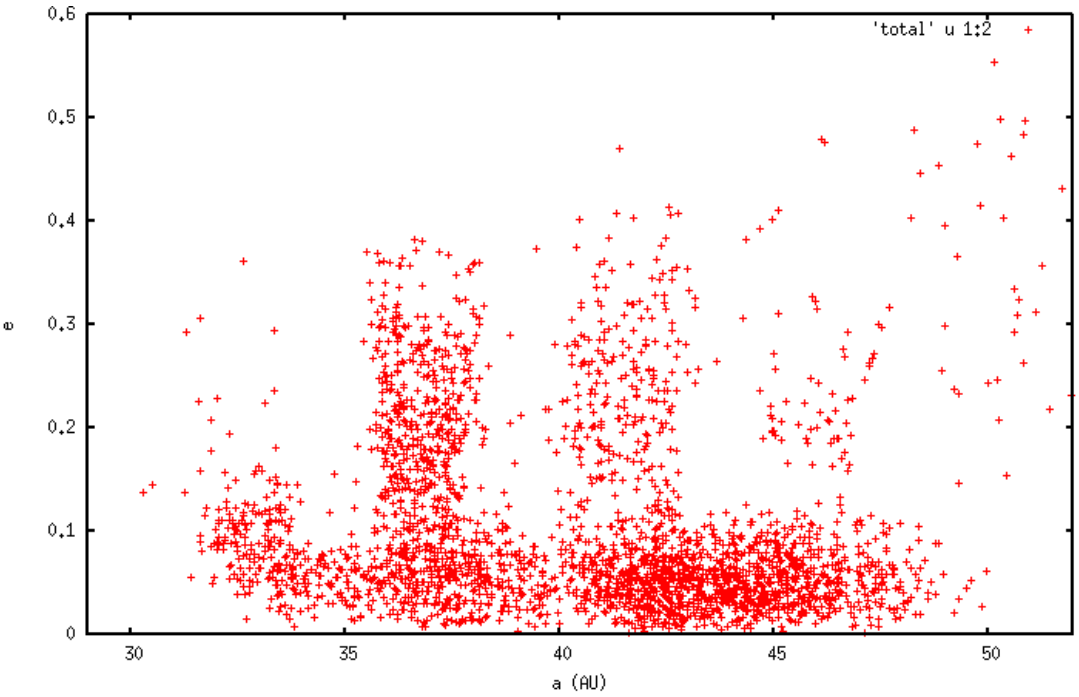

Figure 6.7: *Superposition of 1 Myr, 2 Myr, 3 Myr and 4 Myr dust simulations for the outer region, in presence of one massive planet, in which the eccentricity of the dust particles is plotted in function of their semi-major axes. The various distance-growing resonances, occurring in the same locations as in Figure 6.6, indicate that eccentricity's trend is related to inclination's trend, likely due to mean motion resonances. However, the most of the particles maintain small eccentricities* $< 0,1$*, in agreement to the observed data.*

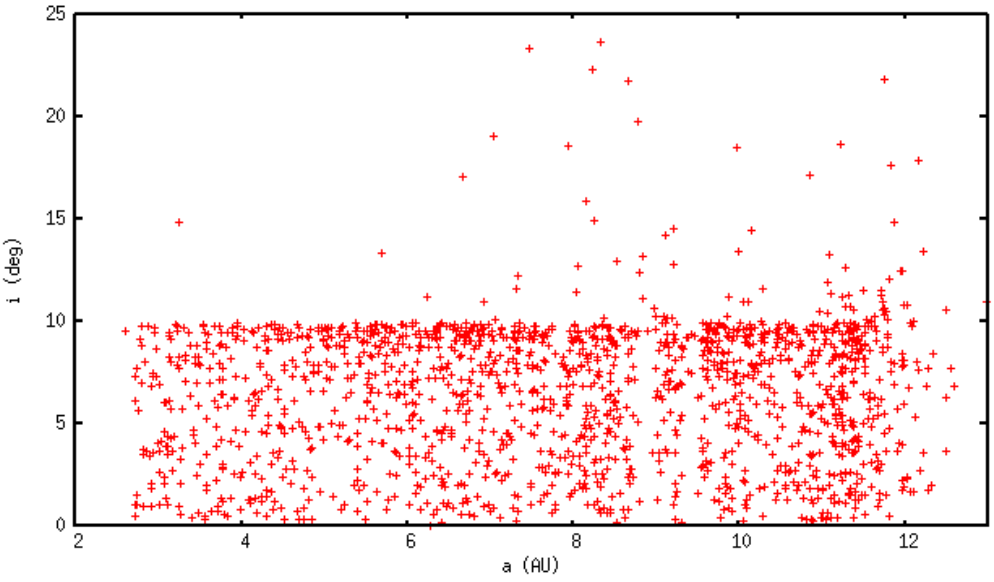

Figure 6.8: *The Figure represents the evolution of the dust, in the inner region, in presence of one massive planet, plotting dust particles inclination as a function of their semi-major axes. The flat profile in inclination still remains, being the planetesimals uniformly distributed with inclination of* $\sim 10°$ *or less; some of them show higher inclinations, but it is not possible to find any resonance.*

vinced us in changing their relative positions (we do not consider dust evolution, since planetesimals evolution is clearly misleading, as we will discuss shortly).

In the *"wrong"* case we simulated the evolution of the same number of planetesimals ($N = 4000$), among which there are two planets presenting the following features:

Planets parameters	
M_1 (M_J)	$0,33$
M_2 (M_J)	$0,50$
r_1 (AU)	18
r_2 (AU)	24
i_1 ($^\circ$)	0
i_2 ($^\circ$)	5

Following the previous procedure, we distinguish the two regions of interest.

- *Outer region* - In the external region, Figure 6.9 shows that the inclinations of the planetesimals does not change in a relevant way with the variation of their semi-major axes, mostly remaining below $\sim 6^\circ$; only at $a \sim 42$ AU it is possible to notice what could be a resonance, but its position is too external to fit the expected ~ 30 AU ring.

- *Inner region* - As regards the internal region, a resonance does occur, as is possible to infer from Figures 6.10 and 6.11, in which the plot involves the planetesimals inclinations and eccentricities, respectively, in function of their semi-major axes. These Figures show both the perturbations caused by the planets, inducing semi-periodical variations in some cases[15], and the two-body interactions causing scattering (which is what we are interested in). However, the resonance pushes planetesimals up to $\sim 10^\circ$, which is above the expected inclination for the dust ($\sim 8^\circ$); moreover, its position of ~ 9 AU is too internal to be in agreement with the expectations of a ~ 13 AU ring. The possible explaination of this resonance could be that the external - and most massive - planet excites the internal planet, which in turn raises planetesimals in inclination and eccentricity through the mean motion resonance.

Given these results from the planetesimals evolution, we did not simulate the dust evolution since dust would have been excited in inclination (and in eccentricity) even more than what planetesimals experienced, leading to excessive resonances which are in disagreement with the SPHERE data. Moreover, dust would have moved inward, decreasing the semi-major axis in correspondence of the resonance in the interior region, and then stepping away from the expectations. Thus, we conclude that the case in which we consider two low-mass planets, of which the most massive is orbiting externally with respect to the other, does not coincide with our expectations derived by the SPHERE data[16].

Henceforth, we will analyze the scenario in which the *most massive planet* is orbiting *internally* with respect to the other planet, showing that in this case we obtain good aggreements with the observed SPHERE data.

[15]This often results in spiral arms on the disks.

[16]In order to state such a sentence, we simulated various combinations of masses, semi-major axes and inclinations of the planets: however, the results were always, qualitatively, in agreement with the aforementioned case, which we reported in detail.

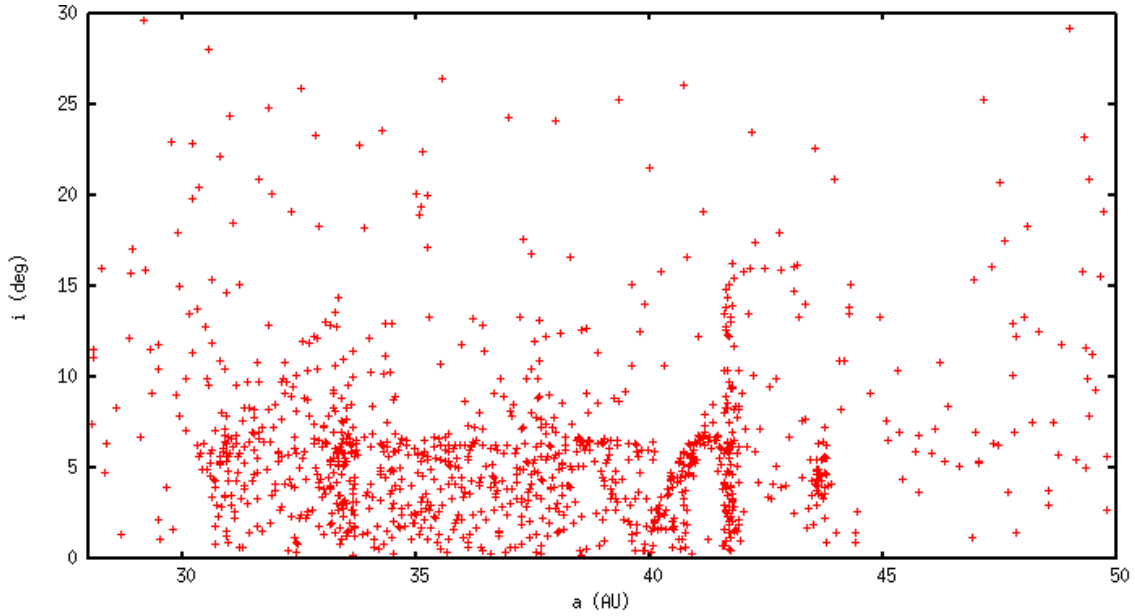

Figure 6.9: *The Figure represents the planetesimals evolution in the outer region, in presence of two planets (of which the most massive orbits externally with respect to the other), where the planetesimals inclination is plotted in function of their semi-major axes. It is possible to deduce that no clear resonance occurs, eccept for one at* ~ 42 *AU, which is not compatible with the observed data; the rest of the region remains approximately uniform in inclination.*

In the *"correct"* case we simulated, as in the previous case, the evolution of $N = 4000$ planetesimals/dust particles with the presence of two planets of masses of ∼Saturn and ∼Neptune, presenting the following parameters:

Planets parameters	
M_1 (M_J)	$0,330$
M_2 (M_J)	$0,033$
r_1 (AU)	20
r_2 (AU)	26
i_1 (°)	2
i_2 (°)	8

In this case, we considered the evolution of both planetesimals and dust, as regards the inner and the outer regions, separately.

Planetesimals evolution

- *Outer region* - The distribution of the planetesimals inclination after the evolutionary stage, in the most external region, is shown in Figure 6.12. The presence of many resonances is not a problem, since they damp with the increase of the semi-major axis: the only one which is relevant is the first, located at ~ 35 AU, which is due to scattering and presents maximum inclinations of $\sim 4°$. As previously discussed, we expect that the subsequent evolution of the dust particles, besides bringing them inward, will induce higher excitations in inclination and

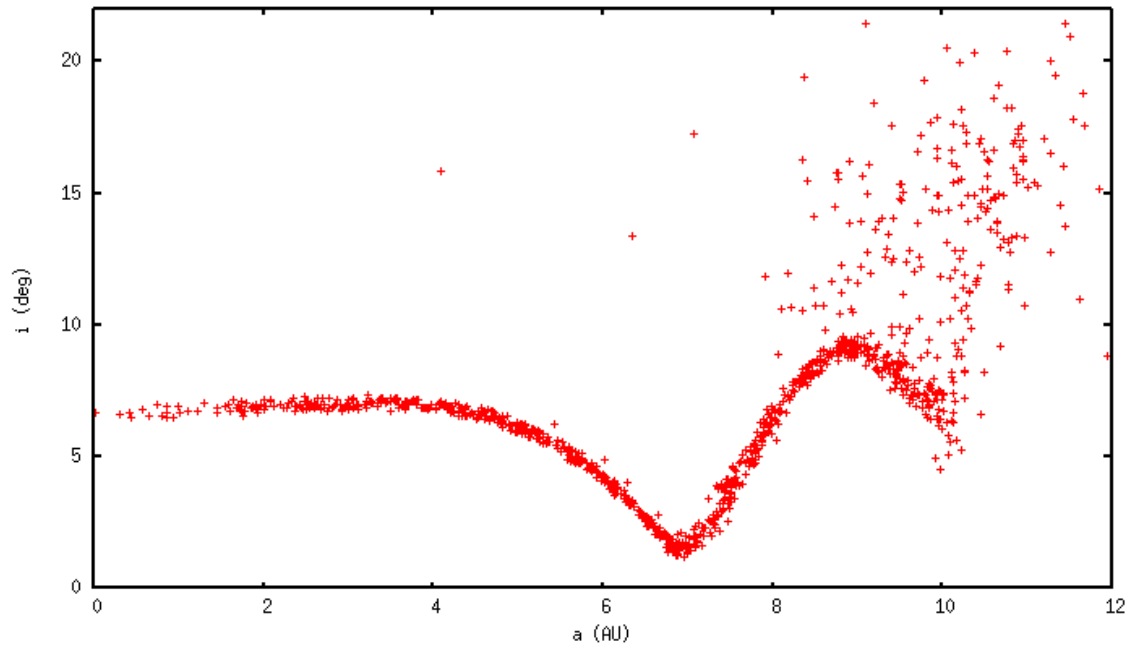

Figure 6.10: *The Figure represents the planetesimals evolution in the inner region, in presence of two planets (of which the most massive orbits externally with respect to the other), where the planetesimals inclination is plotted in function of their semi-major axes. A clear resonance in correspondence of* ~ 9 *AU occurs, but its location is too internal and the excitation in inclination is too high to be in agreement with the observed data. The high correlation between the inclination and the semi-major axis is due to secular perturbations that act in the first few Myr of the system's lifetime (V4046 Sgr is young).*

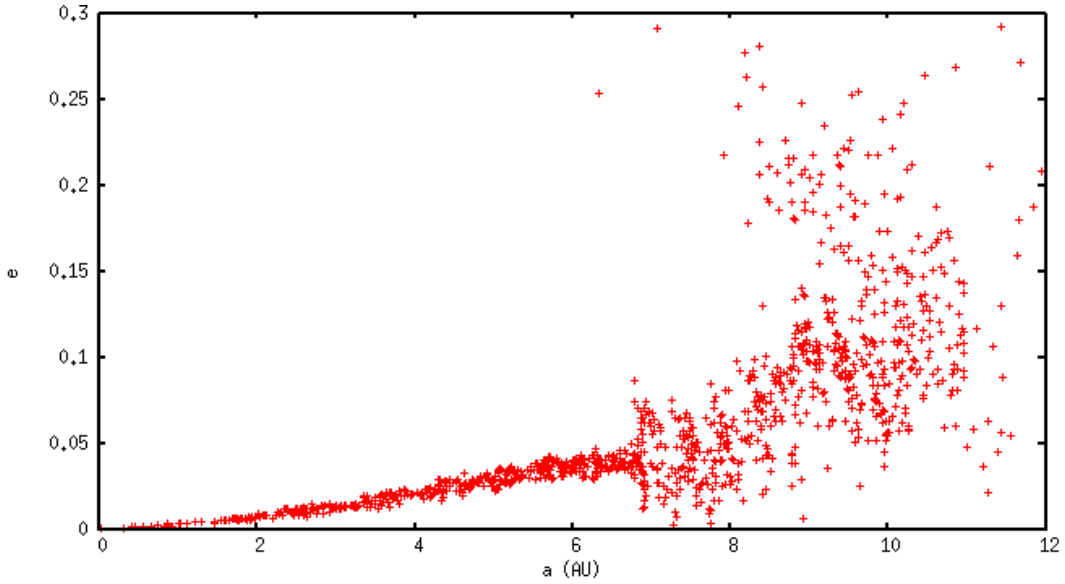

Figure 6.11: *The Figure represents the same situation depicted in Figure 6.10, plotting the eccentricity (instead of the inclination) in function of the semi-major axis: here, it is even more evident that planetesimals are excited and scattered in an excessive measure, since the eccentricity reaches values of* $\sim 0,25$ *in the most external region. The high correlation between the eccentricity and the semi-major axis in the region internal to 6 AU is due to the fact that the most external planetesimals are more influenced by the planets, since they are near them, and then they scatter.*

eccentricity: thus, the scenario obtained in this premilinary simulation represents a good basis for the future comparison with the expectations.

- *Inner region* - As regards the internal region of the disk, composed of planetesimals, it results that the highest resonance in inclination (which corresponds to the most external, too) is in agreement with its expected location of $\sim$ 13 AU, whereas the maximum inclination does not exceed the value of $3,5°$ - which is less than the half of the observed value for dust particles. Other inner resonances, which are smaller and are probably due to the effects of the proximity to the binary, are present. The overall situation in this region provides reliable elements for the subsequent evolution of dust.

The emerging picture from the planetesimals evolution is virtually in agreement with our expectations, since there are two relevant regions presenting high excitement as a consequence of scattering, which correspond to the external and internal boundaries of the inner and outer regions, respectively. In correspondence of these locations, planetesimals exhibit higher positions and lower excitations in inclination with respect to the observed rings, and this is reliable since planetesimals are the first evolutionary phase, after which dust will be attracted by the binary and excited more than planetesimals.

Dust evolution

- *Outer region* - The distribution of dust particles in inclination and eccentricity, after the evolutionary phase, in the external region of the disk is depicted in Figures 6.13 and 6.14, respectively.

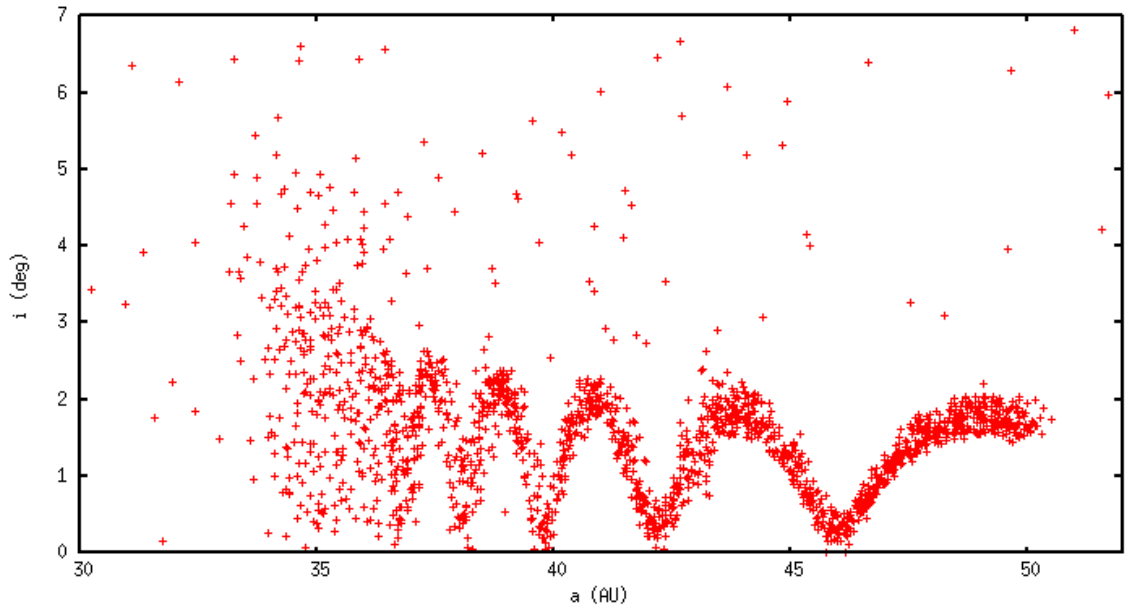

Figure 6.12: *The Figure represents the planetesimals evolution in the outer region, in presence of two planets (of which the most massive orbits internally with respect to the other), where the planetesimals inclination is plotted in function of their semi-major axes. Various resonances decrease when increasing the semi-major axis; the first of them, which more properly represents the scattered planetesimals, is located near the expected position (~ 35 AU) and has a maximum inclination of 5°.*

As regards the resonances in inclination, the region of scattering which we considered previously in the planetesimals evolution has moved inward, locating at ~ 28 AU, and has increased its maximum value, reaching $\sim 12° \div 13°$, as expected; the other resonances are fainter than the excitement of this region, and decrease over the semi-major axis, thus we do not consider them. This scenario is completely (within the uncertainties) compatible to the observed SPHERE data.

Considering the eccentricity, it is clear that the corresponding scattering region of the distribution of inclination is still located around the same position, but it is not well defined in shape and tends to spread over the semi-major axis: in fact, some dust particles seem to move away from this region towards higher semi-major axes and higher eccentricities, as a more evident consequence of scattering.

- *Inner region* - The dust evolution in the inner region is presented in Figure 6.15. The most external resonance in inclination is also the greatest: it is located at ~ 11 AU and exhibits maximum inclinations of $\sim 4,5°$. Both these values are slightly lower than the expected ones (~ 14 AU and $\sim 6°$), but still compatible.

For these reasons, Figure 6.13 together with Figure 6.15 represent the best fit with the observational data, obtained through our simulations, supporting the scenario of two low-mass planets of which the most massive orbits internally with respect to the other.

The eccentric case

The same two planets considered in the previous Section (the *"correct case"*) are now studied in the case they present a non-negligible eccentricity, whereas their inclination

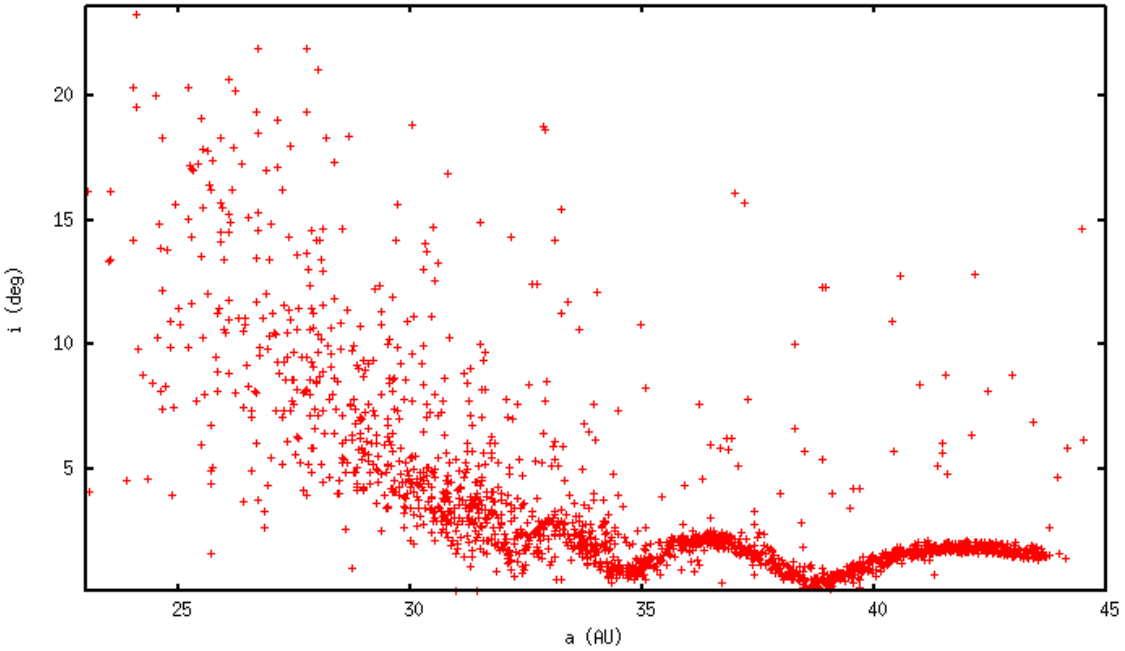

Figure 6.13: *The Figure represents the dust evolution in the outer region, in presence of two planets (of which the most massive orbits internally with respect to the other), where the inclination of dust particles is plotted in function of their semi-major axes. The first region, followed by some damping resonances, has the highest excitations due to scattering and it is relatively spread over the semi-major axis, but it reaches its maximum of* $\sim 12^{\circ}$ *at* ~ 28 *AU, which is well in agreement with the expectations.*

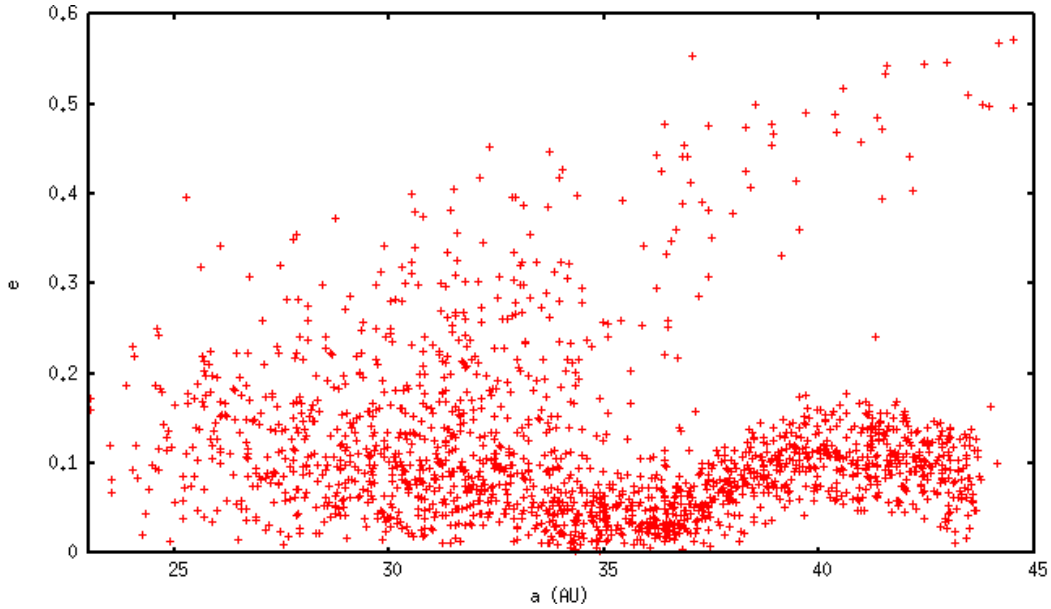

Figure 6.14: *The Figure represents the dust evolution in the outer region, in presence of two planets (of which the most massive orbits internally with respect to the other), where the eccentricity of the dust particles is plotted in function of their semi-major axes. The behaviour in this case does not completely resemble that of Figure 6.13, since scattering sends the particles to higher eccentricities towards higher semi-major axes.*

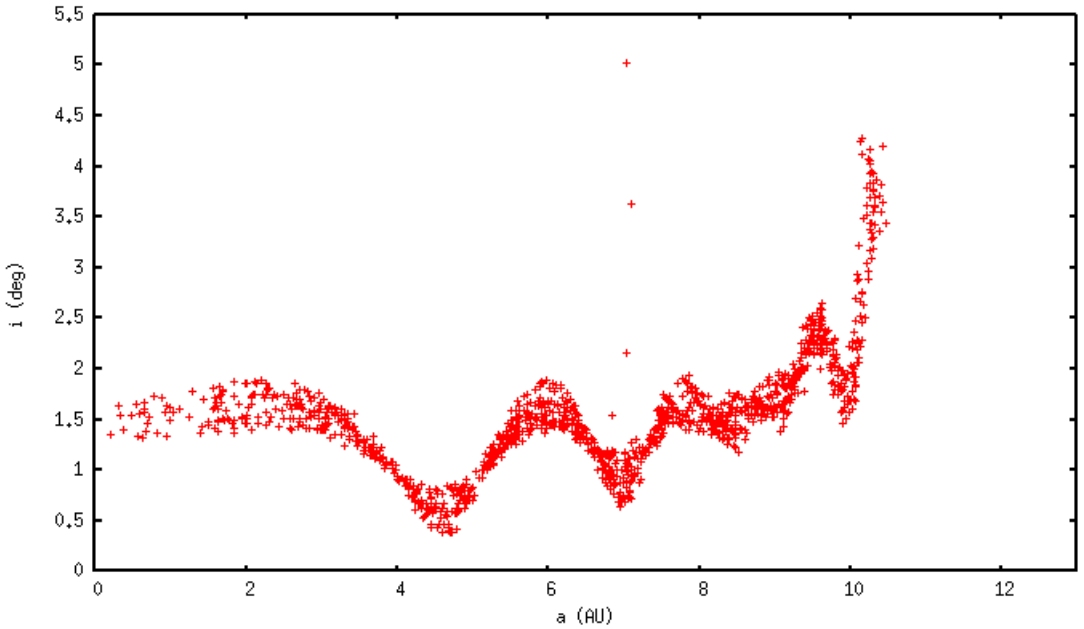

Figure 6.15: *Representation of the dust evolution in the inner region, in presence of two planets (of which the most massive orbits internally with respect to the other), where the inclination of the dust particles is plotted in function of their semi-major axes. The major and most external resonance occurs at* ~ 11 *AU, which is slightly inferior to the expected value, with an inclination of* $\sim 4,5°$ *that is also lower that the observed value, but still compatible.*

has been slightly reduced, as reported in the following table.

Planets parameters	
M_1 (M_J)	$0,330$
M_2 (M_J)	$0,033$
r_1 (AU)	20
r_2 (AU)	26
i_1 (°)	2
i_2 (°)	6
e_1	$0,14$
e_2	$0,20$

It has been sufficient to analyze the evolution of planetesimals ($N = 4000$) from simulations to state that the eccentric case excites them too much to reproduce the observed SPHERE data, as shown in Figures 6.16 and 6.17 for the outer and inner regions of the disk, respectively. In particular, planetesimals in the outer region are largely dispersed in inclination (reaching high values) from ~ 30 to ~ 40 AU, where a small peak is present[17], which decreases from approximately 43 AU outwards until it becomes null. As concerns the inner region, the major resonance in inclination is located at ~ 14 AU, but it excites planetesimals at inclinations of nearly 12°, which is incompatible with the observations; however, the trend is correct, since the other resonances rapidly decrease while moving inward.

[17]Moreover, its position is too distant from the binary to account for the expectations.

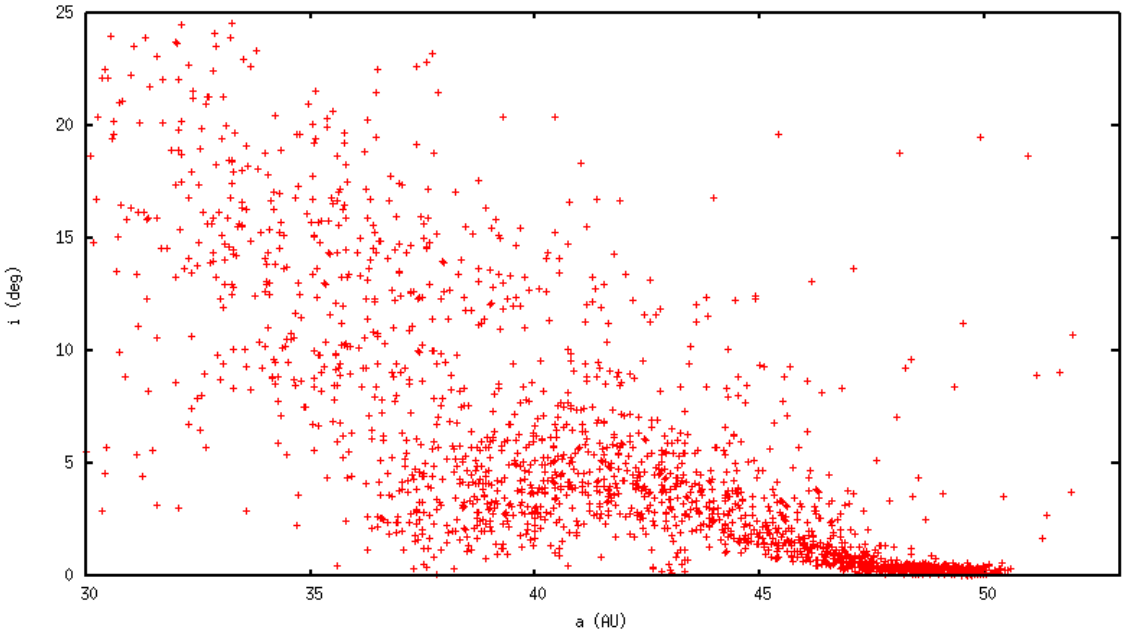

Figure 6.16: *Representation of the planetesimals evolution in the outer region, in presence of two eccentric planets (of which the most massive orbits internally with respect to the other), where the planetesimals inclination is plotted in function of their semi-major axes. Clearly, a resonance in correspondence of* ~ 43 *AU and the dispersion in inclination at about* $30 \div 35$ *AU are not in agreement with the expected trend.*

Finally, it is possible to exclude the case in which the two low-mass planets present non-negligible eccentricities, since they induce excessive excitation on the planetesimals, and even more on dust grains.

6.3.3 Comparison of different dust grains sizes

As discussed in Section 4.3 and reported in [37] and [38], observations demonstrate that there is a relevant difference in the composition of dust, in terms of size, between the inner and the outer regions: small $\sim \mu$m-sized (or bigger) grains populate the former, whereas large ~ 10 μm-sized grains coexist with small grains in the latter region (Figure 6.18, in which, however, the *mid* grains correspond to $\sim$cm-sized particles, greater than our "large" grains). Moreover, the most internal region, with semi-major axes inferior to ~ 14 AU, is devoid even of small particles[18].

In order to account for these observations, we provide a comparison between the distributions of large and small grains in both the outer and inner regions, resulting from the simulations of the *"correct case"*, which is in agreement with these observational considerations.

Large 5 μm-radius dust grains

Concerning large dust particles, of radius of 5 μm, their distribution in eccentricity after the evolutionary phase is depicted in Figure 6.19. The emerging picture clearly identifies the region within $\sim 25 \div 30$ AU to be populated by a negligible fraction of grains, as expected. In fact, large grains are concentrated in the external region of the

[18]This is possibly due to the presence of another (more internal) gap.

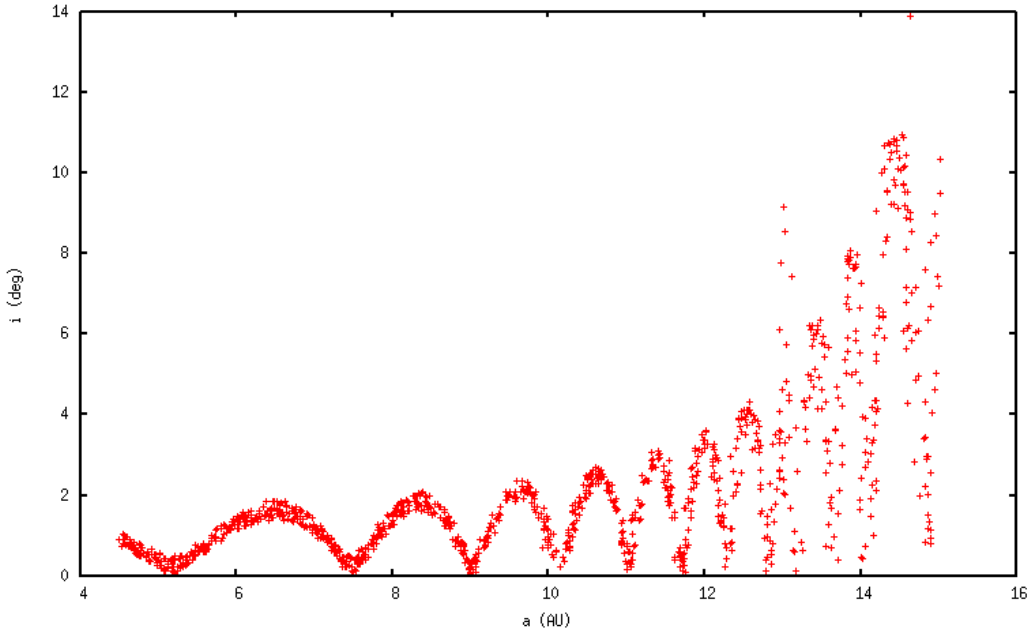

Figure 6.17: *The same situation of Figure 6.16, for the inner region. The most external resonance at* ~ 14 *AU, which is also the higher, reaches an inclination of* $\sim 12°$*, then planetesimals are too much excited to account for the observed SPHERE data.*

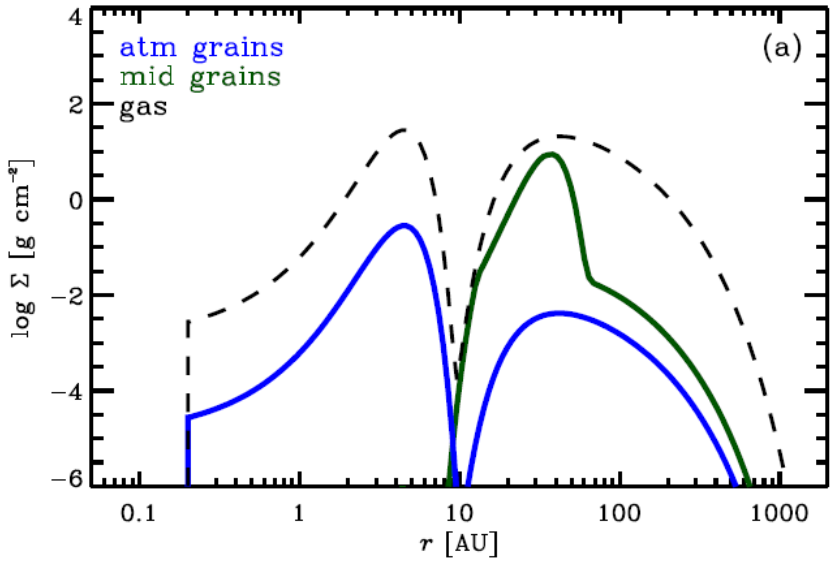

Figure 6.18: *Surface density profiles for the gas (dashed), the large "midplane" (green) and small "atmosphere" (blue) grain populations, resulting from a model (adopted in [38]) that succesfully reproduces the observations. The large-grains peak around 30 AU clearly reproduces the outer ring, whereas the inner* ~ 14 *AU ring does not result to be evident from this Figure.*

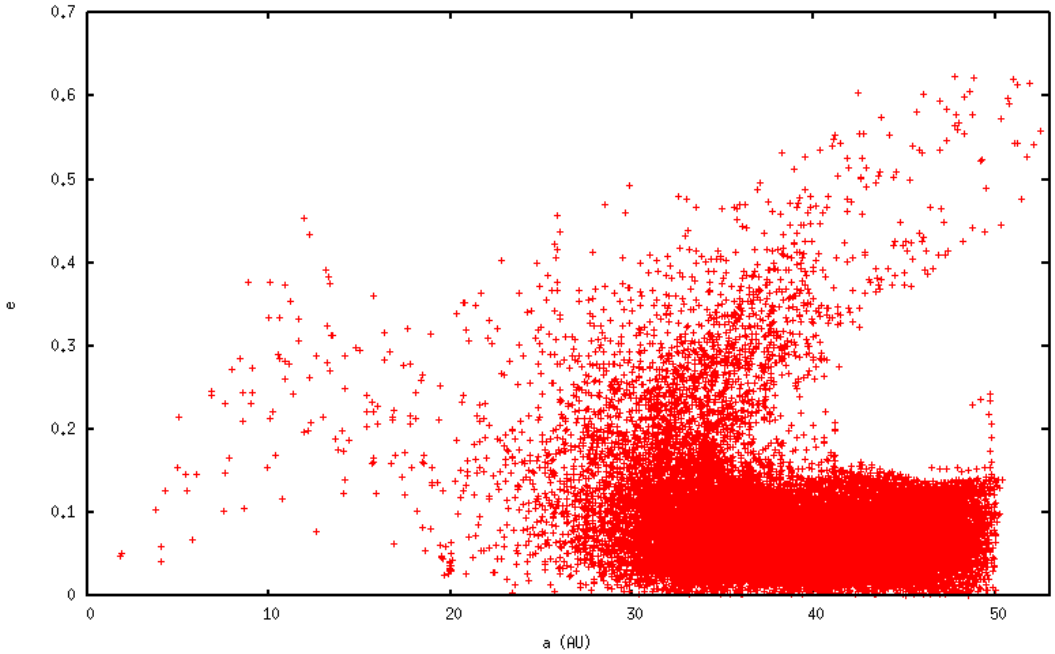

Figure 6.19: *Plot of the eccentricities of evolved dust particles of radius 5 μm in function of their semi-major axes, both in the inner and outer regions, resulting from the superposition of 10 evolutionary ages from 0 to 2 Myr. Only a negligible fraction migrates from the outer region towards the binary, whereas almost the totality is concentrated from about 30 AU to outer radii, with a branch of particles moving towards higher semi-major axes and enhancing their eccentricities.*

disk, outside $\sim$ 30 AU, with a branch presenting increasing eccentricities while moving outward. We can then assess that large grains do not migrate from the outer towards the inner region, remaining outside.

Small 0,5 μm-radius dust grains

In the case of smaller dust grains, of radius of 0,5 μm, instead, Figure 6.20 illustrates their distribution in eccentricity over the semi-major axis in an evolved situation. Evidently, there is a branch of grains migrating inward, from the outer region, while decreasing eccentricity[19]: they are nearly uniformly distributed between $\sim$ 10 and $\sim$ 20 AU, whereas they rapidly decrease in number and in eccentricity's dispersion towards the binary[20]. This latter behaviour could approximately account for the evidence of the emptying of even small grains within 14 AU, whereas the population of the region within $\sim$ 30 AU greatly follows the observations. Finally, the fact that even in the outer region these small grains are present in a relevant number represents the expectations.

We must remind, however, that coupling the SMA observations with the SED is inherently degenerate, namely there is not a univocal correspondence between the dust temperature and its radial position in the disk, because this relation also depends on the grains composition and size (and then these latter parameters must be considered).

[19]The same branch continues increasing towards the external part of the disk, following the trend of the branch observed in the simulations of large grains (Figure 6.19).

[20]This is due to the circolarization of their orbits while moving towards the binary as a consequence of the drag force (A.2.2).

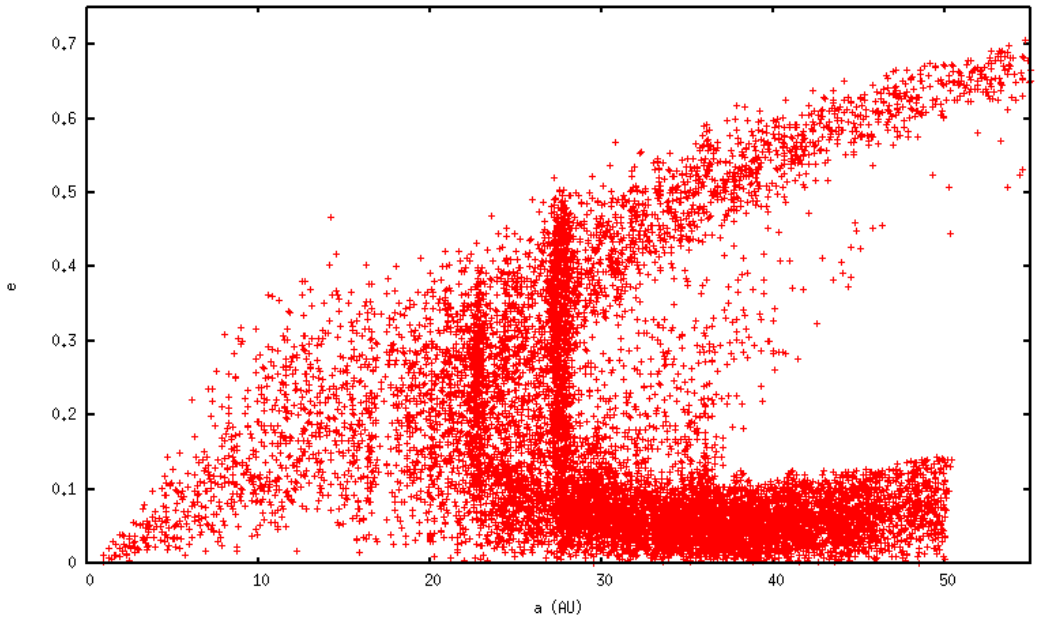

Figure 6.20: *Plot of the eccentricities of evolved dust particles of radius 0,5 μm in function of their semi-major axes, both in the inner and outer regions, resulting from the superposition of 10 evolutionary ages from 0 to 2 Myr. These smaller grains evidently migrate from the outer region towards the binary, with a continuously decreasing branch that reaches a null eccentricity in the proximity of the binary. Similarly to Figure 6.19, most of the particles are outside $\sim$ 25 AU, some of which are pushed outward and excited.*

Consequently, Figure 6.18 has not to be over-interpreted[21].

Possible mechanisms responsible for the dust-size distribution

In order to physically justify the observed (and reproduced by our simulations) distribution of dust particles as a function of their size, we present here the two most probable mechanisms that could have generated such a scenario.

- Poynting-Robertson drag force (P-R) could act differently on the dust particles, as a function of their size and inclination. In fact, large grains are less affected by the P-R, whereas small grains are more rapidly forced to spiralize towards the binary. Then, the characteristic time of the P-R (τ_{PR}) required for a particle to cover a radial distance equal to $2r_H$ (being r_H the Hill radius of the planet(s)[22]) has to be compared with the orbital period of the planet(s) (τ_{pl}). Typically, $\tau_{PR} \gg \tau_{pl}$, then

[21] Moreover, SPHERE has greater resolution than SMA for semi-major axes > 10 AU and for $\sim \mu$m-sized grains, so this fact leads to a not self-consistent situation, since in [38] SPHERE data are not taken into account (being precedent to SPHERE's start). The implementation with SPHERE data could represent an interesting study for an improved characterization of the disk.

[22] The Hill radius of a planet (of semi-major axis a) defines its surrounding zone into which a body is more gravitationally attracted by the planet with respect to the star, and is then destined to accrete onto the planet:

$$r_H(a) = a \cdot \sqrt[3]{\frac{M_{planet}}{3M_\star}}.$$

it could seem that one particle cannot overcome a planet's clearing zone without being captured by it, if lying on the planet's orbit. However, if the planet(s) and the grains are mutally inclined, the time in which the grain's orbit intersects (or is in proximity of the intersection) the planet's orbit - being then subject to the gravitational force of the planet - is a small fraction of the planet's period: this fact enhances the possibility for a grain to pass the gap and then migrate towards the star. In the case of large grains, inclination could not be sufficient to allow them to pass the gap, since their τ_{PR} is higher than that of small grains.

Thus, the P-R effect could efficiently act on small and inclined grains, allowing them to populate the inner region from the outer region.

- Another scenario, for which inclination is not a relevant parameter and which does not contemplate any planet within the inner and outer regions, suggests instead the presence of a more internal planet: in this case, this < 14 AU planet could have generated the ~ 14 and ~ 30 AU resonances (rings). The dust-size distribution could then be explained by the different collisional time occurring between particles of the same size: in fact, since this characteristic time is proportional to the square of the particles density ($\tau \propto n^2$), large grains will collide less frequently than small grains because their density is strongly lower. As a consequence, large grains will spend a long time in correspondence of the resonances without impacting on another large grain, being strongly perturbed by the resonances and then increasing their speed: at the moment of the collision, they could present a consistent relative speed that could induce their fragmentation into smaller grains. Subsequently, these small grains will undergo more rapid collisions that will thermalize them, making them less susceptible to the resonances and allowing P-R to efficiently force them to spiralize towards the binary.

  However, in this situation it seems difficult to account for the presence of the gap separating the inner from the outer region.

The possibility for the occurrence of one of these mechanisms is currently under investigation.

6.4 Discussion

It is finally possible to summarize the results obtained through our simulations in this Section. We analyzed the possibility for the presence of one or more planets orbiting the very tight V4046 Sgr binary, taking into account SPHERE's detectability limits as concerns the masses of the eventual planets. Moreover, besides considering the evidence for two rings at radii of ~ 14 AU and ~ 30 AU which defines a gap between them and constraints the range in which it is possible to simulate the presence of planets, we had to reproduce the observed separation in the dust-size distribution between the inner and outer regions.

Our main conclusions, based on these considerations, are listed as follows.

- The presence of *one planet* has been *rejected*, since its (even high) mass did not reproduce the observed flaring of the disk, showing instead a flat profile in inclination. This is possibly due to the fact that one single inclined planet must be balanced by the planetesimals (and dust particles) in order to preserve angular

momentum, and this fact does not lead to resonances which are responsible for the observed rings. Furthermore, the planet would have been detected since its mass exceedes the detectability limits.

- The presence of *two low-mass planets*, in which the most massive orbits *externally* with respect to the other, has been *rejected* since the simulated resonances are too high to account for our expectations. The cause for this trend is imputable to the high excitation induced by the external (more massive) planet on the internal one, which is less massive and then more susceptible to perturbations.

- The presence of *two low-mass planets*, in which the most massive orbits *internally* with respect to the other and both are *eccentric*, has been *rejected*, because even in this case the resulting excitations are superior than what actually observed, and this is due to the eccentricities of the planets, whose eccentric motions excite the planetesimals (and thus the dust particles).

- The presence of *two low-mass planets*, in which the most massive orbits *internally* with respect to the other and both are *not eccentric*, can *represent* the observed scenario: in fact, this case is well in agreement with the SPHERE data since both the rings are reproduced with comparable inclinations/eccentricities as well as positions for the dust disk simulation. Moreover, the low mass of these planets does not allow them to be detected by SPHERE, and their traces, left in the disk during its evolution, are reproduced with satisfactory accuracy by our simulation.

- The observed *dust-size distribution*, showing the absence of large ($r \sim 5$ μm) grains inside ~ 30 AU and the lack of even small ($r \sim 0,5$ μm) grains below ~ 14 AU, has been *reproduced* in the latter ("correct") scenario with relevant precision as regards the outer region, whereas the inner boundary below which the disk is devoid of dust results to be ~ 10 AU from the simulations, which is slightly lower than the observed value[23].

[23]However, the qualitative trend has been confirmed; anyway, a more complex code involving other physical effects of disk dispersal is invoked in order to explain this discrepancy.

Chapter 7

Conclusions

In this final Chapter we draw the conclusions of this thesis, listing the main achieved results as well as the limitations encountered.

It is noteworthy the fact that our subjects, namely the binary system V4046 Sgr and its coplanar surrounding disk, result to be particularly favorable for the study we led due to their spatial disposition, because the disk is viewed with a relatively small inclination, which implies a lower darkening caused by the rings on the regions of the disk beyond them with respect to nearly edge-on disks. In fact, an extended darkened region of the disk could hide a planet, making its detection more complicated.

Our main results involve the shadow observed in V4046 Sgr disk, examined in Chapter 5, and the study, reported in Chapter 6, of the effects due to the presence of one or more planets in the disk as well as the dust distribution throughout the disk.

- As regards the shadow, through its observed radius we could infer that the disk is flared, obtaining an upper limit for the flaring index $\Psi = 2,66$ based on geometrical assumptions. Exploiting this value, we then found the angle which the shadow forms with the binary plane, namely $\alpha_S \simeq 14,8°$; this angle has been used to provide the estimation of the minimum radial extent of the shadow $r_S(\alpha_S) \simeq 31$ AU. It is true that the observed radius[1] is $r_S \simeq 42$ AU, but both values are affected by not-negligible uncertainties, deriving from the approximations used, in the case of $r_S(\alpha_S)$, and from the fact that the shadow does not clearly exhibit a net boundary. Nevertheless, the lower limit imposed by $r_S(\alpha_S)$ is in agreement with the minimum observed extension of the shadow. Moreover, the analysis of the shadow has allowed to confirm the observed disposition of the stars with respect to the shadow, with the major star being partially eclipsed by the other, at a certain observational epoch. Finally, we proved that limb darkening does not relevantly affect the characterization of the shadow in V4046 Sgr disk.

- Considering now the simulations, the most important resulting scenario, which is in agreement with the expectations based on the SPHERE data, indicates the presence of two planets orbiting V4046 Sgr in the gap formed between the inner ($r < 13$ AU) and outer ($r > 30$ AU) regions. These planets have masses of ∼Saturn and ∼Neptune; the former orbits at $r = 20$ AU and has an inclination of 2° over the binary plane, whereas the latter is more external, namely at 26 AU, with an inclination of 8°. Their presence induces, during the planetesimals evolution and the subsequent dust evolution, the formation of two rings of scattered (and then

[1] Limited by the region where it is possible to detect scattered light.

excited in both inclination and eccentricity, forming resonances) dust particles in correspondence - or in proximity - of the observed rings at ~ 14 and ~ 30 AU, reaching $\approx 4,5^\circ$ and $\approx 13^\circ$ in inclination, respectively. We rejected the case in which the planets possess not-negligible eccentricities (of $\sim 0,2$), since in this configuration the particles are excited too much. The noteworthy result is that, besides the fact that there could be two candidate planets responsible for the observed disk's features of V4046 Sgr, the most massive planet should be orbiting internally with respect to the other, qualitatively similar to the configurations of the giant planets in our Solar System. However, we must underline that, even though our assumptions on the planets parameters led to a simulated scenario which approximately follows the observed one - whereas other assumptions did not reproduce the expectations, this fact does not exclude the possibility that even other different scenarios could reproduce the SPHERE data. In fact, our limited time for performing calculations did not allow us to explore a great variety of configurations.

- Furthermore, our simulations have accounted for the observed separation in the dust-size distribution over the disk: in fact, we determined that outside ~ 30 AU the disk is well populated by both large ($r \sim 5$ μm) and small ($r \sim 0,5$ μm) grains of dust, whereas large grains (differently from small grains) do not migrate from the outer region to the zone below ~ 10 AU and there is a low and vanishing flux of small grains towards the binary; in the intermediate region, instead, a stable flux of small grains is present. Qualitatively, this distribution corresponds to the observations, even though there is a small difference as regards the boundary of the inner region below which the disk does not exhibit the presence of dust, while our simulations provide a small flux there: it is likely that the disk has dispersed its more internal dust by other effects which have not been considered in our N-body program. It is straightforward that an improved code should explain this circumstance; however, it surely needs more performant computers. Finally, what is possible to hypothesize, in order to physically justify this dust-size distribution, is that the Poynting-Robertson drag force allows the most inclined and small dust particles to migrate towards the binary, or that the presence of a planet internal to 14 AU without any planet between the inner and outer region has originated resonances in correspondence of the observed rings that could have determined the observed dust-size distribution.

In conclusion, then, this work widens our knowledge of the binary system V4046 Sgr but also leaves some unanswered questions due to the unavoidable limitations encountered; furthermore, it puts the basis for future improved and more detailed analysis of this peculiar environment. In fact, future studies involving improved instruments are required in order to achieve the following results:

- detectability of Saturnian-sized or even less massive planets, which allows to widen the possibility for the search for new exoplanets or, as in the case of V4046 Sgr, to verify what results from the simulations;

- more detailed imaging of the dust emission, in order to better constraint several disk's features which have implications also on planet formation processes.

Appendix A

Orbital elements and interactions

A.1 Orbital elements

The orbital elements are six[1], and refer to the orbit of a determined object orbiting in an inclined plane with respect to a plane of reference, whose intersection determines two nodes (see Figure A.1):

- a is the semi-major axis of the celestial body's elliptical orbit;
- e is the eccentricity of its orbit;
- i is the inclination of its orbital plane with respect to the reference plane;
- M is the mean anomaly[2], which is a measure of time referred to the orbiting body, in particular it is the fraction of the orbital period passed from the last passage to the periapsis, expressed as an angle;
- ω is the argument of periapsis, namely the angle from the ascending node (it is the node at which the celestial body passes from being below the plane of reference to being above it, during its orbital motion) to the periapsis in the celestial body's orbital plane;
- Ω is the longitude of ascending node, namely the angle of the ascending node from a reference direction in the reference plane.

A.2 Orbital interactions

A.2.1 Radiation pressure

We consider dust particles which are perfectly absorbent. Let us now concentrate on the energy flux per unit time and area which a dust particle, orbiting elliptically around

[1]To be precise, they are seven, if considering the parameter that characterizes an epoch. However, this is not important for our simulations.

[2]Actually, the mean anomaly is a mathematically convenient "angle" which varies linearly with time, but which does not correspond to a real geometric angle. It can be converted into the true anomaly ν, which does represent the real geometric angle in the plane of the ellipse, between periapsis (closest approach to the central body) and the position of the orbiting object at any given time. Thus, the true anomaly is shown as the red angle ν in Figure A.1, and the mean anomaly is not shown.

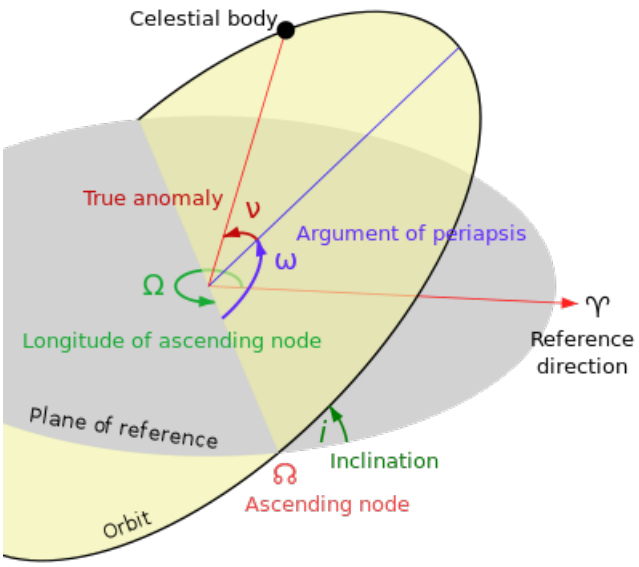

Figure A.1: *The orbital elements of a celestial body.*

the binary (which is assumed as a single star, being the binary's separation negligible with respect to the distance from the dust particles), receives:

$$\mathbf{S} \equiv \frac{\mathbf{E} \times \mathbf{B}}{\mu_0}.$$

It is the *Poynting's vector*[3], directed radially from the star towards the particle, and clearly **E** and **B** represent the electric and magnetic field of the radiation, respectively.

In the reference system of the dust particle which absorbes this energy, however, we must consider that, in an elliptical trajectory, the radiation hitting the particle is subject to the Doppler effect, since in certain positions the particle is increasing its distance from the star, whereas in other locations it is approaching it, as shown in Figure A.2. This fact implies that the Poynting's vector becomes (in module)

$$S \to S' = S\left(1 - \frac{\dot{r}}{c}\right),$$

where $\dot{r}$ is the radial velocity of the particle[4], and c the speed of light.

Concentrating on the force to which the particle is subject due to this incoming energy flux, it is certainly directed in the same verse of the Poynting's vector, then radially and outwards (Figure A.2), and it could be estimated (from dimensional analysis[5]) as

$$\mathbf{F} = \frac{S' \cdot A}{c}\hat{\mathbf{S}}, \tag{A.2.1}$$

where A is the surface of the particle hitted by the radiation. Equation A.2.1 is

[3]Its typical value at 1 AU from the Sun is $S_0 = 1,35 \cdot 10^6 \frac{\text{erg}}{\text{s} \cdot \text{cm}^2}$. In our case, being the total luminosity of the two stars of V4046 Sgr $L \approx 0,8 L_\odot$ (because $L \propto R^2 T^4$), we then have $S_0 \to S_0' = S_0 \cdot 0,8$, which is the energy flux at 1 AU from the binary.

[4]$\dot{r} > 0$ if the particle is increasing its distance from the star: in fact, the red shift implies longer wavelengths of the radiation and then less energy on the particle.

[5]In fact, Equation A.2.1 represents a flux of momentum per unit time, since $p = E/c$.

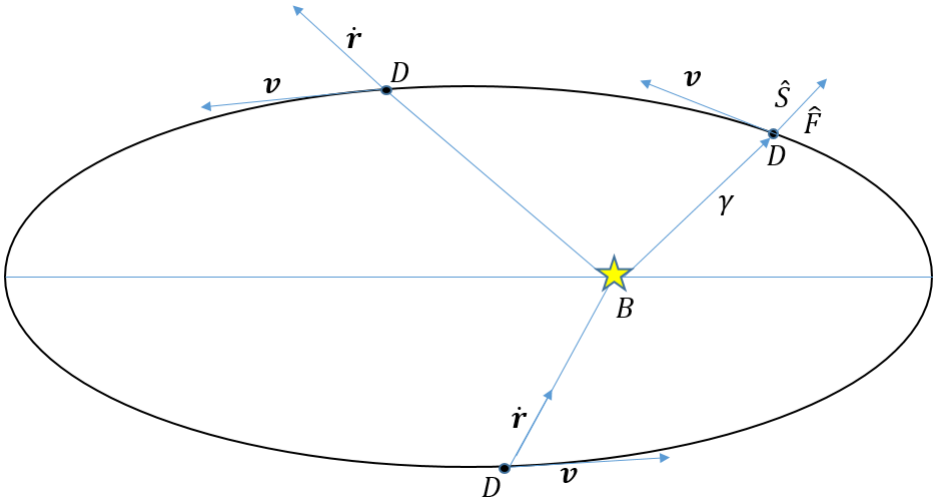

Figure A.2: *Illustration of the dust particle (D) orbiting, with velocity* $\boldsymbol{v}$*, the tight binary (B) at various orbital positions, allowing to see its outward or inward radial velocity* $\dot{\boldsymbol{r}}$ *in function of its location. The third position only shows that both the force* $\boldsymbol{F}$ *and the Poynting's vector* $\boldsymbol{S}$ *are in the same (radial and outward) verse.* γ *is the radiation beam coming from the stars.*

known as the *Robertson's formula* and it represents the force acting on the dust particle caused by the *radiation pressure*.

A.2.2 Poynting-Robertson drag force

Referring to the radiation pressure (Section A.2.1), we observe that the dust particle, once it has been hit by the radiation from the star and then has absorbed its energy, must reissue it in order to preserve its thermal equilibrium. The reissue implies to eject photons (in the infrared) possessing momentum p: thus, the reissue of energy (since $p = E/c$) implies to eject mass, being energy and mass related by the equation $E = mc^2$. Consequently, being $E = S' \cdot A \cdot t$, where t is the time required for the absorption of an amount of energy E, it results that

$$m = \frac{S'}{c^2} At \implies \mathrm{d}m = \frac{S'}{c^2} A \cdot \mathrm{d}t.$$

Moving along $\mathbf{v}$, then $\frac{S'}{c^2} A \mathrm{d}t \cdot v = p$, since $v \cdot \mathrm{d}m = \mathrm{d}p$. This means that the dust particle recoils, because the reissue of the energy occurs along the trajectory and points forward: this is equivalent to isotropically reissue in the infrared. The *Poynting-Robertson drag force* is then

$$\mathbf{F}_D = -\frac{S'}{c^2} A \mathbf{v}, \tag{A.2.2}$$

and is opposite to the velocity because it slows the particle, inducing them to orbit into spirals towards the binary.

Then, the total force to which a perfectly absorbent dust particle is subject, due to both the radiation pressure and the Poynting-Robertson drag, results to be the sum of

Equations A.2.1 and A.2.2:

$$\mathbf{F}_{TOT} = \frac{S'}{c} A\hat{\mathbf{S}} - \frac{S'}{c^2} A\mathbf{v}. \tag{A.2.3}$$

However, in the more general case in which the particles can both be partially absorbent and reflective, the factors f and g, for which $f + g = 1$, are introduced: they represent the fraction indicating how much a particle is absorbent or reflective, respectively[6]. Moreover, the quantity $Q_{PR} \equiv 1 + g$ is introduced in order to rewrite Equation A.2.3, taking into account these parameters, as follows:

$$\mathbf{F}_{TOT} = \frac{S'}{c} A \cdot Q_{PR} \left(\mathbf{S} - \frac{\mathbf{v}}{c} \right), \tag{A.2.4}$$

which is known as the *Robertson's general formula*. A simple consideration to justify the latter equation could be done in the case of pure reflectors: in fact, when a photon with momentum of module $p = E/c$ hits one of them, it is completely reflected and then its momentum's variation is $\Delta p = 2E/c$, meaning that the force on the particle doubles: in fact, since $Q_{PR} = 2$, the same result can be obtained by Equation A.2.4.

[6]Clearly, pure absorbents have $f = 1, g = 0$ whereas pure reflectors have $f = 0, g = 1$.

Bibliography

[1] Philip J Armitage. *Astrophysics of planet formation*. Cambridge University Press, 2010.

[2] Eric E Mamajek. Initial conditions of planet formation: lifetimes of primordial disks. In *AIP Conference Proceedings*, volume 1158, pages 3–10. AIP, 2009.

[3] D Lynden-Bell and JE Pringle. The evolution of viscous discs and the origin of the nebular variables. *Monthly Notices of the Royal Astronomical Society*, 168(3): 603–637, 1974.

[4] Philip J Armitage. Physical processes in protoplanetary disks. *arXiv preprint arXiv:1509.06382*, 2015.

[5] D. V. Martin. Populations of planets in multiple star systems. *ArXiv e-prints*, February 2018.

[6] Pawel Artymowicz and Stephen H Lubow. Dynamics of binary-disk interaction. 1: Resonances and disk gap sizes. *The Astrophysical Journal*, 421:651–667, 1994.

[7] David R Rodriguez, Joel H Kastner, David Wilner, and Chunhua Qi. Imaging the Molecular Disk Orbiting the Twin Young Suns of V4046 Sgr. *The Astrophysical Journal*, 720(2):1684, 2010.

[8] Kevin Wagner, Ruobing Dong, Patrick Sheehan, Daniel Apai, Markus Kasper, Melissa McClure, Katie M Morzinski, Laird Close, Jared Males, Phil Hinz, et al. The Orbit of the Companion to HD 100453A: Binary-Driven Spiral Arms in a Protoplanetary Disk. *arXiv preprint arXiv:1801.03900*, 2018.

[9] Andrew F Nelson and Francesco Marzari. Dynamics of circumstellar disks. III. The case of GG Tau A. *The Astrophysical Journal*, 827(2):93, 2016.

[10] A-M Lagrange, M Langlois, R Gratton, A-L Maire, J Milli, J Olofsson, A Vigan, V Bailey, D Mesa, G Chauvin, et al. A narrow, edge-on disk resolved around HD 106906 with SPHERE. *Astronomy & Astrophysics*, 586:L8, 2016.

[11] Laetitia Rodet, H Beust, M Bonnefoy, A-M Lagrange, PAB Galli, C Ducourant, and R Teixeira. Origin of the wide-orbit circumbinary giant planet HD 106906-A dynamical scenario and its impact on the disk. *Astronomy & Astrophysics*, 602: A12, 2017.

[12] Erika R Nesvold, Smadar Naoz, and Michael P Fitzgerald. HD 106906: A Case Study for External Perturbations of a Debris Disk. *The Astrophysical Journal Letters*, 837(1):L6, 2017.

[13] William F Welsh, Jerome A Orosz, Joshua A Carter, and Daniel C Fabrycky. Recent Kepler Results On Circumbinary Planets. *Proceedings of the International Astronomical Union*, 8(S293):125–132, 2012.

[14] Christian Thalmann, Silvano Desidera, Mariangela Bonavita, Markus Janson, Tomonori Usuda, Thomas Henning, Rainer Köhler, J Carson, Anthony Boccaletti, Carolina Bergfors, et al. SPOTS: The Search for Planets Orbiting Two Stars-I. Survey description and first observations. *Astronomy & Astrophysics*, 572:A91, 2014.

[15] Mariangela Bonavita, Silvano Desidera, Christian Thalmann, Markus Janson, Arthur Vigan, Gael Chauvin, and Justine Lannier. SPOTS: The Search for Planets Orbiting Two Stars-II. First constraints on the frequency of sub-stellar companions on wide circumbinary orbits. *Astronomy & Astrophysics*, 593:A38, 2016.

[16] Jean-Luc Beuzit, Markus Feldt, Kjetil Dohlen, David Mouillet, Pascal Puget, Francois Wildi, Lyu Abe, Jacopo Antichi, Andrea Baruffolo, Pierre Baudoz, et al. SPHERE: a planet finder instrument for the VLT. In *proc. SPIE*, volume 7014, page 701418, 2008.

[17] Markus Kasper and Dimitri Mawet. Gearing up the SPHERE. *Messenger*, 149(9): 17–21, 2012.

[18] Arthur Vigan, Maud Langlois, Claire Moutou, and Kjetil Dohlen. Exoplanet characterization with long slit spectroscopy. *Astronomy & Astrophysics*, 489(3): 1345–1354, 2008.

[19] Wahhaj Z. Very Large Telescope SPHERE User Manual. *7th public release*, 2017-06-11.

[20] D Mesa, A Vigan, V D'Orazi, C Ginski, S Desidera, M Bonnefoy, R Gratton, M Langlois, F Marzari, S Messina, et al. Characterizing HR 3549 B using SPHERE. *Astronomy & Astrophysics*, 593:A119, 2016.

[21] D Mesa, JL Baudino, B Charnay, V D'Orazi, S Desidera, A Boccaletti, R Gratton, M Bonnefoy, P Delorme, M Langlois, et al. New spectro-photometric characterization of the substellar object HR 2562 B using SPHERE. *arXiv preprint arXiv:1712.05828*, 2017.

[22] Christian Marois, Bruce Macintosh, Travis Barman, B Zuckerman, Inseok Song, Jennifer Patience, David Lafrenière, and René Doyon. Direct imaging of multiple planets orbiting the star HR 8799. *Science*, 322(5906):1348–1352, 2008.

[23] Christian Marois, René Racine, René Doyon, David Lafrenière, and Daniel Nadeau. Differential imaging with a multicolor detector assembly: a new exoplanet finder concept. *The Astrophysical Journal Letters*, 615(1):L61, 2004.

[24] Christian Marois, René Doyon, Daniel Nadeau, René Racine, Martin Riopel, Philippe Vallée, and David Lafrenière. TRIDENT: an infrared differential imaging camera optimized for the detection of methanated substellar companions. *Publications of the Astronomical Society of the Pacific*, 117(833):745, 2005.

[25] William B Sparks and Holland C Ford. Imaging spectroscopy for extrasolar planet detection. *The Astrophysical Journal*, 578(1):543, 2002.

[26] René Racine, Gordon AH Walker, Daniel Nadeau, René Doyon, and Christian Marois. Speckle noise and the detection of faint companions. *Publications of the Astronomical Society of the Pacific*, 111(759):587, 1999.

[27] A Vigan, M Bonnefoy, C Ginski, H Beust, R Galicher, Markus Janson, J-L Baudino, E Buenzli, J Hagelberg, V D'Orazi, et al. First light of the VLT planet finder SPHERE-I. Detection and characterization of the substellar companion GJ 758 B. *Astronomy & Astrophysics*, 587:A55, 2016.

[28] Cyril Petit, Jean-Francois Sauvage, Thierry Fusco, Anne Costille, David Mouillet, Jean-Luc Beuzit, Kjetil Dohlen, Markus E Kasper, Marcos Suárez Valles, Christian Soenke, et al. SAXO: the extreme adaptive optics system of SPHERE (I) system overview and global laboratory performance. *Journal of Astronomical Telescopes, Instruments, and Systems*, 2(2):025003, 2016.

[29] Antonio Garufi, Myriam Benisty, Tomas Stolker, Henning Avenhaus, Jos De Boer, Adriana Pohl, Sascha P Quanz, Carsten Dominik, Christian Ginski, Christian Thalmann, et al. Three years of SPHERE: the latest view of the morphology and evolution of protoplanetary discs. *arXiv preprint arXiv:1710.02795*, 2017.

[30] G Chauvin, S Desidera, A-M Lagrange, A Vigan, R Gratton, M Langlois, M Bonnefoy, J-L Beuzit, M Feldt, D Mouillet, et al. Discovery of a warm, dusty giant planet around HIP 65426. *Astronomy & Astrophysics*, 605:L9, 2017.

[31] A-L Maire, M Bonnefoy, C Ginski, A Vigan, S Messina, D Mesa, R Galicher, R Gratton, S Desidera, TG Kopytova, et al. First light of the VLT planet finder SPHERE-II. The physical properties and the architecture of the young systems PZ Telescopii and HD 1160 revisited. *Astronomy & Astrophysics*, 587:A56, 2016.

[32] A Zurlo, A Vigan, R Galicher, A-L Maire, D Mesa, R Gratton, G Chauvin, M Kasper, C Moutou, M Bonnefoy, et al. First light of the VLT planet finder SPHERE-III. New spectrophotometry and astrometry of the HR 8799 exoplanetary system. *Astronomy & Astrophysics*, 587:A57, 2016.

[33] Mickael Bonnefoy, A Zurlo, JL Baudino, P Lucas, D Mesa, A-L Maire, A Vigan, R Galicher, D Homeier, F Marocco, et al. First light of the VLT planet finder SPHERE-IV. Physical and chemical properties of the planets around HR8799. *Astronomy & Astrophysics*, 587:A58, 2016.

[34] Valerie A Rapson, Benjamin Sargent, G Germano Sacco, Joel H Kastner, David Wilner, Katherine Rosenfeld, Sean Andrews, Gregory Herczeg, and Nienke Van Der Marel. A Combined Spitzer and Herschel Infrared Study of Gas and Dust in the Circumbinary Disk Orbiting V4046 Sgr. *The Astrophysical Journal*, 810(1):62, 2015.

[35] HC Stempels and GF Gahm. The close T Tauri binary V 4046 Sagittarii. *Astronomy & Astrophysics*, 421(3):1159–1168, 2004.

[36] Katherine A Rosenfeld, Sean M Andrews, David J Wilner, and HC Stempels. A disk-based dynamical mass estimate for the young binary V4046 Sgr. *The Astrophysical Journal*, 759(2):119, 2012.

[37] Valerie A Rapson, Joel H Kastner, Sean M Andrews, Dean C Hines, Bruce Macintosh, Max Millar-Blanchaer, and Motohide Tamura. Scattered Light from Dust in the Cavity of the V4046 Sgr Transition Disk. *The Astrophysical Journal Letters*, 803(1):L10, 2015.

[38] Katherine A Rosenfeld, Sean M Andrews, David J Wilner, JH Kastner, and MK McClure. The structure of the evolved circumbinary disk around V4046 Sgr. *The Astrophysical Journal*, 775(2):136, 2013.

[39] E Sissa, J Olofsson, A Vigan, J C Augereau, V D'Orazi, S Desidera, R Gratton, et al. A new disk discovered with VLT/SPHERE around the M star GSC 7396-0759*. *Astronomy & Astrophysics*, 2018.

[40] Sean M Andrews, David J Wilner, Catherine Espaillat, AM Hughes, CP Dullemond, MK McClure, Chunhua Qi, and JM Brown. Resolved images of large cavities in protoplanetary transition disks. *The Astrophysical Journal*, 732(1):42, 2011.

[41] David F Gray. *The observation and analysis of stellar photospheres*. Cambridge University Press, 2005.

[42] C Lazzoni, S Desidera, F Marzari, A Boccaletti, M Langlois, D Mesa, R Gratton, Q Kral, N Pawellek, J Olofsson, et al. Dynamical models to explain observations with SPHERE in planetary systems with double debris belts. *arXiv preprint arXiv:1710.03019*, 2017.

[43] Edgar Everhart. An efficient integrator that uses Gauss-Radau spacings. In *International Astronomical Union Colloquium*, volume 83, pages 185–202. Cambridge University Press, 1985.